

**SYSTEM IDENTIFICATION, UNCERTAINTY QUANTIFICATION, AND  
INFERENCE OF CONSTITUTIVE RELATIONS IN ELECTROCHEMISTRY**

---

---

**SYSTEM IDENTIFICATION, UNCERTAINTY QUANTIFICATION, AND  
INFERENCE OF CONSTITUTIVE RELATIONS IN ELECTROCHEMISTRY**

---

---

BY

AVESTA AHMADI, B.ENG., M.SC.

A THESIS SUBMITTED TO THE SCHOOL OF COMPUTATIONAL SCIENCE & ENGINEERING AND THE  
SCHOOL OF GRADUATE STUDIES OF McMASTER UNIVERSITY IN THE PARTIAL FULFILLMENT OF THE  
REQUIREMENTS FOR THE DEGREE OF DOCTOR OF PHILOSOPHY

© COPYRIGHT BY AVESTA AHMADI

SEPTERMBER 2024

ALL RIGHTS RESERVED

Doctor of Philosophy 2024  
Computational Science & Engineering

McMaster University  
Hamilton, Ontario, Canada

**TITLE:** System Identification, Uncertainty Quantification, and Inference of  
Constitutive Relations in Electrochemistry

**AUTHOR:** Avesta Ahmadi  
M.Sc. Computational Science & Engineering  
McMaster University, Hamilton, Ontario

**SUPERVISOR:** Dr. Bartosz Protas

**NUMBER OF PAGES:** xviii, 172

# Abstract

This thesis consists of three parts, each part addressing a challenging question as regards mathematical and computational modeling in electrochemistry, with particular applications to Lithium-ion batteries. The first problem concerns the mean-clustering approach to modeling the evolution of lattice dynamics, which finds application in describing the lattice structure of Lithium-ion cathodes. Instead of tracking the state of individual lattice sites, this approach describes the time evolution of the concentrations of different cluster types. It leads to an infinite hierarchy of ordinary differential equations which must be closed by truncation using a so-called closure condition. The pair approximation is the most common form of such closure. Here, we consider its generalization, termed the “optimal approximation”, which we calibrate using a robust data-driven strategy. The form of the obtained optimal approximation allows us to deduce a simple sparse closure model. In addition to being more accurate than the classical pair approximation, this “sparse approximation” is also physically interpretable, which allows us to *a posteriori* refine the hypotheses underlying construction of this class of closure models. On the other hand, parametrization of the mean-cluster model closed with the pair approximation is shown to lead to an ill-posed inverse problem.

In the second problem we investigate the question of the state-of-charge estimation in cells operating under dynamic loading conditions. We use a hybrid data-driven strategy, referred to as “sparse identification of nonlinear dynamics”, in order to obtain a sparse representation of the dynamics of the system based on a provided library of candidates terms in the evolution equation. This strategy leverages the measurement data acquired using Electrochemical Impedance Spectroscopy and the sparse regression techniques. The dynamical system identified in this way is then used in combination with a suitable Kalman-type filter in order to enhance the estimates of the state of the system based on the measurement data while in operation.

In the third problem we construct a data-driven model describing Lithium plating in a battery cell,

which is a key process contributing to degradation of such cells. Starting from the fundamental Doyle-Fuller-Newman (DFN) model, we use asymptotic reduction and spatial averaging techniques to derive a simplified representation to track the temporal evolution of two key concentrations in the system, namely, the total intercalated Lithium on the negative electrode particles and total plated Lithium. This model depends on an a priori unknown constitutive relation representing the plating dynamics of the cell in function of the state variables. An optimal form of this constitutive relation is then deduced from experimental measurements of the time-dependent concentrations of different Lithium phases acquired through Nuclear Magnetic Resonance spectroscopy. This is done by solving an inverse problem in which this constitutive relation is found subject to minimum assumptions as a minimizer of a suitable constrained optimization problem where the discrepancy between the model predictions and experimental data is minimized. This optimization problem is solved using a state-of-the-art adjoint-based technique. In contrast to some of the earlier approaches to modeling Lithium plating, the proposed model is also able to predict non-trivial evolution of the concentrations in the relaxation regime when no current is applied to the cell. When equipped with an optimal constitutive relation, the model provides accurate predictions of the time evolution of both intercalated and plated Lithium across a wide range of charging/discharging rates. It can therefore serve as a useful tool for prediction and control of degradation mechanism in battery cells.

# Acknowledgements

First and foremost, I am deeply grateful to Dr. Bartosz Protas for not only serving as my supervisor but also as a mentor throughout my Master's and PhD journey. I appreciate your belief in me and for accepting me to work under your guidance. Over the past six years, you have been my mentor, supervisor, and guide, providing invaluable mental support and encouragement in every aspect of my work, especially during challenging research periods. As a supervisor, you have raised the standards very high for other supervisors and I am grateful for that. I hope to one day pass on the knowledge and wisdom you have shared with me.

I would like to express my gratitude to Dr. Jamie Foster for our illuminating discussions about research. Your success in the field has been a guiding inspiration for me. I am fortunate to have had you as a committee member during both my Master's and PhD studies. Our conversations consistently illuminated paths that I might otherwise have missed. Additionally, I want to extend my appreciation to Dr. Li Xi for your ongoing encouragement throughout my studies. Your guidance and insights have been instrumental in shaping my research journey. I also wish to acknowledge Dr. Gillian Goward and Dr. Kevin Sanders for generously providing the experimental data and their expertise in the field. Your contributions have played a crucial role in guiding our research efforts.

I would also like to extend my thanks to Dr. Essam Elsahwi and Ben Maxwell from Pulsenics Inc. for giving me the opportunity to collaborate with you and access the innovations you have introduced to the field. Our discussions have uncovered new research opportunities for us. I am grateful for the chance you provided and have gained invaluable knowledge from this experience. I would also like to extend my gratitude to the MITACS community for facilitating this collaboration.

Thank you to McMaster University and the School of Computational Science and Engineering for providing me with the opportunity to complete my studies. I would also like to extend my gratitude to all the staff, faculty members, and students of the School of Computational Science and Engineering for

their warm support, which has made this journey pleasant and rewarding.

Finally, I extend a special thank you to my family for their unwavering support, encouragement, and boundless love. I am especially grateful to my sister, Hoda Ahmadi, for her constant mental support and invaluable encouragement during the challenging periods of this journey. I also want to express my heartfelt gratitude to my beloved, Paniz Poursharif, for her infinite love and unwavering support throughout this journey. Your kindness and love have made this journey much more enjoyable for me. I look forward to sharing many more experiences and celebrating numerous achievements together as a family. Your presence in my life is a blessing for which I am forever thankful. Additionally, I would like to thank Paniz's family for their support and for welcoming me as a part of their own family.

---

# *Contents*

---

<b>Abstract</b>	<b>iii</b>
<b>Acknowledgments</b>	<b>v</b>
<b>Declaration of Authorship</b>	<b>xvii</b>
<b>1 Introduction</b>	<b>1</b>
<b>2 Data-Driven Optimal Closures for Mean-Cluster Models: Beyond the Classical Pair Approximation</b>	<b>7</b>
2.1 Introduction . . . . .	7
2.2 Model Problem . . . . .	10
2.3 Cluster Approximation . . . . .	12
2.3.1 Production and Destruction of 2-Clusters . . . . .	13
2.4 Closure Approximations . . . . .	16
2.4.1 Pair Approximation . . . . .	17
2.4.2 Optimal Approximation . . . . .	19
2.4.3 Results for Optimal Approximation . . . . .	22
2.4.4 Sparse Approximation and its Interpretation . . . . .	22
2.4.5 Prediction Capability of the Closure Models . . . . .	27
2.5 Determining Reaction Rates via Bayesian Inference . . . . .	29
2.5.1 Results of Bayesian Analysis . . . . .	31

2.6	Summary & Conclusions . . . . .	35
<b>3</b>	<b>State-of-Charge Estimation of Cells Under Dynamic Loading Conditions using Identification of Nonlinear Dynamics and Filtering</b>	<b>37</b>
3.1	Introduction . . . . .	37
3.1.1	Experimental Techniques . . . . .	40
3.1.2	Coulomb Counting . . . . .	41
3.1.3	Physical Modeling . . . . .	43
3.1.4	Equivalent Circuit Modeling . . . . .	43
3.1.5	Filtering Techniques . . . . .	44
3.1.6	Data-Driven Techniques . . . . .	45
3.1.7	Sparse Identification of Nonlinear Dynamics . . . . .	46
3.1.8	Outline . . . . .	46
3.2	Electrochemical Impedance Spectroscopy . . . . .	47
3.3	Experimental Data . . . . .	51
3.4	Extended Kalman Filtering . . . . .	53
3.4.1	Mathematical Background . . . . .	54
3.4.2	Results . . . . .	60
3.5	Sparse Identification of Nonlinear Dynamics . . . . .	62
3.5.1	Mathematical Background . . . . .	63
3.5.2	The Feature Library . . . . .	65
3.5.3	Results . . . . .	70
3.5.4	Interpretation of Results . . . . .	75
3.6	Unscented Kalman Filtering . . . . .	76
3.6.1	Mathematical Background . . . . .	77
3.6.2	Results . . . . .	79
3.7	Discussion . . . . .	81
<b>4</b>	<b>Data-Driven Approach to Learning Optimal Forms of Constitutive Relations in Models Describing Lithium Plating in Battery Cells</b>	<b>83</b>
4.1	Introduction . . . . .	83
4.2	Experimental Data . . . . .	87
4.3	Physical Modeling . . . . .	90
4.3.1	DFN Model . . . . .	93

4.3.2	Dimensionless Model . . . . .	99
4.3.3	Asymptotic Reduction and Averaging . . . . .	101
4.3.4	Comparison to SPMe+SR Model . . . . .	111
4.3.5	Linearizing Relaxation Dynamics . . . . .	113
4.4	Inverse modeling . . . . .	115
4.4.1	Relaxation Dynamics . . . . .	116
4.4.2	Excitation Dynamics . . . . .	118
4.4.3	Problem with Aggregated Data . . . . .	126
4.5	Results . . . . .	128
4.5.1	Relaxation Dynamics . . . . .	128
4.5.2	Excitation Dynamics . . . . .	129
4.6	Discussion . . . . .	136
<b>5</b>	<b>Summary, Conclusion and Outlook</b>	<b>140</b>
<b>Appendix A</b>	<b>Data-Driven Optimal Closures for Mean-Cluster Models</b>	<b>143</b>
A.1	Rotational Symmetry . . . . .	143
A.2	Bayesian Inference . . . . .	143
<b>Appendix B</b>	<b>Small-Signal Excitation by Electrochemical Impedance Spectroscopy</b>	<b>147</b>
B.1	Small-Signal Perturbation . . . . .	147
<b>Appendix C</b>	<b>Learning Optimal Forms of Constitutive Relations in Models Describing Lithium Plating</b>	<b>149</b>
C.1	Relaxation Dynamics . . . . .	149
C.2	Model Validation . . . . .	151
C.2.1	Validation of Gradients . . . . .	151
C.2.2	Validation of Computational Framework . . . . .	152

---

## *List of Figures*

---

2.1	The $\text{Li}[\text{Li}_{1/3}\text{Mn}_{2/3}]\text{O}_2$ lattice considered in [1] and shown here in (a) a 3D view and (b) a 2D view. The red, green and blue elements represent the Oxygen, Lithium and the transition metal (either Lithium or Manganese), respectively. . . . .	11
2.2	(a) Initial random state and (b) the final ordered state of the lattice for the $\text{Li}_{1/3}\text{Mn}_{2/3}$ system obtained via simulated annealing [1]. Black and green dots represent Li ions (more generally, negative elements) and Mn ions (more generally, positive elements), respectively. . . . .	12
2.3	An example of a linear chain 3-cluster on a 2D lattice. . . . .	12
2.4	All unique (up to rotational and translational symmetries) reversible reactions to destroy or produce clusters $(\oplus\oplus)$ and $(\oplus\ominus)$ . . . . .	14
2.5	All unique (up to rotational and translational symmetries) reversible reactions to destroy or produce clusters $(\ominus\ominus)$ and $(\oplus\ominus)$ . . . . .	14
2.6	Schematic of a 2D triangular lattice with chains of 3-clusters, namely, linear, angled and triangular clusters. The clumping intensity of this lattice is equal to the proportion of the triangles over all triplets types, which is equal to $\frac{2}{5}$ . . . . .	18
2.7	The mean-square errors (2.14) for the pair approximation (PA) and optimal approximation subject to hard regularization for (a) the system $\text{Li}_{1/2}\text{Mn}_{1/2}$ (OA-1/2) and (b) for the system $\text{Li}_{1/3}\text{Mn}_{2/3}$ (OA-1/3). . . . .	23

2.8	The mean-square reconstructions errors (2.14) for the pair approximation, the optimal approximation constructed subject to hard regularization based on the data for the system $\text{Li}_{1/2}\text{Mn}_{1/2}$ and for the corresponding sparse approximation for different cluster types, cf. Table 2.3. Note that the results for the last two closures differ only for the clusters marked with (**). . . . .	25
2.9	Dependence of the mean error (2.21) characterizing the accuracy of the different closure relations on the stoichiometry for (a) hard regularization and (b) soft regularization employed in the solution of optimization problem (2.15) with parameters indicated in the legend for $\text{Li}_{1/3}\text{Mn}_{2/3}$ system. “PA” and “OA” refer to, respectively, the pair and the optimal approximation. . . . .	29
2.10	The mean error (2.21) characterizing the accuracy of the different closure relations indicated in the legend for a range of different stoichiometries. . . . .	29
2.11	Posterior probability densities $\mathbb{P}(\mathbf{K} \tilde{\mathbf{C}})$ obtained using Algorithm 4 for problem (2.23) with system (2.8) closed using (a) the pair approximation and (c) the optimal approximation with exponents determined subject to hard regularization (OA-1/2). The parameters $k_1$ , $k_2$ and $k_3$ are represented in term of the Cartesian coordinates whereas the remaining three nonzero rate constants are encoded in terms of the color of the symbols via the color maps shown in panel (b) and (d). The size of the symbols in panels (a) and (c) is proportional to $J(\mathbf{K})^{-1}$ . . . . .	33
2.12	Histograms of the error functional $\mathcal{J}(\mathbf{K})$ obtained along the Markov chains for problem (2.23) with system (2.8) closed using (a) the pair approximation and (b) the optimal approximation with exponents determined subject to hard regularization (OA-1/2). The black vertical lines represent the values of the error functional $\mathcal{J}(\alpha_1^*, \alpha_2^*)$ obtained when the model based on the SA closure is used. . . . .	33
2.13	Time evolution of pair concentrations (a) $C_{++}$ , (b) $C_{--}$ and (c) $C_{+-}$ obtained by solving system (2.8) closed with the pair approximation, the optimal approximation with exponents subject to hard regularization and the sparse approximation. The concentrations obtained from the simulated annealing experiment are shown as well. . . . .	34
3.1	Terminal voltage across the cell as a function of its SoC in two different operating modes: charge and discharge. A constant-current charge/discharge with three rest periods at approximately $z = 0.25$ , $z = 0.5$ and $z = 0.75$ is used in this cycle. Note that the open-circuit voltage in this graph is approximated using a polynomial fit to charge and discharge terminal voltages. . . . .	40

3.2	Nyquist plot (a), and Bode plot (b) at the beginning of charge in a constant-loading experiment. Real( $Z$ ) and Imag( $Z$ ) refer to the real and imaginary parts of impedance, respectively.	49
3.3	Schematic of a Thevenin equivalent circuit model used as a large-signal model. The terminal voltage of the cell $u_t$ [V], the polarization potential $u_p$ [V], the open-circuit potential $u_{oc}$ [V], the current applied to the cell $I$ [A], the ohmic resistance $R_0$ [ $\Omega$ ], the charge-transfer resistance $R_p$ [ $\Omega$ ], and the double-layer capacitance $C_p$ [F] are shown. . . . .	50
3.4	Terminal voltage $u_t$ (a), and the evolution of electrochemical parameters, $R_0(t)$ (b), $R_p(t)$ (c), and $C_p(t)$ (d) in time for a 60A constant-current charge and discharge cycle. The electrochemical parameters are collected every 25 seconds. . . . .	51
3.5	SoC of a cell determined via the CC method (3.3) under static loading conditions with 20 minutes rest periods after each 0.2 increment of SoC during charge/discharge. The effect of relaxation dynamics of the cell and its self-discharge during the rest period is neglected.	52
3.6	Current $I(t)$ (a), terminal voltage $u_t(t)$ (b), and state-of-charge $z(t)$ (c) of the cell for one cycle operating under dynamic loading conditions. . . . .	53
3.7	The absolute error of SoC estimation at $t = t_2$ , $\mathcal{E}$ , cf. (3.10), using FCC (blue) and EKF (orange), for ten different cycles operating under dynamic loading conditions. . . . .	60
3.8	SoC evolution determined via FCC and EKF (a), and terminal voltage estimation using EKF (b) for one of the experiments under dynamic loading conditions. Note that the plots are magnified such that only the dynamic loading part of the experiment is shown ( $t_1 < t < t_2$ ). . . . .	61
3.9	Schematic of SINDy framework. . . . .	64
3.10	Error $\mathcal{J}_2$ computed for SoC according to (3.39) (a), and $\mathcal{J}_1$ computed for the polarization potential according to (3.38) (b) by comparing the reference state of the cell with the solution of the forward ODE model in (3.28) for each cycle. The identified model is obtained by minimizing the cost functional (3.30) with respect to the vector of coefficients using three different sparsity levels for each cycle. The indices on the vertical axes represent the data sets (cycles) used to solve problem (3.30), whereas the indices on the horizontal axes represent the data sets used to test the accuracy of the obtained models. Note that "Th" on the y-axis of each sub-figure refers to the Thevenin model (3.11). Also, some of the errors presented in (a) and (b) attain large values, and hence, their values are replaced with 0.5 and 0.1, respectively, for ease of visualization. . . . .	71

3.11 Results of fitting model (3.28) via the SINDy framework using composite data of all cycles at four different sparsity levels for the polarization potential. The threshold for the coefficients of the feature library terms for SoC is adjusted such that only one term (the CC term) is preserved in its dynamics. . . . .	72
3.12 Time evolution of the polarization potential $u_p(t)$ for one cycle as the solution of the forward problem (3.28) obtained by solving minimization problem (3.30) via the SINDy framework and by using composite data of all cycles, with different thresholding levels. . . . .	73
3.13 Time evolution of polarization potential $u_p(t)$ for one cycle as the solution of the forward problem (3.28) obtained by solving minimization problem (3.30) via the SINDy framework and using composite data of all cycles with the threshold set at $\Lambda = 2 \times 10^{-10}$ . The time evolution is shown over a part of the cycle only. The performance of the Thevenin model and the model obtained by SINDy are compared with reference data. . . . .	74
3.14 Results of fitting model (3.28) via the SINDy framework using composite data of all cycles at four different sparsity levels for SoC estimation. The threshold for the coefficients of the feature library terms for the polarization potential is set at $\Lambda = 2 \times 10^{-10}$ . . . . .	75
3.15 Time evolution of SoC by solving the ODE system (3.41) in time, and the confidence intervals of SoC estimates for all cycles obtained using the AUKF algorithm 2. The reference SoC values and the SoC estimates by FCC model are also shown for comparison. . . . .	80
3.16 The mean absolute error of SoC estimates (3.44) using the FCC model and the AUKF algorithm. The errors are computed by comparing to the reference state. . . . .	81
 4.1 Terminal voltage and current applied to the cell (a,c,e,g,i), and evolution of Li content in time in different phases via Li-NMR spectroscopy method (b,d,f,h,j) using different test protocols of the cell. . . . .	89
4.2 Evolution of Li content in time in negative electrode solid phase corresponding to intercalated Li (a), and plated Li (b) for different C-rates. Note that the variables are normalized. . . . .	90
4.3 Schematic of a Li-ion cell in the charging state. Li ions deintercalate from the positive electrode surface, migrate toward the negative electrode through the electrolyte, and intercalate into negative particles. Electrons will migrate through the external circuit toward the negative electrode. The domain of the system is highlighted in red. . . . .	95
4.4 Cost functional history $\mathcal{J}_1(\beta)$ relative to its initial value as a function of iteration number. . . . .	129



4.10	The dependence of the state variable $C_1(t)$ on time in the solution of the forward problem (4.37) using the optimal parameters values and optimal forms of the constitutive relation $(\bar{\beta}, \bar{\alpha}, \bar{\omega})$ reconstructed by calibrating system (4.37) using aggregated data $\mathcal{D}_t$ for charge, discharge and OCV regimes, cf. Section 4.4.3. The dashed green and the solid blue lines represent the experimental concentrations and the solution of the forward problem (4.37) using optimal parameters and constitutive relations, respectively. . . . .	137
4.11	The dependence of the state variable $C_2(t)$ on time in the solution of the forward problem (4.37) using the optimal parameters values and optimal forms of the constitutive relation $(\bar{\beta}, \bar{\alpha}, \bar{\omega})$ reconstructed by calibrating system (4.37) using aggregated data $\mathcal{D}_t$ for charge, discharge and OCV regimes, cf. Section 4.4.3. The dashed green and the solid blue lines represent the experimental concentrations and the solution of the forward problem (4.37) using optimal parameters and constitutive relations, respectively. . . . .	138
C.1	The behaviour of $\kappa_1(\epsilon)$ (a), $\kappa_2(\epsilon)$ (b), and $\kappa_3(\epsilon)$ (c), over a wide range of $\epsilon$ values, by using $\omega_1^{(0)} = \omega_2^{(0)} = 0.7$ , $\alpha^{(0)} = 3$ as the starting point, and using different perturbations of constitutive relations and parameters. Two different discretizations of the interval $\mathcal{L}$ are used, namely, $N = 100$ (dashed lines) and $N = 5000$ (solid lines). Note that discretization of the state interval $\mathcal{L}$ does not affect the quantity $\kappa_3(\epsilon)$ , as its partial derivative (4.63) is computed without discretizing the state space $\mathcal{L}$ . Note that $\beta = [-0.1, -0.1, -0.1, -0.1]$ in this experiment. . . . .	152
C.2	$\nabla_{\omega_1}^{L^2} \mathcal{J}_2$ (a), $\nabla_{\omega_2}^{L^2} \mathcal{J}_2$ (c), $\nabla_{\omega_1}^{H^1} \mathcal{J}_2$ (b), and $\nabla_{\omega_2}^{H^1} \mathcal{J}_2$ (d) at the first iteration of Algorithm 3. Note the mean of the gradient in (d), as it is reconstructed in $H_0^1$ space. . . . .	153
C.3	Performance evaluation of the iterative algorithm according to Algorithm 3. The mean squared error between the true and the reconstructed constitutive relations (a), the relative decay of cost functional normalized with respect to its initial value (b), and the evolution of parameter $\alpha$ (c) are shown as functions of iterations $n$ . . . . .	154
C.4	Time history of concentrations $C_1(t)$ (a) and $C_2(t)$ (b) obtained using the true parameter and constitutive relations (dotted green line), the initial guess of parameter and relations (dashed red line), and the optimal reconstructed parameter and relations (solid blue line). . . . .	155
C.5	Constitutive relations (a) $\omega_1(C_1)$ , (b) $\omega_2(C_2)$ , and (c) $\omega(C_1, C_2)$ . Optimally reconstructed constitutive relations $\bar{\omega}$ (blue), along with the initial guess of relations $\omega^{(0)}$ (red) and the true relations $\tilde{\omega}$ (green) are shown. Note that grey vertical lines in panels (a) and (b) denote the identifiability region for the last iteration of the Algorithm 3. . . . .	156

---

## *List of Tables*

---

2.1	The functional forms of the closures based on the pair approximation and on the proposed optimal closures for each triplet type. Unknown parameters (exponents) are indicated in the last column. . . . .	20
2.2	Exponents defining the optimal closure models, cf. Table 2.1, found by solving problem (2.15) with hard regularization ( $\beta_1 = 0$ , $\beta_2 = \delta = 2$ ) based on the data for the system $\text{Li}_{1/3}\text{Mn}_{2/3}$ (OA-1/3) and the system $\text{Li}_{1/2}\text{Mn}_{1/2}$ (OA-1/2) for each 3-cluster type indicated in the first column. For comparison, the exponents characterizing the pair approximation (PA) are also shown. The results are rounded to two decimal places. . . . .	23
2.3	Closure relations for 3-clusters of different types derived based on the pair approximation, the optimal approximation using the data for the system $\text{Li}_{1/2}\text{Mn}_{1/2}$ , cf. Table 2.2, and the sparse approximation discussed in Section 2.4.4. . . . .	24
3.1	Candidate relations for the polarization potential and their time derivatives. The time derivative relations are included in the feature library of the SINDy framework. Note that the prefactors are dropped from the time derivative relations as they will be determined as part of the optimization process (3.30). Note that the time dependency is dropped from the variables, and $k$ , $k_1$ , $k_2$ , $k_3$ and $k_4$ are arbitrary constants. . . . .	68
3.2	State and control variables included in the control library $\mathbf{U}$ for each of the state variables.	69

# Declaration of Authorship

I, Avesta Ahmadi, declare that this thesis titled “System Identification, Uncertainty Quantification, and Inference of Constitutive Relations in Electrochemistry” and the work presented in it are my own. Below is the list of authorship for each chapter.

- Chapter 1: Introduction
  - This chapter is my own work.
- Chapter 2: Data-Driven Optimal Closures for Mean-Cluster Models: Beyond the Classical Pair Approximation
  - The content used in this chapter has been published in the American Physical Society journal, Physical Review E, with the DOI No: 10.1103/PhysRevE.106.025313.
  - This chapter is a work of myself, Dr. Jamie Foster, and Dr. Bartosz Protas.
- Chapter 3: State-of-Charge Estimation of Cells Under Dynamic Loading Conditions using Identification of Nonlinear Dynamics via SINDy
  - The data used in this chapter are the property of Pulsenics Inc.
  - This chapter is a work of myself and Dr. Bartosz Protas, in collaboration with Dr. Essam Elsahwi and Ben Maxwell from Pulsenics Inc.
- Chapter 4: Data-Driven Approach to Learning Optimal Forms of Constitutive Relations in Models Describing Lithium Plating in Battery Cells
  - The content used in this chapter is under review by the John Wiley & Sons journal, Journal of Computational Chemistry.

- The data used in this chapter was provided by Dr. Kevin Sanders and Dr. Gillian Goward.
  - This chapter is a work of myself and Dr. Bartosz Protas, in collaboration with Dr. Kevin Sanders and Dr. Gillian Goward.
- Chapter 5: Summary, Conclusion and Outlook
    - This chapter is my own work.

All chapters of this thesis are edited based on Dr. Bartosz Protas's suggestions.

# *Chapter 1*

---

## *Introduction*

---

In recent decades, there has been a growing demand for green energy solutions, driving the prominence of electrochemical systems in shaping a sustainable future. Lithium (Li) batteries, renowned for their high energy density and extended cycle life, have emerged as pivotal electrochemical energy storage solutions. They are extensively employed across various industries, including portable electronic devices [2], grid storage [3], and electric vehicles [4]. Given the increasing demand for green technologies, addressing challenges related to the reliability and performance of these systems becomes vital. Substantial research efforts are dedicated to understanding the physical and electrochemical mechanisms governing Li-ion cell operations. A complete understanding of these dynamics is essential for enhancing the efficiency, lifetime, and reliability of such systems. This study focuses on improving our ways of describing the dynamics of various processes within the cell using computational and mathematical tools.

An electrochemical cell consists of several components: a porous positive electrode, a porous negative electrode, a separator, and an electrolyte. These components play crucial roles during the operation of the Li-ion cell through cycling. The positive and negative electrodes are separated by a porous separator and immersed in a liquid electrolyte. Two current collectors are attached to the electrodes at the two opposite ends, providing electrical connections to an external circuit. Lithium, the main constituent of the cell, exists in both the electrolyte and the cathode material. During the cell cycling, Li ions migrate from one electrode to another, on the surface of which the intercalation/deintercalation processes occur. Intercalation involves the electrochemical reaction of Li ions with the anode or cathode material, bonding with the material. During charging, Li ions deintercalate from the positive electrode, releasing an electron. These

electrons travel through the current collectors and the external circuit to the negative electrode's solid phase, while Li ions dissolve into the electrolyte, diffuse toward the negative electrode, and intercalate into its solid phase. Charging continues until the negative electrode reaches maximum capacity to accept Li ions (all free sites are occupied). During discharge, the reverse occurs. The positive electrode typically consists of a Lithium-rich substrate like Lithium-Nickel-Manganese-Cobalt Oxide (NMC cathode) [5], while common choices for the negative electrode are graphite or silicon, capable of absorbing Li during intercalation [6]. Intercalation and deintercalation of Li ions at the electrodes are crucial mechanisms in cell operation. These desired processes are accompanied by certain undesired mechanisms, leading to degradation or inefficiencies affecting cell operations [7, 8]. Degradation mechanisms involve complex physical and chemical processes that can degrade the cell over time, reduce its performance efficiency, and limit cycle life. To understand, analyze, mitigate, and control the impact of these mechanisms, researchers use experimental [9, 10] and modeling techniques [11, 12]. One contribution of the present research is to enhance our understanding of cell processes by leveraging experimental methodologies and computational and mathematical techniques. Specifically, our work focuses on understanding the lattice structure of the cathode material, modeling cell operation inefficiencies in harsh operating conditions, and identifying a quantitative model describing a primary degradation mechanism in the negative electrode known as Lithium plating [13].

To comprehend and characterize the operation of Li-ion cells, researchers have developed mathematical models that represent the processes within these cells. These models are crucial for analyzing and optimizing cell performance. Various modeling frameworks are found in the literature, including equivalent circuit modeling [14, 15], physics-based modeling [16], and machine-learning based modeling [17, 18]. Equivalent circuit modeling involves assigning an equivalent circuit element to each physical phenomenon in the cell. This method models the aggregate behavior of different processes within the cell as a circuit, which mimics the overall dynamics of the cell without spatial resolution. In contrast, physics-based models utilize partial differential equations to simulate cell behavior in both space and time. They usually have the form expressing certain conservation principles (such as the conservation of mass or charge) combined with suitable constitutive relations describing the dependence of thermodynamic fluxes on state variables. While computationally intensive, these models effectively capture cell dynamics while maintaining model interpretability. On the other hand, machine-learning based models are typically purely predictive and lack direct connections to the physical principles governing the cell operation. Consequently, these models sacrifice interpretability as they usually do not incorporate the underlying physics of the cell. Hybrid machine-learning based models [19, 20] address this limitation by integrating physical information into their predictive structures. Each modeling technique has distinct

advantages and drawbacks. Throughout this thesis, we select modeling approaches based on the specific requirements of each application. Generally, for comprehending the intricate dynamics of cells across scales, physics-based models and hybrid data-driven based models are preferred.

One significant focus of this research is inverse modeling and data assimilation, representing the process of integrating observational data, which can be distributed across time and space, with mathematical models to enhance the prediction accuracy. The primary objective of data assimilation is to minimize prediction errors generated by mathematical models and reduce uncertainties, thereby improving the accuracy of forecasts regarding the system's future states or behaviors. Various computational techniques are employed for this purpose, including deterministic methods based on variational approaches, probabilistic methods grounded in Bayesian inference, and filtering techniques [21]. Deterministic techniques, such as variational methods, aim to minimize discrepancies between observational data and model outputs with respect to unknown parameters. However, these methods usually do not explicitly quantify uncertainties in their estimations. In contrast, Bayesian inference and filtering techniques minimize the mismatch between model output and observations and at the same time quantify the uncertainties associated with model predictions, making them more robust for handling real-world data assimilation challenges.

Variational techniques in inverse modeling are used to develop accurate predictive models for various applications and derive insights from them. Inverse modeling techniques find application across different scientific and engineering domains such as atmosphere modeling studies [22], reservoir characterization in petroleum engineering [23], fluid dynamics [24, 25], and medical imaging tomography [26]. Researchers have also explored inverse modeling in electrochemical systems both in deterministic frameworks [27–32] and probabilistic frameworks [33, 34]. Inverse modeling utilizes experimental data to calibrate mathematical models, ensuring optimal alignment between model outputs and empirical measurements by adjusting unknown parameters or functions. This approach is instrumental in the electrochemistry field for optimizing material properties and constitutive relations, such as constant diffusion coefficients in the solid phase of electrodes [28], constant reaction rates for intercalation/deintercalation processes at solid-electrolyte interface [28], space-dependent diffusion coefficients in the solid phase of electrodes [35], space-dependent conductivities of electrodes [36], state-dependent diffusion coefficient in solid phase and the transference number in electrolyte phase [27], and state-dependent ion intercalation parameters [31]. In this study, the inverse modeling technique is leveraged in Chapters 2, 3 and 4 for calibrating mathematical models.

In this study, we encounter various types of inverse problems across different contexts. The sim-

plest type, encountered in Chapter 2, involves inverse models with constant control parameters. Standard optimization approaches in finite dimension will be employed to solve such problems, supplemented by regularization techniques to enhance the robustness, stability and the smoothness of the solution. Chapter 3 utilizes a similar optimization approach but integrates sparse regularization techniques in its framework. This method aims to achieve a sparse representation of parameter vectors, enhancing model interpretability, reducing its complexity, and striking a balance between model accuracy and complexity. The second type of inverse problems are obtained when model parameters vary spatially, a well-explored area involving optimization constrained by partial differential equations (PDEs). The adjoint analysis method is commonly applied here to solve PDE-constrained optimization problems. In Chapter 4, the focus shifts to a different type of inverse problem where model parameters vary as functions of state variables (dependent variables) rather than independent variables. This approach, distinct from previous chapters, involves state-dependent constitutive relations to be calibrated through data-driven techniques. Bukshynov et al. [37,38] investigated similar problems using adjoint analysis to derive gradient information. Subsequently, gradient-based optimization techniques were employed to optimize a cost functional, with minimal prior assumptions about the functional forms of constitutive relations. Examples of optimal reconstruction of constitutive relations in the electrochemistry research can be found in [27,31], where material properties are assumed to be a function of state variables, and the dependence is determined through data-driven approach. This computational technique is used in Chapter 4 for optimal reconstruction of constitutive relations describing the plating process in the cell.

Inverse problems encountered across various scientific and engineering domains are typically ill-posed, implying that their solutions are highly sensitive to noise in measurement data, thereby introducing uncertainty. Even small variations in measurement data can lead to substantial changes in the identified optimal solutions. To quantify this uncertainty and assess the degree of ill-posedness, techniques in uncertainty quantification are employed [21]. Bayesian inference, a probabilistic method, addresses this question by using measurement data to assign relative probabilities to different possible solutions of an inverse problem [39]. This approach has found application in different fields such as ecology [40], physics [41], and electrochemistry [33,34]. In the Bayesian framework, unknown parameters and constitutive relations are treated as random variables, and the accuracy of their reconstruction depends on the quality of measurements and the inherent ill-posed nature of the inverse problem. Sampling techniques, particularly Markov-chain Monte Carlo (MCMC) methods, are commonly employed to effectively explore the posterior space and construct probability distributions. This iterative process involves repeated solution of the forward model to sample the posterior space of random variables, navigating toward more favorable regions while intermittently also exploring less promising areas. Rather than yielding a sin-

gle point estimate as in deterministic approaches to solving inverse problems, the Bayesian framework provides a posterior probability distribution for random variables representing the solution of the inverse problem, thereby, capturing its uncertainty in a probabilistic manner. This methodology will be employed in Chapter 2 to quantify uncertainty in mean-cluster models.

Variational methods and Bayesian inference techniques for solving inverse problems typically involve using observational data in an offline manner. In this context, "offline" means that observational data is extracted and then utilized collectively for model calibration. Conversely, filtering techniques, such as Kalman filters [21], operate in real-time to minimize discrepancies between model outputs and current observations as data becomes available. These techniques leverage past data iteratively to recursively update and optimize estimates of the system's state, while also quantifying uncertainties at each time step. Kalman filters are mathematical algorithms specifically designed for recursive optimal estimation of a dynamical system state from noisy observations over time. While variational methods and Bayesian inference techniques are suitable for offline model calibration using historical data, filtering techniques excel in real-time applications where continuous updates and uncertainty quantification are crucial. In Chapter 3 of this thesis, Kalman filters are utilized for online estimation of the state-of-charge of cells. Key aspects of this research related to inverse modeling techniques include:

- Development of an inverse modeling framework utilizing regularization techniques to estimate constant reaction rates in mean-field clustering models. Chapter 2 focuses on parameter estimation and uncertainty quantification of these parameters.
- Establishment of an inverse modeling framework employing sparse regularization techniques to identify cell dynamics from a predefined library of candidate terms. This investigation is detailed in Chapter 3.
- Development of an inverse modeling framework to estimate constant parameters and state-dependent constitutive relations for identifying and predicting intercalation and plating mechanisms in cells. This is accomplished in Chapter 4.

The thesis is structured as follows. In Chapter 2, a mathematical model is developed for predicting the lattice structure of the NMC layer in cathodes. Both deterministic and probabilistic solutions to the inverse problem are explored. Chapter 3 investigates the state-of-charge estimation of cells under dynamic loading conditions. A hybrid data-driven model is implemented to enhance the accuracy of state estimations. Chapter 4 focuses on developing a mathematical model to describe Lithium plating in the negative electrode of cells where suitable. Constitutive relations are reconstructed using measurement

data. Chapter 5 summarizes the key conclusions drawn from the thesis and some more technical material is collected in several appendices.

## *Chapter 2*

---

# *Data-Driven Optimal Closures for Mean-Cluster Models: Beyond the Classical Pair Approximation*

---

### **2.1. Introduction**

Evolution of particles on a structured lattice is typically described by discrete lattice models rather than continuous space models. These models are usually not solvable exactly and have to be studied through computer simulations. One approach to describing the evolution of particles on a structured lattice is to keep track of all interacting particles as is done in various Monte-Carlo techniques such as simulated annealing. However, these methods are costly as they determine the lattice structure which is unnecessary in many applications. What is often sufficient is knowledge of the type and the number of different clusters in the lattice, which can then be used for model fitting purposes along with experimental measurements such as, e.g., Nuclear Magnetic Resonance (NMR) data [1]. Hence, as an alternative to Monte-Carlo methods, one can develop a simplified description of particle interactions in terms of evolving probabilities of particle clusters of different types in the form of a dynamical system which is sufficient for many applications. These approaches are referred to as “mean-field clustering methods” and find applications in many areas of science and engineering. The Ising model, as a canonical application of mean-field methods, is a model of ferromagnetism describing the evolution of magnetic moments in a lattice. Both

Monte-Carlo methods [42] and mean-field methods [43] have been employed to study this problem. Another example of the application of such models is the contact process which is a stochastic process describing the growth of a population on a structured or unstructured lattice. Cluster approximations are used to find mean-field properties of such systems. Population dynamics in ecology [44, 45] is one example of such processes. Another example is the disease spread in epidemiology that has been widely studied on structured networks [46–52] and complex networks [53, 54]. Failure propagation [55] and emergence of marriage networks [56] are some other examples of contact processes.

The focus of the present study is on cluster-based modeling of systems of interacting particles on two-dimensional (2D) structured lattices. The specific application which motivates the present study is related to prediction of the structure of materials used in Lithium-ion batteries [1]. Using a cluster approximation method, one can construct a hierarchical dynamical system describing the evolution of concentrations of different clusters in the lattice during a real annealing process. In other words, the evolution of concentrations of clusters of size  $n$  involves concentrations of clusters of size  $(n + 1)$ . To solve this system of equations one is required to close it by prescribing the evolution of concentrations of  $(n + 1)$  clusters, which in turn will be determined by probabilities of clusters of a still higher order. This process therefore gives rise to an infinite hierarchy of equations which is exact but is intractable both analytically and computationally. Thus, one needs to truncate and close this infinite hierarchy of equations. Various moment closure approximations have been used for this purpose. Ben-Avraham et al. [57] proposed a class of approximations for 1D lattices with extensions developed in higher dimensions, namely, the mean-field and pair approximations. These techniques take into account local interactions between neighbouring elements only and completely neglect interactions between non-nearest neighbours on a lattice. While the pair approximations have been used to model many physical systems defined on triangular lattices, it is known that this approach is not very effective when the lattice suffers from “frustration” effects occurring when the interactions between the degrees of freedom on the lattice are incompatible with the lattice geometry [58]. Such effects usually arise in the presence of magnetic interactions where minimization of the classical lattice energy of the system is not possible. As a result, the energy of the system converges to degenerate ground states with some pair interactions remaining at higher energy levels. For simplicity, we will not consider such situations in the present study.

A lot of research on cluster models has been carried out in the field of equilibrium statistical mechanics focusing primarily on improving the mean-field approximation models, e.g., via the Bethe-Peierls approximation [59] or the cluster variation method [60]. These models aim to find a mean-field solution by making some additional assumptions about the particular system under study. Applications of mean-

field and pair approximation methods to various problems in science and engineering can also be found in [49, 53, 61, 62] and in [46, 47, 49, 53, 54, 61–63], respectively. Some extensions of the pair approximation technique are also introduced in [64] where interactions between different elements are considered to be generic functions of distance. In the present study our goal is to develop and validate a general data-driven methodology that will allow us to optimally close (in a mathematically precise sense) the infinite hierarchy of equations. We will refer to this approach as the “optimal approximation”. This approach leads to a general, simple and mathematically interpretable closure model.

As an emerging application of lattice dynamics, Harris et al. [1] used a simulated annealing approach to investigate the crystalline structure of cathode materials used in state-of-the-art Lithium-ion batteries. More precisely, they focused on layers of NMC (Nickel-Manganese-Cobalt) used in most modern commercial Li-ion batteries. These cathodes are described by the chemical formula  $\text{Li}(\text{NMC})\text{O}_2$ , where 2D layers of Lithium, Oxygen and NMC are stacked on top of each other. The capacity enhancement observed in such materials is attributed to changes in the local microscopic structure of the cathode layers [65, 66], however, important aspects of this structure are not yet completely understood. Hence, further refinement of this battery technology requires more information about the arrangement of elements inside these layers. In [1] simulated annealing was used to generate statistical information about arrangements of different species on the lattice in the NMC layer of a cathode, which was very costly and did not scale up to large lattice sizes. The model developed in the present study aims to address this limitation. While the proposed approach is general and can be applied to many lattice systems, to fix attention, we will develop it here for the problem from [1] as an example. Other applications of approaches based on lattice dynamics in physics and chemistry include organic synthesis reactions in the fields of heterogeneous catalysis and materials engineering [67], adsorption models of binary mixtures [68] and microstructure mapping of perovskite materials [69].

In this work, we use the mean-clustering approach to build a hierarchical system of equations for the evolution of concentrations of different clusters inside a structured lattice of the NMC cathode layer. We assume a triangular lattice compatible with the structure of the NMC layer [1]. This spatial structure is important in detecting the rotational symmetries of the system. A dynamical system is constructed to describe reactions between different species which are limited to swaps between nearest-neighbour elements. The underlying principle is that as the “temperature” decreases the lattice converges to a certain equilibrium state through a series of element swaps, controlled by specific rate constants. Our new approach consists of two distinct steps: first, the truncated hierarchical dynamical system is closed using an optimal approximation whose parameters are inferred from simulated annealing data; it is demonstrated

that such an optimal closure is in fact both simpler and more accurate than the nearest-neighbour approximation proposed in [57]. Additionally, robustness of the predictive performance of the obtained model is demonstrated based on problems with different stoichiometries. Second, the reaction rates parameterizing the dynamical system with the three types of closure, i.e., pair approximation, optimal approximation and sparse approximation, are inferred from the simulated annealing data using a Bayesian approach which also allows us to estimate the uncertainty of these reconstructions; this will show that the model with the optimal closure is also less prone to calibration uncertainty than the model closed with the nearest-neighbour approximation.

The paper is organized as follows: further details about our model problem are presented in Section 2.2; then, in Section 2.3 we introduce a dynamical system governing the evolution of the concentrations of different clusters and in Section 2.4 we describe and analyze the closure models we consider, which are the pair approximation and the optimal closure, the latter of which leads to the new sparse approximation; reactions rates in the resulting dynamical systems are then inferred using a Bayesian approach in Section 2.5; finally, summary and conclusions are deferred to Section 2.6 and some technical material is collected in Appendix A.

## 2.2. Model Problem

In this section we provide some details about a lattice evolution problem that will serve as our test case. In [1] Harris et al. used a simulated annealing method to identify an evolving arrangement of particles on the lattice and keep track of their interactions. One material similar to the materials actually used in Li-ion batteries is  $\text{Li}[\text{Li}_{1/3}\text{Mn}_{2/3}]\text{O}_2$ , where 2D sheets of an Oxygen layer, transition metal layer and Lithium layer are stacked on top of each other, as shown in Figure 2.1. Transition metal layer consists of Manganese and Lithium.

In the simulated annealing method, the energy of the system is calculated by considering the local charge neutrality at oxygen sites. Each oxygen element is surrounded by six nearest neighbours, cf. Figure 2.1. The energy of each oxygen site is then determined by considering the charge contributions of the neighbouring sites to its charge balance with the goal of achieving neutrality. The simulated annealing approach attempts to find a 2D lattice configuration minimizing the total energy of the system  $E = \sum_i E_i$  corresponding to a specific “temperature”, where  $E_i$  is the energy over each oxygen site. This is a probabilistic approach to finding global optima in a discrete space described by the Boltzmann distribution and mimics the annealing process applied to actual materials. These materials are annealed at a high

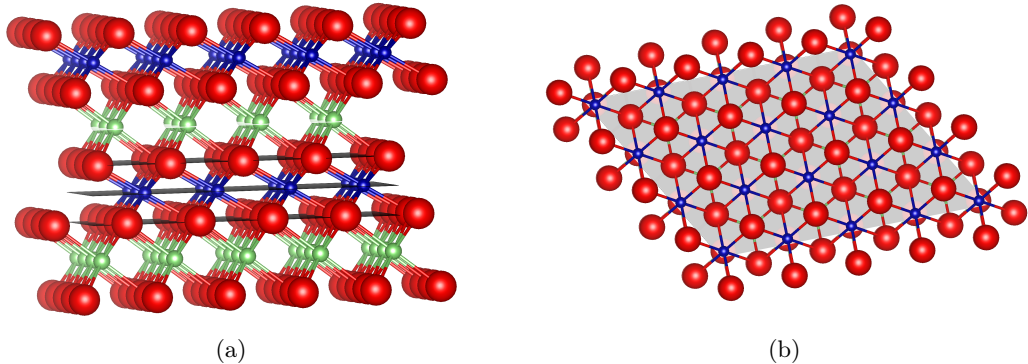


Figure 2.1: The  $\text{Li}[\text{Li}_{1/3}\text{Mn}_{2/3}]\text{O}_2$  lattice considered in [1] and shown here in (a) a 3D view and (b) a 2D view. The red, green and blue elements represent the Oxygen, Lithium and the transition metal (either Lithium or Manganese), respectively.

temperature, followed by quenching to the desired temperature. The choice of how the temperature is decreased is in principle arbitrary, however, the equilibrium state must be reached at the end of the annealing process for every arbitrarily chosen temperature profile (we note that here “temperature” does not refer to the thermodynamic temperature of the system). The details of this approach we consider can be found in [1].

In the crystal structure of the annealed metal layer of  $\text{Li}[\text{Li}_{1/3}\text{Mn}_{2/3}]\text{O}_2$  each triangle consists of two Mn elements and one Li element. In this structure, the energy  $E_i$  over each oxygen site becomes zero and the total energy of the system will be zero accordingly, as shown in Figure 2.2b. In the simulated annealing study of this structure the temperature was reduced in a stepwise manner and enough time was allowed for the structure to stabilize at an equilibrium at each intermediate temperature. The results obtained for the system with  $\text{Li}_{1/3}\text{Mn}_{2/3}$  are shown in the form of the final lattice structure in Figure 2.2. Annealing experiments with the same protocol were also performed for systems with different ratios of Li and Mn in  $\text{Li}_x\text{Mn}_{1-x}$  where  $x \in \{0.25, 0.30, 0.33, 0.36, 0.42, 0.50, 0.58, 0.64, 0.70, 0.75\}$ , but these results are not shown here for brevity. Our goal is to build a model that will accurately predict the evolution of concentrations of different particle clusters present in the lattice without having to solve the entire annealing problem. We note that the elements Mn and Li have charges, respectively, of (+4) and (+1). However, the cluster approximation model, cf. Section 2.3, makes no assumptions about the charges of the elements and hence for simplicity the symbols (+) and (-) will hereafter represent the elements Mn and Li, respectively. The concentrations  $\widetilde{C}_i$ ,  $i \in \{(++)\}, ((-), (--) \}$  of 2-clusters as functions of time (or temperature) will be used as data to construct the optimal closure approximation and to infer the reaction rates in the model. The lattice evolution in this method does not have a natural time scale and for concreteness we will assume that the unit of time is set by an individual iteration of the

simulated annealing experiment. Notably, in this model all concentrations are independent of location on the lattice due to spatial homogeneity.

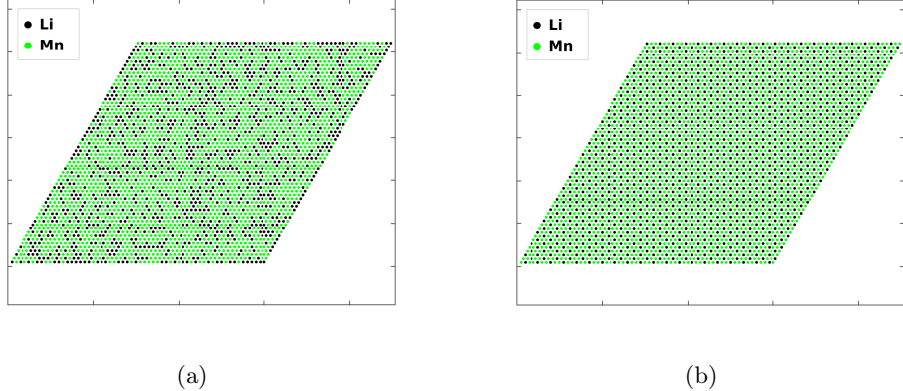


Figure 2.2: (a) Initial random state and (b) the final ordered state of the lattice for the  $\text{Li}_{1/3}\text{Mn}_{2/3}$  system obtained via simulated annealing [1]. Black and green dots represent Li ions (more generally, negative elements) and Mn ions (more generally, positive elements), respectively.

### 2.3. Cluster Approximation

In this section we develop a system of evolution equations for concentrations of clusters in a two-element system with elements denoted (+) (or  $\oplus$ ) and (−) (or  $\ominus$ ). In this study, a cluster of size  $n$  is referred to as a  $n$ -cluster and elements inside the cluster form a closed or an open chain. The concentration of a cluster is defined as the probability of finding that particular cluster among all clusters of the same shape but with different compositions. As an example, the concentration of the 3-cluster shown in Figure 2.3 is denoted  $C_{ijk}$ , where  $i, j, k \in \{+, -\}$ .

**Remark.** *The normalization condition requires that the sum of the concentrations of all possible  $n$ -clusters with the same geometry must be equal to one [57]:*

$$\sum_{S_1, S_2, \dots, S_n} C_{S_1 S_2 \dots S_n} = 1, \quad (2.1)$$

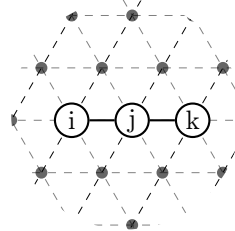


Figure 2.3: An example of a linear chain 3-cluster on a 2D lattice.

where the indices  $1, 2, 3, \dots, n$  enumerate different sites within a cluster with two consecutive ones corresponding to nearest neighbours and  $S_i \in \{+, -\}$  denotes the state of that specific site. Applying this to 1-clusters and 2-clusters in our model, the following equations are derived from the normalization condition:

$$C_+ + C_- = 1 \quad (2.2a)$$

$$C_{++} + C_{--} + C_{+-} + C_{-+} = 1. \quad (2.2b)$$

The concentrations of the  $(+-)$  and  $(-+)$  clusters are the same due to the rotational symmetry of the system, as stated in Theorem A.1.1 in the Appendix, such that  $C_{+-} = C_{-+}$ . Hence, the normalization condition becomes

$$C_{++} + C_{--} + 2C_{+-} = 1. \quad (2.3)$$

The aim is to deduce a dynamical system describing the evolution of the probabilities of 2-clusters. There are three different types of 2-clusters found on the lattice, namely,  $\oplus\oplus$ ,  $\ominus\ominus$  and  $\oplus\ominus$ .

### 2.3.1 Production and Destruction of 2-Clusters

The rate of change of the concentration of specific clusters is determined by the rate at which they are produced and destroyed. Production or destruction of a certain cluster occurs through swaps among nearest-neighbour elements on the lattice. Each swap of nearest-neighbour elements is called here a reaction. The rate equations can then be derived using the window method [57]. In this approach we consider all possible reactions that change the composition of a particular 2-cluster in a certain window containing this cluster, via a swap between one of the elements inside the window and one of its nearest-neighbour elements outside the window. For example, in order to derive the rate equation for the  $(\oplus\oplus)$  cluster, in Figure 2.4 we show all possible reactions that will produce or destroy this cluster via nearest-neighbour element swaps. We note that all of these reactions occur in a 2D sheet rather than on a 3D lattice, which is compatible with our model problem introduced in Section 2.2. In each of the reactions, the neighbour element (highlighted in red) will swap with one of the elements of the window (highlighted in blue) to produce a  $(\oplus\oplus)$  cluster in the forward reaction. Conversely, reverse reactions destroy the  $(\oplus\oplus)$  cluster and produce a  $(\oplus\ominus)$  cluster. The rotational symmetry of the lattice allows us to reduce the number of possible reactions to those shown in Figure 2.4. Moreover, reactions taking place inside a triangular-shaped 3-cluster do not change the total count of 2-clusters inside the triangle and are therefore

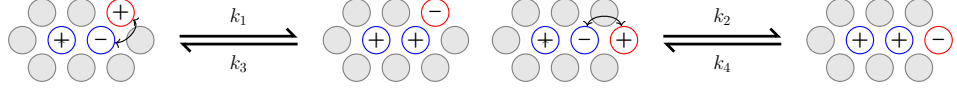


Figure 2.4: All unique (up to rotational and translational symmetries) reversible reactions to destroy or produce clusters  $(\oplus\oplus)$  and  $(\ominus\ominus)$ .

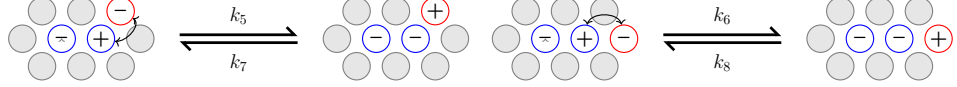


Figure 2.5: All unique (up to rotational and translational symmetries) reversible reactions to destroy or produce clusters  $(\ominus\ominus)$  and  $(\oplus\ominus)$ .

disregarded. This observation eliminates the number of possible reactions and hence simplifies the model. Each reaction has a unique rate constant denoted  $k_1, k_2, \dots, k_8$ . Note that these rate constants are required to be non-negative.

As can be observed in Figure 2.4, 3-clusters with three types of bonds are involved in the derivation of rate equations. The first type is the linear 3-cluster in which the two bonds are colinear. The second type is the cluster in which there is an obtuse angle of 120 degrees between the bonds due to the triangular shape of the lattice. The third type is the triangular cluster in which the elements form a triangle with 60 degrees between the bonds. We will refer to these as the linear, angled and triangular clusters, respectively. For simplicity, linear clusters will be represented as a combination of elements with a straight line  $[(\bullet\bullet\bullet)]$ , angled clusters as a combination of elements with a hat sign  $\widehat{[(\bullet\bullet\bullet)]}$  and triangular clusters as a combination of elements with a triangle  $\widehat{\widehat{[(\bullet\bullet\bullet)]}}$ , where  $\bullet$  is either  $+$  or  $-$ . The set of all 3-cluster types will be denoted

$$\Theta = \left\{ \overline{++}, \overline{--}, \overline{+-}, \overline{-+}, \overline{+-}, \overline{-+}, \right. \\ \widehat{++}, \widehat{--}, \widehat{+-}, \widehat{-+}, \widehat{+-}, \widehat{-+}, \\ \widehat{\widehat{++}}, \widehat{\widehat{--}}, \widehat{\widehat{+-}}, \widehat{\widehat{-+}} \left. \right\}. \quad (2.4)$$

The rate equations for the  $(\ominus\ominus)$  and  $(\oplus\ominus)$  clusters can be derived in a similar way, by considering all possible reactions that produce or destroy these two clusters as shown in Figure 2.5. We thus obtain the following system of rate equations for the concentrations  $C_{++}$ ,  $C_{--}$  and  $C_{+-}$

$$\frac{d}{dt}C_{++} = 4k_1C_{\widehat{+-}} + 2k_2C_{\widehat{--}} - 4k_3C_{\widehat{\widehat{+-}}} - 2k_4C_{\widehat{\widehat{--}}}, \quad (2.5a)$$

$$\frac{d}{dt}C_{--} = 4k_5C_{\widehat{+-}} + 2k_6C_{\widehat{--}} - 4k_7C_{\widehat{\widehat{+-}}} - 2k_8C_{\widehat{\widehat{--}}}, \quad (2.5b)$$

$$\begin{aligned} \frac{d}{dt}C_{+-} &= 2k_3\widehat{C_{++}} + 2k_7\widehat{C_{--}} + k_4\widehat{C_{++}} + k_8\widehat{C_{--}} \\ &\quad - 2k_1\widehat{C_{++}} - 2k_5\widehat{C_{--}} - k_2\widehat{C_{++}} - k_6\widehat{C_{--}}. \end{aligned} \tag{2.5c}$$

We note that in deriving the rate equations for the  $(++)$  and  $(--)$  clusters, cf. (2.5a)–(2.5b), each reaction is accounted for in proportion to the number of its rotational symmetries on the lattice. For example, destruction of the  $(\widehat{+-+})$  cluster shown in Figure 2.4 can also occur in 3 other configurations of the cluster obtained by rotating the original cluster. Hence, a coefficient of 4 appears in equations (2.5a)–(2.5b) to account for these symmetries. We note that, on the other hand, the linear clusters have only 2 possible symmetries, hence a coefficient of 2 appears in front of the relevant terms. Moreover, as regards the rate equation for the  $(+-)$  cluster, the number of rotational symmetries for each 3-cluster is half of those considered for the other two cases such that in equation (2.5c) the corresponding coefficients are 2 and 1. The reason is that the  $(+-)$  and  $(-+)$  clusters are distinguished in the model and to clarify this, consider a  $(++)$  cluster inside a  $(\widehat{+-+})$  cluster. A swap between elements  $(+)$  and  $(-)$  will result in the production of a  $(+-)$  cluster. However, if we rotate this 3-cluster, we get a  $(-++)$  cluster and a swap between the elements  $(+)$  and  $(-)$  will result in the production of a  $(-+)$  cluster. Hence, the rate equations for the evolution of the  $(+-)$  and  $(-+)$  clusters have to be derived individually. In system (2.5), the rate equation for the  $(-+)$  cluster is not included, as it will be accounted for via the normalization condition (2.2b). Again, due to the rotational symmetry, the concentrations of the  $(+-)$  and  $(-+)$  clusters are equal, hence the normalization condition simplifies to (2.3).

An important aspect of system (2.5) is its hierarchical structure in the sense that the rates of change of concentrations of 2-clusters are given in terms of the concentrations of 3-clusters and if one were to write down equations for their rates of change they would involve concentrations of 4-clusters, etc. Thus, system (2.5) is not closed and needs to be truncated which we will do so here at the level of 2-clusters. Two strategies for closing the truncated system are discussed in Section 2.4.

In addition, the normalization condition (2.3) can be modified to a dynamic form by taking the derivative with respect to time

$$\frac{d}{dt}C_{++} + \frac{d}{dt}C_{--} + 2\frac{d}{dt}C_{+-} = 0. \tag{2.6}$$

As can be verified, this equation is satisfied automatically by system (2.5a)–(2.5c). Moreover, the rate of the forward reaction will be equal to the rate of corresponding reverse reaction in the chemical equilibrium. As we are interested in the equilibrium state of reactions, the following relations can be written for

each pair of forward and reverse reactions in equilibrium

$$k_1 \widehat{C_{+-}} = k_3 \widehat{C_{++}} \implies Q_1 = \frac{k_1}{k_3} = \frac{\widehat{C_{++}}}{\widehat{C_{+-}}}, \quad (2.7a)$$

$$k_2 \widehat{C_{--}} = k_4 \widehat{C_{--}} \implies Q_2 = \frac{k_2}{k_4} = \frac{\widehat{C_{--}}}{\widehat{C_{--}}}, \quad (2.7b)$$

$$k_5 \widehat{C_{-+}} = k_7 \widehat{C_{-+}} \implies Q_3 = \frac{k_5}{k_7} = \frac{\widehat{C_{-+}}}{\widehat{C_{-+}}}, \quad (2.7c)$$

$$k_6 \widehat{C_{-+}} = k_8 \widehat{C_{-+}} \implies Q_4 = \frac{k_6}{k_8} = \frac{\widehat{C_{-+}}}{\widehat{C_{-+}}}, \quad (2.7d)$$

where  $Q_i$ ,  $i = 1, \dots, 4$ , denote the equilibrium constants for each reversible reaction.

## 2.4. Closure Approximations

In this section we discuss two strategies for closing system (2.5), by which we mean expressing the concentration of 3-clusters on the right-hand side (RHS) of this system in terms of a suitable function of the concentrations of 2-clusters. In other words, the goal is to replace each of the triplet concentrations  $C_i$ ,  $i \in \Theta$ , in (2.5) with suitably chosen functions  $g_i(\mathbf{c})$ , where  $\mathbf{c} = [C_+, C_-, C_{++}, C_{--}, C_{-+}]$ , such that the closed system will have the form

$$\frac{d}{dt} C_{++} = 4k_1 g_{+-}(\mathbf{c}) + 2k_2 g_{-+}(\mathbf{c}) - 4k_3 g_{++}(\mathbf{c}) - 2k_4 g_{--}(\mathbf{c}), \quad (2.8a)$$

$$\frac{d}{dt} C_{--} = 4k_5 g_{-+}(\mathbf{c}) + 2k_6 g_{-+}(\mathbf{c}) - 4k_7 g_{-+}(\mathbf{c}) - 2k_8 g_{--}(\mathbf{c}), \quad (2.8b)$$

$$\begin{aligned} \frac{d}{dt} C_{-+} = & 2k_3 g_{+-}(\mathbf{c}) + 2k_7 g_{-+}(\mathbf{c}) + k_4 g_{++}(\mathbf{c}) + k_8 g_{--}(\mathbf{c}) \\ & - 2k_1 g_{+-}(\mathbf{c}) - 2k_5 g_{-+}(\mathbf{c}) - k_2 g_{-+}(\mathbf{c}) - k_6 g_{--}(\mathbf{c}). \end{aligned} \quad (2.8c)$$

The first approach to finding these functions is the pair approximation based on the classical method introduced in [57] and the second is a new optimal closure approximation. The problem of finding the rate constants  $k_1, \dots, k_8$  in (2.5) will be addressed in Section 2.5.

### 2.4.1 Pair Approximation

The pair approximation is a classical approach to closing truncated hierarchical dynamical systems. It was first used by Dickman [70] in a surface-reaction model and later by Matsuda et al. [44] for a structured lattice appearing in a population dynamics problem. In our model, we use the pair approximation approach in order to close the dynamical system (2.5) at the level of 2-clusters. The state of a site is denoted  $i, j, k \in \{+, -\}$  for a two-element system. Global concentrations are denoted  $C_i$  giving the probability that a randomly chosen site in the lattice is in state  $i \in \{+, -\}$ . Similarly,  $C_{ij}$  is the global concentration of 2-clusters in state  $ij$ . In addition, *local* concentrations are denoted  $P_{j|i}$  and give the conditional probability that a randomly chosen nearest neighbour of a site in state  $i$  is in state  $j$ . These local concentrations can be expressed in terms of global concentrations using the rules governing conditional probabilities as [44, 71]

$$C_{ij} = C_{ji} = C_i P_{j|i} = C_j P_{i|j}, \quad (2.9a)$$

$$\sum_{i \in \{+, -\}} C_i = 1, \quad (2.9b)$$

$$\sum_{i \in \{+, -\}} P_{i|j} = 1 \text{ for any } j \in \{+, -\}. \quad (2.9c)$$

Equation (2.9a) is invariant with respect to the rotational symmetries of the lattice, cf. Appendix A.1. Also, the global concentration of a triplet in state  $(ijk)$  can be derived in a similar approach as Equation (2.9a),

$$C_{ijk} = C_i P_{j|i} P_{k|ij} = C_{ij} P_{k|ij}. \quad (2.10)$$

The  $P_{k|ij}$  term in this equation involves 3 elements in a triplet. In order to break down the triplet concentration in terms of pair and singlet concentrations, one is required to find an equivalent expression for the  $P_{k|ij}$  term. The underlying assumption of the pair approximation method is to neglect the interaction between the non-nearest neighbour elements,  $i$  and  $k$  in this case, according to Figure 2.3 [44, 45, 71]. This results in an approximation at the level of 3-clusters expressed in terms of quantities defined at the level of 2-clusters as

$$P_{k|ij} \approx P_{k|j}. \quad (2.11)$$

A different approach could also be adopted to derive the pair approximation formulation resulting in the same closure model. In this approach, assuming a triplet in state  $(ijk)$  on a random lattice (in which all

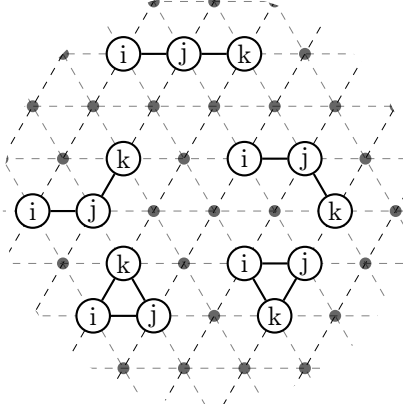


Figure 2.6: Schematic of a 2D triangular lattice with chains of 3-clusters, namely, linear, angled and triangular clusters. The clumping intensity of this lattice is equal to the proportion of the triangles over all triplets types, which is equal to  $\frac{2}{5}$ .

non-nearest-neighbour elements are decoupled), the global concentration of this triplet can be written as

$$C_{ijk} = C_i C_j C_k Q_{ij} Q_{jk} T_{ijk}, \quad (2.12a)$$

$$Q_{ij} = \frac{C_{ij}}{C_i C_j}, \quad (2.12b)$$

where  $C_i$ ,  $C_j$  and  $C_k$  denote the global concentrations of singlets,  $Q_{ij}$  and  $Q_{ik}$  are the pair correlations of nearest neighbours and  $T_{ijk}$  is the triple correlation of the chain. Note that element  $i$  and element  $k$  on a random lattice are considered not to be nearest-neighbours. Also, there is no factor  $Q_{ik}$  in equation (2.12a) as the correlation of non-nearest-neighbours is represented by  $T_{ijk}$ . According to the underlying assumption of pair approximation, the non-nearest-neighbour elements are decoupled. There is no deterministic way of calculating correlations of non-nearest neighbour elements [72] and some additional assumptions have to be made in order to close (2.5). The standard pair approximation method neglects all triple correlations such that  $T_{ijk} = 1$ . This is an equivalent approximation to Equation (2.11).

Each regular lattice can be described by two parameters: the number of neighbours per site ( $m$ ) and the proportion of triangles to triplets ( $\theta$ ), which determines the clumping intensity of the lattice. A triangular lattice has  $m = 6$  neighbours per site and  $\theta = \frac{2}{5}$ , as shown in Figure 2.6. Similarly, chain-like triplets in a triangular lattice can be categorized into two groups: linear triplets with 180-degree bonds, and angled triplets with 120-degree bonds. As is evident from Figure 2.6, the probability of finding a triplet in a closed form, angled form and linear form is equal to  $\frac{2}{5}$ ,  $\frac{2}{5}$ , and  $\frac{1}{5}$ , respectively. As the shape of triplets is important in our model, these probabilities have to be taken into account as coefficients when calculating the corresponding concentrations. Morris [73] and Keeling [51] have proposed formulas for approximating the fraction of closed and open chains in a certain state ( $ijk$ ) on a regular lattice by taking

into account the clumping effect of triangles in the lattice. Following these studies, the concentrations of each type of triplet are approximated as

$$C_{\overline{ijk}} \approx g_{\overline{ijk}} = (1 - \theta) \frac{1}{3} \frac{C_{ij} C_{jk}}{C_j}, \quad (2.13a)$$

$$C_{\widehat{ijk}} \approx g_{\widehat{ijk}} = (1 - \theta) \frac{2}{3} \frac{C_{ij} C_{jk}}{C_j}, \quad (2.13b)$$

$$C_{\widehat{\overline{ijk}}} \approx g_{\widehat{\overline{ijk}}} = \theta \frac{C_{ij} C_{jk} C_{ki}}{C_i C_j C_k}, \quad (2.13c)$$

where  $\overline{ijk}$ ,  $\widehat{ijk}$ , and  $\widehat{\overline{ijk}}$  denote a linear, angled and triangular triplet, respectively. The specific forms taken by expressions (2.13a)–(2.13b) for different  $i, j, k \in \{+, -\}$  are collected in Table 2.1. Using this model in relations (2.8a)–(2.8c) produces a closed system of equations providing an approximate description of the problem.

#### 2.4.2 Optimal Approximation

As will be shown in Section 2.4.3, the closure based on the pair approximation introduced above is not very accurate. In order to improve the accuracy of the closure, here we propose a new approach based on nonlinear regression analysis of simulated annealing data. This is a data-driven strategy where an *optimal* form of the closure is obtained by fitting an expression in an assumed well-justified form to the data. The pair approximation scheme attempts to predict the concentrations of the higher-order clusters in terms of concentrations of lower-order ones using expressions with the functional forms given in (2.13). In the new approach, we close system (2.5) using relations generalizing the expressions in (2.13) which depend on a number of adjustable parameters. These parameters, representing the exponents of different concentrations, are then calibrated against the simulated annealing data by solving a suitable constrained optimization problem. Information about the new more general closure relations and how they compare to the pair approximation for different 3-clusters is collected in Table 2.1 where we also group the parameters to be determined in the vector  $\mathbf{V}_i$ , with  $i \in \Theta$  representing different cluster types.

Notably, the new functional forms are generalizations of the expressions used in the pair approximation obtained by allowing for more freedom in how the new expressions for closures depend on the cluster concentrations. The numerators of the new expressions involve concentrations of *all* nearest-neighbour 2-clusters such that the effect of non-nearest-neighbour clusters is still neglected. The denominators, on the other hand, involve the concentrations of singlets present in the triplet which makes the functional form of the new closure different from the pair approximation in some cases. The parameters (exponents) defining the proposed optimal closures in Table 2.1 are subject to the following constraints ensuring

Triplet Type	Pair Approximation	Optimal Approximation	Parameters (exponents)
$i$	$g_i(C_+, \dots, C_{+-})$	$g_i(C_+, \dots, C_{+-}; \mathbf{V}_i)$	$\mathbf{V}_i$
$+++$	$\frac{1}{5} \frac{C_{++}^2}{C_+}$	$\frac{1}{5} \frac{C_{++}^{\gamma_1}}{C_+^{\xi_1}}$	$\mathbf{V}_{+++} = [\gamma_1 \xi_1]$
$---$	$\frac{1}{5} \frac{C_{--}^2}{C_-}$	$\frac{1}{5} \frac{C_{--}^{\gamma_1}}{C_-^{\xi_1}}$	$\mathbf{V}_{---} = [\gamma_1 \xi_1]$
$+-+$	$\frac{1}{5} \frac{C_{+-}^2}{C_-}$	$\frac{1}{5} \frac{C_{+-}^{\gamma_1}}{C_+^{\xi_1} C_-^{\xi_2}}$	$\mathbf{V}_{+-+} = [\gamma_1 \xi_1 \xi_2]$
$-+-$	$\frac{1}{5} \frac{C_{+-}^2}{C_+}$	$\frac{1}{5} \frac{C_{+-}^{\gamma_1}}{C_+^{\xi_1} C_-^{\xi_2}}$	$\mathbf{V}_{-+-} = [\gamma_1 \xi_1 \xi_2]$
$++-$	$\frac{1}{5} \frac{C_{++} + C_{+-}}{C_+}$	$\frac{1}{5} \frac{C_{++}^{\gamma_1} C_{+-}^{\gamma_2}}{C_+^{\xi_1} C_-^{\xi_2}}$	$\mathbf{V}_{++-} = [\gamma_1 \gamma_2 \xi_1 \xi_2]$
$--+$	$\frac{1}{5} \frac{C_{--} + C_{+-}}{C_-}$	$\frac{1}{5} \frac{C_{--}^{\gamma_1} C_{+-}^{\gamma_2}}{C_+^{\xi_1} C_-^{\xi_2}}$	$\mathbf{V}_{--+} = [\gamma_1 \gamma_2 \xi_1 \xi_2]$
$\widehat{+++}$	$\frac{2}{5} \frac{C_{++}^2}{C_+}$	$\frac{2}{5} \frac{C_{++}^{\gamma_1}}{C_+^{\xi_1}}$	$\mathbf{V}_{\widehat{+++}} = [\gamma_1 \xi_1]$
$\widehat{---}$	$\frac{2}{5} \frac{C_{--}^2}{C_-}$	$\frac{2}{5} \frac{C_{--}^{\gamma_1}}{C_-^{\xi_1}}$	$\mathbf{V}_{\widehat{---}} = [\gamma_1 \xi_1]$
$\widehat{+-+}$	$\frac{2}{5} \frac{C_{+-}^2}{C_-}$	$\frac{2}{5} \frac{C_{+-}^{\gamma_1}}{C_+^{\xi_1} C_-^{\xi_2}}$	$\mathbf{V}_{\widehat{+-+}} = [\gamma_1 \xi_1 \xi_2]$
$\widehat{-+-}$	$\frac{2}{5} \frac{C_{+-}^2}{C_+}$	$\frac{2}{5} \frac{C_{+-}^{\gamma_1}}{C_+^{\xi_1} C_-^{\xi_2}}$	$\mathbf{V}_{\widehat{-+-}} = [\gamma_1 \xi_1 \xi_2]$
$\widehat{++-}$	$\frac{2}{5} \frac{C_{++} + C_{+-}}{C_+}$	$\frac{2}{5} \frac{C_{++}^{\gamma_1} C_{+-}^{\gamma_2}}{C_+^{\xi_1} C_-^{\xi_2}}$	$\mathbf{V}_{\widehat{++-}} = [\gamma_1 \gamma_2 \xi_1 \xi_2]$
$\widehat{--+}$	$\frac{2}{5} \frac{C_{--} + C_{+-}}{C_-}$	$\frac{2}{5} \frac{C_{--}^{\gamma_1} C_{+-}^{\gamma_2}}{C_+^{\xi_1} C_-^{\xi_2}}$	$\mathbf{V}_{\widehat{--+}} = [\gamma_1 \gamma_2 \xi_1 \xi_2]$
$\widehat{\widehat{+++}}$	$\frac{2}{5} \frac{C_{++}^3}{C_+^3}$	$\frac{2}{5} \frac{C_{++}^{\gamma_1}}{C_+^{\xi_1}}$	$\mathbf{V}_{\widehat{\widehat{+++}}} = [\gamma_1 \xi_1]$
$\widehat{\widehat{---}}$	$\frac{2}{5} \frac{C_{--}^3}{C_-^3}$	$\frac{2}{5} \frac{C_{--}^{\gamma_1}}{C_-^{\xi_1}}$	$\mathbf{V}_{\widehat{\widehat{---}}} = [\gamma_1 \xi_1]$
$\widehat{\widehat{+-+}}$	$\frac{2}{5} \frac{C_{+-}^3}{C_-^2 C_+}$	$\frac{2}{5} \frac{C_{+-}^{\gamma_1} C_{+-}^{\gamma_2}}{C_+^{\xi_1} C_-^{\xi_2}}$	$\mathbf{V}_{\widehat{\widehat{+-+}}} = [\gamma_1 \gamma_2 \xi_1 \xi_2]$
$\widehat{\widehat{-+-}}$	$\frac{2}{5} \frac{C_{+-}^3}{C_+^2 C_-}$	$\frac{2}{5} \frac{C_{+-}^{\gamma_1} C_{+-}^{\gamma_2}}{C_+^{\xi_1} C_-^{\xi_2}}$	$\mathbf{V}_{\widehat{\widehat{-+-}}} = [\gamma_1 \gamma_2 \xi_1 \xi_2]$

Table 2.1: The functional forms of the closures based on the pair approximation and on the proposed optimal closures for each triplet type. Unknown parameters (exponents) are indicated in the last column.

well-posedness of the resulting system (2.8)

- the difference of the sums of the exponents in the numerators and in the denominators is equal to one, i.e.,  $\sum_j \gamma_j - \sum_j \xi_j = 1$ , ensuring that the terms representing the closure have the units of concentration,
- the exponents in the numerators need to be non-negative, i.e.,  $\gamma_j \geq 0$ , since otherwise the corresponding terms representing the closure model may become unbounded as the concentration approaches zero, causing solutions of the ODE system (2.8) to blow up,
- the exponents in the numerators need to be bounded  $\gamma_1, \gamma_2 \leq \delta$ , where  $\delta$  is the upper bound on the exponent which needs to be specified, as otherwise the corresponding terms representing the

closure model may also become large causing solutions of the ODE system (2.8) to blow up,

4. while denominators involve concentrations of singlets only, which are time independent, in some cases it is necessary to restrict the corresponding exponents as otherwise the terms representing the closure model will have large prefactors which may also cause the solutions of the ODE system (2.8) to blow up; hence, we impose  $\beta_1 \leq \xi_1, \xi_2 \leq \beta_2$ , where  $\beta_1$  and  $\beta_2$  are the lower and upper bounds on the exponents to be specified;

Optimal parameters  $\mathbf{V}_i$  of the closure model are obtained separately for each cluster type  $i$  by minimizing the mean-square error between the experimental concentration data  $\tilde{C}_i(t)$  obtained from simulated annealing experiments, and the predictions of the corresponding ansatz function

$g_i(\tilde{C}_+, \tilde{C}_-, \tilde{C}_{++}(t), \tilde{C}_{--}(t), \tilde{C}_{+-}(t); \mathbf{V}_i)$ , cf. Table 2.1, obtained with the parameter vector  $\mathbf{V}_i$  over the time window  $[0, T]$ , where  $T$  corresponds to the end of the simulated annealing process. Then, for each  $i \in \Theta$ , error functional is defined as

$$J_i(\mathbf{V}_i) = \frac{1}{2} \int_0^T [g_i(\tilde{C}_+, \tilde{C}_-, \tilde{C}_{++}(t), \tilde{C}_{--}(t), \tilde{C}_{+-}(t); \mathbf{V}_i) - \tilde{C}_i(t)]^2 dt \quad (2.14)$$

which leads to the following family of constrained optimization problems

$$\begin{aligned} & \min_{\mathbf{V}_i} J_i(\mathbf{V}_i), \\ \text{subject to: } & \begin{cases} 0 \leq \gamma_j \leq \delta, & 1 \leq j \leq \Gamma_i \\ \beta_1 \leq \xi_j \leq \beta_2, & 1 \leq j \leq \Xi_i \\ \sum_j \gamma_j - \sum_j \xi_j = 1 \end{cases}, \end{aligned} \quad (2.15)$$

for each  $i \in \Theta$ , where  $\Gamma_i, \Xi_i \in \{1, 2\}$  are the numbers of the exponents appearing in the numerator and the denominator for a given cluster type, cf. Table 2.1.

We note that choosing different values of the adjustable parameters  $\delta, \beta_1$  and  $\beta_2$ , which determine how stringent the constraints in the optimization problem (2.15) are, has the effect of regularizing the solutions of this problem. We will consider the following two cases (when the lower/upper bound is equal to  $-\infty/\infty$ , this means that effectively there is no bound)

- “soft” regularization with  $\beta_1 = -\infty, \beta_2 = \infty, \delta = 6$ , and
- “hard” regularization with  $\beta_1 = 0$  and  $\beta_2 = \delta = 2$ .

In each case optimization problem (2.15) is solved numerically in MATLAB using the nonlinear programming routine `fmincon`. The optimal closures determined in these two ways are compared to the pair approximation in Section 2.4.3.

### 2.4.3 Results for Optimal Approximation

In this section we determine the optimal structure of the closure models given in Table 2.1 by solving optimization problem (2.15) for each type of 3-cluster in the set  $\Theta$ , cf. (2.4), as described in Section 2.4.2. Parameters of the closure relations given in Table 2.1 are determined separately for each cluster type by solving problem (2.15) and the obtained results are collected in the form of the values of the exponents in Table 2.2, where, for comparison we also show the exponents corresponding to the pair approximation, cf. Section 2.4.1. We recall that for each 3-cluster type problem (2.15) is solved with both soft and hard regularization. In Table 2.2, the optimal results are presented for solving problem (2.15) subject to hard regularization ( $\beta_1 = 0$ ,  $\delta = \beta_2 = 2$ ) by separately fitting the closure models to the data obtained for two systems with  $\text{Li}_{1/2}\text{Mn}_{1/2}$  and  $\text{Li}_{1/3}\text{Mn}_{2/3}$ . The first system is interesting since, as we shall see below, due to the symmetry in the concentrations of Li and Mn, closure models calibrated based on the data from this system are particularly robust with respect to different stoichiometries. The second system is considered in our analysis due to its interesting behaviour at low temperatures where physically relevant crystalline microstructure are obtained, as discussed in Section 2.2. This system is also used as a benchmark in [1]. In Table 2.2 we note that most of the exponents in the optimal closure approximation tend to be different from the corresponding exponents in the pair approximation. Interestingly, we observe that many exponents obtained for the optimal closure by fitting to the data for the system  $\text{Li}_{1/2}\text{Mn}_{1/2}$  are equal to zero or one, opening the possibility of finding a simpler closure model to be investigated in Section 2.4.4.

The mean-square error (2.14) for each 3-cluster type for the pair approximation and the optimal closure fitted to  $\text{Li}_{1/2}\text{Mn}_{1/2}$  and  $\text{Li}_{1/3}\text{Mn}_{2/3}$  systems is shown in Figure 2.7. For both systems and for almost all 3-cluster types the optimal closure leads to a more accurate description with errors (2.14) smaller by a few orders of magnitude than when the pair approximation is used. In the next section we will simplify the obtained optimal closure and will propose an interpretation of the resulting structure.

### 2.4.4 Sparse Approximation and its Interpretation

In this section we investigate the exponents characterizing the optimal closure presented in Table 2.2. As can be observed, many exponents in the optimal closure relations are equal or close to zero and this trend is more pronounced in the optimal closure obtained by fitting the data for the symmetric system

Triplet Type	PA	OA-1/3	OA-1/2	PA	OA-1/3	OA-1/2	PA	OA-1/3	OA-1/2	PA	OA-1/3	OA-1/2
	$\gamma_1$			$\xi_1$			$\gamma_1$			$\xi_1$		
$\overline{+++}$	2	1.12	1.00	1	0.12	0.00	-	-	-	-	-	-
$\overline{-+-}$	2	1.19	1.00	1	0.19	0.00	-	-	-	-	-	-
$\widehat{+++}$	2	1.00	1.00	1	0.00	0.00	-	-	-	-	-	-
$\widehat{-+-}$	2	1.39	1.00	1	0.39	0.00	-	-	-	-	-	-
$\widehat{\overline{+++}}$	3	2.00	2.00	3	0.99	0.99	-	-	-	-	-	-
$\widehat{\overline{-+-}}$	3	1.76	1.18	3	0.76	0.18	-	-	-	-	-	-
$\gamma_1$			$\xi_1$			$\gamma_1$			$\xi_1$			
$\overline{+-+}$	2	1.00	0.99	1	0.00	0.00	0	0.00	0.00	-	-	-
$\overline{-+-}$	2	2.00	0.99	1	0.99	0.00	0	0.00	0.00	-	-	-
$\widehat{+-+}$	2	1.00	1.00	1	0.00	0.00	0	0.00	0.00	-	-	-
$\widehat{-+-}$	2	0.99	1.00	1	0.00	0.00	0	0.00	0.00	-	-	-
$\gamma_1$			$\gamma_2$			$\xi_1$			$\xi_2$			
$\overline{+-+}$	1	2.00	0.00	1	0.00	1.00	1	0.00	0.00	0	1.00	0.00
$\overline{-+-}$	1	0.38	0.00	1	0.62	1.00	1	0.00	0.00	0	0.00	0.00
$\widehat{+-+}$	1	2.00	0.72	1	0.52	0.28	1	1.52	0.00	0	0.00	0.00
$\widehat{-+-}$	1	0.66	0.15	1	0.34	0.85	1	0.00	0.00	0	0.00	0.00
$\widehat{\overline{+-+}}$	1	2.00	0.00	2	0.00	1.00	2	0.00	0.00	1	0.99	0.00
$\widehat{\overline{-+-}}$	1	0.60	0.00	2	0.40	1.00	1	0.00	0.00	2	0.00	0.00

Table 2.2: Exponents defining the optimal closure models, cf. Table 2.1, found by solving problem (2.15) with hard regularization ( $\beta_1 = 0$ ,  $\beta_2 = \delta = 2$ ) based on the data for the system  $\text{Li}_{1/3}\text{Mn}_{2/3}$  (OA-1/3) and the system  $\text{Li}_{1/2}\text{Mn}_{1/2}$  (OA-1/2) for each 3-cluster type indicated in the first column. For comparison, the exponents characterizing the pair approximation (PA) are also shown. The results are rounded to two decimal places.

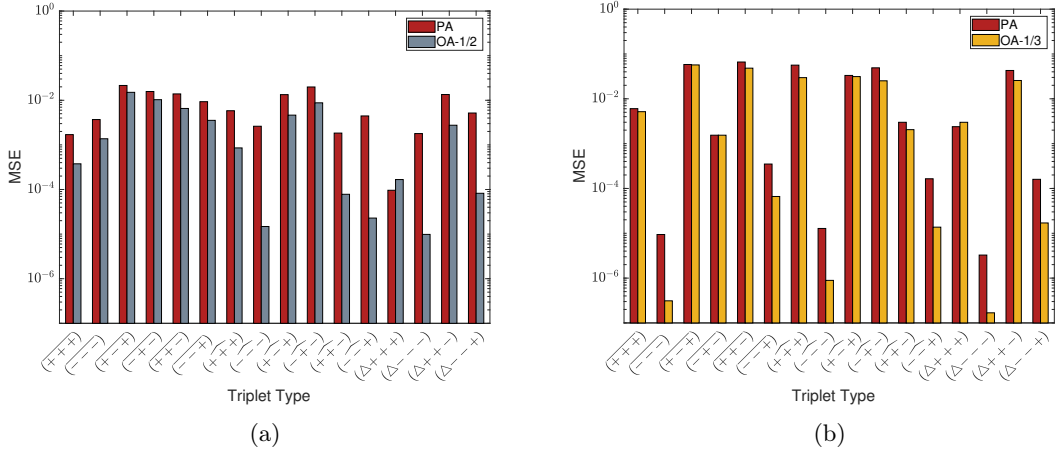


Figure 2.7: The mean-square errors (2.14) for the pair approximation (PA) and optimal approximation subject to hard regularization for (a) the system  $\text{Li}_{1/2}\text{Mn}_{1/2}$  (OA-1/2) and (b) for the system  $\text{Li}_{1/3}\text{Mn}_{2/3}$  (OA-1/3).

$\text{Li}_{1/2}\text{Mn}_{1/2}$  (when an exponent is zero, then the closure relation does not depend on the corresponding 2-cluster concentration). Thus, as is evident from Table 2.3, the resulting structure of the closure is much simpler (“sparser”) for the optimal approximation than for the closure obtained based on the pair

approximation. More specifically, note that for all triplet types, except for  $(\widehat{++-})$ ,  $(\widehat{-+-})$ ,  $(\widehat{++})$  and  $(\widehat{-}-)$ , the optimal closure depends on the concentration of one 2-cluster only. In order to make the structure of the closure model more uniform which will facilitate its interpretation, we adjust the expressions which do not follow the pattern. More specifically, in the optimal closure relations for the clusters  $(\widehat{-+-})$  and  $(\widehat{-}-)$  the exponents are rounded up and down to the nearest integer, whereas for  $(\widehat{++-})$  and  $(\widehat{++})$  the change is more significant and involves adjusting the structure of the closure relation. We refer to this simplified closure model as the *Sparse Approximation* (SA) and its functional form is presented in Table 2.3.

Triplet Type	Pair Approximation	Optimal Approximation	Sparse Approximation
$\overline{+++}$	$\frac{1}{5} \frac{C_{++}^2}{C_+}$	$\frac{1}{5} C_{++}$	$\frac{1}{5} C_{++}$
$\overline{---}$	$\frac{1}{5} \frac{C_-^2}{C_-}$	$\frac{1}{5} C_{--}$	$\frac{1}{5} C_{--}$
$\overline{+-+}$	$\frac{1}{5} \frac{C_{+-}^2}{C_-}$	$\frac{1}{5} C_{+-}$	$\frac{1}{5} C_{+-}$
$\overline{-+-}$	$\frac{1}{5} \frac{C_{+-}^2}{C_+}$	$\frac{1}{5} C_{+-}$	$\frac{1}{5} C_{+-}$
$\overline{++-}$	$\frac{1}{5} \frac{C_{++} C_{+-}}{C_+}$	$\frac{1}{5} C_{+-}$	$\frac{1}{5} C_{+-}$
$\overline{-++}$	$\frac{1}{5} \frac{C_{--} C_{+-}}{C_-}$	$\frac{1}{5} C_{+-}$	$\frac{1}{5} C_{+-}$
$\widehat{++}$	$\frac{2}{5} \frac{C_{++}^2}{C_+}$	$\frac{2}{5} C_{++}$	$\frac{2}{5} C_{++}$
$\widehat{--}$	$\frac{2}{5} \frac{C_-^2}{C_-}$	$\frac{2}{5} C_{--}$	$\frac{2}{5} C_{--}$
$\widehat{+-+}$	$\frac{2}{5} \frac{C_{+-}^2}{C_-}$	$\frac{2}{5} C_{+-}$	$\frac{2}{5} C_{+-}$
$\widehat{-+-}$	$\frac{2}{5} \frac{C_{+-}^2}{C_+}$	$\frac{2}{5} C_{+-}$	$\frac{2}{5} C_{+-}$
$\widehat{++-}$	$\frac{2}{5} \frac{C_{++} C_{+-}}{C_+}$	$\left[ \frac{2}{5} C_{++}^{0.72} C_{+-}^{0.28} \right]$	$\frac{2}{5} C_{+-}$
$\widehat{-++}$	$\frac{2}{5} \frac{C_{--} C_{+-}}{C_-}$	$\left[ \frac{2}{5} C_{+-}^{0.15} C_{++}^{0.85} \right]$	$\frac{2}{5} C_{+-}$
$\widehat{++}$	$\frac{2}{5} \frac{C_{++}^3}{C_+^3}$	$\left[ \frac{2}{5} \frac{C_{++}^2}{C_+} \right]$	$\frac{2}{5} C_{++}$
$\widehat{--}$	$\frac{2}{5} \frac{C_-^3}{C_-^3}$	$\left[ \frac{2}{5} \frac{C_{--}^2}{C_-} \right]$	$\frac{2}{5} C_{--}$
$\widehat{+-}$	$\frac{2}{5} \frac{C_{++} C_{+-}^2}{C_+^2 C_-}$	$\frac{2}{5} C_{+-}$	$\frac{2}{5} C_{+-}$
$\widehat{-+}$	$\frac{2}{5} \frac{C_{--} C_{+-}^2}{C_+ C_-^2}$	$\frac{2}{5} C_{+-}$	$\frac{2}{5} C_{+-}$

Table 2.3: Closure relations for 3-clusters of different types derived based on the pair approximation, the optimal approximation using the data for the system  $\text{Li}_{1/2}\text{Mn}_{1/2}$ , cf. Table 2.2, and the sparse approximation discussed in Section 2.4.4.

We now comment on how to interpret the structure of the sparse approximation. As discussed in Section 2.4.1, the pair approximation model neglects the correlation between non-nearest neighbour elements. This is due to the lack of information about the triple correlation term  $T_{ijk}$  in (2.12a). Considering relations (2.12) for the sparse approximation, the triplet correlation term is  $T_{ijk} = \frac{C_j}{C_{ij}}$  for the linear and angled triplets, and  $T_{ijk} = \frac{C_i C_j C_k}{C_{ij} C_{jk}}$  for the triangular triplets. This is contrary to the assumption that  $T_{ijk} = 1$  which is central to the pair approximation. With the data in Table 2.3 we are now in the position

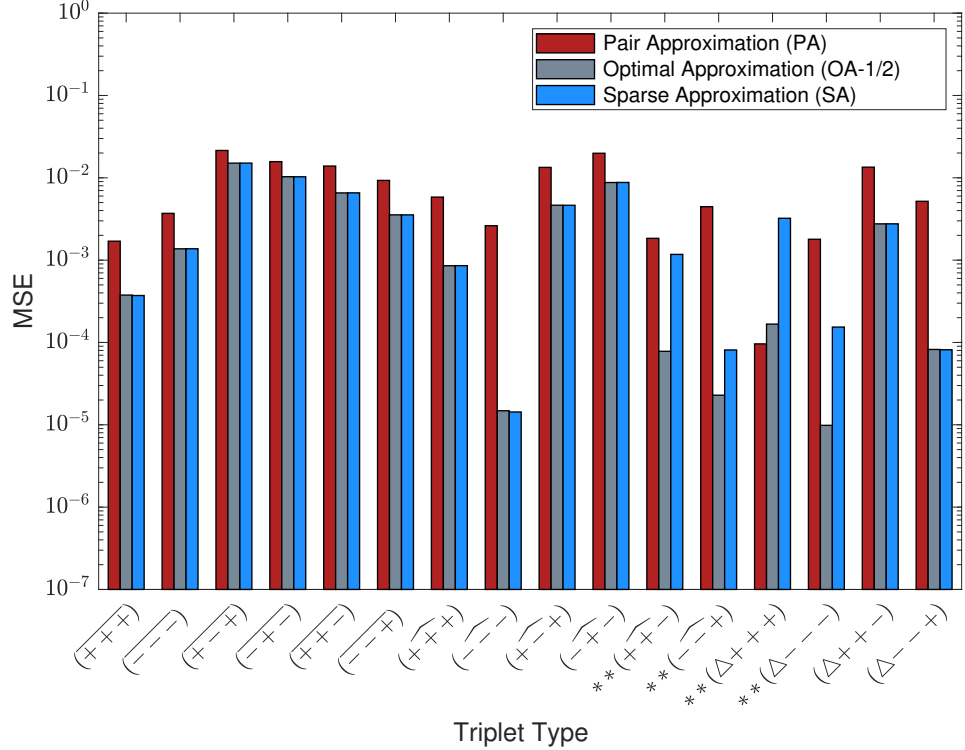


Figure 2.8: The mean-square reconstructions errors (2.14) for the pair approximation, the optimal approximation constructed subject to hard regularization based on the data for the system  $\text{Li}_{1/2}\text{Mn}_{1/2}$  and for the corresponding sparse approximation for different cluster types, cf. Table 2.3. Note that the results for the last two closures differ only for the clusters marked with (\*\*).

to refine the assumptions underlying these approximations. Referring to relations (2.12), the concentration of the triplet ( $C_{ijk}$ ) can be written as the global pair concentration ( $C_{ij}$ ) times the conditional probability of finding a nearest-neighbour element to the pair in a certain state ( $P_{k|ij}$ ). Considering the linear and angled triplets in the sparse approximation formulation, we obtain

$$C_{ijk} = C_i C_j C_k Q_{ij} Q_{jk} T_{ijk} = C_i C_j C_k \frac{C_{ij}}{C_i C_j} \frac{C_{jk}}{C_j C_k} \frac{C_j}{C_{ij}} = C_{ij} \frac{C_{jk}/C_j}{C_{ij}/C_j} = C_{ij} \frac{P_{k|j}}{P_{i|j}}. \quad (2.16)$$

In a similar way one can consider the triangular triplets where

$$C_{ijk} = C_i C_j C_k Q_{ij} Q_{jk} Q_{ik} T_{ijk} = C_{ij} \frac{C_{ik}/C_i}{C_{ij}/C_i} \frac{C_{jk}/C_j}{C_{ij}/C_j} = C_{ij} \frac{P_{k|i}}{P_{j|i}}. \quad (2.17)$$

We thus deduce

$$P_{k|ij} = \frac{P_{k|j}}{P_{i|j}}, \quad \text{for linear and angled clusters,} \quad (2.18a)$$

$$P_{k|ij} = \frac{P_{k|i}}{P_{j|i}}, \quad \text{for triangular clusters.} \quad (2.18b)$$

These relations break down the probability of a 3-cluster in terms of probabilities of two 2-clusters. They can be regarded as generalizations of the pair approximation model, cf. relation (2.11), with the inclusion of a term in the denominator. To understand the meaning of this extension of the pair approximation, we refer to relation (2.11). It is clear that closure is achieved using the pair approximation by assuming that the conditional probability of an element  $k$  being a nearest-neighbour of  $j$  is equal to the conditional probability of  $k$  being a nearest-neighbour of an  $ij$  pair. In other words, the pair approximation model assumes that an element  $j$  is always a nearest-neighbour of  $i$ , and we cannot find an element  $j$  which is not a nearest-neighbour of  $i$ . However, we know that this simplifying assumption is not correct in general and there is always a possibility of finding an element  $j$  which is not a nearest-neighbour of  $i$ . By re-arranging relation (2.18a) in the form  $P_{k|j} = P_{i|j}P_{k|ij}$ , it is evident that the SA model assumes that  $j$  might not always be a nearest-neighbour of  $i$  and accounts for this possibility through the term  $P_{i|j}$ . A similar interpretation can be adopted for triangular clusters.

The accuracy of the optimal approximation is certainly affected when the exponents in the closure relations for the four triplet types are adjusted as discussed above, cf. Table 2.3. Figure 2.8 shows the reconstruction errors for triplet concentrations obtained using different closure models for the system  $\text{Li}_{1/2}\text{Mn}_{1/2}$ . As can be expected, the SA model is less accurate in comparison to the OA model for the triplets  $(\widehat{+-})$ ,  $(\widehat{-+})$ ,  $(\widehat{++})$  and  $(\widehat{--})$ . However, the performance of SA model is still better than that of the pair approximation model for the triplets  $(\widehat{+-})$ ,  $(\widehat{-+})$  and  $(\widehat{--})$ . To conclude, the adjustments to the OA model sacrifice a degree of the accuracy in reconstructing the triplet concentration for  $(\widehat{++})$  while achieving a simpler and interpretable model.

As a result of the simple structure of the SA closure, cf. Table 2.3, system (2.8) closed with this model becomes linear and hence analytically solvable. It takes the form

$$\frac{d}{dt}C_{++} = 2\alpha_1 C_{+-}, \quad (2.19a)$$

$$\frac{d}{dt}C_{--} = 2\alpha_2 C_{+-}, \quad (2.19b)$$

$$\frac{d}{dt}C_{+-} = (-\alpha_1 - \alpha_2) C_{+-}, \quad (2.19c)$$

where the parameters  $\alpha_1 = \frac{4}{5}k_1 + \frac{1}{5}k_2 - \frac{4}{5}k_3 - \frac{1}{5}k_4$  and  $\alpha_2 = \frac{4}{5}k_5 + \frac{1}{5}k_6 - \frac{4}{5}k_7 - \frac{1}{5}k_8$  are linear combinations of the reaction rates. The solution then is

$$C_{+-}(t) = \mu_1 e^{(-\alpha_1 - \alpha_2)t}, \quad \mu_1 = C_{+-0}, \quad (2.20a)$$

$$C_{++}(t) = \frac{2\alpha_1\mu_1}{-\alpha_1 - \alpha_2} e^{(-\alpha_1 - \alpha_2)t} + \mu_2, \quad \mu_2 = C_{++0} - \frac{2\alpha_1\mu_1}{-\alpha_1 - \alpha_2}, \quad (2.20b)$$

$$C_{--}(t) = \frac{2\alpha_2\mu_1}{-\alpha_1 - \alpha_2} e^{(-\alpha_1 - \alpha_2)t} + \mu_3, \quad \mu_3 = C_{--0} - \frac{2\alpha_2\mu_1}{-\alpha_1 - \alpha_2}, \quad (2.20c)$$

where  $C_{+-0}$ ,  $C_{++0}$  and  $C_{--0}$  are the initial concentrations of the corresponding 2-clusters. The two parameters  $\alpha_1$  and  $\alpha_2$  instead of eight reaction rates  $k_1$  to  $k_8$  are sufficient to describe the evolution of concentrations of different clusters in time. If the growth rates  $\alpha_1$  and  $\alpha_2$  are negative, which will be shown to be indeed the case in Section 2.5.1, then as is evident from (2.20a), the concentration  $C_{+-}$  grows exponentially with the growth rate  $-(\alpha_1 + \alpha_2)$ . On the other hand, the concentrations  $C_{++}$  and  $C_{--}$  decay exponentially in time. As will be shown in Section 2.5.1, the growth of the concentration  $C_{+-}$  and the decay of the concentrations  $C_{++}$  and  $C_{--}$  is in fact qualitatively consistent with the early-time evolution, but not with the late-time evolution, of the 2-cluster concentrations obtained from the simulated annealing experiment. In addition to producing an analytically solvable model, an advantage of the SA closure is that the inverse problem (2.23) also simplifies and needs to be solved with respect to  $\alpha_1$  and  $\alpha_2$  only which does not require Bayesian inference.

#### 2.4.5 Prediction Capability of the Closure Models

In order to assess the predictive capability of the truncated model closed with the optimal approximation or the sparse approximation, the 3-cluster concentrations are reconstructed as functions of time from 2-cluster concentrations. We are interested in evaluating the prediction accuracy of these models in comparison to the model equipped with the pair approximation. In order to assess the robustness of these predictions, we will do this for stoichiometries other than the one for which the models were calibrated, cf. Sections 2.4.3 and 2.4.4. More specifically, while the simulated annealing data for the system with the composition  $\text{Li}_{1/3}\text{Mn}_{2/3}$  was used for calibration, accuracy of the models will be analyzed here for 10 different stoichiometries  $\text{Li}_x\text{Mn}_{1-x}$ ,  $x \in \{0.25, 0.30, 0.33, 0.36, 0.42, 0.50, 0.58, 0.64, 0.70, 0.75\}$ . In particular, we are interested in the effect of regularization — soft versus hard with different parameters  $\delta$ ,  $\beta_1$  and  $\beta_2$  — in the solution of problem (2.15).

Robustness of the model performance will be assessed in terms of the mean-square error (2.14) aver-

aged over all types of 3-clusters, i.e.,

$$\mathcal{E} = \frac{1}{|\Theta|} \sum_{i \in \Theta} J_i, \quad (2.21)$$

where  $|\Theta| = 16$  is the total number of 3-clusters, cf. (2.4), and the true 3-cluster concentrations  $\widetilde{C}_i(t)$  are obtained from simulated annealing experiments performed for each considered stoichiometry. This diagnostic is designed to assess only the accuracy of the closure relations given in Table 2.3, rather than of the entire truncated model (2.8).

Error (2.21) is shown as function of the stoichiometry for the optimal closure obtained for the system  $\text{Li}_{1/3}\text{Mn}_{2/3}$  subject to hard and soft regularization in Figures 2.9a and 2.9b, respectively. In addition, in these figures we also show the errors obtained with the model based on the pair approximation. As can be observed, harder regularization results in larger prediction errors for stoichiometries close to  $\text{Li}_{1/3}\text{Mn}_{2/3}$  in comparison to softer regularization strategies. On the other hand, harder regularization reveals better predictive performance for stoichiometries different from  $\text{Li}_{1/3}\text{Mn}_{2/3}$ . In other words, less aggressive regularization performs better on stoichiometries close to the stoichiometry for which the calibration of the closure relations from Table 2.1 was performed in Section 2.4.3, and the performance gradually degrades as the stoichiometries become more different from  $\text{Li}_{1/3}\text{Mn}_{2/3}$ . We thus conclude that there is a trade-off between robustness and accuracy of the closure models, in the sense that models optimized for a particular stoichiometry tend to be less robust when used to describe other stoichiometries.

Finally, robustness of the closures based on the pair approximation, the optimal approximation subject to hard regularization for the system  $\text{Li}_{1/3}\text{Mn}_{2/3}$  and the corresponding sparse approximation is compared for a range of stoichiometries in Figure 2.9. Note that solving the minimization problem (2.15) subject to hard regularization produces more versatile closure models that can be applied to a range of stoichiometries without significant loss of accuracy. Hence, the optimal approximation models of interest are achieved by hard regularization in (2.15). Figure 2.10 shows the mean error (2.21) for a range of stoichiometries for the three aforementioned closure models. A significant improvement with respect to the performance of the pair approximation model is achieved by the optimal closure models for all stoichiometries. As can be observed, the SA model performs better than the OA-1/3 model for most of the stoichiometries, except the ones that are close to the system  $\text{Li}_{1/3}\text{Mn}_{2/3}$ . This is due to the fact that in the OA-1/3 model the minimization problem (2.15) is solved for the system  $\text{Li}_{1/3}\text{Mn}_{2/3}$ , and hence fits are more accurate in the neighbourhood of this stoichiometry. We conclude by noting that when averaged over all stoichiometries, the performance of the sparse approximation model is improved by 36.13% over the performance of the pair approximation model.

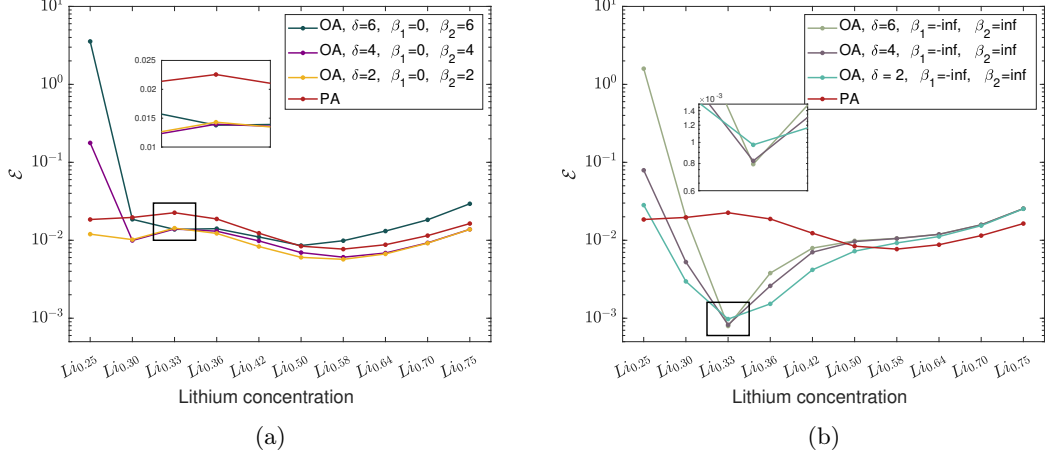


Figure 2.9: Dependence of the mean error (2.21) characterizing the accuracy of the different closure relations on the stoichiometry for (a) hard regularization and (b) soft regularization employed in the solution of optimization problem (2.15) with parameters indicated in the legend for  $Li_{1/3}Mn_{2/3}$  system. “PA” and “OA” refer to, respectively, the pair and the optimal approximation.

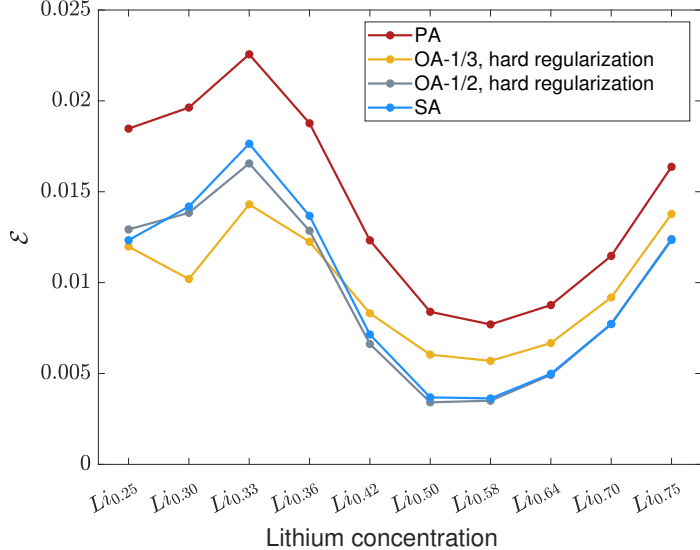


Figure 2.10: The mean error (2.21) characterizing the accuracy of the different closure relations indicated in the legend for a range of different stoichiometries.

## 2.5. Determining Reaction Rates via Bayesian Inference

In order for the truncated model (2.8) closed with either the pair or optimal approximation to predict the time evolution of 2-cluster concentrations, it must be equipped with correct values of the rate constants  $k_1, \dots, k_8$ , cf. Figures 2.4 and 2.5. Here we show how these constants can be determined by solving an appropriate inverse problem. It will be demonstrated that this problem is in fact ill-posed and a suitable

solution will be obtained using Bayesian inference which also provides information about the uncertainty of this solution.

We define the error functional as

$$\mathcal{J}(\mathbf{K}) = \frac{1}{2} \int_0^T \|\mathbf{C}(t, \mathbf{K}) - \widetilde{\mathbf{C}}(t)\|_2^2 dt + \alpha \|\mathbf{Q}(\mathbf{K}) - \widetilde{\mathbf{Q}}\|_2^2, \quad (2.22)$$

where  $\widetilde{\mathbf{C}}(t) = [\widetilde{C}_{++}(t), \widetilde{C}_{--}(t), \widetilde{C}_{+-}(t)]$  is the vector of pair concentrations obtained from the simulated annealing experiment,  $\mathbf{K} = [k_1, k_2, \dots, k_8]$  is the vector of unknown rate constants, and  $\mathbf{C}(t, \mathbf{K})$  is the vector of pair concentrations predicted by model (2.8) equipped with the rate constants  $\mathbf{K}$ . The second term in (2.22) is the mean-square error between the equilibrium constants  $\mathbf{Q}(\mathbf{K}) = [Q_1, Q_2, Q_3, Q_4]$ , cf. relation (2.7), predicted by model (2.8) equipped with parameters  $\mathbf{K}$  and the equilibrium constant  $\widetilde{\mathbf{Q}} = [\widetilde{Q}_1, \widetilde{Q}_2, \widetilde{Q}_3, \widetilde{Q}_4]$  obtained experimentally via simulated annealing. We note that the equilibrium constants in (2.7) are written in terms of 3-cluster concentrations and one of the closure models (i.e., the pair or the optimal approximation) is used to express the equilibrium constants in terms of 2-cluster concentrations. The parameter  $\alpha$  weights the relative importance of matching the equilibrium constants versus matching the time-dependent concentrations in (2.22).

The optimal reaction rates are then obtained by solving the problem

$$\begin{aligned} & \min_{\mathbf{K} \in \mathbb{R}^8; \mathbf{K} \geq \mathbf{0}} \mathcal{J}(\mathbf{K}) \\ & \text{subject to system (2.8)} \end{aligned}, \quad (2.23)$$

where the notation  $\mathbf{K} \geq \mathbf{0}$  means that each component of vector  $\mathbf{K}$  is non-negative, separately for the case of the pair and the optimal approximations. We note that the minimization problems (2.15) and (2.23) are in fact quite different: in the former the mismatch between the evolution of 3-cluster concentrations is minimized with respect to a suitably-parameterized structure of the closure model, whereas in the latter one seeks to minimize the mismatch between the evolution of 2-clusters in order to find the optimal reaction rates in the closed system (2.8).

Inverse problems such as (2.23) are often ill-posed, in the sense that they usually do not admit a unique exact solution, but rather many, typically infinitely many, approximate solutions. This is a result of the presence of multiple local minima, which is a consequence of the non-convexity of the error functional (2.22), and the fact that these minima are often “shallow” reflecting weak dependence of the model predictions  $\mathbf{C}$  on the parameters  $\mathbf{K}$ . As will be evident from the results presented below, it is thus not very

useful to solve problem (2.23) directly using standard methods of numerical optimization [74]. Instead, we will adopt a probabilistic approach based on Bayesian inference where the unknown parameters in the vector  $\mathbf{K}$  and the corresponding model predictions  $\mathbf{C}$  will be represented in terms of suitable conditional probability densities. This will allow us to systematically assess the relative uncertainty of the many approximate solutions admitted by problem (2.23). In this framework, the distribution of the parameters in  $\mathbf{K}$  is given by a *posterior* probability distribution  $\mathbb{P}(\mathbf{K}|\tilde{\mathbf{C}})$  defined as the probability of obtaining parameters  $\mathbf{K}$  given the observed experimental data  $\tilde{\mathbf{C}}$ . Inverse problem (2.23) is nonlinear, in the sense that the map  $\mathbf{C} = \mathbf{C}(t, \mathbf{K})$  from the model parameters to model predictions is not linear, and therefore we cannot expect the posterior distribution to have a simple form. A Markov-Chain Monte-Carlo (MCMC) sampling method is then used in order to sample the posterior parameter space (we remark that a Monte-Carlo sampling technique is also independently used in the simulated annealing approach to generate data describing the evolution of the lattice as discussed in Section 2.2). MCMC methods are commonly used to sample arbitrary distributions known up to a normalizing factor, in particular, for distributions defined in high dimensions where exploration of the entire space with classical methods is computationally intractable. They have found applications in many different fields such as electrochemistry [33], medical imaging [75, 76], environmental and geophysical sciences [77, 78], ecology [79] and statistical mechanics [80]. The mathematical foundations of Bayesian inference are reviewed in the monographs [21, 81, 82] whereas details of our approach are provided in Appendix A.2.

### 2.5.1 Results of Bayesian Analysis

The reaction rates  $k_1, \dots, k_8$  in system (2.8) are determined in probabilistic terms using Bayesian inference for the pair approximation and the optimal closure models. On the other hand, for the sparse approximation there are only two unknown parameters ( $\alpha_1$  and  $\alpha_2$ ) so they can be inferred by solving the problem  $\min_{(\alpha_1, \alpha_2) \in \mathbb{R}^2} \mathcal{J}(\alpha_1, \alpha_2)$  where the concentrations in the error functional are evaluated using the closed-form relations (2.20). Although this minimization problem is not convex, a global minimum can be found using standard optimization methods.

In the problems involving the pair approximation and the optimal closure models some of the reaction rates were found to be essentially equal to zero (or vanishingly small), so here the results are presented for the remaining rates only. In Figures 2.11a and 2.11c we visualize the Markov chains obtained with Algorithm 4, cf. Appendix A.2, for system (2.8) closed with, respectively, the pair approximation, the optimal approximation with exponents determined subject to hard regularization (OA-1/2), cf. Table 2.2. The Cartesian coordinates of each point in Figures 2.11a,c represent three of the parameters characterizing an individual Monte-Carlo sample, whereas information about the remaining parameters is encoded in the

color of the symbol via the red-green-blue (RGB) mapping, as shown in the color maps in Figures 2.11b,d. The size of the symbols is proportional to  $\mathcal{J}(\mathbf{K})^{-1}$  such that parameter values producing better fits stand out as they are represented with larger symbols. Note that, for clarity, the entire Markov chains are not presented in Figure 2.11 as the data is filtered based on the value of the cost function (i.e., data points are shown only if  $\mathcal{J}(\mathbf{K})$  is smaller than some threshold).

It is evident from Figures 2.11a,c that in each case parameter values producing good fits form a number of clusters, which reflects the fact that problem (2.23) indeed admits multiple local minima. The complicated form of the posterior distributions shown in these figures is a consequence of the nonlinearity of the inverse problem (2.23). It is also interesting to see that good fits are obtained with some of the reaction rates varying by 200% or more which is a manifestation of the ill-posedness of problem (2.23) when the outputs  $\mathbf{C}(\mathbf{K})$  reveal weak dependence on some of the parameters in  $\mathbf{K}$ . In order to compare the quality of fits obtained with the pair and optimal approximations, in Figures 2.12a,b we show the histograms of the values of the error functional  $\mathcal{J}(\mathbf{K})$  obtained along the Markov chains. Overall, the quality of the fits is comparable in both cases and exhibits significant uncertainty, although poor fits appear more likely when the closure based on the pair approximation is used. The optimal parameter values for the closure based on the SA model are  $(\alpha_1^*, \alpha_2^*) = (-0.083, -0.166)$  and, as we can see in Figures 2.12a,b, while the accuracy of the fit is lower than in the previous two cases, there is effectively no uncertainty in the determination of the parameters.

Finally, the time evolution of pair concentrations is determined by solving system (2.8) closed with one of the closure models discussed, i.e., the pair approximation (PA), optimal approximation with exponents subject to hard regularization (OA-1/2) or sparse approximation (SA). However, in order to solve problem (2.8), one needs to find a point estimate of the parameters of the model (the reaction rates), rather than their probability distribution. This can be done in two ways. In the first approach, one finds the a posteriori probability distribution of parameters  $\mathbf{K}$  and then the mode of this distribution, known as the *Maximum-a-Posteriori* (MAP) estimation, can be used as a point estimate maximizing the posterior probability distribution. The second approach is to find a parameter vector  $\mathbf{K}$  by solving the optimization problem (2.23) using a classical optimization technique. It is known that the MAP point estimate obtained using a normally distributed prior is in fact equivalent to solving a minimization problem with the error functional subject to Tikhonov regularization, such as our problem (2.23) [83]. Here the latter approach has been adopted for determining the point estimates.

The point estimates obtained as described above are used to solve the initial value problem (2.8) and the results are shown in Figure 2.13. As can be observed, system (2.8) closed with the OA-1/2

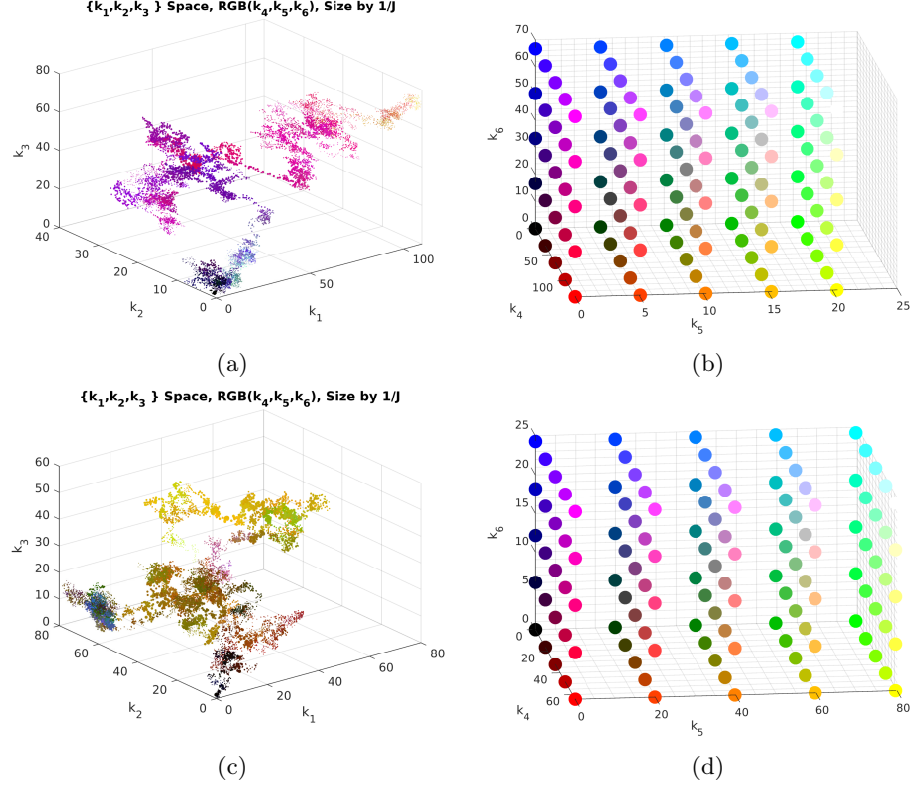


Figure 2.11: Posterior probability densities  $\mathbb{P}(\mathbf{K}|\widetilde{\mathbf{C}})$  obtained using Algorithm 4 for problem (2.23) with system (2.8) closed using (a) the pair approximation and (c) the optimal approximation with exponents determined subject to hard regularization (OA-1/2). The parameters  $k_1$ ,  $k_2$  and  $k_3$  are represented in term of the Cartesian coordinates whereas the remaining three nonzero rate constants are encoded in terms of the color of the symbols via the color maps shown in panel (b) and (d). The size of the symbols in panels (a) and (c) is proportional to  $J(\mathbf{K})^{-1}$ .

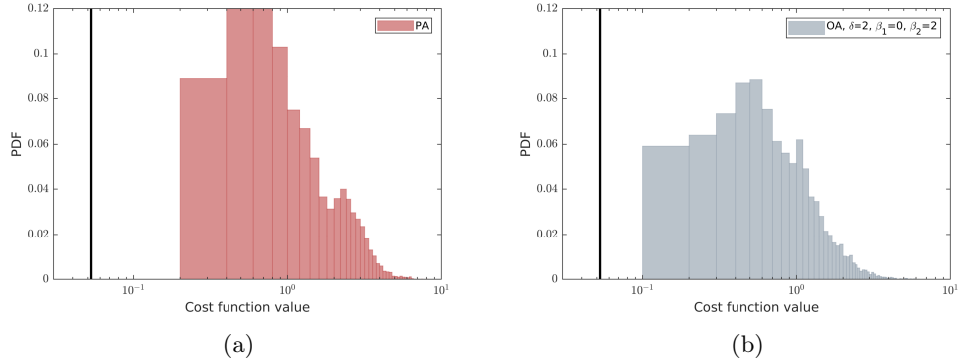


Figure 2.12: Histograms of the error functional  $\mathcal{J}(\mathbf{K})$  obtained along the Markov chains for problem (2.23) with system (2.8) closed using (a) the pair approximation and (b) the optimal approximation with exponents determined subject to hard regularization (OA-1/2). The black vertical lines represent the values of the error functional  $\mathcal{J}(\alpha_1^*, \alpha_2^*)$  obtained when the model based on the SA closure is used.

and PA closure models is more accurate in terms of predicting the evolutions of the pair concentrations than when it is closed with the SA model. The reason is that both the OA-1/2 and the PA closures offer

more flexibility in fitting the experimental data as there are 8 parameters in  $\mathbf{K}$  to be tuned. On the other hand, the sparse approximation involves two parameters,  $\alpha_1$  and  $\alpha_2$ , only. Moreover, as explained in Section 2.4.4, the analytic solution (2.20) of system (2.8) closed with the sparse approximation predicts exponential behaviour of pair concentrations such that for large times these concentrations tend to  $\pm\infty$ . This is clearly inconsistent with the long-time behavior of the pair concentrations in the experiment where they converge to finite equilibrium values. However, predictions of the SA closure are valid for short time scales which are in fact long enough to cover at least half of the time window of interest, cf. Figure 2.13. We thus conclude that, as expected, there is a trade-off between the simplicity (interpretability) of the model and its accuracy and the sparse approximation sacrifices accuracy in favor of simplicity and robustness.

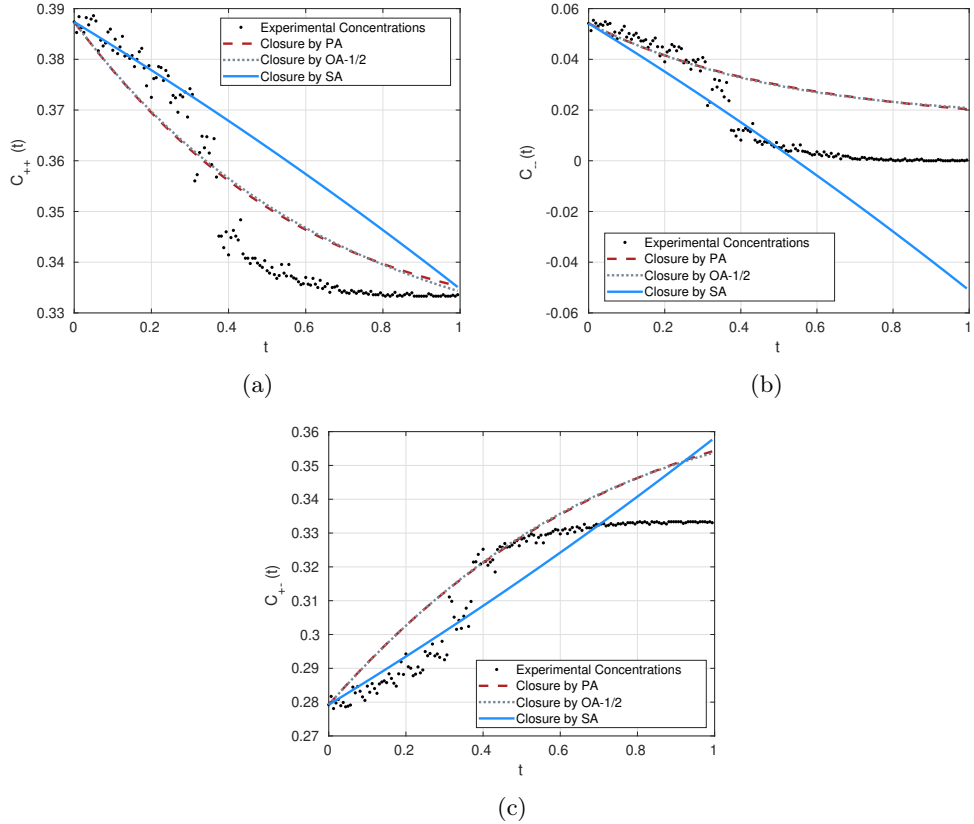


Figure 2.13: Time evolution of pair concentrations (a)  $C_{++}$ , (b)  $C_{--}$  and (c)  $C_{+-}$  obtained by solving system (2.8) closed with the pair approximation, the optimal approximation with exponents subject to hard regularization and the sparse approximation. The concentrations obtained from the simulated annealing experiment are shown as well.

## 2.6. Summary & Conclusions

We have considered a mathematical model for the evolution of different cluster types in a structured lattice. We focused our attention on the structured lattice of a nickel-based oxide similar to those used in Li-ion batteries. That being said, the approach used here is much more broadly applicable. As is usual, the mean-clustering approach gives rise to an infinite hierarchy of ordinary differential equations, where concentrations of clusters of a certain size are described in terms of concentrations of clusters of higher order. This infinite hierarchy must be truncated at an arbitrary level and closed with a suitable closure model (or closure condition) in order to be solvable. This closure requires an approximation of the concentrations of the higher-order clusters in terms of the concentrations of lower-order ones. As a point of departure, we consider the pair approximation which is a classical closure model, and then introduce its generalization referred to as the optimal approximation which is calibrated using a novel data-driven approach.

The optimal approximation can be tuned for different levels of accuracy and robustness by adjusting the degree of regularization employed in the solution of the optimization problem. Our analysis shows that the model subject to soft regularization results in highly accurate approximations for the local stoichiometry but the accuracy deteriorates for other stoichiometries. On the other hand, the model subject to hard regularization has a lower accuracy at the local stoichiometry but is more robust with respect to changes of stoichiometry. The model subject to hard regularization produces more accurate results than the pair approximation for a broad range of stoichiometries. More importantly, the closure model found in this way turns out to have a simple structure with many exponents having nearly integer values. Exploiting this structure, we arrive at the sparse approximation model which is linear and therefore analytically solvable.

In addition to being simpler, the sparse approximation model is also more accurate and robust than the pair approximation, in that it can be applied to a wide range of stoichiometries without a significant loss of accuracy. This model is interpretable as it makes it possible to refine some of the simplifying assumptions at the heart of the pair approximation. One of these assumptions states that the conditional probability of  $k$  being a nearest neighbour of  $i/j$  in a triplet  $(ijk)$  is equal to that of  $k$  being a nearest neighbour of  $j$ . In other words, it is assumed that every  $j$  element in the lattice has a nearest neighbour in state  $i$ . The sparse approximation refines this assumption by adding a term that takes into account the conditional probability of  $j$  being a nearest neighbour of  $i$ . This correction makes the model both simpler and more accurate.

The reaction rates in system (2.8) closed using one of the closure models are determined by formulating a suitable inverse problem. We solve these problems using a state-of-the-art Bayesian inference approach which also allows us to estimate the uncertainties of the reconstructed parameters. The results obtained show that the inverse problem is in fact ill-posed in the case of the closures based on the pair and optimal approximation, in the sense that the corresponding optimization problems admit multiple local minima. Moreover, these minima tend to be “shallow” reflecting the low sensitivity of the models closed with the pair and optimal approximations to the reaction rates. As a result, the inferred values of these parameters suffer from uncertainties on the order of 200%. In contrast, the model closed using the sparse approximation is well-posed with respect to  $\alpha_1$  and  $\alpha_2$  which are linear combinations of reaction rates. This model is analytically solvable which completely eliminates the uncertainty in the reconstruction of its parameters. However, we note that this simplicity and robustness are achieved by sacrificing some accuracy of the model predictions. Namely, while the sparse approximation predicts the evolution of pair concentration at short time scales, it fails to predict their convergence to equilibrium values for longer times.

Notably, the mean-cluster modeling approach considered in the present work can be used to describe the evolution of clusters of arbitrary size and type defined on structured lattices various types. The size and shape of the cluster and the structure of the lattice determine the reactions between elements. More complicated lattices and bigger cluster sizes involve more possible nearest-neighbour element swaps, resulting in a larger number of parameters in the model. The sparse approximation methodology could be utilized in a similar way to close the corresponding hierarchical models. We add that the sparse approximation has been realized by inferring the structure of the closure from the results obtained using the optimal closure approximation. The optimal closure approximation could in principle be generalized to other lattice structures and cluster evolution types and, although the sparse approximation involves a heuristic aspect, it does lead to refined probabilistic rules describing lattice evolution on short time scales. It is therefore an interesting question if these rules could be used to improve closure models for other, more complicated, lattice configurations.

## *Chapter 3*

---

# *State-of-Charge Estimation of Cells Under Dynamic Loading Conditions using Identification of Nonlinear Dynamics and Filtering*

---

### **3.1. Introduction**

Lithium-ion batteries (LIBs) have found extensive applications due to their high energy density, long cycle life, and low self-discharge. One of the challenging questions in this field is the accurate and reliable estimation of the State-of-Charge (SoC) and State-of-Health (SoH) of battery cells. Reliable estimates of the state of the cell help prevent overcharge and overdischarge during charge/discharge cycles, which can extend its lifetime and prevent destructive degradation mechanisms such as Lithium (Li) plating [84]. Additionally, many other parameters require accurate estimates of the internal state of the system, such as power calculations, cell balancing in a battery pack, and the SoH of the cell. The SoH of a cell is defined as the ratio of the maximum available capacity of the battery that can be used during a full charge/discharge of the cell to its nominal capacity

$$SoH = \frac{Q_{max}}{Q_n}, \quad (3.1)$$

where  $SoH \in [0, 1]$  is the state-of-health of the cell,  $Q_n[A \cdot hr]$  and  $Q_{max}[A \cdot hr]$  are the nominal capacity and the maximum available capacity of the cell, respectively. The capacity of the cell is determined by the quantity of the cycleable Lithium in the cell and the extent to which the negative and positive electrode particles can participate in the electrochemical reactions. This capacity is affected by several degradation mechanisms, e.g., Li plating. On the other hand, the SoC of a cell is defined as the ratio of available charge in the cell to be discharged while in operation, to its maximum available capacity,

$$z = \frac{Q}{Q_{max}}, \quad (3.2)$$

where  $z \in [0, 1]$  is the SoC of the cell, and  $Q[A \cdot hr]$  is the available charge in the cell to be used for charge/discharge processes. Note that throughout this study the state-of-charge of the cell is denoted SoC in the text and  $z$  in the mathematical context. Another important factor in determining the state of a cell is its polarization potential, defined as the overpotential at the solid-electrolyte interface caused by the electrochemical reaction. The electrochemical reaction, giving rise to the polarization potential, is the main cause of deviation of the terminal voltage of the cell from its Open-Circuit Voltage (OCV) at a particular SoC of the cell. The terminal voltage is measured as the difference in potential between the two ends of current collectors in the cell (two ends of the cell), and the OCV is defined as the terminal voltage of the cell while the cell is at equilibrium at a particular state-of-charge. Other ohmic resistances in the cell are additional sources of the deviation of terminal voltage from its OCV value. The SoC and polarization potential of the cell are referred to as the "internal states" or "states" of the cell, which are the matters of interest in this chapter.

The problem of state estimation is challenging due to the highly nonlinear nature of Li-ion cells. The state of the cell depends on many internal and external factors. The nature of the cell involves many multi-physics and multi-scale phenomena, e.g., ion diffusion in the electrolyte and solid electrode, charge transfer, etc. Different physical processes evolving at different temporal and spatial scales make it highly complex to estimate the state of the cell. Furthermore, fluctuations in external control parameters, such as temperature, can significantly affect the internal electrochemical behavior of the cell. Cell-to-cell differences are another important reason that makes modeling LIBs a significant challenge. Hence, developing advanced state estimators for LIBs is important for the reliable, stable, and optimal operation of cells, which has gained extensive attention. Some of the relevant work is summarized in [85–89].

There are multiple sources of error involved in the estimation of the state of the cell, as outlined by Espedal et al. [86], including capacity-induced errors, initial SoC errors, measurement errors, and model prediction errors. Capacity-induced errors refer to the decline in the nominal capacity of the cell

due to aging effects, affecting the SoH of the cell. Minimizing this error requires frequent calibration of the cell to obtain its current capacity. Initial SoC errors are the discrepancies between the actual and theoretical initial states of the cell, which can be minimized by re-calibrating the cell to its fully discharged state. Current and voltage measurement errors can occur due to sensor inaccuracy, bias, and noise in measurements, which are difficult to eliminate. Lastly, model prediction errors refer to the discrepancy between the predicted terminal voltage of the cell, as the output of a mathematical model, and the actual measurement from the cell. This information is typically used in conjunction with closed-loop models to provide feedback to the system. Overall, these types of errors can contaminate the computations of the state of the cell.

The main contribution of this chapter is in improving the modeling of the internal states of the cell by using measurement data, which could potentially reduce the effect of modeling errors and increase the robustness and reliability of the designed models. Different techniques could be used for modeling polarization potential, including physics-based models and machine-learning-based models. Also, different methodologies for approaching the state estimation problem are proposed in the literature, including experimental techniques, Coulomb Counting, physical modeling [16, 90], data-driven nonlinear mapping (AI techniques) [91], and model-based techniques [92, 93]. A brief summary of each of these methods, their pros and cons, and their relevance to this work is presented below. Note that all the data-driven-based techniques for modeling the state of the cell require information about the state of the cell to be used as training data for calibrating the model. However, the task of inferring the SoC of the cell is challenging while the cell is in operation, and hence, there is no known method for finding the "true" state of the system. For this reason, we use a series of experimental and computational techniques together with some assumptions in order to approximate the state of the system. We refer to the approximated state as the "reference state" of the cell, which might be different from the unknown "true" state of the cell. We use the reference state as our "experimental data" for calibrating the proposed mathematical models. Note that in this study a commercial Lithium-iron-phosphate (LFP) cell with a nominal capacity of  $Q_n = 200$  [A.hr], is used for collection of the data and the reference state of the cell is determined while the cell is operating under dynamic loading conditions.

In this study, we begin by using standard modeling approaches to obtain a reference state for the cell while the cell is in operation. We then employ a hybrid approach for identifying the nonlinear dynamics of the system based on a method known as the Sparse Identification of Nonlinear Dynamics (SINDy), in which the state of the system is identified based on data while using some knowledge about the physics of the cell. Once the system dynamics are identified, we use this model for estimating the state of the cell

along with quantifying the uncertainties involved. To the best knowledge of the author, this is the first instance of using SINDy as a system identification technique in modeling internal states of Li-ion cells. This research proposes new avenues to be further explored in this field.

### 3.1.1 Experimental Techniques

The most conventional technique in SoC estimation of cells relies on monitoring the OCV of the cell. The OCV of the cell is a function of its SoC. The conventional method of obtaining the OCV of the cell at a particular state generally involves leaving the cell uninterrupted for a sufficient amount of time until the potential stops to change and the equilibrium potential of the cell is achieved. The SoC of the cell is then inferred via a lookup table according to its OCV. The lookup table is normally obtained by cycling the cell and collecting information about its OCV at different states of the cell (Note that the SoC itself will be approximated using the Coulomb Counting technique as highlighted in Section 3.1.2). Despite its simplicity, this technique is not suitable for online applications, as the terminal voltage across the cell deviates from its equilibrium potential due to polarization and ohmic resistances in the cell. Figure 3.1 demonstrates the behavior of the cell potential as a function of the SoC in two different operating modes for this cell, charge and discharge. Note that SoC in this graph is estimated using the Coulomb Counting method as explained in Section 3.1.2. As will be discussed below, the estimates of SoC remain reliable for a single constant-current cycle.

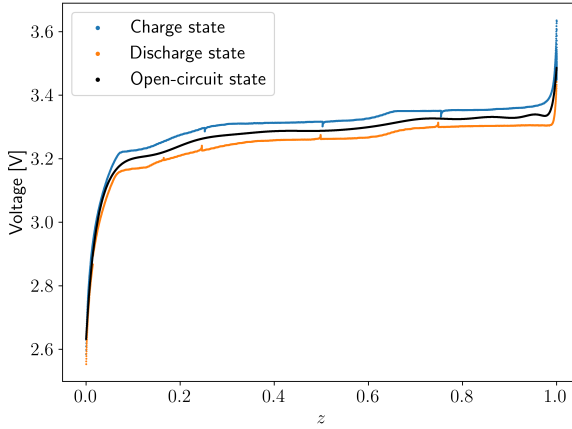


Figure 3.1: Terminal voltage across the cell as a function of its SoC in two different operating modes: charge and discharge. A constant-current charge/discharge with three rest periods at approximately  $z = 0.25$ ,  $z = 0.5$  and  $z = 0.75$  is used in this cycle. Note that the open-circuit voltage in this graph is approximated using a polynomial fit to charge and discharge terminal voltages.

A constant-current charge/discharge with three rest periods at approximately  $z = 0.25$ ,  $z = 0.5$ , and

$z = 0.75$  was used in this experiment. As it is not trivial to infer the equilibrium potential of the cell while in operation, a polynomial fit to both charge and discharge potentials is used to infer the OCV-SoC relationship (black solid line in Figure 3.1) from the terminal potential of the cell (blue dotted line in charge state and orange dotted line in discharge state in Figure 3.1). As can be observed, the terminal voltage of the cell (OCV in this case) approaches the equilibrium potential while at rest (note that the OCV of the cell is different from its equilibrium potential, and it converges to equilibrium potential once the cell is put at rest). This phenomenon is fundamental in describing battery dynamics and is present in most battery chemistries with different levels of intensity [94]. In particular, LFP cells demonstrate significant deviation from open-circuit potential, as shown in Figure 3.1. Additionally, these batteries have a nearly horizontal OCV-SoC relation for most of their operating range. Thus, the lookup table method becomes inappropriate for estimating the state of the LFP cells, while in operation.

To infer the SoC via lookup tables, cells need to be put in the rest mode for a sufficient amount of time until equilibrium is achieved. Although this method is time-consuming, it can yield accurate estimations of the state of the battery for some chemistries, since there is a unique relation between the OCV and SoC that only depends on temperature. Although this technique cannot be applied to cells in operation, the OCV-SoC relation shown in Figure 3.1 will be used in conjunction with other techniques such as Equivalent Circuit Modeling (ECM), to estimate the OCV of the cell while in operation, as described in Section 3.2.

### 3.1.2 Coulomb Counting

Another common approach to estimating the SoC of a cell is the Coulomb Counting (CC) technique. It is an easy-to-implement and computationally inexpensive method based on counting the amount of charge passed to the cell during charge/discharge. The current passing through the cell during operation is integrated over time to compute its SoC at a given time as

$$\begin{aligned}\dot{z} &= \frac{\eta I(t)}{Q_n}, \\ z(t_f) &= z(0) + \frac{1}{Q_n} \int_0^{t_f} \eta I(\tau) d\tau,\end{aligned}\tag{3.3}$$

where  $I(t)$  [ $A$ ] is the current applied to the cell,  $\eta \in (1, \infty)$  is the Coulombic efficiency of the cell and is the inverse of its *SoH*, and  $t_f$  is the final time of integration. This technique will be referred to as the Forward Coulomb Counting (FCC), from now on. In this technique, the amount of charge passed to the cell is computed by moving forward in time. In contrast, when working with the data in an offline manner, one can compute the amount of charge passed to the cell by moving backward in time, a method

referred to as the Backward Coulomb Counting (BCC). The current passing through the cell is integrated backwards in time to compute the SoC at a given time  $t$  as

$$z(t) = z(t_f) + \frac{1}{Q_n} \int_{t_f}^t \eta I(\tau) d\tau. \quad (3.4)$$

There are a few drawbacks to the Coulomb Counting technique in general as outlined below.

1. It relies on accurate initial SoC estimates for tracking the true state of the cell.
2. It only relies on excitation dynamics of the cell (driven by exciting the cell using the current applied to the cell) and does not take into account the relaxation dynamics (driven by the internal dynamics of the cell in the absence of external excitation). The relaxation dynamics might cause the self-discharge of the cell while it is in open-circuit condition. Better estimates of the internal states of the cell are obtained when both excitation and relaxation dynamics are modelled. The modeling of polarization potential, as the main contribution of this study, will be discussed in more detail in Section 3.5.
3. The true SoH of the cell is required for this technique. Hence, periodic recalibration of the cell to obtain its maximum capacity is required.
4. Errors due to sensor drifts will accumulate over long periods, making it unsuitable for real-time estimations over extended durations.

In our application, the cells begin to operate from a fully discharged state, eliminating the initial SoC error. The self-discharge and periodic recalibration issues are not considered in this study. Note that the SoC estimates obtained by the CC method are reliable for short durations, and become unreliable over extended durations due to error accumulation and absence of a feedback loop. Despite such issues, the simplicity of this method makes it an interesting choice for state estimation.

In this study, the CC method is used for inferring SoC estimates for short durations as a reliable technique to infer an approximation of the "true" state of the cell. However, the SoC estimates obtained with this method over extended durations deviate from the true state. In Section 3.4 we will discuss how the CC method is used in short durations as an open-loop technique for inferring the "near-true" state of the cell, and in extended durations as a closed-loop technique for inferring a "reference" state of the cell. Note that the reference state is different from the true state of the cell as there is no known way of inferring the true state. In other words, the near-true estimates obtained by the CC method in short durations will be used as a guide to improve SoC estimates by the CC method in extended durations to infer the reference

state of the cell during the extended duration, a method explained in Section 3.4. Data-driven modeling techniques and filtering techniques will be utilized along with the CC method to increase the reliability of this technique by adding a feedback loop and a probabilistic aspect to the estimations.

### 3.1.3 Physical Modeling

Another common approach to estimating the state of cells is to model the physical processes in the cell. The number of Lithium ions intercalated/deintercalated on the negative electrode of the cell during charge/discharge operation can be deduced using continuum models. Different levels of complexity can be adopted for such models depending on the specific application. Microscale models, homogenized models, Doyle-Fuller-Newman type models, and single-particle models are the most common approaches in modeling Li-ion cells, as summarized by Planella et al. [95]. The single-particle model is the simplest type, where the entire positive and negative electrode is represented as single particles. As a result of its simplicity, the performance of this model is poor, particularly at high charge rates. Increasing the complexity of such models, one can obtain the Doyle-Fuller-Newman type models, where electrodes are represented as a collection of particles of the same size and shape. By removing some of the simplifying assumptions of this modeling technique, one can obtain microscale models in which the phenomena are modeled at the microscale. All these models are described in terms of complex partial differential equations which require significant computing resources to solve, hence making them inappropriate for most online applications. Additionally, they incorporate a large number of physical parameters which are difficult to obtain. For these reasons, physical modeling of electrochemical cells is not the optimal choice for estimating the state of the cell [86].

In this work, we intend to leverage data-driven techniques to gain insight into the physical dynamics of the cell without explicitly modeling all of the physical processes present in the cell. However, we will utilize the classical Butler-Volmer (BV) relation [96] to model the polarization potential of the cell, as described in Section 3.5.

### 3.1.4 Equivalent Circuit Modeling

Yet, another common approach to modeling LIBs is the ECM technique, which can be used in conjunction with Electrochemical Impedance Spectroscopy (EIS) to replace the physical modeling of cells, in order to capture the overpotential effects and infer the electrochemical parameters [97, 98]. This method has gained popularity due to its simplicity and the potential for online applications. In this technique, instead of explicitly modeling the physical processes (e.g., Lithium intercalation), an equivalent circuit element is assigned to each physical process in the cell. The effect of physical processes is then isolated from

the OCV of the cell. In other words, the electrochemical parameters (representing circuit elements) can be used for extracting the overpotentials in the system (due to electrochemical processes and ohmic resistances in the cell) from the terminal voltage of the cell. This type of modeling requires EIS data (to be collected using special instruments) in addition to knowledge about the chemistry of the cell to adopt suitable equivalent circuits. The choice of equivalent models for the battery chemistry is challenging and nontrivial; however, using a suitable model, one can monitor the evolution of the electrochemical parameters in time in an online operation. Common ECMs for battery modeling are reviewed in [85, 97]. The electrochemical parameters could be used in conjunction with filter-based models for SoC estimation as described in Section 3.4. Also, the electrochemical parameters can be utilized to build more sophisticated machine learning models for SoC estimation. A more detailed description of the ECM and EIS techniques is presented in Section 3.2.

### 3.1.5 Filtering Techniques

A complementary approach to the Coulomb Counting method for SoC estimation relies on model-based Bayesian estimators. The most common Bayesian estimators used in the state estimation of cells are different variants of Kalman filters. In this approach, a battery model is used in conjunction with a state estimation filter/observer to infer the internal state of the system. The prior estimates of the internal state are obtained based on prior knowledge about the cell and an underlying mathematical model. The prior estimates of the state of the cell are then updated using an optimization approach to minimize the deviation of the theoretical response of the system with respect to a measured one, to obtain the posterior estimates. This iterative algorithm can be used for online SoC estimation. While a linear Kalman filter is an optimal choice for a linear system, the cell dynamics are nonlinear. The OCV-SoC relation is nonlinear, as shown in Figure 3.1, and linear Kalman filters cannot be explicitly used in this case. The Extended Kalman Filter (EKF) [99, 100] utilizes local linearization of the nonlinear system at each time step of the iterative algorithm. The Adaptive Extended Kalman Filter (AEKF) [101–103] corresponds to the case where the parameters of the model are adaptively updated according to the measurements to lower the possibility of algorithm divergence. The Unscented Kalman Filter (UKF) [104] and Adaptive Unscented Kalman Filter (AUKF) [105] are extensions of Kalman filters to nonlinear systems using more efficient sampling techniques, referred to as unscented transformation. Particle filters [106] and H-infinity filters [107] are other commonly used variants of the filters for enhancing SoC estimates of cells.

This approach, if combined with an ECM as the underlying model, requires real-time electrochemical measurements of the system. One method for inferring such information is by leveraging the EIS technique in real-time, as described in Section 3.2. Although these models are capable of tracking the state of

the system, they have a few drawbacks. First, these algorithms require proper underlying ECM models; hence, they might rely on additional equipment for inferring electrochemical parameters. Second, the convergence of the posterior state estimates to their reference values is not guaranteed in the presence of nonlinearity in the system, and especially when the underlying model is not capable of capturing the system dynamics. As one of the goals of this work, we propose a data-driven technique for identifying an underlying dynamical model for the system, which can be used in conjunction with a suitable filter to enhance the robustness of the estimation process. The details of this technique will be presented in Sections 3.4 and 3.6.

### 3.1.6 Data-Driven Techniques

In order to estimate the SoC of a cell, one can learn the nonlinear relation between the inputs into the system and its internal states. In this regard, machine learning techniques [91, 108, 109] could be used to find a nonlinear map between the inputs and outputs of the system with minimal domain-specific knowledge about the physical processes involved. The inputs of the model could include both DC domain data (DC current and terminal voltage of the cell) and AC domain data (electrochemical parameters and impedance data at different frequencies). Different neural network architectures have been used for this purpose, namely, Deep Neural Network [110], Gated Recurrent Unit [111], Long Short Term Memory [112] and Convolution Neural Network [113]. Although machine learning models have the capability of learning highly nonlinear relations at the expense of model complexity, they suffer from a few drawbacks. First, these models are data-greedy. A large amount of data for training and testing of such models is required that should cover all possible operating conditions. Hence, these models are prone to overfitting/underfitting issues and the robustness of such models is questionable. Second, the performance of such models is highly affected by the quality of the data and the methods used for training the models. Third, no insight into the physical processes in the system is obtained via such models and they are purely predictive. As noted by How et al. [87], if the model of the cell is fully known a priori, the model-based techniques could be viewed as superior to data-driven techniques from the statistical and physical point of view. However, if the underlying system is not fully understood, data-driven techniques can outperform other approaches. In this study, we are interested in developing a hybrid data-driven technique in order to not only train a predictive model, but also to gain insight into the dynamics of the cell. For this purpose, a SINDy framework is proposed.

### 3.1.7 Sparse Identification of Nonlinear Dynamics

The SINDy framework was first introduced by Brunton et al. [114] as a purely data-driven methodology for identifying the dynamics of a physical system via sparse regression techniques. In this approach, the measurements of the state of the system are collected as the system evolves in time. No *a priori* functional form is assumed for the underlying dynamical system in this technique. However, a large library of linear and nonlinear candidate terms describing the dynamics of the system is formed, from which a small number of terms are used to represent the dynamics of the cell. In order to find a suitable collection of terms describing the dynamics of the cell, sparse regression techniques are used to minimize the mismatch between the predicted state and the measured data by promoting sparsity in the solution of the optimization problem. This powerful technique has recently found applications in fluid mechanics [115–117], biology [118, 119], and epidemiology [120, 121]. In this research, we intend to employ sparse regression techniques for identifying the dynamics of a cell based on experimental measurements, a method that could be seen as an improvement over classical techniques for modeling LIBs. This method is computationally inexpensive and requires a minimal amount of data for training purposes compared to machine learning techniques. The robustness of the model (understood as model transferability from one experiment to another) could be enhanced using data from multiple cycles of the cell, as discussed in Section 3.5. This technique can lead to interpretable improvements in modeling the dynamics of the system, which facilitates the task of estimating SoC. In general, there is a trade-off between model complexity and model accuracy. In this approach, our aim is to find an optimal balance between these two aspects, while also gaining insights into the internal dynamics of the cell. The proposed methodology could be extended to different battery chemistries and operating conditions.

### 3.1.8 Outline

The modeling steps are listed below.

1. Collect DC domain and AC domain data from a cell running under dynamic loading conditions, as outlined in Section 3.3. The AC domain data is used to select a simple ECM by capturing the ohmic resistance, interfacial capacitance and charge-transfer resistance as the dynamics of the cell in real-time using EIS as an *operando* technique, as outlined in Section 3.2. ECM parameters, referred to as "electrochemical parameters", are collected in time for the duration of the cycle.
2. Use the BCC method in short durations of time (near the end of the time window) to obtain a "near-truth" state of the cell at a single point in time and use this point as a guide to enhance the SoC estimates for the entire cycle. Use the FCC method complemented with an EKF for longer times to

approximate the SoC of the cell for the entire cycle using the precomputed "near-true" state of the cell as a guide. The approximated SoC will serve as the "reference" state of the cell. This technique is explained in Section 3.4. The inferred reference state of the cell will be used as training data for the SINDy framework.

3. Implement the SINDy framework for identifying the dynamics of the cell using reference data, as described in Section 3.5.
4. Design an AUKF for enhancing state estimation using the identified model of SINDy, and quantify the uncertainty in estimations, as described in Section 3.6.

In general, this modeling framework focuses on improving the understanding of the dynamics of the cell while it is running under dynamic loading conditions, using the identified dynamics to estimate the internal state of the cell, and complementing this analysis by developing a feedback loop for enhancing estimates. The modeling prediction error is reduced using this framework. This chapter is organized as follows: the details of the EIS are described in Section 3.2; the experimental measurements are presented in Section 3.3; the mathematical background for the EKF is described in Section 3.4; the mathematical details and the results obtained with the SINDy framework are presented in Section 3.5; the AUKF technique is explained in Section 3.6; whereas the conclusions are deferred to Section 3.7.

### 3.2. Electrochemical Impedance Spectroscopy

EIS is a well-established non-invasive diagnostic tool for determining the dynamic behavior of electrochemical processes in a cell without interfering with its normal operation. In this technique, a low-amplitude (to ensure the linearity of the system response) AC signal is injected into the system over a wide range of frequencies. The response of the system to this excitation signal is obtained, and the impedance is calculated as the ratio of the AC voltage to the AC current, as described in Equations (3.5)-(3.7). Impedance is defined as the resistance to the current flow when an AC signal is applied to the system. In a purely resistive medium, there is no phase shift between the AC voltage and current signals; hence, the impedance of the system is represented by its real component, which is pure resistance. In the presence of inductive and capacitive effects, there will be a phase shift between the voltage and current signals, and the internal impedance of the circuit is then represented by the real and imaginary components for ohmic and non-ohmic effects, respectively. The impedance of the cell is computed at a wide range of frequencies. Different physical processes in the cell exhibit different time constants (a measure of time scale of the process), hence leaving unique signatures (phase shifts) on the impedance response. If a low

amplitude AC voltage at a particular frequency  $\omega$  is applied to the cell as

$$V_{AC}(t) = V_m \sin(\omega t), \quad (3.5)$$

in the time domain (or  $\tilde{V}(\omega) = V_m$  in the frequency domain), the resulting AC current as the response of the cell at the same frequency is measured as

$$I_{AC}(t) = I_m \sin(\omega t + \phi), \quad (3.6)$$

in the time domain (or  $\tilde{I}(\omega) = I_m e^{j\phi}$  in the frequency domain where  $j = \sqrt{-1}$  is the imaginary unit). The total impedance of the cell at that particular frequency can be computed as

$$Z(\omega) = \frac{\tilde{V}(\omega)}{\tilde{I}(\omega)} = \frac{V_m}{I_m} e^{-j\phi}, \quad (3.7)$$

where the  $\omega = 2\pi f$  is the angular frequency,  $t$  is time,  $\phi$  is the phase shift between AC voltage and current, and  $V_m$  and  $I_m$  are the amplitudes of AC voltage and current, respectively.

In a Li-ion cell, Li particles are involved in various physical processes, such as mass transfer in the electrolyte during charge/discharge and electrochemical reactions at the interface of the solid phase and the electrolyte, known as charge transfer reactions. In order to infer information about these processes in the cell, one is required to model each physical process in the system via an equivalent circuit element, a method referred to as Equivalent Circuit Modeling. Each of these physical processes is represented by resistive, capacitive, or inductive types of components in an ECM. The resistive effects stem from the bulk of the electrodes, current collectors, the electrolyte, and the charge-transfer reactions at the solid-electrolyte interface. Capacitive effects arise from the double layer formed on the surface of the solid-electrolyte interface. The porous nature of the electrodes leads to inductive effects. Various ECMs have been proposed in the literature to account for different processes according to the specific battery chemistry. Since the time constants associated with each process are different, these processes are separated using different frequencies for measuring the impedance. For instance, the mass transfer process is slow and hence dominant at lower frequencies. In the ECM technique, the theoretical impedance response of the equivalent circuit model is matched with the true impedance of the system using optimization techniques to infer the electrochemical parameters of the cell. This technique can be viewed as a macro-scale modeling of cells, where the spatial resolution of the cell is neglected, and only the temporal evolution of some key electrochemical parameters in the cell is traced.

In this study, using the Pulsenics Probe [122], hereafter referred to as "The Probe", the cell impedance is obtained for a range of frequencies in an *operando* mode using Equations (3.5)-(3.7), while the battery is running under constant-loading or dynamic-loading conditions. The Nyquist plot, containing the real and imaginary parts of the cell impedance at different frequencies, and the Bode plot, containing the magnitude and phase shift of impedance measurements for a battery running in the constant-loading condition, are shown in Figures 3.2a and 3.2b, respectively, at one snapshot of time corresponding to the beginning of charging under constant loading at 60A. The impedance information is collected at a temporal resolution of 25 seconds, across 30 different frequencies ranging from 5Hz to 600Hz.

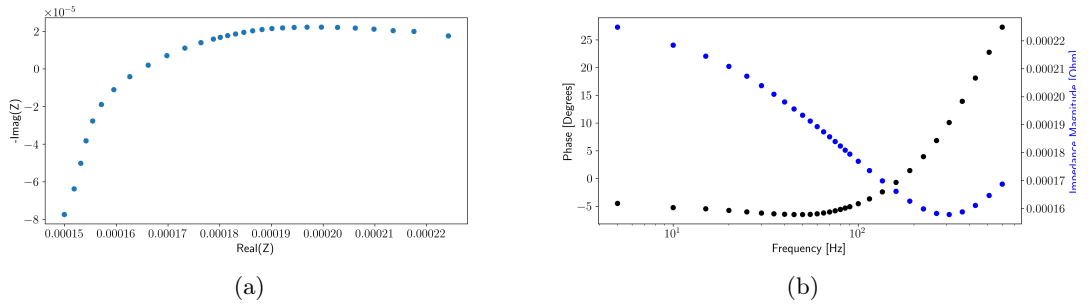


Figure 3.2: Nyquist plot (a), and Bode plot (b) at the beginning of charge in a constant-loading experiment. Real( $Z$ ) and Imag( $Z$ ) refer to the real and imaginary parts of impedance, respectively.

To analyze the response of the system to the excitation signal (3.7), an equivalent model can be used. One of the simplest and most common equivalent circuits used for electrochemical systems is the Thevenin model [123] shown in Figure 3.3. In this circuit, the interfacial charge-transfer phenomena (intercalation of Li ions on the surface of the negative electrode during charging and deintercalation of Li ions during discharge) is represented by a resistor in parallel with a capacitor accounting for the double layer capacitance formed on the surface of the solid-electrolyte interface, and in series with a resistance representing the bulk resistance of the electrolyte due to ohmic resistances in the cell. An ideal voltage source represents the ideal behaviour of the cell at open-circuit when at equilibrium. Note that the equivalent circuit model presented in Figure 3.3 is used as a large-signal model where the dynamics of the cell can be potentially nonlinear, as described in Equation (3.11). The small-signal model can be obtained by linearizing the nonlinear model of the equivalent circuit around an operating point. The details of the impedance computation for the small-signal excitation of this circuit is presented in Appendix B.1.

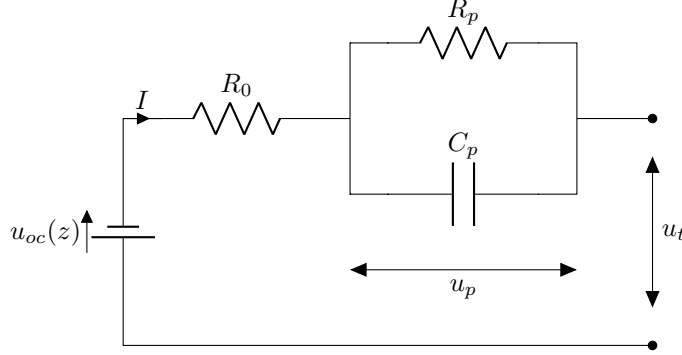


Figure 3.3: Schematic of a Thevenin equivalent circuit model used as a large-signal model. The terminal voltage of the cell  $u_t$  [V], the polarization potential  $u_p$  [V], the open-circuit potential  $u_{oc}$  [V], the current applied to the cell  $I$  [A], the ohmic resistance  $R_0$  [ $\Omega$ ], the charge-transfer resistance  $R_p$  [ $\Omega$ ], and the double-layer capacitance  $C_p$  [ $F$ ] are shown.

The ohmic resistance ( $R_0$ ), the charge-transfer resistance ( $R_p$ ), and the double-layer capacitance ( $C_p$ ), referred to here as the electrochemical parameters of the cell  $\boldsymbol{\theta} = [R_0, R_p, C_p]$ , are computed by minimizing a mismatch between the theoretical and the measured impedance of the cell. The theoretical impedance of the Thevenin circuit in Figure 3.3 is calculated using Ohm's law as (refer to Appendix B.1)

$$Z(\omega; \boldsymbol{\theta}) = R_0 + \frac{R_p}{1 + (\omega R_p C_p)^2} - j \frac{\omega R_p^2 C_p}{1 + (\omega R_p C_p)^2}, \quad (3.8)$$

where the impedance of the capacitor is  $1/(j\omega C_p)$ . The electrochemical parameters  $\hat{\boldsymbol{\theta}}$  are computed by solving the minimization problem

$$\hat{\boldsymbol{\theta}} = \arg \min_{\boldsymbol{\theta} \in \mathbb{R}^3} \sum_{i=1}^n \left| Z(\omega_i; \boldsymbol{\theta}) - \tilde{Z}(\omega_i) \right|^2, \quad (3.9)$$

where  $n$  is the number of frequencies used in the EIS experiment, and  $\tilde{Z}$  represents the impedance measured by EIS. Standard numerical techniques can be used for solving this problem. The software provided by Pulsenics Inc. is used for inferring electrochemical parameters in this study. Tracking the time evolution of electrochemical parameters serves as a diagnostic tool for evaluating the performance of the cell. Figure 3.4 shows the evolution of electrochemical parameters over time for one charge/discharge cycle of the cell running at 60A in a constant-current mode, with a time resolution of 25 seconds and four rest periods at approximately  $z = 0.2$ ,  $z = 0.4$ ,  $z = 0.6$ , and  $z = 0.8$ .

The Thevenin model is the simplest equivalent circuit model that can capture the interfacial physics of the cell through a charge-transfer resistance and a double-layer capacitance. Note that the semi-empirical Butler-Volmer relation represents the interfacial dynamics of the cell and under some specific conditions it

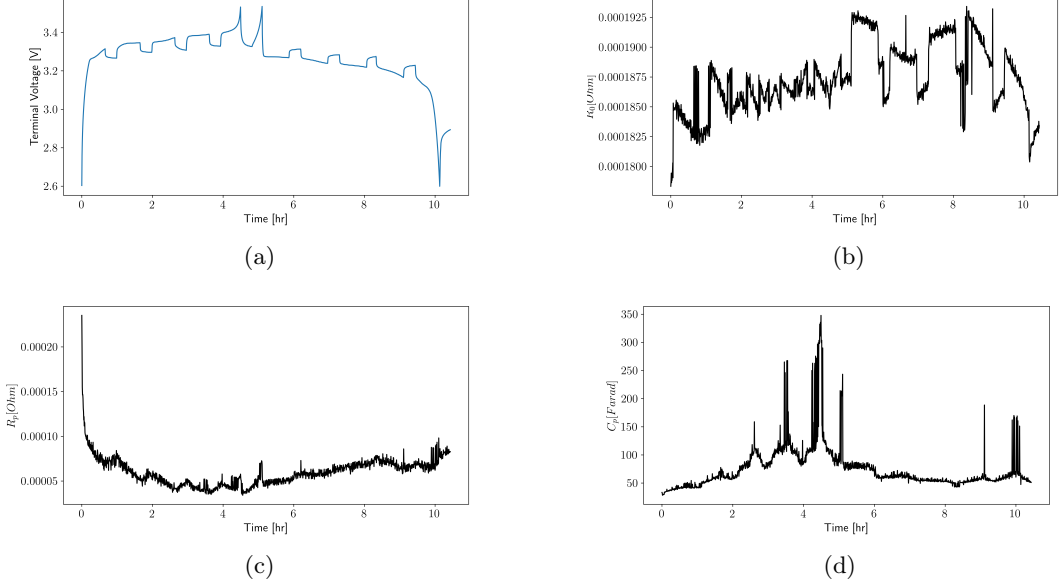


Figure 3.4: Terminal voltage  $u_t$  (a), and the evolution of electrochemical parameters,  $R_0(t)$  (b),  $R_p(t)$  (c), and  $C_p(t)$  (d) in time for a 60A constant-current charge and discharge cycle. The electrochemical parameters are collected every 25 seconds.

admits connections to an equivalent circuit model. In the case of small overpotentials, the Butler-Volmer relation can be linearized as described in (3.37), and the charge-transfer resistance can be computed for small-signal regimes. Different equivalent models suitable for Li-ion cells have been proposed in the literature [97], which are superior to the Thevenin model; however, their complexity is also increased. In particular, estimating the parameters of such more complex models requires solutions of inverse problems, which in turn introduces uncertainties in the estimation of the parameters due to the ill-posed nature of such problems. Hence, in this study real-time inference of electrochemical parameters is performed on the Thevenin model. These electrochemical parameters will be used in conjunction with an EKF to infer the reference SoC estimates of the cell parameters while the cell is running under dynamic loading conditions.

### 3.3. Experimental Data

Before delving into the modeling framework, we will present the experimental data. To assess the performance of a model for SoC estimation, one must assign "true" SoC values to the experimental measurements. As discussed earlier, this task is inherently challenging. The CC technique could be used as a reliable method in short durations for assigning true SoC values based on the system described in Equation (3.3) to experimental data obtained under static loading conditions. The error of such calculations is

small and can be neglected. Figure 3.5 demonstrates the SoC assigned to different cycles operating under constant loading conditions. In the experiments presented in Figure 3.5, the cell is cycled in its voltage

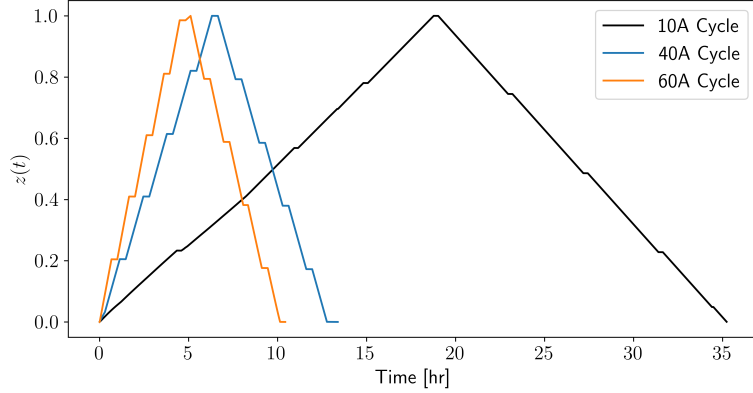


Figure 3.5: SoC of a cell determined via the CC method (3.3) under static loading conditions with 20 minutes rest periods after each 0.2 increment of SoC during charge/discharge. The effect of relaxation dynamics of the cell and its self-discharge during the rest period is neglected.

operating range ( $2.5V - 3.6V$ ). The maximum available capacity of the cell in these experiments can be calculated as the total amount of charge transferred to the cell during a constant-rate charge/discharge of the cell. In this case, the maximum available capacity of the cell is calculated to be  $Q_{max} \approx 190[A.hr]$ , compared to its nominal capacity of  $Q_n = 200[A.hr]$ . This information will be used along with the Coulomb Counting method, Eq. (3.3), in order to determine the reference state of the cell at different cycles during dynamic loading conditions. Figure 3.6 demonstrates the current and terminal voltage of a cell, cycled under dynamic loading conditions. This current profile includes three important steps:

1. charging of the cell from  $z(t_0) = 0$  to almost half of the capacity of the cell, where  $t \in [t_0, t_1]$ ,  $t_0 = 0$  is the beginning of charge from  $z = 0$ , and  $t_1$  is the beginning of dynamic loading experiment,
2. operating under a randomly generated dynamic loading profile for 24 or 48 hours, where  $t \in [t_1, t_2]$ ; this includes a subsequent 5 minute charge/discharge of the cell at a randomly generated rate,  $t_1$  and  $t_2$  are the beginning and ending of the dynamic loading profile, respectively,
3. a full discharge of the cell to  $z(t_f) = 0$ , where  $t \in [t_2, t_f]$  and  $t_f$  is the final time of the experiment.

The SoC of the cell is calculated based on the FCC model (3.3). The challenge arises when the cell is running under dynamic loading conditions, as there is no way of inferring the "true" SoC evolution. Additionally, using the FCC method might lead to the accumulation of errors over extended durations. However, step 3 of the dynamic loading profile consists of a full discharge to  $z(t_f) = 0$ . According to the amount of charge passed through the cell during step 3, one can track back the SoC of the cell using

the BCC model (3.4) to obtain its "near-true" state at  $t = t_2$  (grey vertical lines in Figure 3.6c). This estimation over short durations is assumed to be reliable as the accumulation of error is negligible. Figure 3.6c highlights the state of the system at  $t = t_2$  using both FCC and BCC methods. As observed, there is a discrepancy between the predictions of these two methods. To infer the SoC evolution for  $0 < t < t_2$ , the EKF technique will be used with FCC method to produce reliable estimates of the state of the system, as described in Section 3.4. Ten different cycles are performed on the cell, followed by a similar approach based on dynamic profiles. The error of computing SoC using FCC method in comparison to the BCC method is calculated as

$$\mathcal{E} = |z(t_2) - \tilde{z}(t_2)| \cdot 100, \quad (3.10)$$

where  $z(t)$  and  $\tilde{z}(t)$  are the SoC computed using FCC and BCC methods, respectively.

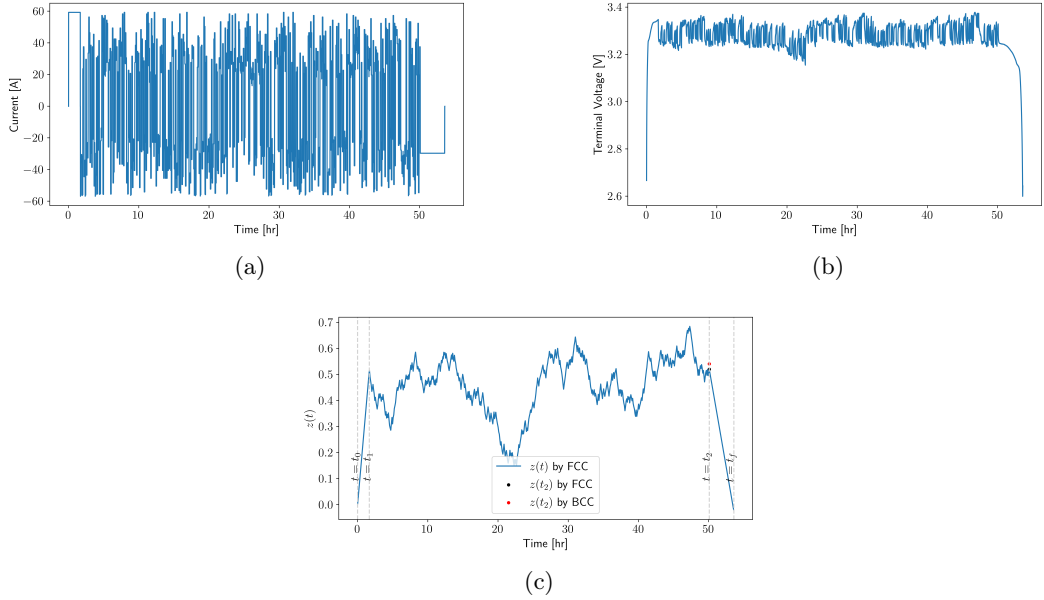


Figure 3.6: Current  $I(t)$  (a), terminal voltage  $u_t(t)$  (b), and state-of-charge  $z(t)$  (c) of the cell for one cycle operating under dynamic loading conditions.

### 3.4. Extended Kalman Filtering

To obtain reference SoC estimates for different cycles, we will use the Kalman filtering technique. This technique relies on an underlying model of the cell representing its dynamics. In order to model the polarization potential, different ECMs could be adapted based on battery chemistry with different levels of complexity. More complex models require more sophisticated inverse modeling techniques to obtain the parameters of the ECM from EIS data. Kalman filters have been extensively investigated in the

literature for this purpose [92, 93, 101–103, 124]. In this section, the model representing the dynamics of the cell is obtained via the CC method (3.3) for estimating SoC, and the Thevenin model as presented in Figure 3.3 for estimating the polarization potential of the cell, while in operation. In the Kalman filtering technique, the internal state of the cell is predicted using the mathematical model, leading to the estimation of the terminal voltage of the cell. The computed terminal voltage is then compared to its measured one and based on the observed error the estimates of the state variables are updated. This technique is used for inferring reference SoC estimates, which then can be used as the training data in Section 3.5 to perform the task of system identification.

### 3.4.1 Mathematical Background

Kalman filtering is a type of sequential probabilistic inference that seeks to enhance the state estimation process in the presence of process and measurement noise. The task of the Kalman filter is to take in information about internal state estimates which is known to be polluted by some errors and uncertainty, filter out the unreliable information by leveraging data from output variable observations and finally improve the state estimates. In our problem, the state variables are SoC and polarization potential, and the observed variable is the terminal voltage of the cell. The Kalman filter is a predictor-corrector filter. In the prediction step, the state variables are advanced in time using the mathematical model, and the terminal voltage of the cell is estimated. In the correction step, the computed terminal voltage is compared to the measurement, and the error of estimation is used for updating the estimates of state variables. There are two types of uncertainties involved in the model. First, the process noise is referred to as the uncertainty in the underlying model. The underlying mathematical model might fail to describe the dynamic behaviour of the system, and this will give rise to the process noise. Second, the measurement noise represents the error in the experimental measurements caused by the noise of the sensors. The task of the Kalman filter is to find a balance between the two sources of uncertainty, i.e., the process noise and measurement noise. In the case of more certain models (small process noise) the filter relies less on measurement data, and vice versa. The process and sensor noise are assumed to be Gaussian random variables. Kalman filters were first introduced for state estimation of linear systems and later extended to nonlinear systems through linear approximations or sampling techniques. A Kalman filter is the optimal solution for a linear system, where the convergence to the true state is guaranteed. The Kalman filter used in this work is based on a nonlinear Kalman filter formulation, also known as the EKF, due to the nonlinear dependency of OCV on SoC, as implemented by [102]. Note that the convergence of nonlinear extensions of Kalman filters such as EKF to the true estimates is not guaranteed, and the obtained solution is referred to as "near-optimal" solution.

In this approach, a Thevenin equivalent circuit model is assumed for the physical processes occurring in the cell, as shown in Figure 3.3, due to its simplicity and the ease of inferring electrochemical parameters via EIS technique. The dynamics of the cell for the polarization potential are obtained from this equivalent circuit, however, the SoC is modelled via the CC method (3.3). The deterministic continuous state equations for the evolution of state variable  $\mathbf{X}(t) = [u_p(t), z(t)]^\top \in \mathbb{R}^2$  are

$$\dot{\mathbf{X}} = \mathbf{A}'\mathbf{X} + \mathbf{B}'\mathbf{U}, \quad (3.11a)$$

$$u_t = h(\mathbf{X}, \mathbf{U}) = u_p + u_{oc}(z) + IR_0, \quad (3.11b)$$

$$\mathbf{A}' = \begin{bmatrix} -\frac{1}{R_p C_p} & 0 \\ 0 & 0 \end{bmatrix}, \quad (3.11c)$$

$$\mathbf{B}' = \begin{bmatrix} \frac{1}{C_p} \\ \frac{\eta}{Q_n} \end{bmatrix}, \quad (3.11d)$$

where  $h : \mathbb{R}^2 \times \mathbb{R} \rightarrow \mathbb{R}$  is a nonlinear observer function,  $\mathbf{A}'$  and  $\mathbf{B}'$  are the system transition matrices representing the dynamics of the cell, and  $\mathbf{U} = [I(t)]$  is the vector of control parameters (in this formulation this vector reduces to the applied current only, however, in later sections, more terms will be added to the vector of control parameters). The terminal voltage of the cell is obtained as the sum of its open-circuit voltage, its polarization potential, and its ohmic resistance, cf. (3.11b). Also, the open-circuit voltage  $u_{oc}(z)$  is evaluated using the polynomial fit to the terminal voltage of the cell in charging and discharge regimes as presented in Figure 3.1. The internal state of the system is unknown, however, the terminal voltage of the cell is observed through experimental measurements. The model introduced in (3.11) is deterministic, however, the model and the measurements might incorporate uncertainties. By incorporating the uncertainties in the model and measurements, and by integrating the state equations

(3.11) in time, one can obtain the stochastic discrete state equations as

$$\mathbf{X}_{k+1} = \mathbf{A}_k \mathbf{X}_k + \mathbf{B}_k I_k + \mathbf{W}_k, \quad (3.12a)$$

$$u_{t,k+1} = h(\mathbf{X}_{k+1}, \mathbf{U}_{k+1}) = u_{p,k+1} + u_{oc}(z_{k+1}) + I_{k+1} R_{0,k+1} + V_{k+1}, \quad (3.12b)$$

$$\mathbf{A}_k = \begin{bmatrix} \exp(-\frac{\Delta t}{R_{p,k} C_{p,k}}) & 0 \\ 0 & 1 \end{bmatrix}, \quad (3.12c)$$

$$\mathbf{B}_k = \begin{bmatrix} R_{p,k}(1 - \exp(-\frac{\Delta t}{R_{p,k} C_{p,k}})) \\ \frac{\Delta t \eta}{Q_n} \end{bmatrix}, \quad (3.12d)$$

$$\mathbf{W}_k \sim \mathcal{N}(\mathbf{0}, \mathbf{Q}_k), \quad (3.12e)$$

$$V_k \sim \mathcal{N}(0, R_k), \quad (3.12f)$$

where  $\mathbf{X}_k(t) \in \mathbb{R}^2$  is the state vector at time step  $k$ ,  $\mathbf{A} \in \mathbb{R}^{2 \times 2}$  and  $\mathbf{B} \in \mathbb{R}^{2 \times 1}$  are the state transition matrices, and  $I_k$  is the current (control variable) at time step  $k$ . The process noise  $\mathbf{W} \in \mathbb{R}^2$  represents the modeling uncertainties, drawn from a normal distribution with mean zero and covariance matrix  $\mathbf{Q} \in \mathbb{R}^{2 \times 2}$ , whereas,  $V_k \in \mathbb{R}$  is the terminal voltage measurement noise drawn from a normal distribution with mean zero and variance  $R_k$ . Also, the model introduced in (3.12) incorporates a nonlinear observation model  $h(\mathbf{X}, \mathbf{U})$  which maps the state space into observed space. As dependence of  $u_{oc}$  on  $z$  is nonlinear, cf. Figure 3.1, the EKF uses local linearization of the corresponding nonlinear term. This term will be linearized by a first-order Taylor series expansion as  $\mathbf{C}_k = [1, \frac{du_{oc}}{dz}]$ . As the internal state variables cannot be measured directly, one needs to leverage the existence of observations on the terminal voltage and design a feedback loop. A correction to the state estimates is performed based on the mismatch between the observations and model-based prediction of the terminal voltage. We seek to minimize the mismatch between the state variable prediction by the mathematical model and the true state of the system, given the observations of the terminal voltage of the cell. In other words, the predicted state of the system in each time step is corrected by solving the minimization problem

$$\min_{\mathbf{K}_k} \mathbb{E} \left[ \|\mathbf{e}_k\|_2^2 | \tilde{u}_{t_k} \right], \quad \mathbf{e}_k = \tilde{\mathbf{X}}_k - \mathbf{X}_k^+, \quad (3.13)$$

where  $\mathbf{e}_k$  is the error of estimating state of system,  $\tilde{\mathbf{X}}_k$  is the true state of the system,  $\mathbf{X}_k^+$  is the posterior state of the system predicted by the mathematical model,  $\mathbf{K}_k$  is the Kalman gain, and  $\tilde{u}_{t_k}$  is the experimental observation of the terminal voltage of the cell at time  $k$ . This minimization problem needs to be solved at each time step, to infer the best estimate of the internal states of the system, subject to experimental observations. The covariance of the process noise and the measurement noise are computed

as

$$\begin{aligned} Q &= E[\mathbf{W}_k \mathbf{W}_k^\top], \\ R &= E[V_k V_k^\top], \end{aligned} \quad (3.14)$$

by assuming that they are stationary. The error covariance matrix of the posterior estimate at time step  $k$  is computed as

$$\mathbf{P}_k^+ = E[\mathbf{e}_k \mathbf{e}_k^\top] = E[(\tilde{\mathbf{X}}_k - \mathbf{X}_k^+) (\tilde{\mathbf{X}}_k - \mathbf{X}_k^+)^\top]. \quad (3.15)$$

Denoting the prior estimate of the state obtained by the mathematical model (3.11)  $\mathbf{X}_k^-$ , we can write the posterior estimate of the state as a combination of its prior estimate and a term proportional to the error of estimating the terminal voltage of the cell as

$$\mathbf{X}_k^+ = \mathbf{X}_k^- + \mathbf{K}_k (\tilde{u}_{t_k} - u_{t_k}), \quad (3.16)$$

where  $(\tilde{u}_{t_k} - u_{t_k})$  is referred to as "innovation", and  $u_{t_k}$  is the estimated terminal voltage of the cell as the output of the mathematical model. Substituting (3.12b) for the terminal voltage in expression (3.16) we get

$$\mathbf{X}_k^+ = \mathbf{X}_k^- + \mathbf{K}_k \left( \mathbf{C}_k \tilde{\mathbf{X}}_k + R_{0,k} I_k + V_k - \mathbf{C}_k \mathbf{X}_k^- - R_{0,k} I_k \right) = \mathbf{X}_k^- + \mathbf{K}_k \left( \mathbf{C}_k \tilde{\mathbf{X}}_k + V_k - \mathbf{C}_k \mathbf{X}_k^- \right). \quad (3.17)$$

Substituting (3.17) into (3.15), we get

$$\mathbf{P}_k^+ = E \left[ \left( (\mathbf{I} - \mathbf{K}_k \mathbf{C}_k) (\tilde{\mathbf{X}}_k - \mathbf{X}_k^-) - \mathbf{K}_k V_k \right) \left( (\mathbf{I} - \mathbf{K}_k \mathbf{C}_k) (\tilde{\mathbf{X}}_k - \mathbf{X}_k^-) - \mathbf{K}_k V_k \right)^\top \right]. \quad (3.18)$$

Note that  $\tilde{\mathbf{X}}_k - \mathbf{X}_k^-$  is uncorrelated with  $V_k$ , and using relations (3.14) and (3.15), equation (3.18) reduces to

$$\mathbf{P}_k^+ = (\mathbf{I} - \mathbf{K}_k \mathbf{C}_k) \mathbf{P}_k^- (\mathbf{I} - \mathbf{K}_k \mathbf{C}_k)^\top + \mathbf{K}_k R \mathbf{K}_k^\top, \quad (3.19)$$

where  $\mathbf{P}_k^-$  is the error covariance matrix based on the prior estimate of state variable. Referring to the definition of the error covariance matrix (3.15), it is clear that the trace of this matrix is equal to the mean-squared-error introduced in (3.13). The objective is to minimize this error with respect to the Kalman gain introduced in (3.16). Thus, we expand (3.19), compute the trace of it, differentiate with respect to the Kalman gain and equate to zero, which gives

$$\frac{\partial \text{tr}(\mathbf{P}_k^+)}{\partial \mathbf{K}_k} = \frac{\partial \text{tr}(\mathbf{P}_k^-)}{\partial \mathbf{K}_k} - 2(\mathbf{C}_k \mathbf{P}_k^-)^\top + 2\mathbf{K}_k (\mathbf{C}_k \mathbf{P}_k^- \mathbf{C}_k^\top + R) = \mathbf{0}. \quad (3.20)$$

Note that the trace of the error covariance matrix is a scalar quantity, whereas the Kalman gain is a vector quantity. The differentiation of the trace of the error covariance matrix with respect to the Kalman gain vector is equivalent to computing the gradient, where  $\frac{\partial}{\partial}$  denotes gradient operator. Rearranging (3.20), we obtain the Kalman gain corresponding to the optimal solution as

$$\mathbf{K}_k = \mathbf{P}_k^- \mathbf{C}_k^\top [ \mathbf{C}_k \mathbf{P}_k^- \mathbf{C}_k^\top + R ]^{-1}. \quad (3.21)$$

Substituting (3.21) into (3.19), we obtain the equation for computing the posterior error covariance matrix as

$$\mathbf{P}_k^+ = [\mathbf{I} - \mathbf{K}_k \mathbf{C}_k] \mathbf{P}_k^-. \quad (3.22)$$

In order to complete the recursive process in the Kalman filter, we need to advance the error covariance matrix in time. We define the error of the prior estimate as

$$\mathbf{e}_k^- = \tilde{\mathbf{X}}_k - \mathbf{X}_k^- = \mathbf{A}_{k-1} \tilde{\mathbf{X}}_{k-1} + \mathbf{B}_{k-1} I_{k-1} + \mathbf{W}_k - \mathbf{A}_{k-1} \mathbf{X}_{k-1}^{-1} - \mathbf{B}_{k-1} I_{k-1} = \mathbf{A}_{k-1} \mathbf{e}_{k-1}^- + \mathbf{W}_k. \quad (3.23)$$

The prior error covariance can be computed by substituting (3.23) into  $\mathbf{P}_k^- = E[\mathbf{e}_k^- \mathbf{e}_k^{-\top}]$  as

$$\mathbf{P}_k^- = \mathbf{A}_{k-1} \mathbf{P}_{k-1}^+ \mathbf{A}_{k-1}^\top + \mathbf{Q}_{k-1}. \quad (3.24)$$

The Kalman filter formulation presented above is the optimal solution for linear problems in the sense of minimizing the estimation error. The linearization involved in the EKF algorithm affects the robustness of the algorithm for nonlinear systems. The recursive Kalman filter algorithm consists of a prediction step and an update step. The former involves the calculation of internal state variables along with their uncertainties using information from previous time step, cf. (3.12) and (3.24); the latter involves updating the estimated state variables using error of estimation in comparison to experimental measurements, cf. (3.16) and (3.22). An advantage of this algorithm in comparison to conventional optimization algorithms is that it can produce estimates in real time and that the optimization process happens in real time. The EKF algorithm is detailed in Algorithm 1. Note that information about how to choose the error covariance matrix  $\mathbf{Q}$  and variance  $R$  is in general not available. Adaptive algorithms for computing this information are used in this case [102]. Note that the adaptive approach presented in Algorithm 1 includes a "forget factor"  $\alpha$ , determining the amount of information to be taken from previous time steps with respect to information from current time step. The initial guesses for  $\mathbf{Q}$  and  $R$ ,

and the forget factor are the parameters to be tuned in this algorithm.

---

**Algorithm 1:** EXTENDED KALMAN FILTER

---

**Input:**  $k$  — Iteration number  
 $\mathbf{X}_k^-$  — Prior internal state at step  $k$   
 $\mathbf{P}_k^-$  — Prior error covariance matrix at step  $k$   
 $\alpha$  — Forget factor

**Output:**  $u_t$  — Estimated terminal voltage  
 $\mathbf{X}_k^+$  — Posterior internal state at step  $k$   
 $\mathbf{P}_k^+$  — Posterior error covariance matrix at step  $k$

---

```

 $k \leftarrow 0$ 
Initialize  $\mathbf{Q}_0, R_0$ :

$$\mathbf{X}_0^+ = E(\mathbf{X}_0)$$


$$\mathbf{P}_0^+ = E[(\mathbf{X}_0 - \mathbf{X}_0^+)(\mathbf{X}_0 - \mathbf{X}_0^+)^T]$$

repeat
   $k \leftarrow k + 1$ 
  Time update: performing prior estimate
    State estimate time update
    
$$\mathbf{X}_k^- = \mathbf{A}_{k-1}\mathbf{X}_{k-1}^+ + \mathbf{B}_{k-1}I_{k-1}$$

    Error covariance time update
    
$$\mathbf{P}_k^- = \mathbf{A}_{k-1}\mathbf{P}_{k-1}^+\mathbf{A}_{k-1}^T + \mathbf{Q}_{k-1}$$

  Measurement update: correction by Kalman gain
    Output estimate
    
$$u_{t,k} = h(\mathbf{X}_k^-, \mathbf{U}_k)$$

    Kalman gain matrix
    
$$\mathbf{K}_k = \mathbf{P}_k^-\mathbf{C}_k^T [\mathbf{C}_k\mathbf{P}_k^-\mathbf{C}_k^T + R_k]^{-1}$$

    State estimate measurement update
    
$$\mathbf{X}_k^+ = \mathbf{X}_k^- + \mathbf{K}_k [u_{t,k} - \tilde{u}_{t,k}]$$

    Error covariance measurement update
    
$$\mathbf{P}_k^+ = (\mathbf{I} - \mathbf{K}_k\mathbf{C}_k)\mathbf{P}_k^-$$

until  $t_k = t_f$ ;
where adaptive covariance matrices are calculated as [102]:

$$d_k = \tilde{u}_{t,k} - u_{t,k} = \tilde{u}_{t,k} - h(\mathbf{X}_k^-, \mathbf{U}_k)$$


$$\epsilon_k = \tilde{u}_{t,k} - h(\mathbf{X}_k^+, \mathbf{U}_k)$$


$$\mathbf{Q}_k = \alpha\mathbf{Q}_{k-1} + (1 - \alpha)(\mathbf{K}_k d_k d_k^T \mathbf{K}_k^T)$$


$$R_k = \alpha R_{k-1} + (1 - \alpha)(\epsilon_k \epsilon_k^T + \mathbf{C}_k \mathbf{P}_k^+ \mathbf{C}_k^T)$$


```

---

Although Kalman filtering is a standard technique for estimating SoC of cells, the innovation in this work is in the derivation of the parameters of the Thevenin model, namely  $R_0, R_p, C_p$ , via the probe. These parameters are drawn in real-time using EIS, and leveraging optimization techniques to infer parameters from impedance measurements [125]. Conventionally, the electrochemical parameters were obtained by formulating inverse problems in the time domain. One drawback of such techniques is that a constant electrochemical parameter is fitted to the whole evolution of the cell, and it does not account for changes in electrochemical parameters while the cell is in operation. The current technique allows us to obtain the evolution of electrochemical parameters in time, rather than using constant parameter values. These electrochemical parameters are used in the mathematical model (3.12) along with the Kalman

filter, to find an estimate for the posterior state of the system.

### 3.4.2 Results

The EKF is run on every cycle and the results are summarized in Figure 3.7. The training of the parameters of the EKF algorithm is performed on individual cycles manually, to ensure accurate SoC estimations for each cycle. Note that in Figure 3.7, the SoC absolute error at  $t = t_2$  is computed using FCC and EKF and compared to the true values (BCC estimates) based on (3.10). As can be observed the SoC estimate at  $t = t_2$  is improved via EKF in comparison to FCC model.

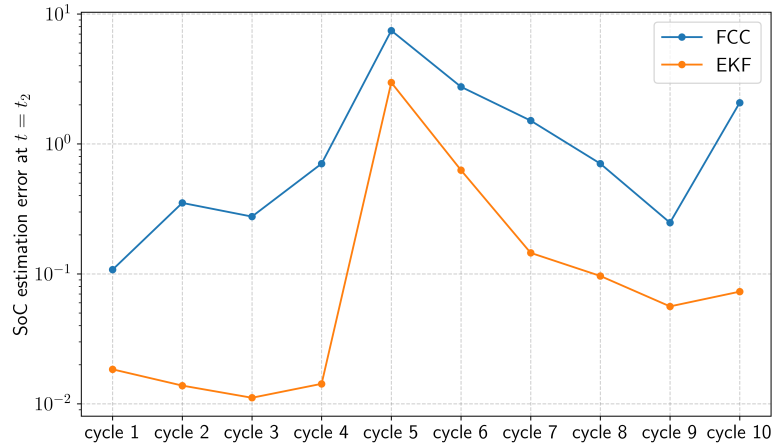


Figure 3.7: The absolute error of SoC estimation at  $t = t_2$ ,  $\mathcal{E}$ , cf. (3.10), using FCC (blue) and EKF (orange), for ten different cycles operating under dynamic loading conditions.

The evolution of the SoC over time and the true and estimated terminal voltage of the cell for one of the cycles are shown in Figure 3.8 for reference. As can be observed, the SoC estimates by EKF align with the SoC estimates of FCC model with slight improvements. However, the prior estimation of the terminal voltage of the cell has major differences with respect to the true terminal voltage, and the EKF is not capable of significantly improving this estimation as the posterior terminal voltage does not predict the behaviour of the system. The reason for this behavior, which is observed in all cycles, is an inaccurate underlying model of the dynamics of the cell. This model is not consistent with the true dynamics of the cell and can lead to discrepancies in the estimation of the terminal potential of the cell. This issue will be investigated in detail in Section 3.5.

In tuning the EKF parameters to the data from different cycles, there are a few criteria to observe.

1. The underlying model of the cell (3.12) uses the CC model for estimating the SoC of the cell, hence,

the evolution of the posterior SoC estimate obtained by the Kalman filter must be in agreement with the CC prediction, as observed in Figure 3.8a.

2. As only one single point exists for assessing the performance of the EKF ( $t = t_2$ ) based on BCC in comparison to FCC, emphasis is put on improving the SoC estimate at this point only.

The EKF parameters are tuned for each cycle in order to improve the SoC estimate at  $t = t_2$  without significantly deviating from the CC dynamics based on the two above criteria.

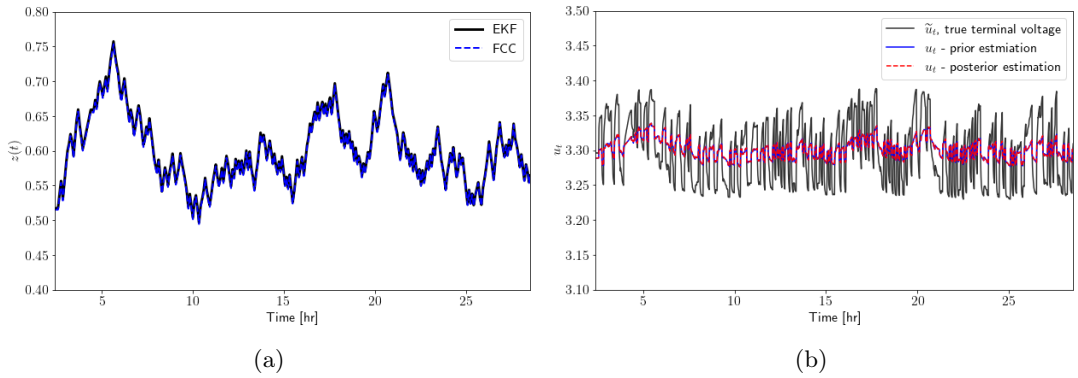


Figure 3.8: SoC evolution determined via FCC and EKF (a), and terminal voltage estimation using EKF (b) for one of the experiments under dynamic loading conditions. Note that the plots are magnified such that only the dynamic loading part of the experiment is shown ( $t_1 < t < t_2$ ).

It is notable that the EKF is not the optimal solution, rather a near-optimal solution for a nonlinear system, which suffers from the divergence issues from the true state of the system. Due to the approximation involved in the framework of EKF, the Kalman filter tends to lose robustness when moving from one cycle to another, giving rise to the possibility of diverging from the reference state. In other words, transferring the parameters tuned on one cycle to another one does not guarantee convergence of the model predictions for the data in the new cycle, especially when the operating conditions deviate from those of the original cycle. Inaccurate initial values for the state variables used to initiate the algorithm could be one source of inconsistency in the results. However, in our case, the cells are cycled starting from step 1, meaning that information about the state of the cell is available. Another important factor affecting the robustness of the algorithm is that the sensor error variance ( $R_k$  in (3.12f)) is not consistent across different cycles, hence, the adaptive algorithm cannot properly predict the uncertainty in the system for all cycles. This source of inconsistency is normally difficult to eliminate. Another important factor resulting in the loss of robustness of the EKF relates to the process noise covariance ( $Q_k$  in (3.12e)). It has been shown that the chosen model for the dynamics of the cell can significantly affect the performance of the Kalman filter [126]. This problem arises when the model (the ECM model in this case) is not a

suitable choice for the system under study. Hence, it introduces significant uncertainty in the modeling process, which could, in fact, affect the robustness of the model. The discrepancy between the true terminal voltage and the predicted one in Figure 3.8b is a consequence of modeling flaws. The EKF framework can be robustified through more reliable estimations of the polarization potential to reduce the modeling noise. The purpose of this study is to improve the design of the Kalman filter to produce an acceptable balance between accuracy and robustness. To do so, we will focus on lowering the process modeling uncertainty by adopting a data-driven approach for identifying the dynamics of the system. This is done via the SINDy framework, which is introduced in the next section.

### 3.5. Sparse Identification of Nonlinear Dynamics

In this section, we intend to use the SINDy framework for identifying system dynamics using minimal *a priori* assumptions about the dynamics and relying solely on measurement data, by employing sparse regression techniques, particularly the  $l_0$  and  $l_1$  norms. Traditional approaches to describing system dynamics involve identifying physical processes, developing mathematical models, tuning model parameters through inverse modeling techniques, and using these models for prediction and control. However, SINDy is different in that it seeks to identify the underlying model itself. It operates by assuming a feature library consisting of arbitrary number of terms, linear or nonlinear, with various functional forms of the dependence on the state and control variables which may describe the system's evolution. The objective of this section is to uncover the potentially nonlinear dynamics of the system to improve state estimations compared to approaches based on the classical model (such as the Thevenin model).

SINDy offers several advantages over other data-driven approaches: (i) lower computational complexity during training compared to other data-driven techniques, (ii) interpretable results compared to other data-driven techniques, and (iii) tunability of complexity/accuracy based on specified parameters. In this study, we employ the SINDy-with-Control framework, as introduced by Fasel et al. [127], to incorporate control variables into the model. It is worth noting that SINDy has a close connection to Dynamic Mode Decomposition [128] and Koopman operator theory [129]. The former aims to extract spatiotemporal coherent structures from discrete-time measurement data by finding a linear dynamical model that best describes the evolution of a dynamical system in time. The latter, however, describes every nonlinear system as an infinite-dimensional but linear operator, with its spectral decomposition characterizing the nonlinear system. Hence, if one formulates SINDy in discrete time with only linear terms in the feature library without sparsification, the solution would be reduced to the DMD model if the choice of the linear terms in the feature library is optimal. Conversely, including all possible nonlinearities in the feature

library would produce a model converging to the Koopman operator. In this study, we aim to deduce an optimal representation of the dynamical system starting from a basis of predefined possible nonlinearities.

### 3.5.1 Mathematical Background

The general form of our continuous dynamical system is

$$\begin{aligned}\dot{\mathbf{X}}(t) &= \mathbf{F}(\mathbf{X}(t), \mathbf{U}(t)), \\ \mathbf{X}(0) &= \mathbf{X}_0,\end{aligned}\tag{3.25}$$

with state  $\mathbf{X}(t) = [u_p(t), z(t)] \in \mathbb{R}^2$ , control inputs included in  $\mathbf{U}(t) \in \mathbb{R}$ , and dynamics  $\mathbf{F} : \mathbb{R}^2 \times \mathbb{R} \rightarrow \mathbb{R}^2$  describing the evolution of the system which needs to be found from data. Note there is one control input to the system, meaning  $\mathbf{U}(t) = I(t)$ ; however, we will see below that the control input matrix will be extended to incorporate more nonlinearities as described in Section 3.5.2. Due to the highly nonlinear nature of the problem, no closed-form expression for  $\mathbf{F}$  is a priori assumed. The only information that is available is the initial condition of state variables at  $t = 0$ ,  $\mathbf{X}_0$ , and the measurement data in the form of full state observations in discrete time as  $\widetilde{\mathbf{X}}(t_k)$ , where  $k$  is the time step. However, one can approximate  $\mathbf{F}$  as a linear combination of predefined basis functions forming a library. Let

$$\Theta(\mathbf{X}(t), \mathbf{U}(t)) = [\theta_1(\mathbf{X}(t), \mathbf{U}(t)), \dots, \theta_n(\mathbf{X}(t), \mathbf{U}(t))]\tag{3.26}$$

be the library of user-defined candidate functions (including linear and nonlinear terms), where  $\Theta(\mathbf{X}, \mathbf{U}) \in \mathbb{R}^n$ ,  $\theta_i : \mathbb{R}^2 \times \mathbb{R} \rightarrow \mathbb{R}$ ,  $i = 1, \dots, n$ , and  $n$  is the number of terms in the feature library. Note that the feature library consists of terms depending both linearly and nonlinearly, on both the state variable  $\mathbf{X}$  and the control variable  $\mathbf{U}$ . One can write

$$\mathbf{F}(\mathbf{X}(t), \mathbf{U}(t)) = \sum_{j=1}^n \theta_j(\mathbf{X}(t), \mathbf{U}(t)) \boldsymbol{\xi}_j,\tag{3.27}$$

where  $\boldsymbol{\xi}_j \in \mathbb{R}^2$  is the coefficient of  $j$ -th term in the feature library such that the governing system becomes

$$\dot{\mathbf{X}}(t) = \Theta(\mathbf{X}(t), \mathbf{U}(t)) \boldsymbol{\Xi},\tag{3.28}$$

where

$$\boldsymbol{\Xi} = [\boldsymbol{\xi}_1 \ \boldsymbol{\xi}_2 \ \dots \ \boldsymbol{\xi}_n]^T\tag{3.29}$$

is the matrix of a priori unknown coefficients for candidate functions in the feature library. The objective is then to find a sparse representation of the matrix  $\Xi$ , which results in the elimination of some of the less important functions in the feature library. This leads to an optimization problem in the form

$$\hat{\Xi} = \arg \min_{\Xi} \frac{1}{2} \left\| \tilde{\dot{\mathbf{X}}} - \Theta(\mathbf{X}, \mathbf{U}) \Xi \right\|_2^2 + \lambda R(\Xi), \quad (3.30)$$

where  $\lambda > 0$  is a regularization parameter,  $R : \mathbb{R}^n \rightarrow \mathbb{R}$  is a regularization function,  $\tilde{\dot{\mathbf{X}}}$  is the vector of state measurements,  $\tilde{\dot{\mathbf{X}}}$  is the time derivative of the state measurements, and  $\|\cdot\|_2$  represents the  $l_2$  norm. Note that in (3.30) the time dependency of the state measurements  $\tilde{\mathbf{X}}$  and the feature library  $\Theta(\mathbf{X}, \mathbf{U})$  is dropped as they represent matrices where each row corresponds to time increments. The vector of state measurements  $\tilde{\mathbf{X}}$  consists of the reference state of the system as obtained in Section 3.4 for the polarization potential and the SoC. The reference SoC of the cell is drawn from the results of the EKF presented in Section 3.4 for each cycle. The reference polarization potential is then computed via  $u_p = \tilde{u}_t - u_{oc}(z) - IR_0$  based on (3.11), and using the reference SoC of the cell and the electrochemical parameter  $R_0$  inferred from EIS. The time derivatives of the state variables will be computed numerically using a finite difference scheme. A schematic of the SINDy framework is presented in Figure 3.9.

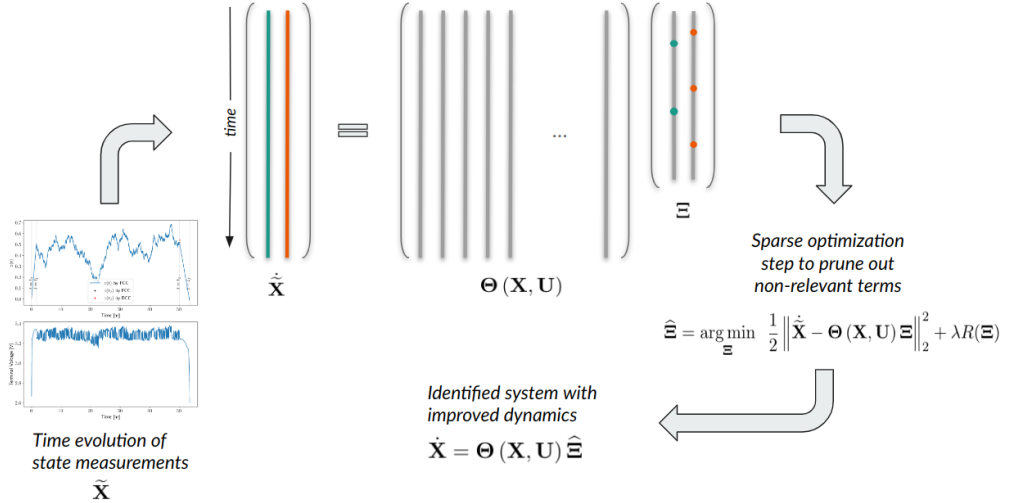


Figure 3.9: Schematic of SINDy framework.

There are different choices for the regularization function usually given by different  $l_p$  norms where  $p = 0, 1, 2$ . The norm  $l_0$  refers to the number of nonzero terms in a vector. It is shown that the  $l_0$  norm is non-convex and leads to an NP-hard optimization problem [130]. However,  $l_1$  and  $l_2$  norms are convex functions. Using the  $l_1$  norm,  $R(\Xi) = \|\Xi\|_1$ , reduces (3.30) to the well-known LASSO problem [130]. LASSO regularization, similar to other regularization methods, penalizes the coefficients

of the model, thus forces them toward zero. According to the intensity of the regularization represented by the parameter  $\lambda$ , some of the coefficients in the vector of coefficients will become zero, however, many of the coefficients will not vanish. In contrast, in the  $l_2$  regularization (known as Ridge regularization [131]), all coefficients will be penalized without becoming zero. Hence, LASSO will naturally result in a sparser representation of the coefficients in comparison to the  $l_2$  regularization. Although this representation is sparse, it turns out that in many applications of SINDy, LASSO regularization results in only mildly sparse models, still retaining many non-zero coefficients. Hence, Brunton et al. [114] have proposed another optimization technique that promotes sparsity in the model, as known as Sequentially Thresholded Least Squares (STLSQ) regression. In this approach the cost functional introduced in (3.30) could use any regularization function. However, the coefficients are sequentially thresholded at each iteration of the optimization algorithm such that the coefficients with magnitude smaller than a certain threshold  $\Lambda$  are pruned. In this case, the parameter  $\Lambda$  determines the sparsity of the resulting model. Large threshold values result in highly sparse models, and vice versa. In this method, the coefficients that are smaller than a pre-defined threshold are eliminated in each iteration until there are no more terms with coefficients smaller than the threshold. Note that some accuracy is lost when using regularization techniques as the coefficients are penalized. So, the optimal model found will lose some accuracy due to the applied penalization. Another technique, namely, Stepwise Sparse Regression (SSR) [132], is also proposed as a greedy algorithm by eliminating the smallest coefficient at each iteration until convergence to a set of terms in the feature library. The SSR method results in more accurate coefficients and lower cost functional values due to the lack of penalization in the model, however, the sparsity level is not tuneable. Recently, Sparse Relaxed Regularized Regression (SR3) technique has been proposed for sparse regression [130] where the regularization is relaxed by introducing an auxiliary variable to account for accuracy and sparsity using two different decision variables in the optimization problem. In this study, we use the STLSQ technique with the  $l_2$  norm as regularization function for sparse optimization through the open source python package PySINDy [133].

### 3.5.2 The Feature Library

There is a large freedom in how one can choose the terms of the feature library to form a finite set of nonlinearities suitable for the SINDy framework. However, basic knowledge of the physics of the system can guide one in choosing a relevant set of functions for the system under consideration. In this study, the terms in the feature library are inspired by empirical relations, equivalent circuit models, and physics-based relations [134, 135].

Electrochemical battery models based on first principles are not suitable for battery management pur-

poses as they require solving large partial differential equations, which is computationally costly. Some purely empirical models are proposed which ignore the thermodynamics of the cell and describe the voltage evolution in the cell. The Shepherd model, the Unnewehr model, the Nernst model, and a combined model are representatives of such empirical models [136, 137]. The empirical relations of Shepherd and Unnewehr simply model the polarization resistance of the cell, whereas the effect of temperature and material activity during electrochemical reaction is described by the Nernst model. These models are listed in Table 3.1.

The second category of models for describing the polarization overpotential is based on equivalent circuit modeling such as the Thevenin model, cf. (3.11). More complex models can also be considered for this case; however, the parameters of such models need to be obtained using sophisticated optimization methods and the EIS data. Hence, we stick with the Thevenin model dynamics based on (3.11) for incorporation into the feature library.

The last category of functions included in the feature library is based on physical modeling of cells. The polarization overpotential of the cells is normally modeled by Butler-Volmer (BV) type equations [96]. In this relation, the current density at the interface is related to overpotential through exponential functions of overpotential as

$$J(t) = J_0 [\exp(\alpha_a f u_p(t)) - \exp(-\alpha_c f u_p(t))], \quad (3.31)$$

where  $J(t)$  [ $\frac{A}{m^2}$ ] is the current density at the interface,  $J_0$  [ $\frac{A}{m^2}$ ] is the exchange current density defined as current density at the equilibrium state,  $\alpha_a$  and  $\alpha_c$  are anodic and cathodic transfer coefficients, and  $f = \frac{F}{RT}$  [ $\frac{1}{V}$ ] is defined as the inverse of thermal voltage of the cell,  $F$  is the Faraday's constant,  $R$  is the ideal gas constant, and  $T$  is temperature,. There are different versions of this relation proposed in the literature based on various approximations and assumptions. Linearized BV, Tafel-type BV, and engineering-type BV are among such models. In this work, symmetric BV, Tafel-type BV, and linearized BV are included in the feature library. The symmetric BV corresponds to the case where the cathodic and anodic transfer coefficients are equal to each other  $\alpha_a = \alpha_c = \alpha$ , hence, the BV equation reduces to

$$u_p(t) = \frac{1}{\alpha f} \operatorname{arcsinh} \left( \frac{J(t)}{2J_0} \right). \quad (3.32)$$

As the time derivatives of state variables are required for the SINDy framework, we compute it as

$$\dot{u}_p(t) = \frac{1}{\alpha f} \frac{\dot{J}(t)}{\left( \left( \frac{J}{2J_0} \right)^2 + 1 \right)^{0.5}}. \quad (3.33)$$

The range of exchange current density for different chemistries of Li-ion cells is reported in the literature to be  $10^{-8} - 10^{-4} [A/cm^2]$  [138], depending on the cell type. As this range is much smaller than the current density values (in the order of  $1 [A/cm^2]$ ), the term  $\frac{J}{2J_0}$  dominates in the denominator, and the time derivative of polarization potential can be approximated as

$$\dot{u}_p(t) \cong \frac{2J_0}{\alpha f} \frac{\dot{J}(t)}{J(t)}. \quad (3.34)$$

This expression will be used to approximate the time derivatives of the polarization potential corresponding to the symmetric BV term (3.32). On the other hand, the Tafel-type BV relation corresponds to the case where  $\alpha_a \gg \alpha_c$  or  $u_p$  is large, and the anodic current density dominates the reaction. The BV relation in this case reduces to

$$J(t) = J_0 \exp(\alpha_a f u_p(t)). \quad (3.35)$$

Rearranging (3.35) we get

$$u_p(t) = \frac{1}{\alpha_a f} \ln \left( \frac{J(t)}{J_0} \right). \quad (3.36)$$

Taking the time derivative of (3.36) results in a similar expression as the time derivative of symmetric BV relation (3.34), where the time derivative of the polarization potential is proportional to  $\frac{\dot{J}(t)}{J(t)}$ . Thus, these two terms are not distinguished in the feature library of the SINDy framework. On the other hand, the linearized BV relation corresponds to the case where the overpotential is small and the BV relation can be linearized as

$$u_p(t) = \frac{1}{\alpha_a f} \frac{J(t)}{J_0}. \quad (3.37)$$

The time derivative of the polarization potential in this case is equal to  $\dot{u}_p(t) = \frac{1}{\alpha f J_0} \dot{J}(t)$ . All terms of the feature library are summarized in Table 3.1. It is notable that the SINDy framework introduced in (3.28) involves two state variables, reflecting the fact that the optimization problem in (3.30) needs to be solved for both state variables simultaneously. However, in practice, the cost functional in (3.30) is minimized for each state variable separately. The reason is that the time derivatives of the state measurements  $\tilde{\mathbf{X}}$  and the feature library on the right-hand-side of (3.28) are both precomputed using the measurement data  $\tilde{\mathbf{X}}$ . For this reason, the evolution in time of one state variable becomes independent of the evolution of the other state variable within the SINDy framework. We note that essentially the state variables are coupled and the evolution of one state variable is dependent on the other state variable. However, within the SINDy framework, both  $\dot{\tilde{\mathbf{X}}}$  and  $\Theta(\tilde{\mathbf{X}}, \mathbf{U})$  in (3.30) are precomputed using the measurement data  $\tilde{\mathbf{X}}$ . Therefore, the optimization problem (3.30) is split into two subproblems, each solved with respect to one state variable.

Category	Model	Equation for $u_p$	Feature Library Term ( $\dot{u}_p$ )
Empirical	Simple Model	$u_p = 0$	$\dot{u}_p \propto 0$
	Shepherd Model	$u_p = \frac{k}{z}$	$\dot{u}_p \propto \frac{\dot{z}}{z^2}$
	Unnewehr Model	$u_p = k \cdot z$	$\dot{u}_p \propto \dot{z}$
	Nernst Model	$u_p = k_1 \ln(z) + k_2 \ln(1-z)$	$\dot{u}_p \propto \frac{\dot{z}}{z}, \frac{\dot{z}}{1-z}$
Physical	Combined Model	$u_p = k_1/z + k_2 \cdot z + k_3 \ln(z) + k_4 \ln(1-z)$	$\dot{u}_p \propto \dot{z}, \frac{\dot{z}}{z}, \frac{\dot{z}}{1-z}, \frac{\dot{z}}{z^2}$
	Thevenin Model	$\dot{u}_p = \frac{I}{C_p} - \frac{u_p}{R_p C_p}$	$\dot{u}_p \propto \frac{I}{C_p}, \frac{u_p}{R_p C_p}$
	Symmetric BV	$u_p = \frac{1}{\alpha f} \operatorname{arcsinh}(\frac{J}{2J_0})$	$\dot{u}_p \propto \frac{j}{J}$
	Tafel-type BV	$u_p = \frac{1}{\alpha f} \ln(\frac{J}{J_0})$	$\dot{u}_p \propto \frac{j}{J}$
Equivalent Circuit	Linearized BV	$u_p = \frac{1}{\alpha_a f} \frac{J}{J_0}$	$\dot{u}_p \propto J$

Table 3.1: Candidate relations for the polarization potential and their time derivatives. The time derivative relations are included in the feature library of the SINDy framework. Note that the prefactors are dropped from the time derivative relations as they will be determined as part of the optimization process (3.30). Note that the time dependency is dropped from the variables, and  $k$ ,  $k_1$ ,  $k_2$ ,  $k_3$  and  $k_4$  are arbitrary constants.

The terms introduced in Table 3.1 for modeling the polarization potential can be used in the SINDy framework for finding an optimal combination of nonlinearities represent the dynamics of the cell. As we are modeling two state variables, SoC and polarization potential, all of the terms in Table 3.1 are included in the feature library for the polarization potential, whereas only some of them are included in the feature library for SoC. The reason is that many candidate terms listed in Table 3.1 contain  $\dot{z}(t)$  which cannot be used for describing the dynamics of SoC in the feature library as the corresponding equation in (3.28) is then satisfied initially. Table 3.2 summarizes the candidate terms used in each subproblem (for each state variable) based on the terms introduced in Table 3.1. Note that each state variable is included in the other variable's function library. Also, the current density variable  $J(t)$  [ $\frac{A}{m^2}$ ] in the expressions in Table 3.1 will be replaced with the current  $I(t)$  [ $A$ ] applied to the cell, as the surface area of the cell will remain constant in all experiments.

Candidate Term	Symbol	Included in SoC control library?	Included in $u_p$ control library?
$\frac{I}{C_p}$	$u_1$	✓	✓
$\frac{u_p}{R_p C_p}$	$u_2$	✓	✓
$\dot{z}$	$u_3$		✓
$\frac{\dot{z}}{z}$	$u_4$		✓
$\frac{\dot{z}}{z^2}$	$u_5$		✓
$\frac{\dot{z}}{1-z}$	$u_6$		✓
$\frac{\dot{I}}{I}$	$u_7$	✓	✓
$\dot{I}$	$u_8$	✓	✓
$I$	$I$	✓	✓
$z$	$z$		✓
$u_p$	$u_p$	✓	

Table 3.2: State and control variables included in the control library  $\mathbf{U}$  for each of the state variables.

For each state variable the minimization problem (3.30) is solved separately. The library of candidate functions for each state variable is constructed using the terms included in Table 3.2. The feature library of candidate functions used for identifying the optimal dynamics of the polarization potential is denoted  $\Theta^u(\mathbf{X}, \mathbf{U}^u)$ , whereas the feature library of candidate functions used for identifying the optimal dynamics of SoC is denoted  $\Theta^z(\mathbf{X}, \mathbf{U}^z)$ . The feature libraries in each case are constructed as described below. Note that  $\theta_i$ ,  $i = 1 \dots, M$ , refers to a functional form defined by the user (e.g. polynomials of different orders, exponential functions, etc), and  $M$  represents the number of functional forms.

- When solving (3.30) for identifying the optimal dynamics of the polarization potential, the library of control variables is constructed as

$\mathbf{U}^u = [z, I, u_1, u_2, \dots, u_8, \theta_i(u_p), \theta_i(z), \theta_i(I), \theta_i(u_1), \dots], i = 1, \dots, M$ . The feature library

for the polarization potential will be constructed as  $\Theta^u(\mathbf{X}, \mathbf{U}^u) = [\mathbf{1}, \mathbf{X}, \mathbf{U}^u, \mathbf{X} \otimes \mathbf{U}^u, \mathbf{X} \otimes \mathbf{X}, \mathbf{U}^u \otimes \mathbf{U}^u]$ , where  $\mathbf{X} \otimes \mathbf{U}^u$  represents all product combinations of elements in  $\mathbf{X}$  and  $\mathbf{U}^u$ .

- When solving (3.30) for identifying the optimal dynamics of SoC, the library of control variables is constructed as  $\mathbf{U}^z = [u_p, I, u_1, u_2, u_7, u_8, \theta_i(z), \theta_i(u_p), \theta_i(I), \theta_i(u_1), \dots], i = 1, \dots, M$ . The feature library for SoC will be constructed as  $\Theta^z(\mathbf{X}, \mathbf{U}^z) = [\mathbf{1}, \mathbf{X}, \mathbf{U}^z, \mathbf{X} \otimes \mathbf{U}^z, \mathbf{X} \otimes \mathbf{X}, \mathbf{U}^z \otimes \mathbf{U}^z]$ .

In order to evaluate the performance of various models, different error metrics can be introduced as

$$\mathcal{J}_1 = \frac{1}{m} \sum_{i=0}^m \left| \left[ \widetilde{\mathbf{X}}(i\Delta t) \right]_1 - \left( \int_0^{i\Delta t} \left[ \Theta^u(\mathbf{X}(\tau), \mathbf{U}^u(\tau)) \widehat{\boldsymbol{\Xi}} \right]_1 d\tau + [\mathbf{X}_0]_1 \right) \right|, \quad (3.38)$$

for the mean absolute error of polarization potential, and

$$\mathcal{J}_2 = \frac{1}{m} \sum_{i=0}^m \left| \left[ \widetilde{\mathbf{X}}(i\Delta t) \right]_2 - \left( \int_0^{i\Delta t} \left[ \Theta^z(\mathbf{X}(\tau), \mathbf{U}^z(\tau)) \widehat{\boldsymbol{\Xi}} \right]_2 d\tau + [\mathbf{X}_0]_2 \right) \right|, \quad (3.39)$$

for the mean absolute error of SoC, where  $m$  is the number of time steps and  $[\mathbf{X}]_k$  refers to the  $k$ -th state variable ( $k = 1, 2$ ).

### 3.5.3 Results

The result of the proposed SINDy framework highly depends on the quality of the measurements, the choice of the functions in the library, and how the solution is sparsified. Failure to find an optimal and accurate sparse model might imply incorrect choice for the functions in the library. In this section, we use SINDy to construct a model for the dynamics of the system using the dynamic loading data presented in Section 3.3. For this purpose, reference SoC and polarization potential estimates of the cell for different cycles obtained in Section 3.4 are used as the training data  $\widetilde{\mathbf{X}}$ . The feature library terms introduced in Table 3.2 will be computed using  $\widetilde{\mathbf{X}}$  and the applied current as the control input. For calculating the time derivatives, the smoothed finite difference routine of PySINDy package is used with order 5 differencing.

In the first attempt, only the terms proposed in Table 3.2 are used as the candidate terms in the feature library, meaning that the terms corresponding to  $\theta_i()$  functional forms in  $\mathbf{U}^u$  and  $\mathbf{U}^z$  are eliminated. The purpose of this simulation is to give a glimpse of how the SINDy framework performs overall with respect to the Thevenin model. Three different sparsity levels (strong, normal, and weak) are considered when minimizing the cost functional (3.30) with respect to the vector of coefficients for each cycle. The obtained model is tested on all other cycles by evaluating the error metrics (3.38) and (3.39). The results are presented in Figure 3.10.

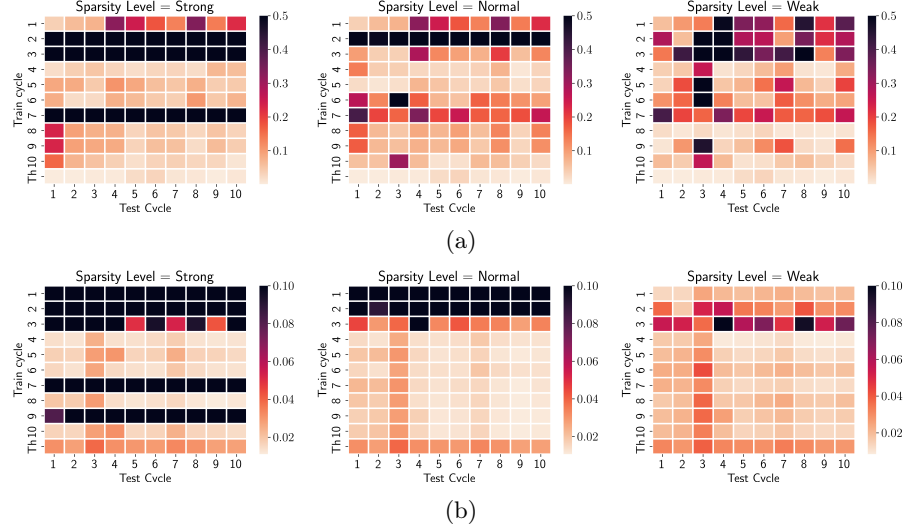


Figure 3.10: Error  $\mathcal{J}_2$  computed for SoC according to (3.39) (a), and  $\mathcal{J}_1$  computed for the polarization potential according to (3.38) (b) by comparing the reference state of the cell with the solution of the forward ODE model in (3.28) for each cycle. The identified model is obtained by minimizing the cost functional (3.30) with respect to the vector of coefficients using three different sparsity levels for each cycle. The indices on the vertical axes represent the data sets (cycles) used to solve problem (3.30), whereas the indices on the horizontal axes represent the data sets used to test the accuracy of the obtained models. Note that "Th" on the y-axis of each sub-figure refers to the Thevenin model (3.11). Also, some of the errors presented in (a) and (b) attain large values, and hence, their values are replaced with 0.5 and 0.1, respectively, for ease of visualization.

As can be observed in Figure 3.10, highly sparsified models obtained with SINDy fail to perform well in estimating the state variables. Moving from strong to weak thresholds, the accuracy of the models increases. Considering polarization potential dynamics, the model identified by SINDy outperforms the Thevenin model in the case of weak thresholding. As can be observed, however, the model is not capable of outperforming the Thevenin model (3.11) for estimating the SoC even at low sparsity levels. Note that in this experiment, we have restricted ourselves to the terms presented in Table 3.2 only, as more complex nonlinearities may give rise to the blow up of the ODE system. Without adding more complex nonlinearities to the reconstruction, the models found by the SINDy framework have been able to improve the polarization potential estimates of the Thevenin model at low sparsity levels in many cases.

Fitting a model via the SINDy framework to only one cycle increases the chance of producing a dynamical system that might underperform against data from other cycles due to the presence of unsuitable terms in the dynamics. Hence, in order to improve the robustness of the models found by SINDy we fit the model using composite data corresponding to all cycles at different sparsity levels, and test the resulted models on all cycles. In this case, the feature library is constructed by considering polynomials of up to third order of the control terms and their products, in addition to sine and cosine functions of control

terms, cf. Table 3.2. Hence, the feature library for SoC and polarization potential consists of 131 and 385 linear and nonlinear terms, respectively. First, we will focus on improving estimates of the polarization potential. In this scenario, we fix the threshold for the SoC dynamics in the SINDy framework such that only one term, representing the CC term, cf. Eq. (3.11), is preserved in its feature library ( $\Lambda = 0.003$ ). Note that the fitting procedure will still be required for this purpose as the prefactor of this term needs to be determined using the SINDy framework. The results are shown in Figure 3.11 at four different sparsity levels for the polarization potential. Note that an excessively sparse solution will significantly underfit, while a barely-sparse model may overfit to the data. Both scenarios must be avoided and a balance between sparsity and goodness of fit should be determined. As shown in Figure 3.11, the sparsity threshold of  $\Lambda = 2 \times 10^{-10}$  produces a model that balances sparsity with accuracy. This model beats the Thevenin model across all cycles without increasing the chance of system blow up, while keeping the least number of terms. In the next section the terms involved in this dynamical system are discussed.

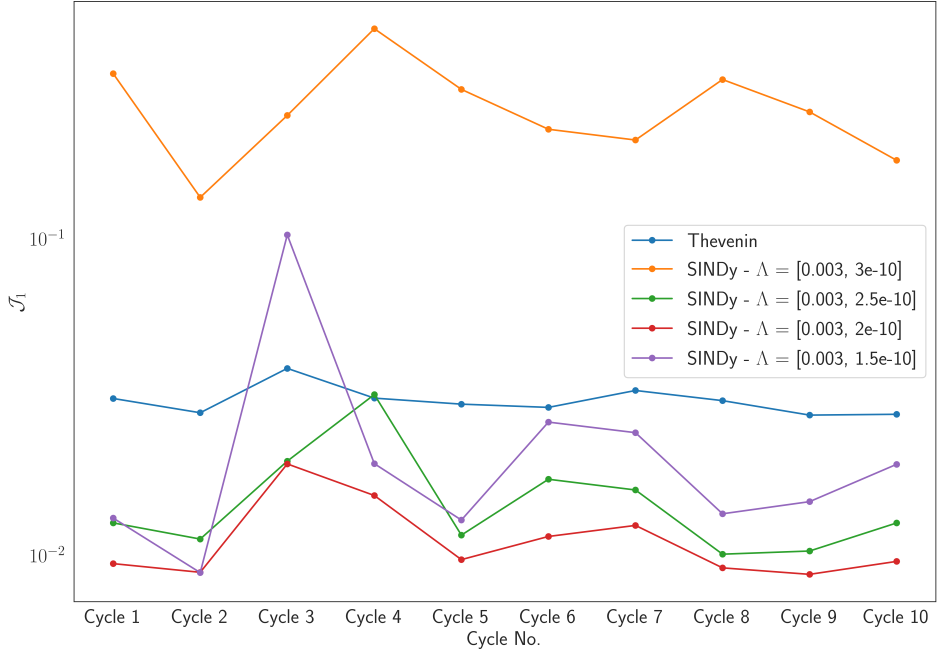


Figure 3.11: Results of fitting model (3.28) via the SINDy framework using composite data of all cycles at four different sparsity levels for the polarization potential. The threshold for the coefficients of the feature library terms for SoC is adjusted such that only one term (the CC term) is preserved in its dynamics.

In order to have a closer look at the performance of the models in Figure 3.11, Figures 3.12-3.13 show the time evolution of the polarization potential constructed by solving the forward model (3.28) obtained

by SINDy at different sparsity levels. As can be observed, there is a tradeoff between the accuracy and sparsity of models. Strong thresholding of the models results in sparser, less accurate models, whereas weak thresholding gives rise to less sparse, more accurate models. In this case, a model needs to be adopted that balances the sparsity and the accuracy. Strong and moderate thresholds ( $\Lambda = 2.5 \times 10^{-10}$  and  $\Lambda = 2 \times 10^{-10}$ ) in Figure 3.12 satisfy these requirements. In Figure 3.13 we show the result obtained with a moderate threshold  $\Lambda = 2 \times 10^{-10}$  magnified over a part of the cycle. Also, the performance of the Thevenin model is compared to the models obtained by SINDy and the reference data. As can be observed, the model obtained by SINDy significantly improves the estimation of the polarization potential.

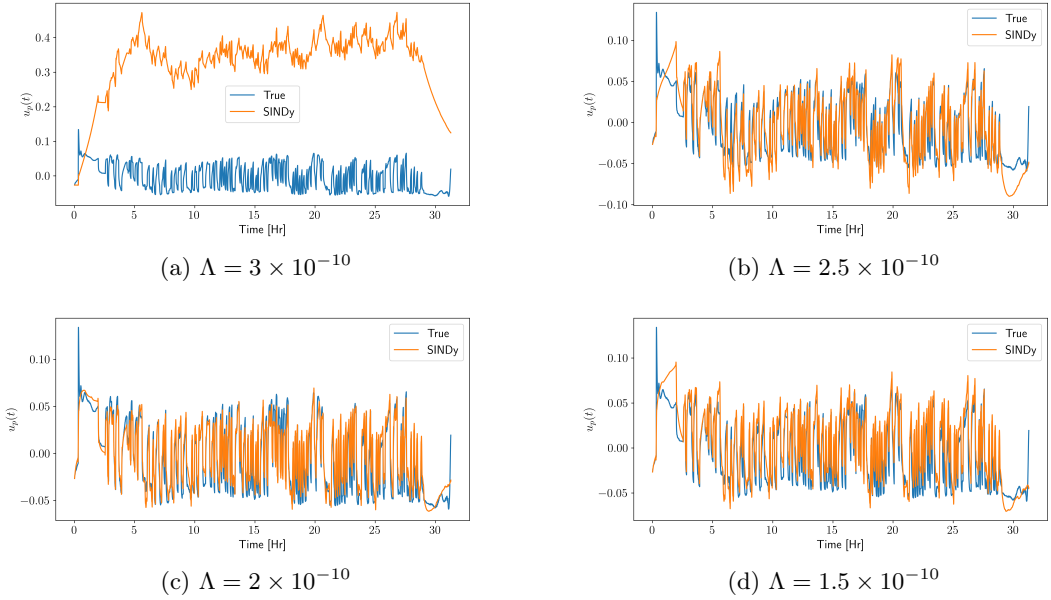


Figure 3.12: Time evolution of the polarization potential  $u_p(t)$  for one cycle as the solution of the forward problem (3.28) obtained by solving minimization problem (3.30) via the SINDy framework and by using composite data of all cycles, with different thresholding levels.

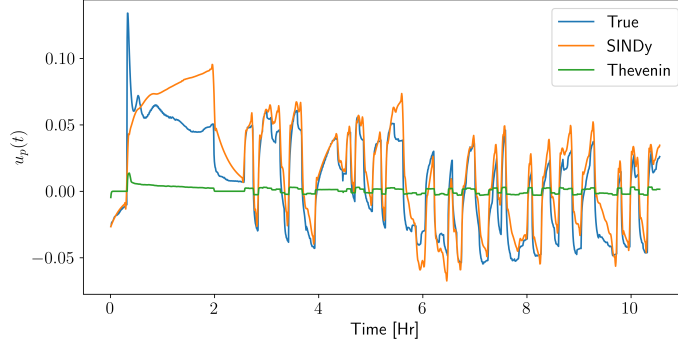


Figure 3.13: Time evolution of polarization potential  $u_p(t)$  for one cycle as the solution of the forward problem (3.28) obtained by solving minimization problem (3.30) via the SINDy framework and using composite data of all cycles with the threshold set at  $\Lambda = 2 \times 10^{-10}$ . The time evolution is shown over a part of the cycle only. The performance of the Thevenin model and the model obtained by SINDy are compared with reference data.

As observed in Figures 3.11-3.13, the SINDy framework has the potential to improve the estimates of the polarization potential, however, the improvement of the SoC estimates is questionable. In order to improve the SoC estimates, we will take the best model found in Figure 3.11 for predicting the polarization potential (obtained with  $\Lambda = 2 \times 10^{-10}$ ), and will try different thresholds on the coefficients of the feature library terms corresponding to the SoC dynamics. The results are shown in Figure 3.14. As can be observed, the SINDy framework is not capable of finding a set of terms that can improve the SoC estimates for a range of cycles over the CC model. This could be due to the possibility that the feature library is populated with nonlinearities that cannot capture the behaviour of the SoC dynamics in a robust and accurate manner. More complicated terms may need to be included in the feature library in order to find a model that can beat the estimates of SoC using the CC model.

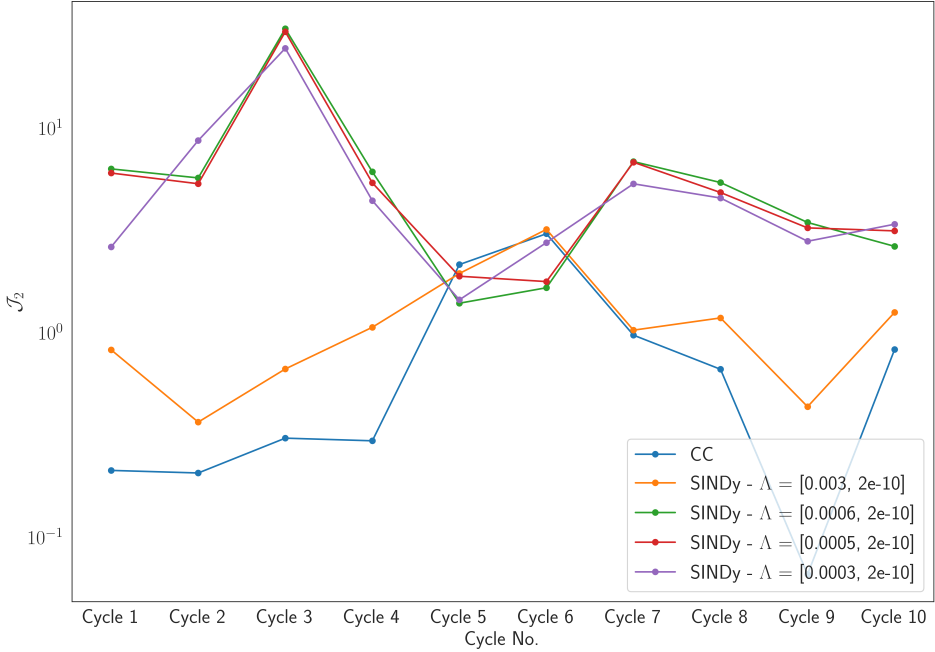


Figure 3.14: Results of fitting model (3.28) via the SINDy framework using composite data of all cycles at four different sparsity levels for SoC estimation. The threshold for the coefficients of the feature library terms for the polarization potential is set at  $\Lambda = 2 \times 10^{-10}$ .

Thus, the SINDy framework with a variety of linear and nonlinear terms in the feature library is capable of significantly and robustly improving the polarization potential estimates, however, the SoC estimates are not improved due to the presence of noise and the choice of nonlinearities in the feature library. In the next section, we will take a closer look at the model obtained by SINDy.

### 3.5.4 Interpretation of Results

The model calibrated with SINDy using data from multiple cycles was able to improve the polarization potential estimates. In particular, using the threshold  $\Lambda = 2 \times 10^{-10}$ , we found a robust model that improves estimates for all cycles. The ODE model corresponding to this threshold level is

$$\begin{aligned} \dot{u}_p = & -5.857714 \cdot u_p + 0.183970 \cdot \frac{I}{C_p} + 0.363350 \cdot \frac{\eta I}{Q_n(1-z)} \\ & -0.000015 \cdot \frac{\dot{I}}{I} + 0.000601 \cdot \dot{I} - 0.005697 \cdot \frac{u_p^2}{R_p C_p}. \end{aligned} \quad (3.40)$$

As can be observed, this model has six terms, linear and nonlinear, from a library of 385 terms, including polynomials of control terms and their products of degree up to three, plus sine and cosine functions

of control terms, cf. Table 3.2. The second term on the right-hand-side of (3.40) is included in the Thevenin model. The third term on the right-hand-side of (3.40) is the time derivative of  $\ln(1 - z)$  as introduced by the Nernst model. The fourth and fifth terms on the right-hand-side of (3.40) correspond to the symmetric BV (or Tafel-type BV) and the linearized BV relations for the polarization potential, respectively. The nonlinear term  $\frac{u_p^2}{R_p C_p}$  is added to complement the dynamics of the cell. As can be observed, the dynamics of the system is captured by a combination of classical dynamics, Nernst model dynamics, approximations of BV and a nonlinear term. It is interesting to note that, apart from the candidate terms introduced in Table 3.2, only one candidate term is preserved out of all the nonlinearities added to the feature library in the form of polynomials and sine and cosine functions. A combination of six terms is sufficient to capture the dynamics of this cell in a robust manner. A collection of all these terms contributes to the estimation of the polarization potential. As an ODE describes the evolution of a system only in the presence of all its terms, this ODE would become incomplete without any of these terms. Hence, interpretations of the significance of each one of these terms is nontrivial.

### 3.6. Unscented Kalman Filtering

In this section, we aim to enhance the estimates of the SoC using a variant of a Kalman filter. As the model obtained by SINDy in (3.40) incorporates nonlinear terms, a nonlinear extension of Kalman filtering must be used. The general methodology remains the same as introduced in Section 3.4; however, in this case, a more sophisticated Kalman filter is designed to handle a nonlinear dynamical system. The EKF approach relies on the first-order Taylor approximation for linearizing the model, whereas the UKF approach retains the original nonlinear system and uses a sampling technique, known as the unscented transformation, for handling nonlinearities. In this framework, a minimal number of points are sampled from the distribution of the state variables (by assuming that the state variables have a Gaussian distribution), referred to as sigma points. The sigma points then are advanced in time using the nonlinear state equations. The mean and covariance of the state variables is determined via the computed sigma points. It has been shown that this technique produces a third-order accuracy and is superior to EKF [139]. In this study, we adopt an Adaptive Unscented Kalman Filter investigated by [105]. The aim is to add a probabilistic aspect to the SoC estimates, as well as improve their accuracy through a feedback loop. The model for polarization potential dynamics (3.40) identified by the SINDy framework, and the CC model for SoC estimation (3.3) are used in this study as the underling nonlinear model of the cell.

### 3.6.1 Mathematical Background

The deterministic continuous state equation used in conjunction with AUKF is

$$\begin{aligned} \dot{\mathbf{X}} &= \mathbf{G}'(\mathbf{X}, \mathbf{U}), \\ \mathbf{G}'(\mathbf{X}, \mathbf{U}) &= \begin{bmatrix} -5.86u_p + 0.18\frac{I}{C_p} + \frac{0.36\eta I}{Q_n(1-z)} - 0.000015\frac{\dot{I}}{I} + 0.000601\dot{I} - 0.005697\frac{u_p^2}{R_p C_p} \\ \frac{\eta I(t)}{Q_n} \end{bmatrix}, \quad (3.41) \end{aligned}$$

$$u_t = h(\mathbf{X}, \mathbf{U}) = u_{oc}(z) + u_p + IR_0,$$

where  $h : \mathbb{R}^2 \times \mathbb{R} \rightarrow \mathbb{R}$  is the nonlinear observer function, and  $\mathbf{G}' : \mathbb{R}^2 \times \mathbb{R} \rightarrow \mathbb{R}^2$  is the nonlinear state transition function. This system can be written in stochastic discrete form as

$$\mathbf{X}_{k+1} = \mathbf{G}(\mathbf{X}_k, \mathbf{U}_k) + \mathbf{W}_k, \quad (3.42a)$$

$$u_{t,k+1} = h(\mathbf{X}_{k+1}, \mathbf{U}_{k+1}) + V_{k+1}, \quad (3.42b)$$

$$\mathbf{W}_k \sim \mathcal{N}(\mathbf{0}, \mathbf{Q}_k), \quad (3.42c)$$

$$V_k \sim \mathcal{N}(0, R_k), \quad (3.42d)$$

where the measurement and process noise is added to equations (3.42a) and (3.42b), and  $\mathbf{G} : \mathbb{R}^2 \times \mathbb{R} \rightarrow \mathbb{R}^2$  is the state transition matrix. A deterministic sampling technique, as known as unscented transformation, is used in order to select sigma points from a distribution of state variables. In the case of two state variables  $n = 2$ , five sigma points are drawn from a joint distribution according to unscented transformation as

$$\mathbf{X}_{k-1}^0 = \mathbf{X}_{k-1}^+, \quad (3.43a)$$

$$\mathbf{X}_{k-1}^i = \mathbf{X}_{k-1}^+ + \left[ \sqrt{(n + \lambda)\mathbf{P}_{k-1}^+} \right]_i, \quad i = 1, 2, \quad (3.43b)$$

$$\mathbf{X}_{k-1}^i = \mathbf{X}_{k-1}^+ - \left[ \sqrt{(n + \lambda)\mathbf{P}_{k-1}^+} \right]_i, \quad i = 3, 4, \quad (3.43c)$$

where the superscript  $i$  refers to each sigma point,  $\mathbf{X}_{k-1}^i$  is the  $i$ -th sigma point at time step  $k - 1$ ,  $\mathbf{X}_{k-1}^+$  is the mean of the state variables,  $\mathbf{P}_{k-1}^+$  is the covariance of the state variables, and  $\lambda = \rho^2(n + s) - n$  determines the dispersion of the sigma points. The parameters  $\rho$  and  $s$  are the scaling parameters that determine the dispersion intensity. Note that in one dimension  $n = 1$ , setting  $s = 0$  and  $\rho = 1$  results in selecting three sigma points: the mean, plus and minus one standard deviation from the mean. Hence, parameters  $\rho$  and  $s$  need to be tuned in order to effectively sample the joint distribution of state variables at each time step. Each sigma point carries a weight, to be used for computing the mean and covariance

at the new time step. The computation of weights is detailed in Algorithm 2. The sigma points selected at each time step are then propagated in time through the nonlinear system of equations (3.42) to obtain the updated estimates in the new time step. The mean and covariance of the distribution is then computed using the updated sigma points at the new time step. The details of this approach are summarized in Algorithm 2. The adaptive laws for computation of process and measurement noise variance used in this study are borrowed from [105].

---

**Algorithm 2:** ADAPTIVE UNSCENTED KALMAN FILTER ALGORITHM.

---

**Input:**  $\rho, s$  — Scaling parameters of sigma points.

$\alpha$  — Forget factor.

**Output:**  $\mathbf{X}_k^+, \mathbf{P}_k^+$  — Posterior state estimation and error covariance matrix at time step  $k$ .

---

Initialize  $\mathbf{X}_0^+$  and  $\mathbf{P}_0^+$

Set  $k \leftarrow 1$

**repeat**

Attain sigma points at time step  $(k - 1)$ : (superscript refers to sigma points)

$$\begin{aligned}\mathbf{X}_{k-1}^0 &= \mathbf{X}_{k-1}^+ \\ \mathbf{X}_{k-1}^i &= \mathbf{X}_{k-1}^+ + \left[ \sqrt{(n + \lambda)} \mathbf{P}_{k-1}^+ \right]_i, \quad i = 1, 2 \\ \mathbf{X}_{k-1}^i &= \mathbf{X}_{k-1}^+ - \left[ \sqrt{(n + \lambda)} \mathbf{P}_{k-1}^+ \right]_i, \quad i = 3, 4\end{aligned}$$

Calculation of weights for sigma points:

$$\begin{aligned}w_m^0 &= \lambda / (n + \lambda) \\ w_c^0 &= \lambda / (n + \lambda) + (3 - \rho^2) \\ w_m^i &= w_c^i = 1/2(n + \lambda), \quad i = 1, 2, 3, 4\end{aligned}$$

Time update: performing prior estimation

$$\begin{aligned}\mathbf{X}_k^- &= \sum_{i=0}^{2n} w_m^i \mathbf{G}(\mathbf{X}_{k-1}^i, \mathbf{U}_{k-1}) \\ \mathbf{P}_k^- &= \sum_{i=0}^{2n} w_c^i (\mathbf{G}(\mathbf{X}_{k-1}^i, \mathbf{U}_{k-1}) - \mathbf{X}_k^-) (\mathbf{G}(\mathbf{X}_{k-1}^i, \mathbf{U}_{k-1}) - \mathbf{X}_k^-)^T + \mathbf{Q}_k\end{aligned}$$

Attain sigma points at time step  $(k)$ :

$$\begin{aligned}\bar{\mathbf{X}}_k^0 &= \mathbf{X}_k^- \\ \bar{\mathbf{X}}_k^i &= \mathbf{X}_k^- + \left[ \sqrt{(n + \lambda)} \mathbf{P}_k^- \right]_i, \quad i = 1, 2 \\ \bar{\mathbf{X}}_k^i &= \mathbf{X}_k^- - \left[ \sqrt{(n + \lambda)} \mathbf{P}_k^- \right]_i, \quad i = 3, 4\end{aligned}$$

Measurement update:

$$u_{t,k}^- = \sum_{i=0}^{2n} w_m^i h(\bar{\mathbf{X}}_k^i, \mathbf{U}_k)$$

Kalman gain

$$\begin{aligned}\mathbf{K}_k &= \mathbf{P}_{xy,k} P_{y,k}^{-1} \\ P_{y,k} &= \sum_{i=0}^{2n} w_c^i (h(\bar{\mathbf{X}}_k^i, \mathbf{U}_k) - u_{t,k}^-) (h(\bar{\mathbf{X}}_k^i, \mathbf{U}_k) - u_{t,k}^-)^T + R_k \\ \mathbf{P}_{xy,k} &= \sum_{i=0}^{2n} w_c^i (\bar{\mathbf{X}}_k^i - \mathbf{X}_k^-) (h(\bar{\mathbf{X}}_k^i, \mathbf{U}_k) - u_{t,k}^-)^T\end{aligned}$$

State update

$$\begin{aligned}\mathbf{X}_k^+ &= \mathbf{X}_k^- + \mathbf{K}_k [u_{t,k} - u_{t,k}^-] \\ \mathbf{P}_k^+ &= \mathbf{P}_k^- - \mathbf{K}_k P_{y,k} \mathbf{K}_k^T\end{aligned}$$

$k \leftarrow k + 1$

**until**  $t = t_f$ ;

where adaptive laws are :

$$\begin{aligned}\epsilon_k &= u_{t,k} - h(\mathbf{X}_k^+, \mathbf{U}_k) \\ \mathbf{Q}_k &= (1 - \alpha) \mathbf{Q}_{k-1} + \alpha (\mathbf{K}_k \epsilon_k \epsilon_k^T \mathbf{K}_k^T + \mathbf{P}_k^+) \\ R_k &= (1 - \alpha) R_{k-1} + \alpha \epsilon_k \epsilon_k^T\end{aligned}$$

Notes:

$[\sqrt{\mathbf{X}}]_i$  refers to the  $i$ -th column of the matrix square root factor of  $\mathbf{X}$

---

### 3.6.2 Results

The results for fitting the AUKF for all cycles are shown in Figure 3.15. Also, the mean absolute error of SoC estimates for all cycles is computed for the AUKF and the Thevenin model by comparing to the reference state of the cell. The results are shown in Figure 3.16. The error metric used in this case is

$$\mathcal{J}_3 = \frac{1}{m} \sum_{k=0}^m |z(t_k) - \tilde{z}(t_k)| \cdot 100, \quad (3.44)$$

where  $\tilde{z}(t_k)$  is the reference state at time step  $k$ , and  $z(t_k)$  is the posterior state. The improved dynamics obtained by the SINDy framework in (3.40) reduces the modeling error with respect to the reference states, whereas the measurement noise is still present and cannot be eliminated. With the help of a more accurate model with lower modeling error for the polarization potential, the AUKF algorithm becomes more robust, meaning that a single set of tuning parameters is used for all cycles for this algorithm. As can be observed in Figure 3.16, in general the SoC estimates by the CC model are better than the SoC estimates by the AUKF algorithm, however, the AUKF framework is superior in the sense that it is capable of quantifying the confidence in state estimates. The reason behind this fact is that the AUKF framework works by striking a balance between the measurement uncertainty and the modeling uncertainty. As the model and measurement noise might exhibit cycle-to-cycle differences, finding the right balance for all cycles is non-trivial, hence some accuracy is lost in some cycles. In most cycles in Figure 3.15 except cycle 5, the true SoC estimate at  $t = t_2$  is contained within the confidence intervals of the AUKF algorithm.

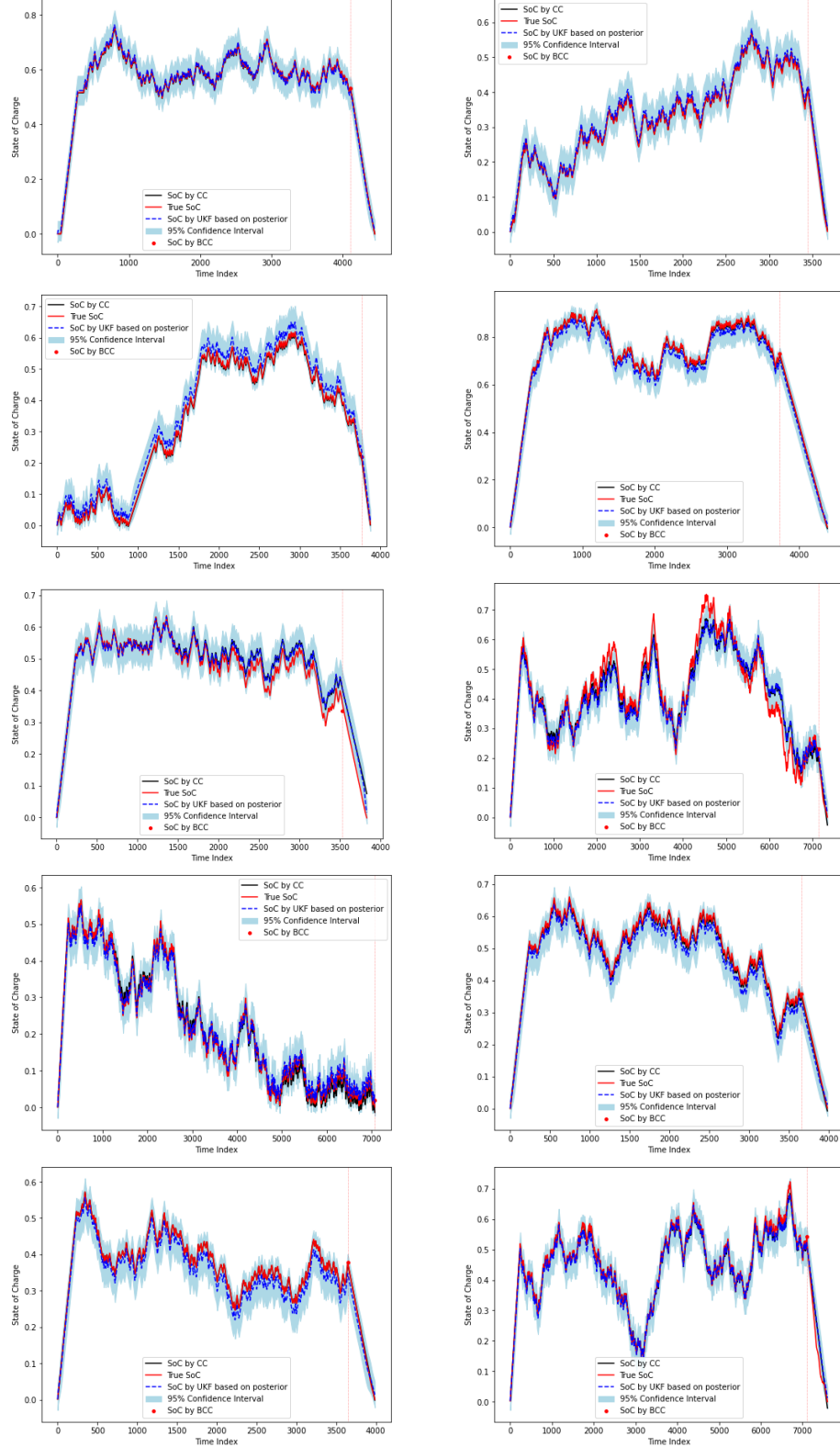


Figure 3.15: Time evolution of SoC by solving the ODE system (3.41) in time, and the confidence intervals of SoC estimates for all cycles obtained using the AUKF algorithm 2. The reference SoC values and the SoC estimates by FCC model are also shown for comparison.

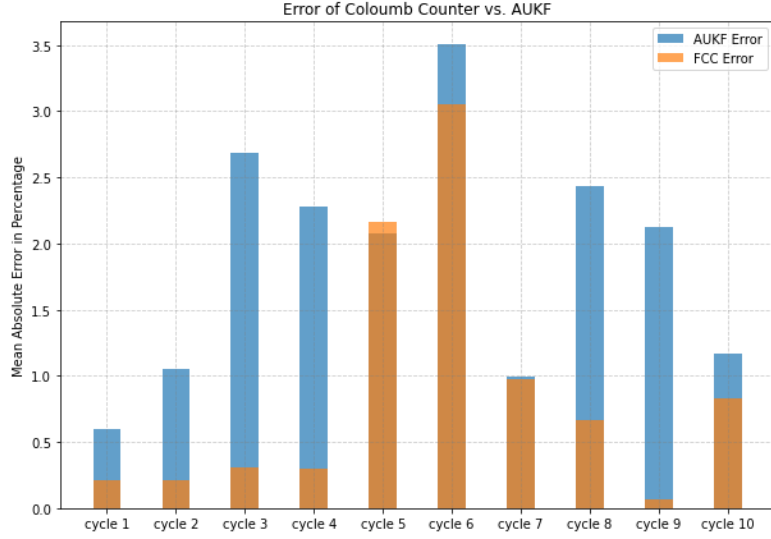


Figure 3.16: The mean absolute error of SoC estimates (3.44) using the FCC model and the AUKF algorithm. The errors are computed by comparing to the reference state.

### 3.7. Discussion

In this work, we investigated the challenging question of SoC estimation of LFP cells operating under dynamic loading conditions. The internal dynamics of the cell contributes to cell relaxation, which may lead to self-discharge and adds complexity to SoC modeling. Quantifying the uncertainty in SoC estimations is crucial for understanding the reliability of estimates and the necessity for cell recalibration. In this study, we explored the problem of uncertainty quantification in SoC estimations and utilized probabilistic models to minimize the discrepancy between model outputs and cell measurements over time. However, such a framework relies on an underlying model that is most suitable for the system under study. Incorrect modeling of the internal dynamics of the cell can result in unreliable estimations and increased uncertainty. This, in turn, can compromise the robustness of the employed filters.

The primary contribution of this study lies in the improved modeling of the internal state of the cell, particularly the polarization potential, under dynamic loading conditions. For this purpose, we adopted a hybrid data-driven approach, where the cell internal dynamics are inferred from experimental data using the SINDy framework. This method is not purely predictive, as it leverages knowledge about the system's physics to optimally select a feature library that describes the cell dynamics. Although the final model robustly predicts the cell dynamics, interpreting the optimal dynamical model (3.40) remains challenging. Our findings suggest that a combination of the Thevenin model (with EIS data) and the Butler-Volmer terms with a minimal nonlinearity can effectively describe the cell dynamics without the

need for highly nonlinear terms or interactions between them. However, explaining why this combination performs best remains elusive. We also observe that relations relying solely on the Butler-Volmer terms are insufficient to describe the evolution of the polarization potential in this case; some terms related to the ECM parameters (obtained via EIS) are also necessary to accurately capture the cell dynamics.

Despite the challenges, with sufficient data, a robust SINDy framework capable of reliably tracking the cell dynamics can be obtained. This model, when combined with uncertainty quantification techniques, provides insights into the uncertainty propagated in the estimations. Moreover, this method is computationally inexpensive and easily adaptable for online estimation and control. While various machine learning algorithms can be used for predictive modeling, their robustness becomes crucial as they lack physical terms describing the dynamics. Combining data-driven predictive models with physics-based cell modeling can yield robust and interpretable predictive models. An important question pertains to the performance of such models across different cells and chemistries. Addressing the reliability of these models across cell-to-cell and chemistry-to-chemistry differences is beyond the scope of this study.

## *Chapter 4*

---

# *Data-Driven Approach to Learning Optimal Forms of Constitutive Relations in Models Describing Lithium Plating in Battery Cells*

---

### **4.1. Introduction**

In recent years, due to the growing demand for green energy and the phasing out of fossil fuels in pursuit of a more sustainable future, rechargeable batteries have assumed a prominent role in the transition to green technologies. Lithium ion (Li-ion) batteries, among the most promising energy storage solutions, have found extensive applications in portable electronic devices, electric vehicles, and grid storage. With the increasing need for clean energy storage technologies, addressing challenges related to the performance and reliability of Li-ion batteries has become crucial. Aging and inefficiency mechanisms in cells contribute to their degradation. Battery degradation involves complex processes, both physical and chemical, within a cell. To comprehend, analyze, mitigate, and control the impact of these mechanisms, sophisticated experimental and computational techniques are essential. Current research aims to contribute to the understanding, prediction, and management of one of the primary degradation mechanisms in Li-ion batteries, commonly known as Lithium plating (Li-plating).

A Li-ion cell is composed of a pair of porous electrodes: the negative electrode (anode) and the positive electrode (cathode), separated by a porous separator, and immersed in a liquid electrolyte. These

components are enclosed between two current collectors, each connected to an external circuit. The porous nature of the electrodes facilitates the movement of Lithium ions within the material. Typically, graphite is used as the material for the negative electrode due to its layered crystalline structure. In recent years, silicon has received significant attention as an alternative to graphite electrodes due to its high capacity and abundance [140]. The cathode material is typically a Lithium-metal-oxide, with Nickel, Manganese, and Cobalt being common metal components. The primary constituent in the electrolyte solution is  $\text{Li}^+$  ions, which migrate between the electrodes during the cell's operation. During the charging process, Li ions are deintercalated from the cathode layers, freeing up electrons. Electrons then travel through the cathode's solid phase to the current collector, through an external circuit, and into the anode solid phase. Simultaneously, Li ions dissolve into the electrolyte and diffuse through the separator pores to the anode layers, where they undergo intercalation. The charging process continues as more Li ions intercalate into the anode. Depending on the capacity of the anode to host Li ions, the charging process continues until most available sites on the anode surface are occupied by Li elements. During cell discharge, reverse process occurs, with Li deintercalating from the anode surface, prompting the migration of Li ions from the anode to the cathode. Intercalation of Li ions on the anode solid phase during the charge process, and their subsequent deintercalation during the discharge process, are the desired mechanisms to the operation of the cell. However, such desired processes are accompanied by (or hindered by) some undesired processes, referred to as degradation mechanisms.

Several degradation mechanisms contribute to the inefficiencies observed in Li-ion cells, most importantly Solid-Electrolyte Interphase (SEI) growth, Li-plating, and binder decomposition. These degradation mechanisms can result in three distinct degradation modes, namely, the loss of cycleable Lithium, loss of active materials, and loss of electrolyte, as noted in different studies [8, 141, 142]. The loss of cycleable Lithium, which leads to significant capacity fade in the cell, is primarily caused by the consumption of Li ions through undesirable side reactions like irreversible Li-plating and SEI growth. Conversely, the loss of active material is linked to structural changes in the anode, potentially leading to a reduction in active sites available for Li intercalation. On the cathode side, the loss of active material can occur due to structural changes in the cathode, transition metal dissolution, and particle cracking. Moreover, the consumption of electrolyte can also contribute to cell degradation. This is driven by interactions with deposited Lithium at the anode interface, ultimately leading to the depletion of cycleable Lithium. The SEI growth is categorized as primary or secondary. The primary SEI growth process pertains to the creation of a SEI layer on the anode surface during the initial cycle of the cell. Although it consumes some cycleable Lithium, its presence is vital for the battery's performance and stability. The secondary SEI growth, on the other hand, pertains to the creation of SEI layer during the subsequent

cycles of the cell, which could be another potential mechanism contributing to degradation of cell. Also, inactive particles within the negative electrode play a crucial role in providing structural stability to the cell. However, binder decomposition can lead to changes in the cell's morphology, ultimately contributing to cell degradation. Additionally, a primary challenge associated with silicon anodes is their substantial volume change during charge/discharge cycles, a characteristic that enhances their energy density due to the presence of free sites for Lithium ions to intercalate. However, the continuous volume fluctuations might lead to the formation of secondary films on the anode surface, increasing the chance of Li-plating, and thereby depleting cycleable Lithium and contributing to capacity fade of the cell over time. Each of these degradation mechanisms could get pronounced in certain circumstances of cell operation such as extreme temperatures, high charge/discharge rates, and overvoltage of the cell due to overcharge and overdischarge.

Li-plating is a critical degradation mechanism that becomes more pronounced under harsh charging conditions, as discussed in a study by Zhang et al. [143]. It is primarily accelerated when metallic Lithium forms during the charging process under conditions such as high charging rates, overcharging at high state-of-charge, and charging at low temperatures. At lower temperatures, the cell's energy density decreases due to several factors, including reduced ionic conductivity and diffusivity in the electrolyte, lower solid-state diffusivity of Li ions in the electrodes, and slower intercalation rates. Higher charge rates introduce greater kinetic and transport overpotentials, contributing to the Li-plating phenomenon, as highlighted by Lin et al. [142]. Additionally, when the state-of-charge of the cell is high, continued charging can lead to an excess of Lithium ions saturating on the anode surface, surpassing the maximum allowable Lithium levels, further accelerating Li-plating. In essence, under low-temperature and high state-of-charge conditions, the diffusion rate of Li ions within the electrolyte toward the anode outpaces the rate of Li ions diffusing into the SEI layer and graphite interlayer. This results in an accumulation of Li ions on the surface of the SEI layer, which subsequently absorbs electrons and forms metallic Lithium. This metallic Lithium is deposited onto the surface of the SEI layer. The Li-plating process can be either reversible or irreversible. The reversible process, known as Lithium stripping, occurs when metallic Lithium maintains electrical contact with the anode, allowing for the release of an electron and the deposition of Li ions back into the electrolyte. Conversely, if the plated Lithium loses electrical contact with the anode, the process becomes irreversible, leading to the loss of cycleable Lithium and the growth of dendrites on the anode surface. This form of metallic Lithium is often referred to as "dead Lithium". The growth of metallic Lithium dendrites on the anode surface can potentially rupture the separator, creating an electrical pathway between the anode and cathode, resulting in a cell short circuit [144]. Furthermore, the high surface area of dead Lithium can contribute to secondary SEI growth

on its surface, further reducing the available cycleable Lithium [145]. Parasitic reactions related to Li-plating can be exacerbated during fast-charging operating conditions [146].

Quantifying plated Lithium in Li-ion batteries has been a long-standing challenge in battery studies. The separate quantification of Solid-Electrolyte Interphase (SEI) and metallic Lithium further complicates this task. Various techniques, categorized as *ex-situ*, *in-situ*, and *operando*, have been proposed for determining the dead Lithium content within the cell, as discussed by Lin et al. [142]. Different experimental techniques could be used for detection of metallic Lithium in the cell including Scanning Electron Microscopy, Nuclear Magnetic Resonance Spectroscopy (NMR), X-ray Photoelectron Spectroscopy, and Electrochemical Impedance Spectroscopy. Detailed discussions about these experimental techniques can be found in references such as [142, 147, 148]. In the current study, in order to better understand the Li-plating phenomena, we leverage experimental data obtained from novel Li-NMR spectroscopy technique, introduced and developed by Sanders et al. [149]. Fang et al. [145] have also used a similar approach for quantification of metallic Lithium using Li-NMR technique as an *operando* approach.

Expanding upon efforts to quantify Lithium plating in the cell, we aim to model the growth and decay of plated Lithium within the cell using mathematical and computational tools, to eliminate the need for experimentation in an online application of cells or battery packs. Building upon advancements in experimental quantification, we seek to track the evolution of different phases of Lithium in *operando* under diverse charge/discharge protocols. Mathematical tools will aid in developing underlying models based on the physical principles governing cell behavior. Additionally, sophisticated computational tools will be employed to calibrate these models, optimizing their alignment with experimental data. The technique of inverse modeling will be utilized for this purpose. Many authors have used inverse modeling in systematic optimization of electrochemistry problems including [27, 29–31], in which the electrochemical parameters of the model are calibrated via experimental data. Also, the optimal reconstruction of constitutive relations in electrochemical problems have been investigated in these studies. In the current study, the techniques of inverse modeling and optimal reconstruction are leveraged to calibrate the mathematical models using experimental data. The calibrated model holds promise for online applications, enabling real-time monitoring, recommending optimal charge/discharge protocols, and ultimately enhancing cell performance while mitigating degradation in the long run.

The paper is organized as follows: details of the experimental data are presented in Section 4.2; then in Section 4.3 we introduce the mathematical modeling framework for the this problem and develop a dynamical system governing the evolution of lumped concentrations of different phases of Lithium in the cell; in Section 4.4 we introduce the inverse modeling framework and the computational tools used for

calibrating the dynamical system; Section 4.5 presents the results of this analysis and compares them to the experimental data; finally, the summary of the work and the conclusions are deferred to Section 4.6.

#### 4.2. Experimental Data

To calibrate the mathematical models for subsequent prediction and control, one requires experimental data tailored for this purpose. The experimental data utilized in this study was collected using the *operando* Li-NMR spectroscopy technique, as introduced in a prior publication by Sanders et al. [149]. This technique enables the identification and quantification of various Lithium phases within the anode while the cell is in operation, as depicted in Figure 4.1.

The anode material used for these experiments is silicon, recognized as one of the most promising materials due to its high energy density. The cathode material employed is NMC622 ( $\text{LiNi}_{0.6}\text{Mn}_{0.2}\text{Co}_{0.2}\text{O}_2$ ). The test protocol of each experiment comprises constant-current (CC) followed by constant-voltage (CV) charge/discharge, and open-circuit resting (OCV) phases. The charge rates for the constant-current phase are C/3 (3-hour charge), C/2 (2-hour charge), 1C (1-hour charge), 2C (30-minute charge), and 3C (20-minute charge); while the discharge rates for the CC phase remain constant at C/3 (3-hour discharge) for all cycles. Here, 'C' denotes the capacity of the cell. Note that in this study, the cycles C/3 and C/2 are denoted C3 and C2, respectively, for the simplicity of notation. The voltage of the cell ranges from 2.5V to 4.2V, with the former representing the cell at full discharge, while the latter corresponds to its fully charged state. The OCV segment after charge and discharge is set for a duration of one hour. *Operando* NMR measurements were conducted at intervals of 5 minutes for the C3 cycle, 3 minutes for the C2 and 1C cycles, and 1.5 minutes for the 2C and 3C cycles. The evolution of various Lithium phases from Li-NMR experiments, alongside their operational current profile and the cell's terminal voltage, is depicted in Figure 4.1.

Several peaks are modelled when fitting NMR spectra to quantify different phases of Lithium, including

1. Lithium in the electrolyte or solid-electrolyte interphase (SEI),
2. Lithium in dilute  $\text{Li}_x\text{Si}$  where  $x < 2.0$  in a locally-ordered environment (referred to as dilute Li),
3. Lithium in concentrated  $\text{Li}_x\text{Si}$  where  $x > 2.0$  in a locally-ordered environment (referred to as concentrated Li),

4.  $\text{Li}_x\text{Si}$  in a disordered environment (referred to as disordered Li), and

5. dendritic and plated Lithium.

These different phases of Lithium manifest distinct chemical shifts in the *operando* NMR data. It is worth noting that all dendritic Lithium formed is irreversible, while plated Lithium may exhibit reversible or irreversible behavior. As depicted in Figure 4.1, the evolution of different phases at constant rates demonstrates a nonlinear behavior during cell operation. Also, the dendritic Lithium content does not appear in all cycles, but in the ones with higher C-rates. In other words, in the cycles with lower C-rates, the formation of dendritic Lithium is smaller than the sensitivity of the measurement device.

In order to pre-process the experimental data depicted in Figure 4.1 and make it suitably formatted for the mathematical model and further analysis, the Lithium in the anode solid phase (dilute Li, concentrated Li, and disordered Li) are added to form the solid phase concentration  $\widetilde{C}_1(t)$ . Similarly, addition of plated and dendritic Li content in the cell forms the Li phase  $\widetilde{C}_2(t)$  corresponding to side reactions. Note that the subscripts 1 and 2 refer to intercalated and side-reacted Lithium, respectively; a notation that is consistent with mathematical the model in Section 4.3.5. These concentrations are normalized and their evolution for each cycle are shown in Figure 4.2. As can be observed in Figure 4.1, the total Li content in the cell does not add up to a constant, and it is changing with the cell operation, due to several factors. First, the Li content in the positive electrode of the cell is not accounted for in the Li-NMR measurements. The complement of the Li content in the cell could be stored in the positive electrode which is not modelled in this case. Second, the presence of noise in Li-NMR measurements is another source of deviation from the normalization condition (conservation of Lithium), cf. Section 4.3.3. It is also notable that two forms of dynamics are evident in the cell: the excitation dynamics as the primary source, and the relaxation dynamics. The excitation dynamics is the response of the system to external current source, which is the dominant form of dynamics in the cell. The relaxation dynamics represents the evolution of the system while the cell is at rest in the absence of an external current source. We note that the dynamics of the system are primarily determined by excitation, and hence, change in the dynamics due to excitation is larger than change in the dynamics due to relaxation. This fact will be used in mathematical modeling, cf. Section 4.3.

The data for each experiment is split into three regimes: the charging regime, the OCV regime, and the discharge regime. To use a proper notation for the amalgamated data,  $\mathcal{D}_t = \bigoplus_i \mathcal{D}_i, i \in \{\text{C3}, \text{C2}, \text{1C}, \text{2C}, \text{3C}\}$ , where  $\mathcal{D}_i$  refers to the total concentration data available for the cycle with rate  $i$ , and  $\bigoplus$  denotes the concatenation operator. Each cycle consists of three regimes:  $\mathcal{D}_i = \bigoplus_j \mathcal{D}_i^j, j \in$

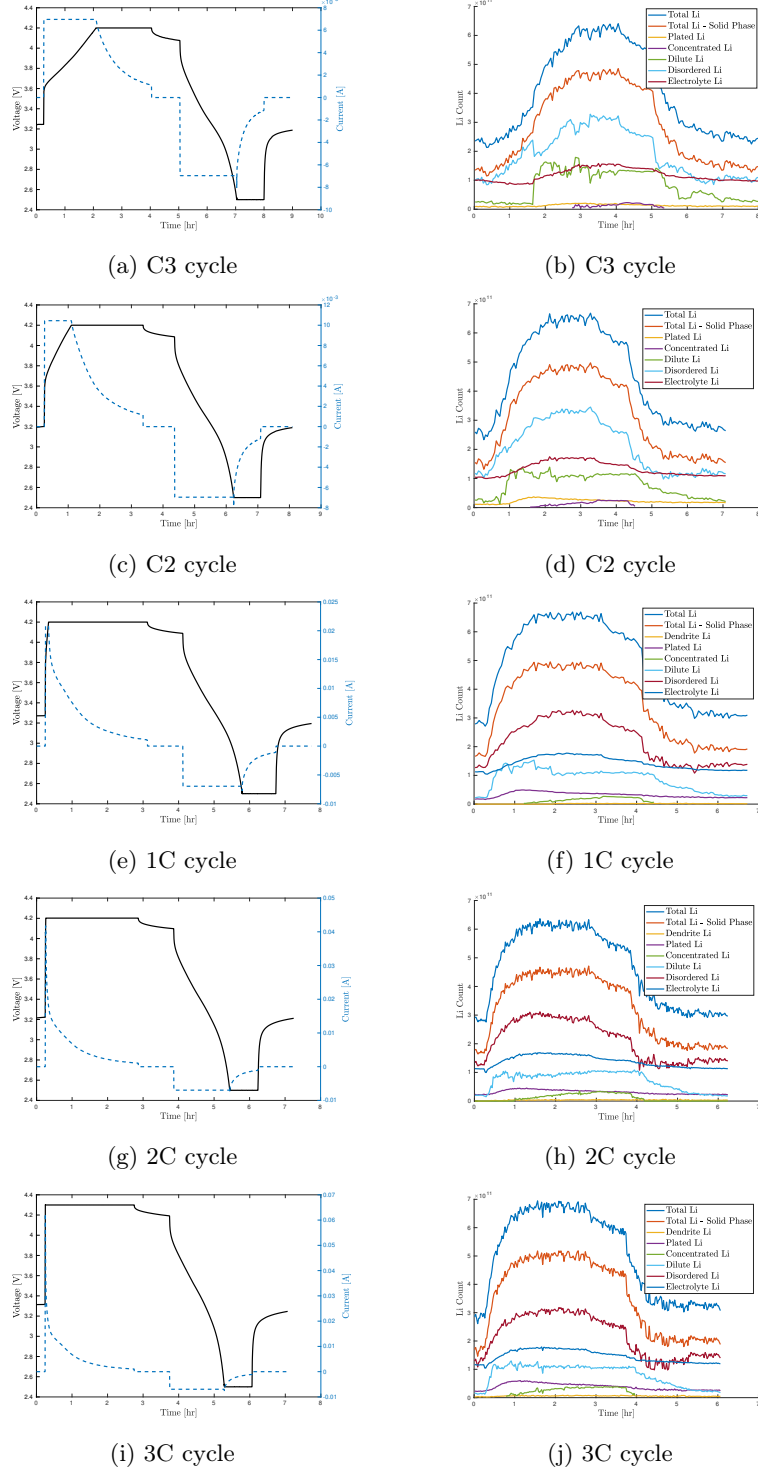


Figure 4.1: Terminal voltage and current applied to the cell (a,c,e,g,i), and evolution of Li content in time in different phases via Li-NMR spectroscopy method (b,d,f,h,j) using different test protocols of the cell.

$\{ch, ocv, dch\}$ , where  $\{ch, ocv, dch\}$  refer to charge, OCV, and discharge regimes of the cell testing protocols, respectively. Different segments of  $\mathcal{D}_t$  will be used for analysis.

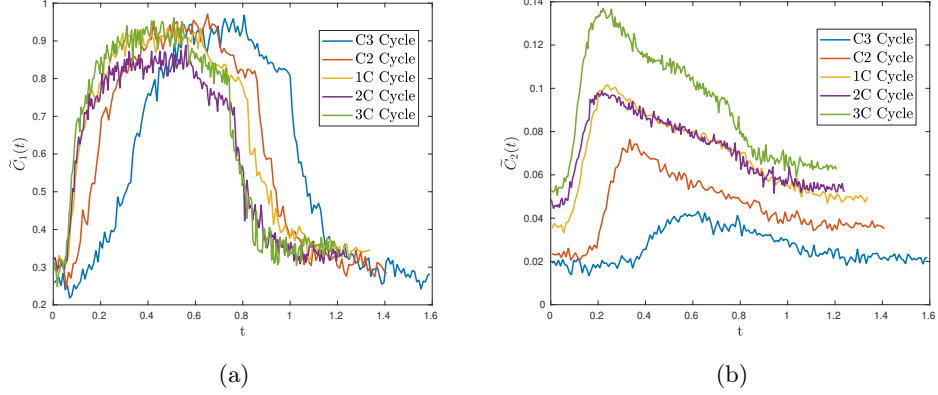


Figure 4.2: Evolution of Li content in time in negative electrode solid phase corresponding to intercalated Li (a), and plated Li (b) for different C-rates. Note that the variables are normalized.

### 4.3. Physical Modeling

Mathematical modeling plays a pivotal role in comprehending the intricate physical processes within a battery cell, exploring degradation mechanisms and their influencing factors, and crafting effective mitigation and control strategies for the challenges encountered in large-scale applications of Li-ion batteries. Various approaches can be employed for mathematical modeling, with two primary paradigms being physics-based modeling and data-driven machine-learning modeling. In this study, we aim to navigate the border between these two paradigms, with more emphasis placed on physics-based modeling of cells. This approach involves utilizing fundamental physical principles to construct a mathematical framework that represents the behavior of the cell, augmenting the model, and leveraging data-driven strategies for calibration. The ultimate objective is to predict the Li-plating dynamics of the cell using experimental data obtained from Li-NMR spectroscopy. The use of Li-NMR spectroscopy data in the modeling process highlights the integration of experimental data into the physics-based framework. This coupling of experimental observations with theoretical modeling can yield highly informative and predictive models for understanding and mitigating the critical issue of Li-plating in Li-ion batteries.

The operation of a Li-ion cell involves a multitude of physical and chemical processes, each occurring at different spatial and temporal scales. This complex multi-physics multi-scale nature of the phenomenon makes it challenging to develop suitable models for specific applications aimed at investigating various aspects of the cell's behavior. One of the most widely accepted physics-based modeling approaches for Li-ion cells is rooted in the porous electrode theory initially introduced by Newman et al. [16]. In these models, the cell is treated as a continuum medium, and it operates on larger temporal and spatial scales compared to discrete particle-level models that necessitate fine-scale resolution. Continuum

models, which are widely regarded as the fundamental approach, serve as the basis for modeling Li-ion cells. Depending on the specific application and research objectives, models of varying levels of complexity can be adapted. These models allow researchers to delve into the intricacies of the cell's behavior, considering the multitude of physical and chemical processes occurring within it. The review by Brosa Planella et al. [95] explores various modeling approaches for Li-ion cells and introduces a systematic reductive framework, called asymptotic reduction, to simplify complex mathematical models using physical assumptions. Among the different modeling approaches, the most intricate is the microscale model, which operates at the finest temporal and spatial scales to capture the detailed physical phenomena within the cell. In microscale modeling, the framework is built upon the conservation laws for Lithium ions and counter-ions in the electrolyte, as well as the conservation of Lithium ions and electrons in the solid phase of the electrodes. Because electrons serve as charge carriers in the solid phase, the conservation of electrons and Lithium ions is treated separately. In contrast, ions act as the charge carriers in the electrolyte phase, resulting in more intricate conservation equations in the electrolyte phase. To close these conservation laws and make them mathematically complete, suitable constitutive relations are employed. These relations establish the connection between the flux of a species (e.g. Lithium ions or electrons) and the thermodynamic forces acting upon them, allowing for a comprehensive representation of the physical processes occurring at the microscale within the Li-ion cell. The process of Lithium intercalation and deintercalation primarily takes place on the surface of the anode particles and is considered as an interfacial phenomenon. The rate of intercalation reactions on the surface of the anode active material depends on the surface overpotential. This overpotential is defined as the difference between the electrochemical potential of Li ions on the surface of the solid phase and the Li ions in the adjacent electrolyte, and is typically represented by the well-known Butler-Volmer (BV) relation. Solid-phase diffusion of Lithium ions within the anode is a complex process that may involve phase transition phenomena. While simplifying assumptions are often applied to this diffusion process, conventional diffusion equations are commonly used to model it. However, recent modeling techniques have relaxed the assumption of linear diffusion and instead incorporate nonlinear diffusion within the solid phase. This nonlinear diffusion accounts for concentration-dependent diffusion coefficients, making it capable of capturing phase-transition behavior [30, 150]. Furthermore, an alternative approach based on the Cahn-Hilliard modeling framework has gained attention due to its ability to naturally capture the dynamics of phase transitions during solid-state diffusion [30, 151]. In the electrolyte, charge transport is described using various theories. Two common theories include (i) Dilute Electrolyte Theory, which is based on Nernst-Planck equations and is applicable to dilute electrolytes where there is limited interaction between species, and (ii) Concentrated Electrolyte Theory, which is based on Stefan-Maxwell type equations and is more suitable for

concentrated electrolyte solutions. These models govern charge transport in the electrolyte phase and are essential components of comprehensive Li-ion cell models. Microscale models offer a highly detailed representation of Li-ion cells, but they come with the drawback of demanding significant computational resources and requiring extensive knowledge about the microstructure of various cell components. They also depend on more parameters which makes them harder to calibrate. As a result, they are not well-suited for online estimation and control, where real-time decision-making is essential.

To address these challenges, one could rely on some simplifying assumptions to transform complex microscale models into more manageable homogenized models [95]. In homogenized models, the porous media within the cell is treated as a continuum, and the equations are modified to incorporate the influence of the microstructure. This approach allows for the resolution of electrolyte flow at the macroscale, while retaining the microscale representation of solid-state diffusion, as this process is typically slow and involves significant concentration gradients in fine spatial scales. In this type of modeling, microstructural information is still required, but the model simplifies this by generalizing a small subdomain to represent the entire domain using periodic boundary conditions. These homogenized models can be reduced to the well-known Doyle-Fuller-Newman (DFN) model by assuming a simpler geometry for all electrode particles, a model that is also referred to as the pseudo-two-dimensional (P2D) or Newman model, firstly introduced by Fuller, Doyle, and Newman [152]. The DFN model simplifies the representation of electrode particles by assuming them to be spherical. Consequently, it solves the solid-state diffusion equations in a 1D radial coordinate, rather than attempting to capture the intricate 3D microstructure of the electrode particles. Similarly, the electrolyte equations are solved in a 1D planar geometry. This simplification results in a model that can be conceptually described as 1D+1D, giving rise to the term “pseudo-two-dimensional”. The P2D model is renowned for its computational efficiency while retaining the capability to capture the internal dynamics and behavior of Li-ion cells.

In pursuit of enhanced computational efficiency and suitability for online estimation and control, reduced-order models have been introduced as alternatives to the comprehensive DFN models. Two notable reduced-order models are the Single-Particle Model (SPM), originally introduced by Atlung et al. [153], and the Single-Particle Model with Electrolyte (SPMe), developed by Prada et al. [154]. The fundamental assumption in these models is that the spherical electrode particles, as considered in the DFN model, are sufficiently similar in nature. This similarity allows these particles to be effectively represented by a single averaged or representative particle. It is assumed that the intercalation and deintercalation processes occur almost uniformly across all electrode particles, making it feasible to describe these processes using a single representative particle. In this setting, the partial differential equations

(PDEs) governing the Li-ion cell behavior can be effectively decoupled into micro and macro scales. It is worth noting that the SPMe model, unlike the simpler SPM model, accounts for the electrolyte dynamics, offering a more comprehensive representation of cell dynamics by considering the behavior of the electrolyte phase. The SPM and SPMe models could be achieved by asymptotic reduction of DFN model as developed by different authors [155–157]. Certain physical assumptions are used by Marquis et al. [156] to systematically reduce the DFN model to a much simpler SPM model which will affect the range of validity of these models. The physical assumptions include high electrical conductivity in the electrodes and electrolyte, and fast Li ion migration in electrolyte in comparison to the discharge timescale. The range of validity of the SPM model according to Brosa Planella et al. [155] is small overpotentials from open-circuit-voltage, and weak side reactions. The two assumptions hold for low to moderate charge rates and will break at high rates. In summary, starting from the most complex microscale model and utilizing a systematic asymptotic reduction framework, the order of complexity can be progressively reduced.

The objective of this research is to adopt a simple model that can effectively capture the internal dynamics of a Li-ion cell, focusing on the interactions among various particles within the cell. The physical model is developed in a manner to match the experimental data obtained from Li-NMR experiments. The physical modeling framework of this study is inspired by the SP model with side reactions, recently introduced by Brosa Planella et al. [155]. This study also finds close connections to a recent study by Sahu et al. [158]. The model used in this study could be seen as a simpler version of the SP model with side reactions, where certain parameters and functions are to be calibrated using experimental data. The final model takes the form of a system of ordinary differential equations (ODE). It involves employing a SP model in the form of partial differential equations (PDE) and applying reduction and averaging techniques to derive a suitable ODE model that describes the evolution of key space-averaged concentrations within the cell. Some aspects of the model are shown to increase its flexibility in fitting the experimental data. We begin by introducing the DFN model in Section 4.3.1, developing the dimensionless model in Section 4.3.2, applying the asymptotic reduction technique in Section 4.3.3, and finally introducing our dynamical system as forward model in Section 4.3.5. The key differences of our model with similar studies are highlighted in Section 4.3.4.

#### 4.3.1 DFN Model

In this study, we begin by presenting the 1D DFN model. The SP model is derived from an asymptotic reduction analysis. This model is then further simplified using averaging techniques to yield a mathematical representation suitable for modeling our experimental data, cf. Section 4.2. It is noteworthy that our modeling approach is inspired by the SPMe+SR (Single-Particle Model with Side Reactions) framework

of Brosa Planella et al. [155], albeit with some modifications to the underlying assumptions, which serve to mitigate certain limitations associated with the Brosa Planella's model. The differences in modeling assumptions are highlighted in Section 4.3.3. The current study also finds close connections to Li plating modeling efforts of Sahu et al. [158]. The SP model assumes the presence of a representative (averaged) particle to describe the transport of species within the solid state of the electrode. The key assumption is that all solid particles within the electrode are indistinguishable, allowing a single particle to serve as a representative for the entire solid phase. It is important to note that the cathode component of the cell is also considered in the modeling effort, however, the final model (presented in Section 4.3.5) eliminates the need for solving for the positive electrode components, as the experimental data does not contain information from the positive electrode domain. The model is composed of five distinct components, namely, charge conservation in the solid phase of positive and negative electrodes, Li Transport in the solid phase of positive and negative electrodes, Li transport in the electrolyte phase, charge conservation in the electrolyte phase, and models of side reactions through interfacial dynamics. Each of these components is explained in more detail below. Note that in our model we only take into account the Li-plating side reaction and we disregard other side reactions in the cell (e.g., SEI growth). We also disregard the film resistance formed on the surface of the anode particle due to side reactions, and porosity change of the anode particles in time is not modelled. Also, the volume change of anode particles (which could be significant in silicon anodes) is not explicitly considered in this model, however, the concentration-dependent constitutive relations can implicitly take this effect into account, as described in Section 4.3.5.

The model geometry consists of the negative electrode ( $\Omega_n$ ), the separator ( $\Omega_s$ ), and the positive electrode ( $\Omega_p$ ) where  $\Omega = \Omega_n \cup \Omega_s \cup \Omega_p$ . The model's geometry is depicted in Figure 4.3, where the 1D macroscale coordinate is indicated on the horizontal axis with  $\Omega_n = [0, L_n]$ ,  $\Omega_s = [L_n, L - L_p]$  and  $\Omega_p = [L - L_p, L]$ , where  $L_n, L_p > 0$  are the widths of the negative electrode and positive electrode, respectively. In contrast, the microscale dimension is described using spherical coordinates with  $r \in \Omega_{rn} = [0, R_n]$  for the negative particle and  $r \in \Omega_{rp} = [0, R_p]$  for the positive particle, where  $R_n$  and  $R_p$  represent the radii of the spherical negative and positive particles, respectively. In our study, each of these sub-models is averaged over its respective spatial domain to eliminate the spatial dependence of the model to match to the experimental data.

Note that in the following sections, where the mathematical model is presented, variables with a hat are dimensionless, variables in bold are vector quantities, and variables with a bar refer to quantities averaged over their spatial domain. Subscripts  $n$ ,  $e$ , and  $p$  refer to the negative electrode solid phase, the electrolyte phase, and the positive electrode solid phase, respectively. In each of the following subsec-

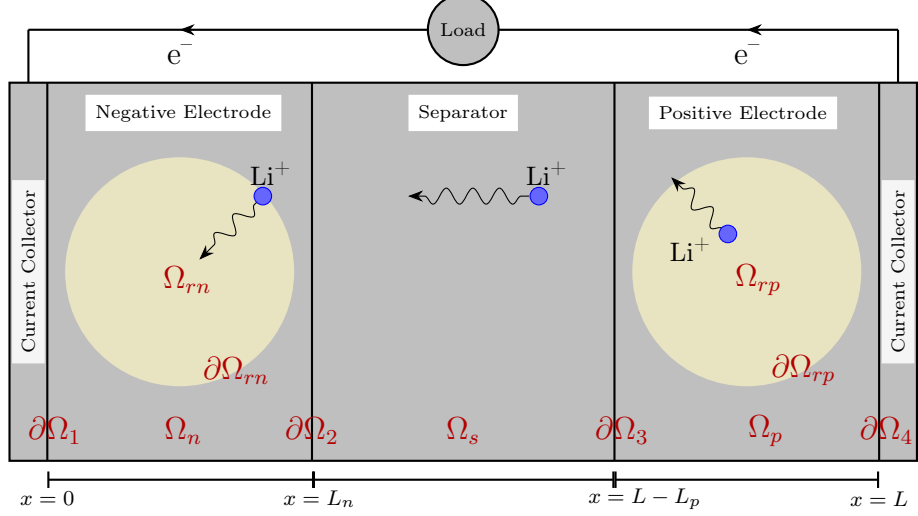


Figure 4.3: Schematic of a Li-ion cell in the charging state. Li ions deintercalate from the positive electrode surface, migrate toward the negative electrode through the electrolyte, and intercalate into negative particles. Electrons will migrate through the external circuit toward the negative electrode. The domain of the system is highlighted in red.

tions, different components of the DFN model are presented.

### Charge Conservation in the Solid Phase

This sub-model describes charge conservation within the solid phase of the negative electrode. The charge conservation equation is stated in macroscale in  $\Omega_n$ . The potential profile in the solid phase is obtained by solving the following equation in 1D as

$$\begin{aligned} \frac{\partial J_n}{\partial x} &= -a_n J_{n,tot}, \\ J_n &= -\sigma_n \frac{\partial \phi_n}{\partial x}, \\ J_n &= J_{app}, \quad \text{at } x = 0, \\ J_n &= 0, \quad \text{at } x = L_n, \end{aligned} \tag{4.1}$$

where  $\phi_n[V]$  is the electrostatic potential in the solid phase,  $J_n[\frac{A}{m^2}]$  is the current density in the solid phase,  $\sigma_n[S/m]$  is the effective conductivity of the solid particles,  $J_{n,tot}[\frac{A}{m^2}]$  is the source/sink term representing the total current density flux at the solid-electrolyte interface of the negative electrode due to intercalation and side reactions,  $J_{app}[\frac{A}{m^2}]$  denotes the current density applied to the cell, and  $a_n = \frac{3}{R_n} [\frac{1}{m}]$  is the effective surface area of the anode particles per unit volume. Similarly, the charge conservation in

the solid phase for the positive electrode in 1D becomes

$$\begin{aligned} \frac{\partial J_p}{\partial x} &= -a_p J_{p,tot}, \\ J_p &= -\sigma_p \frac{\partial \phi_p}{\partial x}, \\ J_p &= 0, \quad \text{at} \quad x = L - L_p, \\ J_p &= J_{app}, \quad \text{at} \quad x = L. \end{aligned} \tag{4.2}$$

Note that the total current density is a source/sink term that is present in negative electrode and positive electrode only and vanishes in the separator, as

$$J_{tot} = \begin{cases} J_{n,tot} = J_{n,int} + J_{n,sr} & 0 \leq x \leq L_n, \\ 0 & L_n \leq x \leq L - L_p, \\ J_{p,tot} = J_{p,int} & L - L_p \leq x \leq L, \end{cases} \tag{4.3}$$

where  $J_{n,int}$ ,  $J_{n,sr}$  and  $J_{p,int}$  represent intercalation and side reaction current densities at the solid-electrolyte interface of the negative electrode and intercalation current density at the solid-electrolyte interface of the positive electrode, respectively. Note that no side reaction is assumed on the positive electrode.

### Li Ion Transport in the Solid Phase

This sub-model describes the slow diffusion of Li ions inside the solid phase. The diffusion equation for Li transport in the solid phase is stated in the microscale in the spherical coordinates for a representative particle (assuming uniformity along all particles). In the 1D spherical coordinates, the system is

$$\begin{aligned} \frac{\partial C_n}{\partial t} &= \frac{1}{r^2} \frac{\partial}{\partial r} \left( r^2 D_n \frac{\partial C_n}{\partial r} \right), & r \in (0, R_n), \\ \frac{\partial C_n}{\partial r} &= 0, & \text{at} \quad r = 0, \\ -D_n \frac{\partial C_n}{\partial r} &= \frac{J_{n,tot}}{F}, & \text{at} \quad r = R_n, \\ C_n &= C_{n_i}(r), & \text{at} \quad t = 0, \end{aligned} \tag{4.4}$$

where  $C_n = C_n(r, t) [\frac{mol}{m^3}]$ ,  $D_n [\frac{m^2}{s}]$ ,  $C_{n_i}(r)$  are the Li concentration, the diffusion coefficient, and initial concentration profile, respectively.  $N_{tot}$  is the total molar flux at the solid-electrolyte interface as  $N_{tot} = N_{int} + N_{sr}$ , where  $N_{int}$  is the molar flux of Li corresponding to the intercalation process, whereas  $N_{sr}$  is the molar flux of Li resulting from side reactions. The Li flux on the surface of the anode particle

is obtained from  $\mathbf{n} \cdot \mathbf{N}_n|_{r=R_n} = -\frac{J_{n,tot}}{F}$ , where  $J_{n,tot}[\frac{A}{m^2}]$  is the current density flux at the interface (obtained from the Butler-Volmer relation), and  $F[\frac{A \cdot s}{mol}]$  is Faraday's constant. Note that the interfacial current density  $J_{n,tot}$  will be replaced with the intercalation current density  $J_{n,int}$  in Section 4.3.3, to account for side reaction as well. Similarly, Li transport in the solid phase of the positive particles in 1D spherical coordinates is governed by

$$\begin{aligned} \frac{\partial C_p}{\partial t} &= \frac{1}{r^2} \frac{\partial}{\partial r} \left( r^2 D_p \frac{\partial C_p}{\partial r} \right), & r \in (0, R_p), \\ \frac{\partial C_p}{\partial r} &= 0, & \text{at } r = 0, \\ -D_p \frac{\partial C_p}{\partial r} &= -\frac{J_{p,tot}}{F}, & \text{at } r = R_p, \\ C_p &= C_{p_i}(r), & \text{at } t = 0. \end{aligned} \quad (4.5)$$

### Charge Conservation in the Electrolyte Phase

This sub-model describes charge conservation within the electrolyte phase. The continuity equation of charge conservation in the electrolyte phase is defined in the macroscale in  $\Omega$  in terms of the potential profile and has the form

$$\begin{aligned} \frac{\partial}{\partial x} J_e &= a J_{tot}, \\ J_e &= -\sigma_e B(x) \left[ \frac{\partial}{\partial x} \phi_e - 2(1-t^+) \frac{RT}{F} \frac{\partial}{\partial x} \log C_e \right], \\ \frac{\partial}{\partial x} \phi_e &= 2(1-t^+) \frac{RT}{F} \frac{\partial}{\partial x} \log C_e, & \text{at } x = 0, L, \end{aligned} \quad (4.6)$$

where  $J_e$  is the current density in the electrolyte phase,  $\phi_e$  is the potential in electrolyte phase,  $\sigma_e$  is the electrolyte conductivity,  $B = B(x, t)$  is the permeability, and  $t^+ = t^+(C_e)$  is the transference number.

### Li Ion Transport in the Electrolyte Phase

This sub-model deals with the transport of Li ions within the electrolyte phase at macroscale. The continuity equation for Li ion conservation in the electrolyte phase is stated on  $\Omega$  in terms of the concentration profile of Li ions and has the following form

$$\begin{aligned} \frac{\partial}{\partial t} (\epsilon C_e) &= -\frac{\partial}{\partial x} N_e + \frac{a}{F} J_{tot}, \\ N_e &= -D_e B(x) \frac{\partial}{\partial x} C_e + \frac{t^+}{F} J_e, \\ \frac{\partial}{\partial x} C_e &= \frac{1}{D_e B(x)} \frac{t^+}{F} J_e, & \text{at } x = 0, L, \\ C_e &= C_{e_i}, & \text{at } t = 0. \end{aligned} \quad (4.7)$$

where  $\epsilon = \epsilon(x, t)$  is the porosity of the domain,  $C_e = C_e(x, t)$  is the Li ion concentration in the electrolyte,  $D_e = D_e(C_e)$  is the diffusion coefficient in the electrolyte phase, and  $J_e$  is the current density vector in the electrolyte phase.

### Interfacial Dynamics

Interfacial processes in the cell are normally modelled through the well-known Butler-Volmer (BV) relation for electrochemical kinetics. It describes how the current density at the solid-electrolyte interface depends on the potential difference between the electrode surface and the neighbouring electrolyte. Several variants of this semi-empirical relation exist in the literature as surveyed by Dickinson et al. [96]. Depending on the nature of the problem and the level of complexity required for a given application, a suitable BV relation could be used. Lithium plating and stripping as interfacial processes can also be modelled by adding an extra BV equation for the side reaction. Essentially, one BV relation can be added for each of the side reactions, representing the intensity of each side reaction as a function of overpotential, as first introduced by Arora et. al. [159] and later expanded by Yang et. al. [160]. The BV relations representing interfacial phenomena at the solid-electrolyte interface are represented by [159, 160]

$$\begin{aligned}
J_{n,int} &= j_{int} [\exp(\alpha_{a,int} f \eta_{int}) - \exp(-\alpha_{c,int} f \eta_{int})], \\
J_{n,sr} &= j_{sr} [\exp(\alpha_{a,sr} f \eta_{sr}) - \exp(-\alpha_{c,sr} f \eta_{sr})], \\
\eta_{int} &= \phi_n - \phi_e - U_n, \\
\eta_{sr} &= \phi_n - \phi_e - U_{sr}, \\
j_{int} &= k_{a,int}^{\alpha_{c,int}} k_{c,int}^{\alpha_{a,int}} C_n^{\alpha_{c,int}} C_e^{\alpha_{a,int}} (C_{max} - C_n)^{\alpha_{a,int}}, \\
j_{sr} &= k_{a,sr}^{\alpha_{c,sr}} k_{c,sr}^{\alpha_{a,sr}} C_e^{\alpha_{a,sr}},
\end{aligned} \tag{4.8}$$

where  $j_{int}$  and  $j_{sr}$  are the exchange current densities for intercalation and side reaction, respectively,  $\eta_{int}$  and  $\eta_{sr}$  are the overpotentials at the solid-electrolyte interface for intercalation and side reactions, respectively,  $U_n$  and  $U_{sr}$  are equilibrium potentials,  $k_{c,int}$ ,  $k_{a,int}$ ,  $k_{c,sr}$ ,  $k_{a,sr}$  are the reaction rates for cathodic and anodic currents of intercalation and cathodic and anodic currents of side reaction, respectively,  $C_{max}$  is the saturation concentration of Li in solid phase, and  $C_n = C_n|_{r=R_n}$  refers to solid phase concentration on the surface of the particle. On the other hand, Escalante et al. [30] use a more sophisticated technique for modeling side reaction in the cell, where one BV relation is used to represent both Li intercalation/deintercalation and plating/stripping as

$$j_{int} = k_0 C_n^{0.5} C_e^{0.5} (C_{max} - C_n)^{0.5} \tanh \left( \gamma \frac{C_{max} - C_n}{C_{max}} \right),$$

where the intercalation exchange current density is multiplied by a factor describing how the total current is divided between the intercalation and side reactions, hence, reducing the formulations for exchange current densities. Thus, the two equations for exchange current density of intercalation and side reaction are replaced with one, with a significantly lower number of parameters. As can be observed, the exchange current densities are concentration dependent, and most authors have used similar functional forms to model this dependency. Daniels et al. [31] leverage a data-driven approach in order to optimally construct the exchange current density as a function of concentration, without assuming any *a priori* functional form for this function. In our modeling approach, we use a combination of aforementioned techniques. We use separate BV relations as in first approach in order to account for the side reaction, cf. (4.8). We also introduce a variable as the ratio of exchange current densities for intercalation and plating processes that represents the competition between the intercalation versus plating, as outlined in Section 4.3.3. This key variable is concentration dependent, and the optimal functional form will be constructed using data-driven inverse modeling techniques. Before we start the analysis, we present a dimensionless version of our model in the next section.

#### 4.3.2 Dimensionless Model

The model introduced in (4.1), (4.2) (4.4), (4.5), (4.6), and (4.7) could be rescaled to a dimensionless form that will facilitate its asymptotic reduction. We focus on the 1D version of the model where the independent and dependent variables are rescaled as follows

$$\begin{aligned}
x &= L\hat{x}, & L_n = Ll_n, & L_p = Ll_p, & r = R_n\hat{r}_n, & r = R_p\hat{r}_p, \\
J_k &= J_t\hat{J}_k, & J_K = J_t\hat{J}_K, & j_{int} = J_t\hat{j}_{int}, & j_{sr} = J_t\hat{j}_{sr}, & \phi_n = \phi_t\hat{\phi}_n, \\
\phi_e &= \frac{1}{f}\hat{\phi}_e, & U_n = \phi_t\hat{U}_n, & \eta_{int} = \frac{1}{f}\hat{\eta}_{int}, & \eta_{sr} = \frac{1}{f}\hat{\eta}_{sr}, & \sigma_e = \sigma_e^{\text{typ}}\hat{\sigma}_e, \\
C_n &= C_n^{\max}\hat{C}_n, & C_p = C_p^{\max}\hat{C}_p, & C_e = C_e^{\max}\hat{C}_e, & C_{sr} = C_n^{\max}\hat{C}_{sr}, & t = \tau\hat{t}, \\
N_e &= \frac{D_e^{\text{typ}}C_e^{\max}}{L}\hat{N}_e, & D_n = D_n^{\text{typ}}\hat{D}_n, & D_e = D_e^{\text{typ}}\hat{D}_e, & D_p = D_p^{\text{typ}}\hat{D}_p,
\end{aligned}$$

where  $\hat{x} \in [0, l]$ ,  $l = 1, k \in \{n, e, p\}$ ,  $K \in \{\text{tot, int, sr, app}\}$ ,  $f = \frac{F}{RT}$ ,  $J_t$  is the typical current density in the cell,  $\phi_t$  is defined as the characteristic change in the potential of the cell from low to high states-of-charge of the cell (note that the order of magnitude of this quantity is large for some chemistries such as NMC and LCO, however, LFP chemistry notoriously exhibits smaller magnitudes of this quantity),  $D_k^{\text{typ}}$  is the typical diffusion coefficient,  $\sigma_e^{\text{typ}}$  is the typical conductivity,  $C_k^{\max}$  is the maximum concentration of Lithium in the corresponding domain, and  $\tau = \frac{FC_n^{\max}L}{J_t}$  is the discharge time scale. Note that  $\frac{1}{f} = \frac{RT}{F}$  has the unit of Volts and is defined as the thermal voltage of the cell. The dimensionless parameters are

then defined as

$$\begin{aligned}\lambda &= \phi_t f, & \Xi_n &= \frac{\sigma_n}{f L J_t}, & \Xi_e &= \frac{\sigma_e^{\text{typ}}}{f L J_t}, & \Xi_p &= \frac{\sigma_p^{\text{typ}}}{f L J_t}, & \mathcal{K}_n &= \frac{R_n^2}{\tau D_n^{\text{typ}}}, \\ \mathcal{K}_e &= \frac{L^2}{\tau D_e^{\text{typ}}}, & \mathcal{K}_p &= \frac{R_p^2}{\tau D_p^{\text{typ}}}, & \gamma_n &= \frac{\tau J_t}{R_n F C_n^{\max}}, & \gamma_e &= \frac{\tau J_t}{L F C_e^{\max}}, & \gamma_p &= \frac{\tau J_t}{R_p F C_p^{\max}}.\end{aligned}$$

The dimensionless system of equations will become

$$\frac{\partial \hat{J}_n}{\partial \hat{x}} = -a_n L \hat{J}_{n,tot}, \quad \text{on } 0 \leq \hat{x} \leq l_n, \quad (4.9a)$$

$$\hat{J}_n = -\lambda \Xi_n \frac{\partial \hat{\phi}_n}{\partial \hat{x}}, \quad \text{on } 0 \leq \hat{x} \leq l_n, \quad (4.9b)$$

$$\mathcal{K}_n \frac{\partial \hat{C}_n}{\partial \hat{t}} = \frac{1}{\hat{r}^2} \frac{\partial}{\partial \hat{r}} \left( \hat{r}^2 \hat{D}_n \frac{\partial \hat{C}_n}{\partial \hat{r}} \right), \quad \text{on } 0 \leq \hat{r} \leq \hat{r}_n, \quad (4.9c)$$

$$\frac{\partial \hat{J}_p}{\partial \hat{x}} = -a_p L \hat{J}_{p,tot}, \quad \text{on } 1 - l_p \leq \hat{x} \leq 1, \quad (4.9d)$$

$$\hat{J}_p = -\lambda \Xi_p \frac{\partial \hat{\phi}_p}{\partial \hat{x}}, \quad \text{on } 1 - l_p \leq \hat{x} \leq 1, \quad (4.9e)$$

$$\mathcal{K}_p \frac{\partial \hat{C}_p}{\partial \hat{t}} = \frac{1}{\hat{r}^2} \frac{\partial}{\partial \hat{r}} \left( \hat{r}^2 \hat{D}_p \frac{\partial \hat{C}_p}{\partial \hat{r}} \right), \quad \text{on } 0 \leq \hat{r} \leq \hat{r}_p, \quad (4.9f)$$

$$\frac{\partial \hat{J}_e}{\partial \hat{x}} = a L \hat{J}_{tot}, \quad \text{on } 0 \leq \hat{x} \leq 1, \quad (4.9g)$$

$$\hat{J}_e = -\Xi_e \sigma_e B(x) \left[ \frac{\partial \hat{\phi}_e}{\partial \hat{x}} - 2(1 - t^+) \frac{\partial \log \hat{C}_e}{\partial \hat{x}} \right], \quad \text{on } 0 \leq \hat{x} \leq 1, \quad (4.9h)$$

$$\frac{\mathcal{K}_e}{\gamma_e} \frac{\partial (\epsilon \hat{C}_e)}{\partial t} = -\frac{1}{\gamma_e} \frac{\partial \hat{N}_e}{\partial \hat{x}} + a L \mathcal{K}_e \hat{J}_{tot}, \quad \text{on } 0 \leq \hat{x} \leq 1, \quad (4.9i)$$

$$\hat{N}_e = -\hat{D}_e B(x) \frac{\partial \hat{C}_e}{\partial \hat{x}} + t^+ \mathcal{K}_e \gamma_e \hat{J}_e, \quad \text{on } 0 \leq \hat{x} \leq 1, \quad (4.9j)$$

$$\hat{J}_{n,int} = \hat{j}_{int} [\exp(\alpha_{a,int} \hat{\eta}_{int}) - \exp(-\alpha_{c,int} \hat{\eta}_{int})], \quad (4.9k)$$

$$\hat{J}_{n,sr} = \hat{j}_{sr} [\exp(\alpha_{a,sr} \hat{\eta}_{sr}) - \exp(-\alpha_{c,sr} \hat{\eta}_{sr})], \quad (4.9l)$$

$$\hat{\eta}_{int} = \lambda [\hat{\phi}_n - \hat{U}_n] - \hat{\phi}_e, \quad \text{at } \hat{r} = \hat{r}_n, \quad (4.9m)$$

$$\hat{\eta}_{sr} = \lambda [\hat{\phi}_n - \hat{U}_{sr}] - \hat{\phi}_e, \quad \text{at } \hat{r} = \hat{r}_n, \quad (4.9n)$$

with following boundary and initial conditions

$$\frac{\partial \widehat{C}_n}{\partial \widehat{r}} = 0, \quad \text{at } \widehat{r} = 0, \quad (4.10a)$$

$$-\widehat{D}_n \frac{\partial \widehat{C}_n}{\partial \widehat{r}} = \mathcal{K}_n \gamma_n \widehat{J}_{n,tot}, \quad \text{at } \widehat{r} = \widehat{r}_n, \quad (4.10b)$$

$$\frac{\partial \widehat{C}_p}{\partial \widehat{r}} = 0, \quad \text{at } \widehat{r} = 0, \quad (4.10c)$$

$$-\widehat{D}_p \frac{\partial \widehat{C}_p}{\partial \widehat{r}} = \mathcal{K}_p \gamma_p \widehat{J}_{p,tot}, \quad \text{at } \widehat{r} = \widehat{r}_p, \quad (4.10d)$$

$$\widehat{J}_n = \widehat{J}_{app}, \quad \widehat{J}_e = 0, \quad \widehat{N}_e = 0, \quad \widehat{\phi}_e = 0, \quad \text{at } \widehat{x} = 0, \quad (4.10e)$$

$$\widehat{J}_n = 0, \quad \widehat{J}_e = \widehat{J}_{app}, \quad \widehat{N}_e = 0, \quad \widehat{\phi}_e = 0, \quad \text{at } \widehat{x} = l_n, \quad (4.10f)$$

$$\widehat{J}_p = 0, \quad \widehat{J}_e = \widehat{J}_{app}, \quad \widehat{N}_e = 0, \quad \widehat{\phi}_e = 0, \quad \text{at } \widehat{x} = l - l_p, \quad (4.10g)$$

$$\widehat{J}_p = \widehat{J}_{app}, \quad \widehat{J}_e = 0, \quad \widehat{N}_e = 0, \quad \widehat{\phi}_e = 0, \quad \text{at } \widehat{x} = l, \quad (4.10h)$$

$$\widehat{C}_e = 1, \quad \widehat{C}_n = \widehat{C}_{n_i}, \quad \widehat{C}_p = \widehat{C}_{p_i}, \quad \text{at } \widehat{t} = 0. \quad (4.10i)$$

To simplify the notation in the analysis below, we opt to drop the hat sign from the dimensionless variables from now on. In the next section, an asymptotic reduction and averaging techniques will be used to reduce the full model (4.9)-(4.10) to a simpler time-dependent ODE system, where the evolution of some key averaged concentrations are tracked.

### 4.3.3 Asymptotic Reduction and Averaging

In the current study the objective is to develop a simplified dynamical model in the form of the system of ODEs, capable of tracking the evolution of key concentrations in the cell. Certain simplifying assumptions are to be made to develop a suitable mathematical model for our application. There are two important techniques used in this analysis that help in simplifying system (4.9)-(4.10). The first technique is asymptotic reduction which assumes that a certain parameter in the system takes a limiting value (either large or small), and the dynamics of the system are investigated in the vicinity of that limiting value by expanding each dependent variable in a Taylor series with respect to that parameter. Asymptotic reduction of the DFN model to the SP model has been considered by various authors [155–157], where different assumptions have been employed in each case to reduce the DFN model to a SP model. Marquis et al. [156] derives an asymptotic reduction of the DFN model to find a simplified SPM with electrolyte. This new model is shown to diverge from the DFN model for charging rates greater than 1C (C referring

to the capacity of the cell). Richardson et al. [157] extends this work with a different assumption for performing the asymptotic reduction, to generate a simple SP model that can perform better under higher charging rates. Brosa Planella et al. [155] extend this work to account for side reactions in the cell, a study that inspired the current investigation. However, certain assumptions in our work are different from work of Brosa Planella et al. Note that only the relevant equations in the system of equations (4.9) will be used in this analysis. In particular, electrolyte equations are not a matter of interest in this work and will not be used in this asymptotic analysis.

The second technique used in this analysis is the averaging of equations over their corresponding spatial domains in order to eliminate the spatial dependency. Some quantities in the DFN model, e.g. concentrations, depend on both time and space (note that in the DFN model "space" means both the microscale variable  $r$  and the macroscale variable  $x$ ) in contrast to our experimental data which is resolved only in time. Hence, averaging space-dependent quantities over their domains will eliminate the spatial dependency, and we will be left with a time-dependent model describing the evolution of lumped quantities. The aforementioned two techniques are used in conjunction. First, we start with the following assumptions needed for this analysis.

### Assumptions

- A1: The parameter  $\lambda$  is large enough, so that the Taylor expansion of state variables in the vicinity of small  $\lambda^{-1}$  remains a valid approximation. Note that the parameter  $\lambda$  is defined as the ratio of the characteristic change in the potential of the cell from low to high states-of-charge of the cell to the thermal voltage of the cell. At room temperature the thermal voltage is approximately  $25\text{mV}$ , and represents the characteristic scale of the overpotential at the interface in BV relation. When the scale of the characteristic change in the potential from low to high states-of-charge is large (in the order of magnitude of 1 Volt), the parameter  $\lambda$  remains large enough for the asymptotic analysis. This assumption refers to the physical case of small deviations from the equilibrium potential (small overpotentials), when the typical variation in the voltage of the electrodes is much larger than the thermal voltage. In this setting, the BV relations can be linearized.
- A2: The cathodic and anodic charge transfer coefficients for an interfacial reaction, cf. (4.9k)-(4.9l), are assumed to add up to one, namely,  $\alpha_a + \alpha_c = 1$ .
- A3: Side reactions in the cell are weak and in the order of  $\lambda^{-1}$  relative to the main intercalation/deintercalation reactions. This assumption allows us to capture the side reaction dynamics as corrections to the main reactions, as explained below.

- A4: The equilibrium potentials of the intercalation and side reactions are dependent on the concentration of the intercalated Lithium and of the Lithium participating in the side reactions, respectively. The local sensitivity of these equilibrium potentials to changes in concentrations is small, thus, these nonlinear relationships can be linearized in the neighbourhood of certain reference values of concentrations. Note that concentrations might exhibit large variations while the cell is in operation, however, if the local sensitivity of the equilibrium potential to concentrations is small (small local variations of equilibrium potentials with respect to concentrations), this simplification remains valid.

Note that the inherent assumption of the SP model states that the electrode particles behave in a similar manner, hence, one representative particle is sufficient to represent the microscale dynamics of the cell. This inherent assumption will be re-derived as part of the asymptotic analysis.

**Relaxation and Excitation Dynamics** Before delving into the asymptotic analysis of the DFN model, we discuss the fundamental sources of dynamics within the cell. The primary driver of dynamics in the cell is the excitation induced by the current applied to it. When the cell is brought to rest or an open-circuit state after an excitation period (charge/discharge), the system continues to evolve until it reaches an equilibrium state corresponding to the specific state-of-charge of the cell. The intensity of this phenomenon varies across different chemistries [161]. Consequently, we can distinguish two main regimes in the operation of the cell: excitation, representing the main process, and the relaxation dynamics of the cell in the absence of external influence. In our modeling effort, both excitation and relaxation dynamics will be captured by the mathematical model.

**Expansion of variables** In order to perform the asymptotic reduction, according to assumption A1 we expand each of the dependent variables in system (4.9)-(4.10) in the vicinity of  $\lambda^{-1} \approx 0$ . The expansion of variables in powers of  $\lambda^{-1}$  takes the form

$$\phi_n = \phi_{n,0} + \lambda^{-1}\phi_{n,1} + \dots,$$

where the subscripts 0 and 1 refer to the leading-order and first-order approximations, respectively. All other dependent variables in the system (4.9)-(4.10) are expanded in a similar manner. The expanded version of variables will be substituted into (4.9)-(4.10) to derive the leading-order and first-order approximation of equations.

**Electrode Potential** We start with the equations for the negative electrode potential. Averaging (4.9a) over the negative electrode domain, using the Gauss divergence theorem, and applying boundary conditions (4.10e) and (4.10f) we get

$$\begin{aligned} \frac{1}{l_n} \int_0^{l_n} \frac{\partial}{\partial x} J_n dx &= -\frac{1}{l_n} \int_0^{l_n} a_n L J_{n,tot} dx = 0 - J_{app}, \\ \bar{J}_{n,tot} &= \frac{J_{app}}{a_n L l_n}, \quad \bar{J}_{n,tot} := \frac{1}{l_n} \int_0^{l_n} J_{n,tot} dx, \end{aligned} \quad (4.11)$$

where  $\bar{J}_{n,tot}$  is the total current density averaged over the domain of the negative electrode. Hence, by averaging over the spatial domain the partial differential equation for the charge conservation in the solid phase reduces to an algebraic equation. This algebraic equation states that all the current applied to the anode during charge/discharge will be consumed at the solid-electrolyte interface for intercalation/deintercalation or side reactions, and acts as a constraint on the system of equations. Performing similar analysis for the positive electrode using (4.9d), (4.10g) and (4.10h) results in  $\bar{J}_{p,tot} = -\frac{J_{app}}{a_p L l_p}$ .

Asymptotic reduction of (4.9b) at the leading-order leads to

$$\frac{\partial \phi_{n,0}}{\partial x} = 0, \quad 0 < x < l_n. \quad (4.12)$$

Thus,  $\phi_{n,0} = \phi_{n,0}(t)$ , and the leading-order potential is homogeneous in space. Also, at the first-order, we have

$$J_{n0} = -\Xi_n \frac{\partial \phi_{n,1}}{\partial x}. \quad (4.13)$$

**Interfacial Kinetics** In the next step, we simplify the BV relations introduced in (4.9k) and (4.9l). For this purpose, we first linearize the BV relation, and second, we also linearize the relations between the equilibrium potentials and concentrations. Using assumption A1, the BV relation (4.9k) can be linearized as

$$J_{int} \cong j_{int}(\alpha_{a,int} + \alpha_{c,int})\eta_{int},$$

and similarly for (4.9l). Invoking assumption A2, they can be further simplified to

$$J_{int} = j_{int}\eta_{int}, \quad (4.14a)$$

$$J_{sr} = j_{sr}\eta_{sr}. \quad (4.14b)$$

Also, the overpotentials in the description of BV relations involve terms related to equilibrium potentials of intercalation and side reaction. As stipulated by assumption A4, the equilibrium potentials are

expanded as

$$U_n(C_n) = U_n|_{C_{n,0}} + \lambda^{-1} \frac{dU_n}{dC_n}|_{C_{n,0}} C_{n,1} + \dots, \quad (4.15a)$$

$$U_{sr}(C_{sr}) = U_{sr}|_{C_{sr,0}} + \lambda^{-1} \frac{dU_{sr}}{dC_{sr}}|_{C_{sr,0}} C_{sr,1} + \dots, \quad (4.15b)$$

where  $C_{n,0}$  and  $C_{sr,0}$  are the leading-order concentrations used as the reference states for linearization, and  $C_{n,1}$  and  $C_{sr,1}$  are the first-order approximations of concentrations i.e.  $C_n \cong C_{n,0} + \lambda^{-1}C_{n,1}$  and  $C_{sr} \cong C_{sr,0} + \lambda^{-1}C_{sr,1}$ . Hence, performing asymptotic reduction on BV relation (4.14a), and using (4.9m) and (4.15a), we get

$$J_{int,0} = (j_{int,0} + \lambda^{-1}j_{int,1}) \left( \lambda \left[ \phi_{n,0} + \lambda^{-1}\phi_{n,1} - U_n|_{C_{n,0}} - \lambda^{-1} \frac{dU_n}{dC_n}|_{C_{n,0}} C_{n,1} \right] - \phi_{e,0} - \lambda^{-1}\phi_{e,1} + \dots \right).$$

Thus, at the leading-order we have

$$J_{int,0} = \underbrace{j_{int,0} \left( \phi_{n,1} - \phi_{e,0} - \frac{dU_n}{dC_n}|_{C_{n,0}} C_{n,1} \right)}_{J_n^\dagger} + \underbrace{j_{int,1} \left( \phi_{n,0} - U_n|_{C_{n,0}} \right)}_{J_n^\ddagger}, \quad (4.16)$$

where  $J_n^\dagger$  and  $J_n^\ddagger$  represent (at the leading-order) the excitation and relaxation dynamics of the cell, respectively. This choice of excitation and relaxation dynamics in (4.16) is justified in two ways. First, as explained in Section 4.3.4, the second term is assumed to be zero in the study by Brosa Planella et al. [155]. However, their assumption leads to the lack of relaxation dynamics in the positive electrode. For this reason, the second term in (4.16) is assumed to take into account the relaxation dynamics of the cell. Second, the second term represents the deviation of the leading-order potential of the negative particle from its equilibrium potential. Setting this term to zero eliminates the relaxation dynamics of the negative particle. Equation (4.16) will be used in subsequent analysis for describing  $(\phi_{n,1} - \phi_{e,0})$ , as

$$\phi_{n,1} - \phi_{e,0} = \frac{J_n^\dagger}{j_{int,0}} + \frac{dU_n}{dC_n}|_{C_{n,0}} C_{n,1}. \quad (4.17)$$

Next, we focus our attention on the side reaction current density. Assuming that the side reactions in the cell are weak as stipulated by assumption A3, we postulate that  $j_{sr} = \lambda^{-1}\tilde{j}_{sr}$ , where  $\tilde{j}_{sr}$  is of a different order of magnitude than  $j_{sr}$ . This choice allows us to capture the side reaction effect at the order of  $\lambda^{-1}$  (smaller order of magnitude than the intercalation). At the leading-order, the side reaction is not observed due to this choice reflecting the assumption of weak side reactions. Therefore, performing

asymptotic reduction on (4.14b), and using (4.9n) and (4.15b), we get

$$J_{sr,0} = \lambda^{-1} \tilde{j}_{sr,0} \left( \lambda \left[ \phi_{n,0} - U_{sr} \Big|_{C_{sr,0}} \right] + \phi_{n,1} - \phi_{e,0} - \frac{dU_{sr}}{dC_{sr}} \Big|_{C_{sr,0}} C_{sr,1} \right), \quad (4.18)$$

and by rearranging this equation we get

$$J_{sr,0} = \tilde{j}_{sr,0} \left( \phi_{n,0} - U_{sr} \Big|_{C_{sr,0}} \right) + \lambda^{-1} \tilde{j}_{sr,0} \left( \phi_{n,1} - \phi_{e,0} - \frac{dU_{sr}}{dC_{sr}} \Big|_{C_{sr,0}} C_{sr,1} \right). \quad (4.19)$$

As already mentioned, the side reaction is only considered at the first-order approximation and vanishes at the leading-order. Hence, to eliminate the term of order  $\mathcal{O}(1)$  in (4.19), we set  $\phi_{n,0} = U_{sr} \Big|_{C_{sr,0}}$ . Therefore,  $U_{sr} \Big|_{C_{sr,0}}$  is also uniform in space (as is  $\phi_{n,0}$ ), which refines the underlying assumption of the SP model in which the behaviour of all solid particles is assumed uniform in space at the macroscale. Note that this assumption will impose the uniformity of  $U_n \Big|_{C_{n,0}}$  in space as well. Hence, starting with particles with the same initial concentrations, they will evolve in exactly same manner. Consequently, solving for one representative particle suffices to capture the dynamics of all solid particles. Note that quantities that are concentration-dependent will then be uniform in space, and can be easily averaged. Thus, the expression for the relaxation dynamic in (4.16) becomes (after averaging quantities)

$$\bar{J}_n^\dagger = j_{int,1} \left( U_{sr} \Big|_{C_{sr,0}} - U_n \Big|_{C_{n,0}} \right). \quad (4.20)$$

By substituting (4.17) into (4.19) for the side reaction current density, we get

$$J_{sr,0} = \lambda^{-1} \tilde{j}_{sr,0} \left( \frac{J_n^\dagger}{j_{int,0}} + \frac{dU_n}{dC_n} \Big|_{C_{n,0}} C_{n,1} - \frac{dU_{sr}}{dC_{sr}} \Big|_{C_{sr,0}} C_{sr,1} \right). \quad (4.21)$$

The averaged current density for the side reaction  $\bar{J}_{sr,0}$  can be computed by averaging (4.21) over the negative electrode domain. Note that the exchange current density is a function of the concentration at the interface, however, due to the inherent assumption in the SP model, where particles are uniform in space, the exchange current density will also be uniform in electrode domain. Also, the excitation current density averaged over the negative electrode domain becomes  $\bar{J}_n^\dagger = \frac{J_{app}}{a_n L l_n}$  according to (4.11). We can then average the expression (4.21) as

$$\bar{J}_{sr,0} = \frac{j_{sr,0}}{a L l_n j_{int,0}} J_{app} + j_{sr,0} \frac{dU_n}{dC_n} \Big|_{C_{n,0}} \bar{C}_{n,1} - j_{sr,0} \frac{dU_{sr}}{dC_{sr}} \Big|_{C_{sr,0}} \bar{C}_{sr,1}. \quad (4.22)$$

Equations (4.20) and (4.22) will be used in subsequent analysis.

**Conservation of Charge** The conservation of charge within the cell implies that the quantity of charge entering the cell is equivalent to the amount exiting the cell at each instance of time. This fundamental principle reflects the balance of electrical charge within the cell, ensuring that the net charge in the cell remains constant throughout the cell processes. The total current density on the negative electrode can be split into two components  $J_{n,tot} = J_{n,tot,0} + \lambda^{-1}J_{n,tot,1}$ , and  $J_{n,tot,0} = J_{n,int,0} + J_{sr,0}$ . At the leading-order  $J_{sr,0}$  vanishes (due to assumption A3), and the leading-order interfacial current density is given entirely by the intercalation current density,  $J_{n,tot,0} = J_{n,int,0}$ . This implies that at the leading-order, the dynamics are driven merely by intercalation (and there are no side reactions). The side reaction will enter as a correction term in the first-order approximation. Also, the intercalation current density at the leading-order can be split into two components, namely, the excitation ( $J_n^\dagger$ ) and relaxation dynamics ( $J_n^\ddagger$ ). Hence, the total current density on the negative electrode becomes  $J_{n,tot} = J_n^\dagger + J_n^\ddagger + \lambda^{-1}(J_{int,1} + J_{sr,1})$ . A similar analysis for the positive electrode can be performed, yielding  $J_{p,tot} = J_p^\dagger + J_p^\ddagger$ . Note that in the positive electrode there is no side reaction, and hence the correction to intercalation process is absent for this electrode.

The Li concentration on the interface of the electrode particle ( $r = 1$ ) is homogeneous over the electrode spatial domain due to the macroscale uniformity of electrode particles assumed in the SP model. Hence the total current density is uniform over space, and is equal to its average value. Averaging each of these relations over the corresponding electrode domains, we get  $\bar{J}_{n,tot} = \bar{J}_n^\dagger + \bar{J}_n^\ddagger + \lambda^{-1}(\bar{J}_{int,1} + \bar{J}_{sr,1})$ , and  $\bar{J}_{p,tot} = \bar{J}_p^\dagger + \bar{J}_p^\ddagger$ . It is also known that the total current density driven by the excitation dynamics in each electrode is proportional to the applied current density as  $\bar{J}_n^\dagger = \frac{J_{app}}{a_n L l_n}$ , and  $\bar{J}_p^\dagger = -\frac{J_{app}}{a_p L l_p}$ . For the conservation of charge to hold in the cell, the total charge flux in the cell must be zero, namely,  $\bar{J}_{n,tot} l_n + \bar{J}_{p,tot} l_p = 0$ . This implies that at the leading order, the current densities driven by the relaxation dynamics for the positive and negative electrodes should interact as  $\bar{J}_p^\ddagger = -\frac{l_n}{l_p} \bar{J}_n^\ddagger$ , and at the first order approximation as  $\bar{J}_{sr,1} = -\bar{J}_{int,1}$ .

With this definition of relaxation dynamics for negative and positive electrodes interfacial current density, the total charge in the cell is conserved. We note that the first-order approximation terms in the negative electrode serve as a correction factor to the intercalation process occurring at the leading-order.

**Transport of Lithium in Particles** We perform asymptotic analysis and averaging on microscale equations of electrode particles to describe the evolution of concentration of intercalated Li. Introducing the asymptotic expansion in (4.9c) and using the boundary conditions in (4.10a) and (4.10b), followed

by averaging over the spherical domain, gives at the leading-order (note the boundary condition at  $r_n = 1$ )

$$\int_0^{r_n} \mathcal{K}_n \frac{\partial C_{n,0}}{\partial t} r^2 dr = \int_0^{r_n} \frac{1}{r^2} \frac{\partial}{\partial r} \left( r^2 D_{n,0} \frac{\partial C_{n,0}}{\partial r} \right) r^2 dr, \quad t \geq 0, \quad (4.23)$$

with the boundary conditions

$$\begin{aligned} \frac{\partial C_{n,0}}{\partial r} &= 0, & \text{at } r = 0, \\ -D_{n,0} \frac{\partial C_{n,0}}{\partial r} &= \mathcal{K}_n \gamma_n J_{n,int,0}, & \text{at } r = r_n. \end{aligned} \quad (4.24)$$

Applying the Gauss divergence theorem, the average rate of growth of concentration at the leading-order is obtained as the net flux out of the boundary, hence

$$\frac{d\bar{C}_{n,0}}{dt} = \frac{\gamma_n}{r_n} \bar{J}_{n,int,0} = \frac{\gamma_n}{r_n} (\bar{J}_n^\dagger + \bar{J}_n^\ddagger) = \frac{\gamma_n}{r_n} \left( \frac{J_{app}}{a_n L l_n} + \bar{J}_n^\ddagger \right), \quad \text{where } \bar{C}_{n,0} = \int_0^{r_n} C_{n,0} r^2 dr. \quad (4.25)$$

On the other hand, at the first-order approximation we get

$$\int_0^{r_n} \mathcal{K}_n \frac{\partial C_{n,1}}{\partial t} r^2 dr = \int_0^{r_n} \frac{1}{r^2} \frac{\partial}{\partial r} \left( r^2 D_n \Big|_{C_{n,0}} \frac{\partial C_{n,1}}{\partial r} + r^2 D'_n \Big|_{C_{n,0}} C_{n,1} \frac{\partial C_{n,0}}{\partial r} \right) r^2 dr, \quad t \geq 0, \quad (4.26)$$

with the boundary conditions

$$\begin{aligned} \frac{\partial C_{n,1}}{\partial r} &= 0, & \text{at } r = 0, \\ \mathcal{K}_n \gamma_n J_{int,1} &= - \left( r^2 D_n \Big|_{C_{n,0}} \frac{\partial C_{n,1}}{\partial r} + r^2 D'_n \Big|_{C_{n,0}} C_{n,1} \frac{\partial C_{n,0}}{\partial r} \right), & \text{at } r = r_n. \end{aligned} \quad (4.27)$$

Note that the boundary condition on the interface of the electrode particle is computed using  $J_{int,1}$ .

Applying the boundary conditions and the Gauss divergence theorem, and knowing that  $J_{int,1} = -J_{sr,0}$ , we obtain

$$\frac{d\bar{C}_{n,1}}{dt} = \frac{\gamma_n}{r_n} \bar{J}_{int,1} = - \frac{\gamma_n}{r_n} \bar{J}_{sr,0}, \quad \text{where } \bar{C}_{n,1} = \int_0^{r_n} C_{n,1} r^2 dr. \quad (4.28)$$

Noting that  $\bar{C}_n \approx \bar{C}_{n,0} + \lambda^{-1} \bar{C}_{n,1}$ , the growth rate of Li concentration in the negative electrode is governed by

$$\frac{d\bar{C}_n}{dt} = \frac{\gamma_n}{r_n} \left( \frac{J_{app}}{a_n L l_n} + \bar{J}_n^\ddagger - \lambda^{-1} \bar{J}_{sr,0} \right), \quad (4.29)$$

where the expression for  $\bar{J}_{sr,0}$  is computed in (4.22).

A similar analysis can be performed for the positive particle. Introducing the asymptotic expansion in (4.9f) and using the boundary conditions (4.10c) and (4.10d), followed by averaging over the spherical

domain gives at the leading-order we get

$$\frac{d\bar{C}_{p0}}{dt} = \frac{\gamma_p}{r_p} \bar{J}_{p,int,0} = \frac{\gamma_p}{r_p} (\bar{J}_p^\dagger + \bar{J}_p^†), \quad \text{where } \bar{C}_{p0} = \int_0^{r_p} C_{p0} r^2 dr. \quad (4.30)$$

**Conservation of Lithium** As the total inventory of Lithium in the cell is conserved, Li assumed to occur in four different phases (anode intercalation, anode side reaction, electrolyte, and cathode solid phase) such that the corresponding rates of change should add up to zero, namely,

$$l_n \frac{d}{dt} \bar{C}_n(t) + l_n \frac{d}{dt} \bar{C}_{sr}(t) + l \frac{d}{dt} \bar{C}_e(t) + l_p \frac{d}{dt} \bar{C}_p(t) = 0, \quad (4.31)$$

where  $A$  denotes the cross-sectional area of the electrode. This normalization condition should be satisfied by the derived system of equations. However, the computation of  $\bar{C}_e(t)$  necessitates information about the concentration gradient at the boundary (after asymptotic reduction and averaging of (4.9g)), which is absent in the time-dependent model. Also, the amount of Lithium in the electrolyte is always conserved as noted in [155], meaning that  $\frac{d}{dt} \bar{C}_e(t) = 0$ . This implies that the Li ions will enter the electrolyte at the same rate that they exit the electrolyte phase in different domains of the cell. Referring to (4.29) and (4.30), we conclude that the side reaction dynamic becomes

$$\frac{d\bar{C}_{sr,1}}{dt} = \frac{\gamma_n}{r_n} \bar{J}_{sr,0}, \quad (4.32)$$

in order to retain the Li conservation in the cell.

**Dynamical Model** The concentration evolution in time of the two key averaged concentrations in the cell can be computed as

$$\begin{aligned} \frac{d\bar{C}_n}{dt} &= \frac{\gamma_n}{r_n} \left( \frac{J_{app}}{a_n L l_n} + \bar{J}_n^\dagger - \lambda^{-1} \bar{J}_{sr} \right), \\ \frac{d\bar{C}_{sr,1}}{dt} &= \frac{\gamma_n}{r_n} \bar{J}_{sr}, \end{aligned} \quad (4.33)$$

where  $\bar{J}_n^\dagger$  and  $\bar{J}_{sr}$  are obtained from (4.20) and (4.22), respectively. Before moving on to the formulation of the inverse problem, we need to prepare the ground by making the following comments about (4.33).

- As discussed in Section 4.3.1, upon consideration of the relations governing the intercalation and plating current densities in the BV equation (4.8), it becomes apparent that these equations are both dependent on the concentrations of the intercalated Li and Li in side reactions, namely,  $j_{sr,0} = j_{sr,0}(\bar{C}_n, \bar{C}_{sr})$  and  $j_{int,0} = j_{int,0}(\bar{C}_n, \bar{C}_{sr})$ , and overpotential  $\eta$ . In our SPM model-

ing framework, the need for solving for the potential profile and the overpotential is eliminated using equation (4.17). The dependency of the exchange current densities on concentrations is unknown, and needs to be determined using data-driven calibration strategies, cf. Section 4.4. As both exchange current densities are concentration dependent, we close the model by introducing a variable  $\omega = \omega(\bar{C}_n, \bar{C}_{sr}) = \frac{j_{sr,0}}{j_{int,0}}$  representing a constitutive relation describing the competition between the side reaction and intercalation exchange current densities. This relation controls how the total current density is split between side reaction and intercalation at each particular state of the cell.

- The concentrations  $C_n$  and  $C_{sr}$  introduced in the asymptotic analysis are expanded up to the first-order in  $\lambda^{-1}$ . Knowing that side reactions are not observed at the leading-order  $\bar{C}_{sr,0} = 0$ , we conclude that  $\bar{C}_{sr} = \bar{C}_{sr,1}$ . The concentration of the intercalated Lithium can then be expressed as  $\bar{C}_n = \bar{C}_{n,0} + \lambda^{-1}\bar{C}_{n,1}$ . Note that when we expand  $\bar{C}_{sr}$  in (4.33), only the first-order approximation of concentration  $\bar{C}_{n,1}$  appears in the expressions (with the leading term  $\bar{C}_{n,0}$  absent). In this case we make the assumption that  $\bar{C}_{n,1} = \zeta\bar{C}_n$  in order to close the mathematical model, where  $\zeta$  is a scalar parameter,  $0 < \zeta \ll 1$ . Note that this assumption is not true, as the parameter  $\zeta$  could be concentration-dependent. However, in order to close the mathematical model we opt to simplify the expression to reduce the computational complexity of the inverse modeling.
- The exchange current density in the cell is defined as the interfacial current density while the cell is in an equilibrium state, for both the forward and the backward interfacial reactions.  $j_{int,0}$  refers to the interfacial current density for Li intercalation or deintercalation on the negative particle surface at the leading-order (assuming no side reactions) while at equilibrium. While the cell is in an equilibrium state, the dynamics are driven by two physical mechanisms active at the electrode-electrolyte interface. The leading one is the Li intercalation/deintercalation at a specific rate ( $j_{int,0}$ ). The second mechanism are the side reactions occurring at the interface and represented by the first-order correction terms. This mechanism can be regarded as the interaction between the intercalated Li and plated Li. In mathematical terms,  $j_{int,1}$  represents the rate at which the intercalated Li is contributing to the growth of the plated Li phase, and vice versa,  $j_{sr,0}$  represents the rate at which the plated Li is contributing to the growth of intercalated Li. This interaction can be viewed as the forward/backward reactions between the two phases. As the local concentrations in each phase must remain stationary at equilibrium, we conclude that  $j_{int,1} = j_{sr,0}$ . We denote this exchange current density by  $j_{sr}$ , and note that the exchange current density is a function of concentration,  $j_{sr} = j_{sr}(\bar{C}_n, \bar{C}_{sr})$ .

Taking into account these considerations, and substituting (4.20) and (4.22) into the system of equations (4.33), we finally get

$$\begin{aligned} \frac{d\bar{C}_n}{dt} &= \underbrace{\frac{\gamma_n}{r_n a_n L l_n} [1 - \lambda^{-1} \omega] J_{app} + \frac{\gamma_n}{r_n} j_{sr} [U_{sr,0} - U_{n,0}] - \frac{\gamma_n}{r_n} j_{sr} U'_n \bar{C}_n}_{\text{Excitation Dynamics}} + \underbrace{\frac{\gamma_n}{r_n} \lambda^{-1} j_{sr} U'_{sr} \bar{C}_{sr}}_{\text{Relaxation Dynamics}}, \\ \frac{d\bar{C}_{sr}}{dt} &= \underbrace{\frac{\gamma_n}{r_n a_n L l_n} \omega J_{app}}_{\text{Excitation Dynamics}} + \underbrace{\frac{\gamma_n}{r_n} j_{sr} U'_n \zeta \bar{C}_n - \frac{\gamma_n}{r_n} j_{sr} U'_{sr} \bar{C}_{sr}}_{\text{Relaxation Dynamics}}, \end{aligned} \quad (4.34)$$

where  $U_{sr,0}$  and  $U_{n,0}$  are scalar reference potentials. Note that the right-hand-side of this system consists of two parts corresponding to the relaxation dynamics and the excitation dynamics. The first term on the right-hand-side of each equation represents the excitation dynamics of the cell. The remaining terms are linear in concentrations and represent the relaxation dynamics of the cell. Thus, this simplified model is capable of both taking into account the relaxation when excitation is absent ( $J_{app} = 0$ ), and also to track the dynamics of the cell when the excitation is present. This concludes the derivation of the ODE model.

#### 4.3.4 Comparison to SPMe+SR Model

This modeling framework is inspired by the SPMe+SR model of Brosa Planella et al. [155]. However, certain assumptions in our modeling approach differ from their work to better suit our specific configuration, particularly in tracking time-dependent concentrations without spatial resolution. After careful consideration of the SPMe+SR model, it is evident that this model has the following drawbacks.

1. A one-sided BV relation is used for modeling plating in the cell, with one exponential term in the corresponding expression. As the output of the exponential term is always positive, the current density of Li plating at the solid-electrolyte interface is always negative. This implies that the model is only capable of predicting Li plating (and not stripping). As noted by Sahu et al. [158], a two-sided BV relation must be used to account for both plating and stripping in the cell. In our framework, we have used a two-sided BV relation in (4.9) to prevent this issue.
2. Once averaged over the spatial domain, the model fails to take into account the relaxation dynamics for the positive electrode, as evidenced by Equations (23)-(25) in [155]. While the space-averaged model adequately accounts for Lithium conservation within the cell, it fails to capture the relaxation dynamics on the positive electrode, and its dynamics are solely driven by excitation.
3. On the negative electrode the terms corresponding to relaxation dynamics of plated Li and intercalated Li possess opposite signs (once the cell is set to rest), meaning that intercalated Li phase and plated Li phase will converge to equilibrium state in different directions. If Li in the interca-

lated phase becomes intercalated (deintercalated) in relaxation regime, the Li in plated phase gets stripped (plated). This contradicts the evidence from experimental data, cf. Section 4.2, in which the deintercalation process is accompanied by the stripping process in relaxation the regime.

These inconsistencies in the SPMe+SR model stem from two key factors:

1. The one-sided BV relation prevents the model from predicting Li stripping, as discussed earlier. The solution to this issue is to use a two-sided BV relation as in (4.9).
2. The relaxation dynamics of the SPMe+SR model are not consistent with the dynamics of the cell due to the underlying assumptions of the asymptotic reduction framework of Brosa Planella et al. [155].

In order to address the second issue (inconsistency in relaxation dynamics), we need to understand the source of this inconsistency in the SPMe+SR model. Referring to this model, if we assume there is no side reaction in the cell, the interfacial current density for the side reaction becomes zero, and hence, the intercalated Li dynamics will only be driven by excitation. In other words, the relaxation dynamics of the Li in negative electrode particles is only accounted for when a side reaction is present, and it is indeed in the reverse direction to the side reaction. In simpler terms, the relaxation dynamics of the Li in the negative electrode is dependant on the side reaction dynamics and this dependence is also observed for the Li dynamics in the positive electrode (no side reaction on the positive electrode results in no relaxation dynamics for Li in positive electrode). This dependency of the relaxation dynamics on the presence of a side reaction is the source of the inconsistency.

This inconsistency arises due to the fact that the relaxation dynamics is not accounted for in the leading-order terms of the interfacial current density (recall that leading-order terms refer to vanishing side reaction, cf. Assumption A3). Specifically, Brosa Planella et al. [155] assume that  $\phi_{n,0} = U_n|_{C_{n,0}}$ . Consequently, the second term on the right-hand side of Equation (4.16) vanishes, refining the underlying assumption of the SP model that all particles exhibit uniform behaviour in space (as  $\phi_{n,0}$  is spatially uniform). We elucidate how this assumption leads to loss of relaxation dynamics at the leading order.

In our modeling framework, we decompose the intercalation process at the leading-order into two components, capturing both the excitation and relaxation dynamics of the cell. This formulation ensures that both dynamics are present in the space-averaged model, and that the relaxation dynamics is independent of the presence of side reactions in the cell. We highlight that failure to include relaxation dynamics terms will result in the space-averaged model to exhibit non-trivial behavior only when a current is applied

to the cell. To achieve that, we relax the assumption that  $\phi_{n,0} = U_n|_{C_{n,0}}$ , and introduce the relaxation dynamics as the second term on the right-hand side in (4.16). In order to refine the inherent assumption of the SPM regarding the uniformity of particles in space, we introduce the assumption  $\phi_{n,0} = U_{sr}|_{C_{sr,0}}$ , as detailed in (4.19). While one might argue that this assumption neglects the relaxation dynamics of the side reaction, it is important to consider the relative magnitudes of the plated Li concentrations compared to the intercalated Li concentrations. The relaxation dynamics is primarily driven by the intercalation process rather than the side reaction. Consequently, this assumption remains valid and allows us to close the mathematical model. We also note that the aforementioned assumptions imply that the relaxation dynamics of the Li in the negative electrode is driven by the difference between the equilibrium potentials of the intercalated Li and plated Li.

By comparing our model to the one introduced by Sahu et al. [158], we remark that they introduced a Heaviside step function in the definition of the Li plating dynamics. The intention of this step function is to ensure that Li stripping process is stopped once the concentration of the plated Li becomes zero. Our mathematical model does not take this into account, however, it could be easily added to the model to ensure proper operation of the model at all concentrations. As we will see in Section 4.5.2, the results of model fitting to experimental data demonstrate the desired behaviour, meaning no stripping occurs below zero concentration. Thus, in the interest of simplicity, we have decided not to include the Heaviside function in our model.

#### 4.3.5 Linearizing Relaxation Dynamics

For simplicity, from now on, we will be using  $C_1$  and  $C_2$  to denote  $\bar{C}_n$  and  $\bar{C}_{sr}$ , respectively. Also, the hat sign on top of variables will be dropped for simplicity of notation. Aggregating all constants, the ODE system (4.34) becomes

$$\begin{aligned}\frac{dC_1}{dt} &= \alpha [1 - \lambda^{-1}\omega(C_1, C_2)] J_{app} + \beta_1 j_{sr}(C_1, C_2) + \beta_2 j_{sr}(C_1, C_2)C_1 + \beta_3 \lambda^{-1} j_{sr}(C_1, C_2)C_2, \\ \frac{dC_2}{dt} &= \alpha\omega(C_1, C_2)J_{app} + \beta_4 j_{sr}(C_1, C_2)C_1 - \beta_3 j_{sr}(C_1, C_2)C_2,\end{aligned}\tag{4.35}$$

where  $j_{sr} = j_{sr}(C_1, C_2)$ ,  $\omega = \omega(C_1, C_2)$ ,  $\alpha \in \mathbb{R}$ , and  $\beta_i \in \mathbb{R}$ ,  $i = 1, \dots, 4$ . As can be observed, the system of equations (4.35) has many unknown parameters (five scalar parameters and two functions), which makes the inverse modeling formulation complicated to solve, as discussed in Section 4.4. Also, both the relaxation and the excitation dynamics components of the mathematical model are nonlinear, adding to the complexity of the inverse problem. As both the relaxation part and the excitation part of the model are functions of the exchange current densities, one needs to solve the inverse problem by

matching the model output against the experimental data for the entire charge/discharge cycle, fitting all unknown parameters and constitutive relation simultaneously. The resulting infinite-dimensional optimization problem is therefore very difficult to solve. One simplifying assumption can break this problem down into two simpler sub-problems. When the cell is excited, specifically through high charge/discharge rates, the contribution of excitation dynamics is much larger than the relaxation dynamics portion. Thus, the problem can be segmented into two parts as follows: (i) solve the inverse problem for the relaxation dynamics when the excitation is zero (eliminating the excitation part from the equations), and (ii) solve the inverse problem for the full model when the cell is excited (with the relaxation part calibrated in step (i)). This formulation will break the inverse problem into two separate sub-problems, each involving a smaller number of unknown parameters, hence decreasing the overall computational complexity. It has however one caveat, namely, the relaxation dynamics part is also a function of the exchange current density (which in turn is a function of concentration). Calibrating the relaxation dynamics first requires finding an optimal form of the constitutive relation  $j_{sr}(C_1, C_2)$ , which will then be used for the excitation dynamics. However, we know that the excitation dynamics plays a stronger role in determining the behavior of the system, and hence, the constitutive relation needs to be determined from the excitation dynamics. This brings us to another simplifying assumption. When the cell is not excited, changes in concentrations are small in comparison to when the cell is excited. This means that the concentrations will exhibit small changes with respect to some reference state, and accordingly, the change in the exchange current density  $j_{sr}$  is also negligible. Therefore, the second assumption is to linearize the relaxation dynamics part around a reference state of the cell. We thus define  $C_1 = \widehat{C}_1 + C'_1$ ,  $C_2 = \widehat{C}_2 + C'_2$ , and linearize the constitutive relation as  $j_{sr} \approx \widehat{j}_{sr}(\widehat{C}_1, \widehat{C}_2) + \frac{\partial j_{sr}}{\partial C_1} \Big|_{\widehat{C}_1} (C_1 - \widehat{C}_1) + \frac{\partial j_{sr}}{\partial C_2} \Big|_{\widehat{C}_2} (C_2 - \widehat{C}_2)$ . Note that  $\widehat{C}_1$  and  $\widehat{C}_2$  denote a reference state of concentrations and deviations from the reference state  $\widehat{C}_1$  and  $\widehat{C}_2$  are small. We substitute these equations into the relaxation portion of equation (4.35), aggregate all constants and after eliminating high-order terms, we get (the constants are again named as  $\beta$ , however, these are different constants than before)

$$\begin{aligned} \frac{dC_1}{dt} &= \beta_1 + \beta_2 C_1 + \lambda^{-1} \beta_3 C_2, \\ \frac{dC_2}{dt} &= \beta_4 C_1 - \beta_3 C_2, \end{aligned} \tag{4.36}$$

for the relaxation dynamics of the cell. Therefore, with this linearization, the full model takes the form (in vector notation)

$$\begin{aligned} \frac{d}{dt}\mathbf{C}(t) &= \mathbf{AC}(t) + \mathbf{B} + \mathbf{F}(J_{app}(t)), \\ \mathbf{C}(0) &= \mathbf{C}_0, \\ \mathbf{C}(t) &= \begin{bmatrix} C_1(t) \\ C_2(t) \end{bmatrix}, \\ \mathbf{B} &= \begin{bmatrix} \beta_1 \\ 0 \end{bmatrix}, \\ \mathbf{A} &= \begin{bmatrix} \beta_2 & \lambda^{-1}\beta_3 \\ \beta_4 & -\beta_3 \end{bmatrix}, \\ \mathbf{F} &= \begin{bmatrix} \alpha [1 - \lambda^{-1}\omega] J_{app} \\ \alpha\omega J_{app} \end{bmatrix}, \end{aligned} \tag{4.37}$$

where  $\boldsymbol{\beta} = [\beta_1, \beta_2, \beta_3, \beta_4] \in \mathbb{R}^4$  are the parameters of the relaxation dynamics, and  $\omega = \omega(C_1, C_2)$  and  $\alpha \in \mathbb{R}$  are the unknown parameters and functions for the excitation dynamics of the cell. There are five scalar parameters and one constitutive relation given in terms of a function of two variables to be determined using inverse modeling. It is notable that the concentrations of different Li phases obtained from NMR spectroscopy experiments do not have a physical unit due to the nature of this methodology and the complexities of the computational post-processing of its data. Hence, it is impossible to match the concentrations of the physical model i.e.,  $C_1(t)$  and  $C_2(t)$ , to the Li content obtained from NMR spectroscopy. The inverse modeling approach will need to be designed to account for the conversion between physical variables in the model and the experimental quantities. The parameters of the model will be tuned from the experimental data, which automatically takes care of this conversion between variables and experimental quantities.

#### 4.4. Inverse modeling

The system of equations in (4.37) is not closed due to the dependence of  $\omega$  on state variables, which is unknown. To address this challenge, one can explore the relationship between  $\omega$  and the two state variables  $C_1$  and  $C_2$  through a data-driven calibration technique. In this methodology, the function  $\omega(C_1, C_2)$  can be determined through either parametric or non-parametric studies. In a parametric study, the functional form describing the dependence of  $\omega$  on the state variables can be identified using data-driven techniques of system identification. In this case, the functional form is assumed and its parameters are calibrated

via data-driven calibration techniques. Conversely, in a non-parametric study, the relationship can be inferred without explicitly assuming a functional form describing how the constitutive relation  $\omega$  depends on the state variables. The only assumptions imposed on the constitutive relation are the regularity of the functional and the behaviour of the functional on the boundaries of the domain. The latter technique is superior, as it removes the assumptions about the underlying functional form of the constitutive relation. In the current investigation, our focus will be on the latter approach.

The inverse problem will be defined as follows: given a set of time-dependent measurements of state variables,  $\tilde{C}_1(t)$  and  $\tilde{C}_2(t)$ , within the time window  $t \in [0, T]$ , cf. Figure 4.2, we seek to reconstruct the constitutive relation  $\omega = \omega(C_1, C_2)$  such that the solution to the ODE system (4.37) will best fit the experimental measurements. Note that in this formulation, no *a priori* assumption regarding the functional form of the constitutive relation is made other than its regularity and behavior for limiting values of the state variables, and we seek to find a non-parametric dependence of the constitutive relation on the state variables. The dynamics of the system is split into two parts: (i) the relaxation dynamics and (ii) the excitation dynamics. In Section 4.4.1 we present the result of formulation of the inverse model for relaxation dynamics, whereas the details of the formulation are deferred to Appendix C.1 due to the similarity of the framework to the excitation dynamics part. In Section 4.4.2 we formulate the computational framework for optimal reconstruction of the excitation dynamics. Finally, in Section 4.4.3 a more robust optimization framework for optimal reconstruction is introduced.

#### 4.4.1 Relaxation Dynamics

In this section, we aim to calibrate model (4.37) for the relaxation dynamics only. When the cell is set to rest, the applied current is zero, and the excitation term  $\mathbf{F}(J_{app}(t))$  on the right-hand-side of the model vanishes. Hence, the problem reduces to finding  $\beta$  using an inverse modeling approach and one can formulate a suitable inverse model to calibrate each of the parameters using cell data by minimizing a

cost functional  $\mathcal{J}_1 : \mathbb{R}^4 \rightarrow \mathbb{R}$  as

$$\begin{aligned}\mathcal{J}_1(\boldsymbol{\beta}) &= \frac{1}{2} \int_0^T \left| \mathbf{W} \mathbf{r}(t; \boldsymbol{\beta}) \right|_2^2 dt, \\ \mathbf{r}(t; \boldsymbol{\beta}) &= \mathbf{C}(t; \boldsymbol{\beta}) - \widetilde{\mathbf{C}}(t), \\ \mathbf{C}(t; \boldsymbol{\beta}) &= \begin{bmatrix} C_1(t; \boldsymbol{\beta}) \\ C_2(t; \boldsymbol{\beta}) \end{bmatrix}, \\ \widetilde{\mathbf{C}}(t) &= \begin{bmatrix} \widetilde{C}_1(t) \\ \widetilde{C}_2(t) \end{bmatrix}, \\ \mathbf{W} &= \begin{bmatrix} 1 & 0 \\ 0 & \sqrt{w} \end{bmatrix},\end{aligned}\tag{4.38}$$

where  $\mathbf{W}$  is a weight matrix,  $T$  is the final time of the cycle,  $|\cdot|_2$  represents the Euclidean norm, and the dependence of the state variables ( $C_1$  and  $C_2$ ) on the parameters  $\boldsymbol{\beta}$  is governed by Eq. (4.37). As the typical magnitudes of the state variables differ by one order of magnitude, the weight matrix  $\mathbf{W}$  is designed to introduce a suitable normalization. Optimal parameter values can be found by solving the minimization problem

$$\bar{\boldsymbol{\beta}} = \arg \min_{\boldsymbol{\beta} \in \mathbb{R}^4} \mathcal{J}_1(\boldsymbol{\beta}).\tag{4.39}$$

For the purpose of solving this problem, a gradient-based optimization approach can be used, defined by the iterative procedure as

$$\begin{aligned}\boldsymbol{\beta}^{(n+1)} &= \boldsymbol{\beta}^{(n)} - \tau^{(n)} \nabla_{\boldsymbol{\beta}} \mathcal{J}_1(\boldsymbol{\beta}^{(n)}), \quad n = 1, 2, \dots, \\ \nabla_{\boldsymbol{\beta}} \mathcal{J}_1(\boldsymbol{\beta}^{(n)}) &= \left[ \frac{\partial}{\partial \beta_1} \mathcal{J}_1(\boldsymbol{\beta}^{(n)}) \quad \frac{\partial}{\partial \beta_2} \mathcal{J}_1(\boldsymbol{\beta}^{(n)}) \quad \frac{\partial}{\partial \beta_3} \mathcal{J}_1(\boldsymbol{\beta}^{(n)}) \quad \frac{\partial}{\partial \beta_4} \mathcal{J}_1(\boldsymbol{\beta}^{(n)}) \right],\end{aligned}\tag{4.40}$$

where  $n$  refers to the iteration number,  $\tau^{(n)}$  refers to the step length along the descent direction at each iteration, and  $\nabla_{\boldsymbol{\beta}} \mathcal{J}_1(\boldsymbol{\beta})$  represents the gradient of cost functional with respect to the each of the unknown parameters. Note that this optimization problem can be solved in two ways. First, the step length  $\tau^{(n)}$  could be computed once in each iteration for the gradient of the cost functional, referred to as the regular gradient descent technique. Second approach is to update each of the parameters one after another in each iteration of the algorithm, and a step length is to be computed for each of them, referred to as the coordinate descent technique. The regular gradient descent technique is used for this case. The mathematical details of computation of the gradient vector are deferred to Appendix C.1. The gradient of

cost functional is obtained as

$$\nabla_{\beta} \mathcal{J}_1 = \left[ -\int_0^T \mathbf{C}^{*\top} \mathbf{I}_0 dt \quad -\int_0^T \mathbf{C}^{*\top} \mathbf{I}_2 \widehat{\mathbf{C}} dt \quad -\int_0^T \mathbf{C}^{*\top} \mathbf{I}_3 \widehat{\mathbf{C}} dt \quad -\int_0^T \mathbf{C}^{*\top} \mathbf{I}_4 \widehat{\mathbf{C}} dt \right]. \quad (4.41)$$

Now that the gradient is computed, we can use the iterative scheme (4.40) to minimize the cost functional with respect to the parameters and find the optimal values of parameters. The computational framework is summarized in Algorithm 3. The model will be trained on the piece of each cycle that corresponds to the relaxation dynamics.

#### 4.4.2 Excitation Dynamics

In this section, we assume that the optimal parameter values of the linear dynamics corresponding relaxation dynamics are determined. Consequently, we would like to train a model that can predict the excitation dynamics of the cell using a nonlinear constitutive relation, via minimizing the mismatch between model predictions and experimental data. The nonlinear dynamics of the excitation consists of a constitutive relation  $\omega(C_1, C_2)$  (representing the competition between intercalation and plating), and a scalar parameter  $\alpha$ . Before introducing the optimization framework, we need to define two intervals on which the state variables are defined:

- $\mathcal{I} := \left[ C_1, C_2 \in \mathbb{R} \mid C_1 \in [C_1^\alpha, C_1^\beta], C_2 \in [C_2^\alpha, C_2^\beta] \right]$  is referred to as the identifiability interval, which is the region of state variables spanned by the solution of Eq. (4.37), note that this interval is a function of iterations of the iterative algorithm 3,
- $\mathcal{L} := \left[ C_1, C_2 \in \mathbb{R} \mid C_1 \in [C_1^a, C_1^b], C_2 \in [C_2^a, C_2^b] \right]$ , where  $C_1^a \leq C_1^\alpha, C_1^b \geq C_1^\beta, C_2^a \leq C_2^\alpha$  and  $C_2^b \geq C_2^\beta$ ; this will be the interval we seek to reconstruct the constitutive relation on, which is generally larger than the identifiability region, i.e.,  $\mathcal{I} \subseteq \mathcal{L}$ ; the aim is to reconstruct the constitutive relation on this larger interval than spanned by the solution of the ODE system in order to make it possible to reconstruct the constitutive relation on a fixed domain.

The constitutive relation defined over  $\mathcal{L}$  is considered to be an element of a Hilbert space  $\mathcal{X}$ . Note that the function  $\omega$  depends on two state variables which is an extension to the problems considered in [27, 37, 38, 162], in which the constitutive relation is a function of one state variable only. This will add another layer of complexity to the problem of identifying constitutive relation. The complexity arises in converting the directional derivative of the objective function (4.46) to its Riesz form by a change of variables in two dimensions, as will be explained below. Hence, to simplify the problem, we will assume

that the constitutive relation depending on two state variables has a separable form, i.e.,

$$\omega(C_1, C_2) = \omega_1(C_1) \cdot \omega_2(C_2). \quad (4.42)$$

Consequently, one can reconstruct each of these factors separately, and then merge the results. The functions  $\omega_1(C_1)$  and  $\omega_2(C_2)$ , and the parameter  $\alpha$  need to be identified from data by solving a suitable inverse problem to minimize the mismatch between the experimental and true measurements of the system by defining the cost functional  $\mathcal{J}_2 : \mathbb{R} \times \mathcal{X} \times \mathcal{X} \rightarrow \mathbb{R}$  as

$$\begin{aligned} \mathcal{J}_2(\alpha, \omega_1, \omega_2) &= \frac{1}{2} \int_0^T \left| \mathbf{W} \mathbf{r}(t; \alpha, \omega_1, \omega_2) \right|_2^2 dt, \\ \mathbf{r}(t; \alpha, \omega_1, \omega_2) &= \mathbf{C}(t; \alpha, \omega_1, \omega_2) - \widetilde{\mathbf{C}}(t), \\ \mathbf{C}(t; \alpha, \omega_1, \omega_2) &= \begin{bmatrix} C_1(t; \alpha, \omega_1, \omega_2) \\ C_2(t; \alpha, \omega_1, \omega_2) \end{bmatrix}, \end{aligned} \quad (4.43)$$

where the dependence of the state variables ( $C_1$  and  $C_2$ ) on the constitutive relation  $\omega$  is governed by Eq. (4.37). The optimal reconstructions of the constitutive relations are obtained by solving the minimization problem

$$[\bar{\omega}_1, \bar{\omega}_2, \bar{\alpha}] = \arg \min_{\omega_1 \in \mathcal{X}, \omega_2 \in \mathcal{X}, \alpha \in \mathbb{R}} \mathcal{J}_2(\alpha, \omega_1, \omega_2), \quad (4.44)$$

where  $\mathcal{X}$  is a suitable Hilbert function space where  $\omega_1$  and  $\omega_2$  belong to. Note that the cost functional  $\mathcal{J}_2(\alpha, \omega_1, \omega_2)$  is a function of two constitutive relations and a parameter. Hence, when solving the inverse problem, three parallel problems need to be solved simultaneously. For simplicity, these three sub-problems are decoupled and solved. In each problem, two of the unknowns are kept constant and the third one is optimized. For the purpose of solving this problem, a gradient-based optimization approach can be used with an iterative procedure as

$$\begin{aligned} \omega_1^{(n+1)} &= \omega_1^{(n)} - \tau_1^{(n)} \nabla_{\omega_1}^{\mathcal{X}} \mathcal{J}_2(\alpha^{(n)}, \omega_1^{(n)}, \omega_2^{(n)}) \quad n = 1, 2, \dots, \\ \omega_2^{(n+1)} &= \omega_2^{(n)} - \tau_2^{(n)} \nabla_{\omega_2}^{\mathcal{X}} \mathcal{J}_2(\alpha^{(n)}, \omega_1^{(n+1)}, \omega_2^{(n)}) \quad n = 1, 2, \dots, \\ \alpha^{(n+1)} &= \alpha^{(n)} - \tau_3^{(n)} \frac{\partial}{\partial \alpha} \mathcal{J}_2(\alpha^{(n)}, \omega_1^{(n+1)}, \omega_2^{(n+1)}) \quad n = 1, 2, \dots, \end{aligned} \quad (4.45)$$

where  $n$  refers to the iteration number,  $\tau_i^{(n)}$ ,  $i \in \{1, 2, 3\}$  refers to the step length along the descent direction at each iteration, and  $\nabla_{\omega_1}^{\mathcal{X}} \mathcal{J}_2(\alpha, \omega_1, \omega_2)$  and  $\nabla_{\omega_2}^{\mathcal{X}} \mathcal{J}_2(\alpha, \omega_1, \omega_2)$  represent the gradients of cost functional with respect to the each of the constitutive relations, and  $\frac{\partial}{\partial \alpha} \mathcal{J}_2(\alpha, \omega_1, \omega_2)$  is the partial derivative of the cost functional with respect to the unknown parameter. Note that relation (4.45) represents the steepest-descent optimization algorithm, however, in practice, one can use more sophisticated techniques

such as the conjugate-gradients method. The Polak-Ribiere conjugate-gradient formulation has been used for this study. In all cases, the key ingredient of the optimization algorithm is the information about the gradient of the cost functional with respect to the constitutive relation. Note that the constitutive relation  $\omega(C_1, C_2)$  is a continuous function of state variables over  $\mathcal{L}$ , hence the gradients  $\nabla_{\omega_1}^{\mathcal{X}} \mathcal{J}_2(\alpha, \omega_1, \omega_2)$  and  $\nabla_{\omega_2}^{\mathcal{X}} \mathcal{J}_2(\alpha, \omega_1, \omega_2)$  are infinite-dimensional sensitivities of the cost functional to the perturbations of these constitutive relations. In order to compute these gradients, adjoint sensitivity analysis is leveraged [37, 38, 162]. An application of this adjoint sensitivity analysis to reconstruction of constitutive relations in electrochemistry field can also be found in [27]. One needs to reconstruct each of the factors  $\omega_1(C_1)$  and  $\omega_2(C_2)$  in (4.42) as the elements of the Sobolev space  $H^1(\mathcal{L})$  to ensure the continuity of the reconstructed constitutive relation, thus, the gradient needs to be obtained with respect to the corresponding inner product. However, to simplify the derivation, we will first obtain the gradient in the space  $\mathcal{X}(\mathcal{I}) = L^2(\mathcal{I})$ , and we will use the results of this derivation to find the Sobolev gradient. Note that the following mathematical derivation focuses solely on the gradient of the cost functional with respect to  $\omega_1$ . The derivation of the gradient with respect to  $\omega_2$  and the partial derivative of the cost functional with respect to  $\alpha$  follow a similar process. In order to obtain convenient expression for the gradient, we begin by computing the Gateaux (directional) derivative with respect to perturbation of  $\omega_1$  as

$$\begin{aligned}\mathcal{J}'_2(\alpha, \omega_1, \omega_2; \omega'_1) &= \lim_{\epsilon \rightarrow 0} \epsilon^{-1} [\mathcal{J}_2(\alpha, \omega_1 + \epsilon \omega'_1, \omega_2) - \mathcal{J}_2(\alpha, \omega_1, \omega_2)] \\ &= \int_0^T (\mathbf{w} \mathbf{r}(t; \alpha, \omega_1, \omega_2))^{\top} \mathbf{C}'(\alpha, \omega_1, \omega_2; \omega'_1) dt, \\ \mathbf{C}'(\alpha, \omega_1, \omega_2; \omega'_1) &= \begin{bmatrix} C'_1(\alpha, \omega_1, \omega_2; \omega'_1) \\ C'_2(\alpha, \omega_1, \omega_2; \omega'_1) \end{bmatrix},\end{aligned}\tag{4.46}$$

where  $\mathbf{C}'(\alpha, \omega_1, \omega_2; \omega'_1)$  is the solution to the system of perturbation equations. In order to derive this system, the state variables are perturbed with respect to  $\omega_1$  as

$$\mathbf{C}(\alpha, \omega_1, \omega_2) = \widehat{\mathbf{C}}(\widehat{\alpha}, \widehat{\omega}_1, \widehat{\omega}_2) + \epsilon [\mathbf{C}'(\alpha, \omega_1, \omega_2; \omega'_1)] + \mathcal{O}(\epsilon^2).\tag{4.47}$$

The constitutive relations are perturbed with respect to  $\omega_1$  as (the arguments are dropped for brevity)

$$\begin{aligned}\omega_1 &= \widehat{\omega}_1 + \epsilon \left[ \omega'_1 + \frac{d\omega_1}{dC_1} C'_1 \right] + \mathcal{O}(\epsilon^2), \\ \omega_2 &= \widehat{\omega}_2 + \epsilon \left[ \frac{d\omega_2}{dC_2} C'_2 \right] + \mathcal{O}(\epsilon^2).\end{aligned}\tag{4.48}$$

Note that perturbation of one constitutive relation will affect both concentrations (as  $C_1$  and  $C_2$  are not decoupled). The perturbation of the constitutive relation takes the form

$$\omega = \hat{\omega}_1 \hat{\omega}_2 + \epsilon \left[ \hat{\omega}_2 \omega'_1 + \hat{\omega}_2 \frac{d\omega_1}{dC_1} C'_1 + \hat{\omega}_1 \frac{d\omega_2}{dC_2} C'_2 \right] + \mathcal{O}(\epsilon^2). \quad (4.49)$$

Substituting (4.47) and (4.49) into (4.37), and collecting terms proportional to  $\epsilon$ , we get the perturbation system of equations corresponding to  $\omega'_1$  as

$$\begin{aligned} \frac{dC'_1}{dt} &= \beta_2 C'_1 + \lambda^{-1} \beta_3 C'_2 - \hat{\alpha} \lambda^{-1} J_{app} \left[ \hat{\omega}_2 \omega'_1 + \hat{\omega}_2 \frac{d\omega_1}{dC_1} C'_1 + \hat{\omega}_1 \frac{d\omega_2}{dC_2} C'_2 \right] \\ \frac{dC'_2}{dt} &= \beta_4 C'_1 - \beta_3 C'_2 + \hat{\alpha} J_{app} \left[ \hat{\omega}_2 \omega'_1 + \hat{\omega}_2 \frac{d\omega_1}{dC_1} C'_1 + \hat{\omega}_1 \frac{d\omega_2}{dC_2} C'_2 \right] \end{aligned} \quad (4.50)$$

$$C'_1(\omega'_1)(0) = C'_2(\omega'_1)(0) = 0.$$

Following similar procedure the perturbation system of equations corresponding to  $\omega'_2$  and  $\alpha'$  will be obtained. In matrix form, we get the perturbed system of equations as

$$\frac{d}{dt} \mathbf{C}'(t) = \mathbf{A} \mathbf{C}'(t) + \mathbf{D} \mathbf{C}'(t) + \hat{\omega}_2 \hat{\alpha} \boldsymbol{\rho} \omega'_1, \quad (4.51a)$$

$$\mathbf{C}'(0) = \mathbf{0}, \quad (4.51b)$$

$$\mathbf{D} = \begin{bmatrix} -\hat{\alpha} \lambda^{-1} J_{app} \hat{\omega}_2 \frac{d\omega_1}{dC_1} & -\hat{\alpha} \lambda^{-1} J_{app} \hat{\omega}_1 \frac{d\omega_2}{dC_2} \\ \hat{\alpha} J_{app} \hat{\omega}_2 \frac{d\omega_1}{dC_1} & \hat{\alpha} J_{app} \hat{\omega}_1 \frac{d\omega_2}{dC_2} \end{bmatrix}, \quad (4.51c)$$

$$\boldsymbol{\rho} = \begin{bmatrix} -\lambda^{-1} J_{app} \\ J_{app} \end{bmatrix}. \quad (4.51d)$$

Note that the first term in the right-hand-side of the ODE (4.51a) is the linear sub-problem corresponding to the relaxation dynamics (cf. Eq. (4.36)), and the second and third terms correspond to the excitation dynamics. We will obtain one ODE system for the perturbation of each unknown. Also, in all scenarios of perturbation of  $\alpha$ ,  $\omega_1$  and  $\omega_2$  the matrix  $\mathbf{D}$  appears to be identical, with differences occurring in the definition of the third term in the right-hand-side of (4.51a). The directional derivative of the cost functional can be computed in a different manner than (4.46) by invoking the Riesz representation theorem to the directional derivatives in the functional space as

$$\mathcal{J}'_2(\alpha, \omega_1, \omega_2; \omega'_1) = \langle \nabla_{\omega_1}^{\mathcal{X}} \mathcal{J}_2, \omega'_1 \rangle_{\mathcal{X}(\mathcal{L})}, \quad (4.52)$$

and similarly for  $\mathcal{J}'_2(\alpha, \omega_1, \omega_2; \omega'_2)$ , where  $\langle \cdot, \cdot \rangle_{\mathcal{X}(\mathcal{L})}$  represents the inner product in the Hilbert space  $\mathcal{X}$  over  $\mathcal{L}$  interval. Note that the Riesz representer in a functional space will reduce to the partial derivative in

a finite-dimensional Euclidean space, namely,  $\mathcal{J}'_2(\alpha, \omega_1, \omega_2; \alpha') = \frac{\partial \mathcal{J}_2}{\partial \alpha} \cdot \alpha'$ . Assuming  $\mathcal{X}(\mathcal{L}) = L^2(\mathcal{L})$ , the directional derivative will be expressed in terms of the  $L^2$  inner product as

$$\mathcal{J}'_2(\alpha, \omega_1, \omega_2; \omega'_1) = \int_{C_1^a}^{C_1^b} \nabla_{\omega_1}^{L^2} \mathcal{J}_2 \cdot \omega'_1 ds. \quad (4.53)$$

Note that the Gateaux derivative (4.46) is not consistent with the Riesz form (4.53), as the expression for the perturbation of the constitutive relations is hidden in the perturbations of the state variables  $C'_1(\alpha, \omega_1, \omega_2; \omega'_1)$  and  $C'_2(\alpha, \omega_1, \omega_2; \omega'_1)$  in Eq. (4.46). Also, the integration variable in Gateaux form is time, whereas the Riesz form uses the state variable as the integration variable. In order to tackle the first issue (introducing an explicit dependence on the perturbation of the constitutive relation into the Gateaux differential, as in (4.53)), we will leverage adjoint analysis, in which an adjoint problem is defined in a judicious manner so that expression for directional derivative becomes consistent with its Riesz form (4.53). Whereas, to overcome the latter issue (inconsistency in integration variable) a change of variables is used.

We begin with adjoint analysis. We multiply (4.51) by the vector of adjoint variables  $\mathbf{C}^*(t) = [C_1^*(t), C_2^*(t)]^\top$ , and integrating in time, we obtain

$$\int_0^T \mathbf{C}^{*\top} \frac{d}{dt} \mathbf{C}' dt - \int_0^T \mathbf{C}^{*\top} \mathbf{A} \mathbf{C}' dt - \int_0^T \mathbf{C}^{*\top} \mathbf{D} \mathbf{C}' dt - \int_0^T \mathbf{C}^{*\top} \widehat{\omega}_2 \widehat{\alpha} \boldsymbol{\rho} \omega'_1 dt = 0. \quad (4.54)$$

Performing integration by parts for the first term and applying the initial conditions of the perturbation system (4.50), we get

$$-\mathbf{C}^{*\top}(T) \mathbf{C}'(T) + \int_0^T \frac{d}{dt} \mathbf{C}^{*\top} \mathbf{C}' dt + \int_0^T \mathbf{C}^{*\top} \mathbf{A} \mathbf{C}' dt + \int_0^T \mathbf{C}^{*\top} \mathbf{D} \mathbf{C}' dt + \int_0^T \mathbf{C}^{*\top} \widehat{\omega}_2 \widehat{\alpha} \boldsymbol{\rho} \omega'_1 dt = 0. \quad (4.55)$$

Factoring out  $\mathbf{C}'$ , we get

$$-\mathbf{C}^{*\top}(T) \mathbf{C}'(T) + \int_0^T \left[ \frac{d}{dt} \mathbf{C}^{*\top} + \mathbf{C}^{*\top} \mathbf{A} + \mathbf{C}^{*\top} \mathbf{D} \right] \mathbf{C}' dt + \int_0^T \mathbf{C}^{*\top} \widehat{\omega}_2 \widehat{\alpha} \boldsymbol{\rho} \omega'_1 dt = 0. \quad (4.56)$$

We define the adjoint system of equations in a judicious manner as

$$\begin{aligned} \frac{d}{dt} \mathbf{C}^*(t) + \mathbf{A}^\top \mathbf{C}^*(t) + \mathbf{D}^\top \mathbf{C}^*(t) &= \mathbf{w} \mathbf{r}(t; \omega_1, \omega_2), \\ \mathbf{C}^*(T) &= \mathbf{0}. \end{aligned} \quad (4.57)$$

Note that when performing adjoint analysis for system of equations with respect to perturbation of  $\omega_2$

and  $\alpha$ , the evolution of adjoint variables  $\mathbf{C}^*(t)$  is governed by exactly the same system of equations and terminal conditions and the difference is in how this information is used to determine the corresponding gradient. With this definition of the adjoint system, Eq. (4.56) becomes

$$\int_0^T [(\mathbf{w} \mathbf{r})^\top] \mathbf{C}' dt = - \int_0^T \mathbf{C}^{*\top} \widehat{\omega}_2 \widehat{\alpha} \boldsymbol{\rho} \omega'_1 dt. \quad (4.58)$$

Thus, the directional derivative with respect to  $\omega'_1$  becomes

$$\mathcal{J}'_2(\alpha, \omega_1, \omega_2; \omega'_1) = - \int_0^T \widehat{\omega}_2 \widehat{\alpha} \mathbf{C}^{*\top} \boldsymbol{\rho} \omega'_1 dt, \quad (4.59)$$

due to the choice of the source term in the adjoint system (4.57) so that the expression of Gateaux differential appears in the equation. Likewise, following similar procedure of adjoint analysis for  $\omega'_2$  and  $\alpha'$ , the directional derivatives with respect to each of these unknowns become

$$\mathcal{J}'_2(\alpha, \omega_1, \omega_2; \omega'_2) = - \int_0^T \widehat{\omega}_1 \widehat{\alpha} \mathbf{C}^{*\top} \boldsymbol{\rho} \omega'_2 dt, \quad (4.60a)$$

$$\mathcal{J}'_2(\alpha, \omega_1, \omega_2; \alpha') = - \int_0^T \widehat{\omega}_1 \widehat{\omega}_2 \mathbf{C}^{*\top} \boldsymbol{\rho} \alpha' dt, \quad (4.60b)$$

where

$$\boldsymbol{\rho} = \begin{bmatrix} (\widehat{\omega}^{-1} - \lambda^{-1}) J_{app} \\ J_{app} \end{bmatrix}.$$

As can be observed, the Gateaux differential (4.60a)-(4.60b) is expressed in terms of perturbation of the constitutive relation, which is consistent with Riesz form (4.53). However, the integration variable in relations (4.60a)-(4.60b) (time) is different than the integration variable in Riesz form (state variable). To make them consistent, a change of variables must be used, namely,

$$dt = \frac{dC_1}{\beta_1 + \beta_2 C_1 + \lambda^{-1} \beta_3 C_2 + \widehat{\alpha}(1 - \lambda^{-1} \widehat{\omega}) J_{app}} = \frac{dC_2}{\beta_4 C_1 - \beta_3 C_2 + \widehat{\alpha} \widehat{\omega} J_{app}}, \quad (4.61)$$

which is obtained by rearrangement of the forward model (4.37). This makes it possible to change the integration variable in (4.59) from time ( $dt$ ) to the state ( $dC_1$  and  $dC_2$ ), as required by the Riesz representation (4.53), as the mapping from time to state variable is unique,  $\mathcal{K} := \{\cup_{t \in [0, T]} [C_1(t), C_2(t)]\}$ . As the mapping from time to state variables is unique, the integral over the  $\mathcal{L}$  interval can be expressed as an

integral over the contour  $\mathcal{K}$ . Hence, applying this change of variables to (4.59) and (4.60b), we obtain

$$\begin{aligned}\mathcal{J}'_2(\alpha, \omega_1, \omega_2; \omega'_1) &= - \int_{C_1^\alpha}^{C_1^\beta} \frac{\hat{\omega}_2 \hat{\alpha} \mathbf{C}^{*\top} \boldsymbol{\rho}}{\beta_1 + \beta_2 C_1 + \lambda^{-1} \beta_3 C_2 + \hat{\alpha}(1 - \lambda^{-1} \hat{\omega}) J_{app}} \omega'_1 ds, \\ \mathcal{J}'_2(\alpha, \omega_1, \omega_2; \omega'_2) &= - \int_{C_2^\alpha}^{C_2^\beta} \frac{\hat{\omega}_1 \hat{\alpha} \mathbf{C}^{*\top} \boldsymbol{\rho}}{\beta_4 C_1 - \beta_3 C_2 + \hat{\alpha} \hat{\omega} J_{app}} \omega'_2 ds, \\ \mathcal{J}'_2(\alpha, \omega_1, \omega_2; \alpha') &= \left[ - \int_0^T \hat{\omega}_1 \hat{\omega}_2 \mathbf{C}^{*\top} \boldsymbol{\rho} dt \right] \cdot \alpha'.\end{aligned}\quad (4.62)$$

Note that  $\alpha'$  is independent of time and is taken out of integral. Hence, the  $L^2$  gradients and the partial derivative are computed as

$$\begin{aligned}\nabla_{\omega_1}^{L^2} \mathcal{J}_2 &= - \frac{\hat{\omega}_2 \hat{\alpha} \mathbf{C}^{*\top} \boldsymbol{\rho}}{\beta_1 + \beta_2 C_1 + \lambda^{-1} \beta_3 C_2 + \hat{\alpha}(1 - \lambda^{-1} \hat{\omega}) J_{app}}, \\ \nabla_{\omega_2}^{L^2} \mathcal{J}_2 &= - \frac{\hat{\omega}_1 \hat{\alpha} \mathbf{C}^{*\top} \boldsymbol{\rho}}{\beta_4 C_1 - \beta_3 C_2 + \hat{\alpha} \hat{\omega} J_{app}}, \\ \frac{\partial \mathcal{J}_2}{\partial \alpha} &= - \int_0^T \hat{\omega}_1 \hat{\omega}_2 \mathbf{C}^{*\top} \boldsymbol{\rho} dt.\end{aligned}\quad (4.63)$$

Above, we derived gradient expressions with respect to constitutive relations in the  $L^2$  functional space. However, as noted in earlier studies [37, 38, 162], these gradients are not a suitable choice for reconstruction of constitutive relations as they are generally discontinuous and are undefined outside the identifiability region  $\mathcal{I}$ . Thus, to ensure the regularity and the smoothness of the reconstructed relations over the domain of definition  $\mathcal{L}$ , we will redefine them in the  $H^1$  Sobolev space of functions of the concentrations  $C_1$  and  $C_2$  with square-integrable derivatives. A natural choice is to construct the Sobolev gradients for both constitutive relations by assuming  $\mathcal{X} = H^1(\mathcal{L})$ . Since the constitutive relation in the governing system (4.37) depends on the product  $\omega_1 \cdot \omega_2$ , an optimization formulation in which these two factors are determined independently as in (4.44) is underdetermined, because the mean of the product  $\omega_1 \cdot \omega_2$  can be changed by each of the factors, which can lead to numerical complications. We will therefore amend the formulation such that the mean value of one of the factors will be fixed (for example, at zero). One can achieve this by imposing hard constraints on the mean of the functions so that their mean stays stationary in the optimization framework. In this work, the mean of one of the factors is set to remain constant during the optimization process by ensuring the Sobolev gradients are defined such that they do not modify the mean. This will leave the first factor to capture the mean value of the entire constitutive relation. Also, the physical constraints of the problem imply that the constitutive relations should be bounded between zero and one. For such reasons, one is required to constrain the functions in order to ensure physically plausible solutions. In this framework, we do not impose any restrictions on the mean of the constitutive relation  $\omega$ , thus, the physical constraint is not guaranteed to be satisfied. Thus, two

functional spaces will be used in this framework for extending the  $L^2$  gradients to  $\mathcal{L}$  interval, namely,  $\mathcal{X} = H^1(\mathcal{L})$  and  $\mathcal{X} = H_0^1(\mathcal{L})$  (where the subscript 0 denotes a space of functions of zero mean). The  $H^1$  Sobolev space is endowed with the inner product as

$$\langle \nabla_{\omega_1}^{H^1} \mathcal{J}_2, \omega'_1 \rangle_{H^1} = \int_{C_1^a}^{C_1^b} \left( \nabla_{\omega_1}^{H^1} \mathcal{J}_2 \cdot \omega'_1 + l^2 \frac{d\nabla_{\omega_1}^{H^1} \mathcal{J}_2}{ds} \frac{d\omega'_1}{ds} \right) ds, \quad (4.64)$$

for computing the directional derivative  $\mathcal{J}'_2(\alpha, \omega_1, \omega_2; \omega'_1)$ , where  $0 < l < \infty$  is the length-scale parameter, controlling the intensity of smoothness of gradients. Setting this parameter to zero recovers the  $L^2$  inner product, cf. Eq. (4.53). A similar  $H^1$  inner product is also used for the computation of  $\mathcal{J}'_2(\alpha, \omega_1, \omega_2; \omega'_2)$  with the difference that  $\nabla_{\omega_2}^{H^1} \mathcal{J}_2$  is replaced with  $\mathbb{P}_0 \nabla_{\omega_2}^{H^1} \mathcal{J}_2$  to ensure the zero mean of the reconstructed function. The operator  $\mathbb{P}_0 : H^1 \rightarrow H_0^1$  represents the orthogonal projection on the subspace of functions with zero mean and is defined as  $\mathbb{P}_0 u = u - \bar{u}$ , where  $\bar{u}$  is the mean of the function over the domain. Here we assume that  $\omega'_1 \in H^1(\mathcal{L})$  and  $\omega'_2 \in H_0^1(\mathcal{L})$ . So by invoking the Riesz theorem, we obtain

$$\mathcal{J}'_2(\alpha, \omega_1, \omega_2; \omega'_1) = \langle \nabla_{\omega_1}^{L^2} \mathcal{J}_2, \omega'_1 \rangle_{L^2(\mathcal{L})} = \langle \nabla_{\omega_1}^{H^1} \mathcal{J}_2, \omega'_1 \rangle_{H^1(\mathcal{L})}, \quad (4.65)$$

and similarly for  $\mathcal{J}'_2(\alpha, \omega_1, \omega_2; \omega'_2)$ . Considering (4.64) and (4.65), and performing integration by parts with respect to  $s$ , we obtain

$$\int_{C_1^a}^{C_1^b} \nabla_{\omega_1}^{L^2} \mathcal{J}_2 \cdot \omega'_1 ds = \int_{C_1^a}^{C_1^b} \left( \nabla_{\omega_1}^{H^1} \mathcal{J}_2 \cdot \omega'_1 - l^2 \frac{d^2 \nabla_{\omega_1}^{H^1} \mathcal{J}_2}{ds^2} \omega'_1 \right) ds + \frac{d \nabla_{\omega_1}^{H^1} \mathcal{J}_2}{ds} \omega'_1 \Big|_{C_1^a}^{C_1^b}, \quad (4.66)$$

noting that the perturbations  $\omega'_1$  and  $\omega'_2$  are arbitrary. A similar analysis can be performed for perturbation with respect to  $\omega'_2$ . By imposing the Neumann boundary conditions on the Sobolev gradients, we obtain the following inhomogeneous elliptic boundary-value problems defining the smoothed gradients in the  $H^1$  and  $H_0^1$  space based on the  $L^2$  gradients as

$$\begin{aligned} \nabla_{\omega_1}^{H^1} \mathcal{J}_2 - l^2 \frac{d^2 \nabla_{\omega_1}^{H^1} \mathcal{J}_2}{ds^2} &= \nabla_{\omega_1}^{L^2} \mathcal{J}_2, & \text{on } \mathcal{L}, \\ \frac{d \nabla_{\omega_1}^{H^1} \mathcal{J}_2}{ds} &= 0, & \text{at } s = C_1^a, C_1^b, \end{aligned} \quad (4.67)$$

and

$$\begin{aligned} \nabla_{\omega_2}^{H_0^1} \mathcal{J}_2 - \frac{1}{C_2^b - C_2^a} \int_{C_2^a}^{C_2^b} \nabla_{\omega_2}^{H_0^1} \mathcal{J}_2 ds - l^2 \frac{d^2 \nabla_{\omega_2}^{H_0^1} \mathcal{J}_2}{ds^2} &= \nabla_{\omega_2}^{L^2} \mathcal{J}_2, & \text{on } \mathcal{L}, \\ \frac{d \nabla_{\omega_2}^{H_0^1} \mathcal{J}_2}{ds} &= 0, & \text{at } s = C_2^a, C_2^b. \end{aligned} \quad (4.68)$$

This framework ensures that the gradient of the cost functional with respect to  $\omega_2$  has a zero mean at each

step of the algorithm, hence, the mean of the function  $\omega_2$  remains unchanged during the iteration process. Note that the behaviour of the Sobolev gradients on the boundaries needs to be specified via suitable boundary conditions. The choice of the boundary condition is nontrivial. In this case, the homogeneous Neumann boundary condition is adopted which preserves the values of the derivatives of the functions  $\omega_1$  and  $\omega_2$  at the boundaries, but allows the gradient to modify their values at the boundary. Some other choices of boundary condition are possible based on the physics of the problem. For example, imposing homogeneous Dirichlet boundary conditions would preserve the values of  $\omega_1$  and  $\omega_2$  at the boundaries, but would make it possible to modify their derivatives. Also, extending the gradients to a Sobolev space can be seen as an extrapolation of gradients to the regions of the state space where the sensitivity information is not available, i.e., the  $L^2$  gradient vanishes identically [37]. The computational framework for the solution of optimization problems (4.40) and (4.45) is summarized in Algorithm 3. It is also notable that for solving the forward system (4.37) as part of the computational framework in Algorithm 3 throughout this study the MATLAB routine `ODE45` is used with a loose tolerance. As can be observed in Figure 4.1, the current applied to the cell is discontinuous, hence making the forward problem stiff. However, some analysis revealed that when the tolerance of the ODE solver is loose, the accuracy of the results is satisfactory as the step size of the ODE solver will be large and the effect of sharp changes in current profile will not be pronounced by the solver. On the other hand, using stiff ODE solvers requires very tight tolerances to be able to achieve the required accuracy from the algorithm. Hence, for the sake of saving computational time, the non-stiff solver (`ODE45`) with loose tolerance is used in this work.

#### 4.4.3 Problem with Aggregated Data

The computational framework outlined in Algorithm 3 could be utilized to train models for both relaxation and excitation dynamics based on a single cycle of the cell. In other words, each sequence of data  $\mathcal{D}_i, i \in \mathcal{C}, \mathcal{C} = \{\text{C3, C2, 1C, 2C, 3C}\}$ , could be used as the training data for optimal reconstruction of parameters and constitutive relations. In this scenario, the parameters and the constitutive relations would be adjusted to minimize the mismatch between predictions of the model and the experimental concentrations for a specific cycle. However, it is known that such models suffer from robustness issues, as the trained model tends to exhibit acceptable performance only over a limited range of cycles (C-rates) close to the cycle used for training, cf. Section 4.5.2. To enhance the robustness of the optimal reconstruction framework, one can train the models on a wider range of C-rates by concatenating different sequences of data, each corresponding to a particular C-rate,  $\mathcal{D}_t = \bigoplus_i \mathcal{D}_i, i \in \mathcal{C}$ . In this scenario, the cost functional would be defined as the sum of cost functionals for each sequence of data for relaxation dynamics as  $\mathcal{J}_1(\boldsymbol{\beta}; \mathcal{D}_t^{ocv}) = \sum_{i \in \mathcal{C}} \mathcal{J}_1(\boldsymbol{\beta}; \mathcal{D}_i^{ocv})$ , where  $\mathcal{J}_1(\boldsymbol{\beta}; \mathcal{D}_i^{ocv})$  denotes the

---

**Algorithm 3:** COMPUTATIONAL FRAMEWORK FOR OPTIMAL RECONSTRUCTION OF CONSTITUTIVE RELATIONS
 

---

**Input:**  $\beta^{(0)}, \alpha^{(0)}, \omega_1^{(0)}, \omega_2^{(0)}$  — Initial guesses for parameters and constitutive relations

$N$  — Maximum iteration number

$TOL$  — Tolerance

**Output:**  $\bar{\beta}, \bar{\alpha}, \bar{\omega}(C_1, C_2)$  — Optimally constructed parameters and constitutive relations

---

**Stage I:** Optimal reconstruction of  $\beta$ :

Initialization:

set  $n = 0$ ,

set  $\beta^{(0)}$  as initial guess,

**repeat**

- set  $n = n + 1$ ,
- solve forward problem (4.37) based on prior estimation of  $\hat{\beta}$  to obtain  $C_1(t; \beta^{(n-1)})$  and  $C_2(t; \beta^{(n-1)})$ , assuming  $J_{app} = 0$ ,
- solve adjoint problem (C.7) to obtain  $C_1^*(t; \beta^{(n-1)})$  and  $C_2^*(t; \beta^{(n-1)})$ ,
- compute gradient of cost functional with respect to parameters,  $\nabla_\beta \mathcal{J}_1$  via (4.41),
- determine step length  $\tau^{(n)}$  of optimization iterative scheme (4.40) via Brent's line search scheme as outlined in [163],
- compute the updated parameters for  $\beta^{(n)}$  via (4.40) as the posterior estimation of  $\hat{\beta}$ ,

**until**  $\frac{\mathcal{J}_1(\beta^{(n)})}{\mathcal{J}_1(\beta^{(n-1)})} < TOL$  or  $n > N$ ;

---

**Stage II:** Optimal reconstruction of  $\alpha, \omega_1$  and  $\omega_2$ :

Initialization:

set  $n = 0$ ,

set  $\beta = \bar{\beta}$ ,

set  $\alpha^{(0)}, \omega_1^{(0)}(C_1)$  and  $\omega_2^{(0)}(C_2)$  as initial guesses,

**repeat**

- set  $n = n + 1$ ,
- solve forward problem (4.37) to obtain  $C_1(t; \alpha^{(n-1)}, \omega_1^{(n-1)}, \omega_2^{(n-1)})$  and  $C_2(t; \alpha^{(n-1)}, \omega_1^{(n-1)}, \omega_2^{(n-1)})$ ,
- solve adjoint problem (4.57) to obtain  $C_1^*(t; \alpha^{(n-1)}, \omega_1^{(n-1)}, \omega_2^{(n-1)})$  and  $C_2^*(t; \alpha^{(n-1)}, \omega_1^{(n-1)}, \omega_2^{(n-1)})$ ,
- compute  $L^2$  gradients of cost functional with respect to constitutive relations,  $\nabla_{\omega_1}^{L^2} \mathcal{J}$  and  $\nabla_{\omega_2}^{L^2} \mathcal{J}$ , and  $\frac{\partial \mathcal{J}}{\partial \alpha}$  via (4.63),
- solve the boundary-value problems (4.67) and (4.68) to obtain Sobolev gradients of cost functionals  $\nabla_{\omega_1}^{H^1} \mathcal{J}$  and  $\nabla_{\omega_2}^{H^1} \mathcal{J}$ ,
- determine step length  $\tau^{(n)}$  of optimization iterative scheme (4.45) via Brent's line search scheme as outlined in [163],
- compute the updated relations for  $\alpha^{(n)}, \omega_1^{(n)}$  and  $\omega_2^{(n)}$  via (4.45),

**until**  $\frac{\mathcal{J}_2(\alpha^{(n)}, \omega_1^{(n)}, \omega_2^{(n)})}{\mathcal{J}_2(\alpha^{(n-1)}, \omega_1^{(n-1)}, \omega_2^{(n-1)})} < TOL$  or  $n > N$ ;

Compute  $\bar{\omega}(C_1, C_2) = \bar{\omega}_1^{(n)} \cdot \bar{\omega}_2^{(n)}$

---

cost functional computed by using  $\mathcal{D}_i^{ocv}$  as the experimental data. The cost functional for the excitation dynamics would be defined as  $\mathcal{J}_2(\alpha, \omega_1, \omega_2; \mathcal{D}_t^j) = \sum_{i \in \mathcal{C}} \mathcal{J}_2(\alpha, \omega_1, \omega_2; \mathcal{D}_i^j)$ , where  $j \in \{ch, dch\}$ . With this revised definition of cost functionals for optimization, the gradients need to be computed accordingly. Since the gradient is a linear operator, the gradient of the combined cost functional reduces to the sum of the gradients of cost functionals for each sequence of data  $\mathcal{D}_i$ . More precisely, for the relaxation dynamics we get  $\nabla_{\beta} \mathcal{J}_1(\beta; \mathcal{D}_t^{ocv}) = \sum_{i \in \mathcal{C}} \nabla_{\beta} \mathcal{J}_1(\beta; \mathcal{D}_i^{ocv})$ , and for the excitation dynamics  $\nabla_{\omega_1} \mathcal{J}_2(\alpha, \omega_1, \omega_2; \mathcal{D}_t^j) = \sum_{i \in \mathcal{C}} \nabla_{\omega_1} \mathcal{J}_2(\alpha, \omega_1, \omega_2; \mathcal{D}_i^j)$ , where  $j \in \{ch, dch\}$ , and similarly for  $\nabla_{\omega_2} \mathcal{J}_2(\alpha, \omega_1, \omega_2; \mathcal{D}_t^j)$  and  $\frac{\partial}{\partial \alpha} \mathcal{J}_2(\alpha, \omega_1, \omega_2; \mathcal{D}_t^j)$ . After the computation of the cost functionals and gradients for optimization, the remainder of the computational framework remains unchanged.

## 4.5. Results

In this section, we first present the results for the relaxation dynamics part of the model, as outlined in Section 4.4.1. Once the parameters  $\beta$  of the relaxation dynamics are determined, we solve the inverse problem to compute the optimal forms of the constitutive relations and parameters for the excitation dynamics, namely,  $\omega_1$ ,  $\omega_2$  and  $\alpha$ , using the parameters describing the relaxation dynamics obtained earlier, according to Section 4.4.2. Before doing so, one needs to validate the methodology proposed in Sections 4.4.1 and 4.4.2 for the gradients computed using the adjoint analysis. One can design a computational test that verifies the validity of all the steps involved, and hence the validity of the gradients computed using the proposed methodology. Also, the computational framework presented in Algorithm 3 is validated using synthetic data that is manufactured, in order to reconstruct some known constitutive relations from manufactured data. The results of computational tests are presented in Appendix C.2.

### 4.5.1 Relaxation Dynamics

The computational framework outlined in Stage I of Algorithm 3 is used to find optimal parameter values of the relaxation dynamics of the cell. The parameters to initialize the optimization algorithm are chosen as  $\beta^{(0)} = [-0.1, -0.1, -0.1, -0.1]$ ,  $N = 500$ , and  $TOL = 10^{-6}$ . The interval  $\mathcal{L}$  for the optimization framework is  $(C_1, C_2) \in [-0.5, 1.5] \times [-0.2, 0.5]$ . This choice has been made based on the magnitude of the state variables in different cycles. Also, the optimization framework with aggregated data, cf. Section 4.4.3, has been used here. In other words,  $\mathcal{D}_t = \bigoplus_i \mathcal{D}_i, i \in \mathcal{C}$  has been used as the training data. The relative decay of the cost functional for the iterative scheme, cf. (4.38), is presented in Figure 4.4. As can be observed, the cost functional value is decaying significantly relative to its initial value. The rate of decay is becoming slow at later iterations. The optimal solution found as the result of the iterative scheme

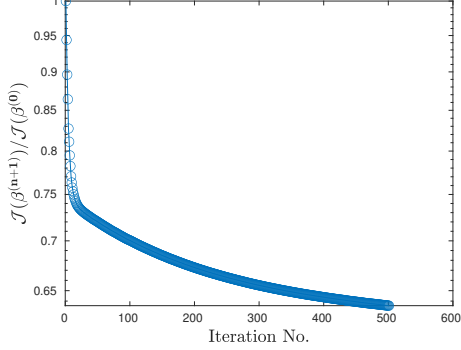


Figure 4.4: Cost functional history  $\mathcal{J}_1(\beta)$  relative to its initial value as a function of iteration number.

is  $\bar{\beta} \approx [0.85, -1.85, 0.55, -0.02]$ . According to (4.37), the matrices in system (4.36) become

$$\mathbf{B} = \begin{bmatrix} 0.85 \\ 0 \end{bmatrix}, \quad \mathbf{A} = \begin{bmatrix} -1.85 & 0.003 \\ -0.02 & -0.55 \end{bmatrix}. \quad (4.69)$$

Note that matrix  $\mathbf{A}$  has two real negative eigenvalues as  $\sigma(\mathbf{A}) = -1.85, -0.55$ . This implies that the linear part of the system corresponding to the relaxation dynamics of the cell has the form of a delay towards an equilibrium point, which is consistent with the behaviour of the cell at relaxation mode, cf. Figure 4.2. The results of predicting the evolution of concentrations for different cycles of the cell using the optimal parameter values are shown in Figure 4.5. As can be observed, the model performs relatively well on a wide range of C-rates. The optimal parameter values for the relaxation dynamics will be used when solving the optimization problem for excitation dynamics.

#### 4.5.2 Excitation Dynamics

In this section, we present the results of the inverse modeling approach presented in Algorithm 3 using the machinery developed in Section 4.4.2. Note that in this section, the parameters of the relaxation dynamics are assumed known, and are given by the results of Section 4.5.1. First, we begin by fitting the unknown constitutive relations and parameter in (4.37) describing the excitation dynamics to the data corresponding to individual cycles, namely,  $\mathcal{D}_i^j, i \in \mathcal{C}, j \in \{ch, dch\}$ . Also, two different regimes are used for solving the inverse problem (4.44), namely, charge and discharge regimes. Thus, a separate inverse problem is solved pertaining to each regime and the results are compared. In order to initialize the stage II of the Algorithm 3, the initial guesses for constitutive relations are set to be  $\omega_1^{(0)}(C_1) =$

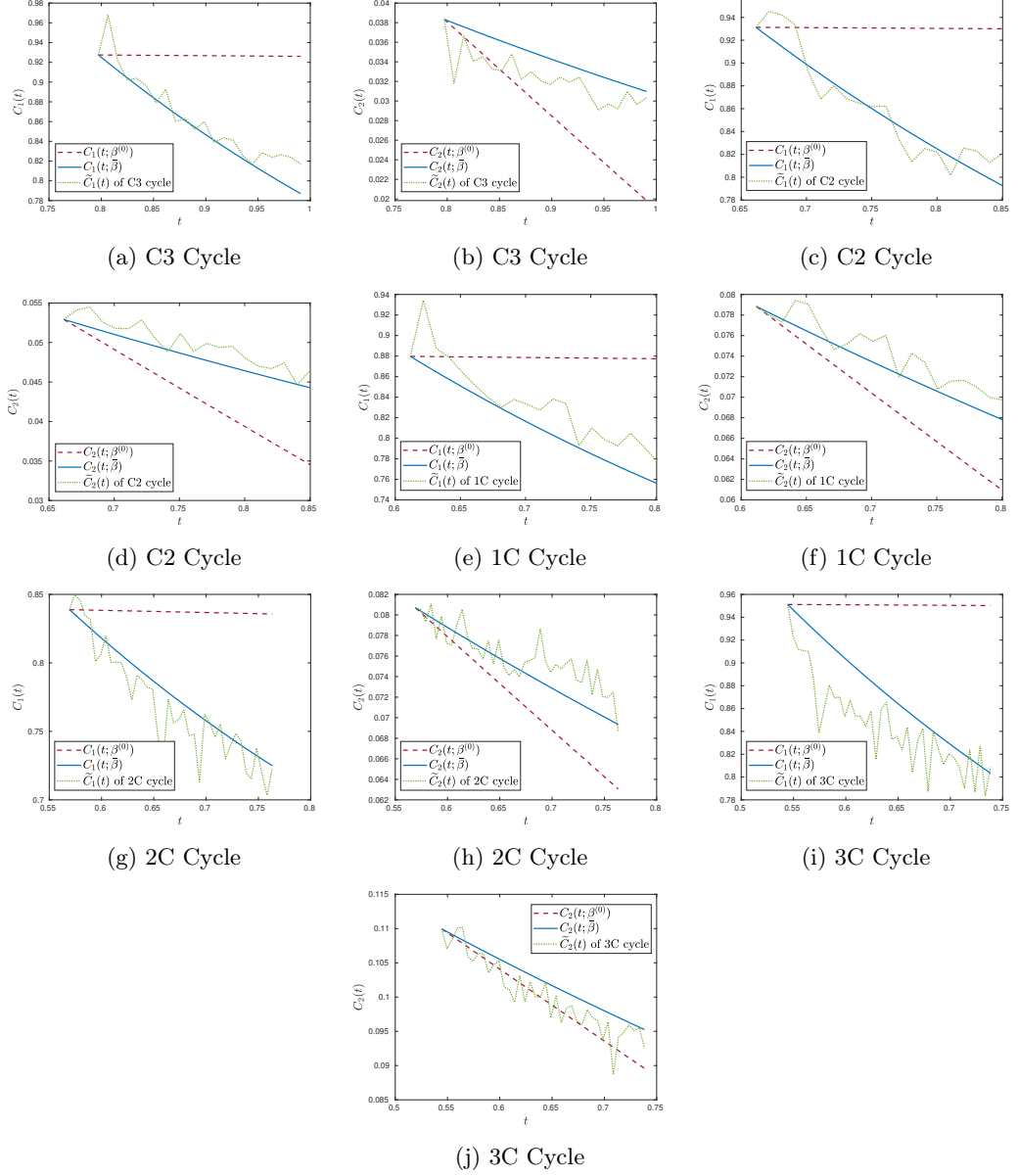


Figure 4.5: Dependence of concentrations  $C_1(t)$  and  $C_2(t)$  on time for different cycles of the cell, using the initial guess for parameters  $\beta^{(0)}$  (dashed red line), and the optimal values of parameters  $\bar{\beta}$  (solid blue line). The experimental concentrations  $\tilde{C}_1(t)$  and  $\tilde{C}_2(t)$  for each cycle are shown as dotted green lines.

$0.25$ ,  $\omega_2^{(0)}(C_2) = 0.25$ ,  $\alpha^{(0)} = 5$ . The choice of this initial guess for constitutive relations is dictated by our knowledge of the physics of the cell, in which the constitutive relation  $\omega(C_1, C_2)$  (defining the competition between intercalation vs. plating) is dominated by the intercalation process, hence attains a value between zero to one, closer to zero. As mentioned in Section 4.4.2, the function  $\omega_1(C_1)$  is reconstructed in space  $H^1$ , however, the function  $\omega_2(C_2)$  is reconstructed in space  $H_0^1$ , where the mean of the function remains stationary. Algorithm 3 is allowed to run for a maximum of  $N = 30$  iterations.

The smoothing parameter in the  $H^1$  inner product is set  $l = 1$ . The interval  $\mathcal{L}$  is set as  $(C_1, C_2) \in [-0.5, 1.5] \times [-0.2, 0.5]$ . The wide choice of interval  $\mathcal{L}$  for each state variable ensures that the choice of the somewhat arbitrary boundary conditions satisfied by the Sobolev gradient, cf. (4.64), has little effect on the behavior of the gradient for concentrations of interest. In other words, if the interval  $\mathcal{L}$  is chosen to be too close to the identifiability region bounds, the behaviour of the function at the end points of the identifiability region will be affected by the choice of boundary conditions in  $H^1$  reconstruction. The results obtained by solving optimization problem (4.44) for the charge and discharge regimes of the 1C cycle are presented in Figure 4.6. As can be observed, the large-scale details of the measurement data

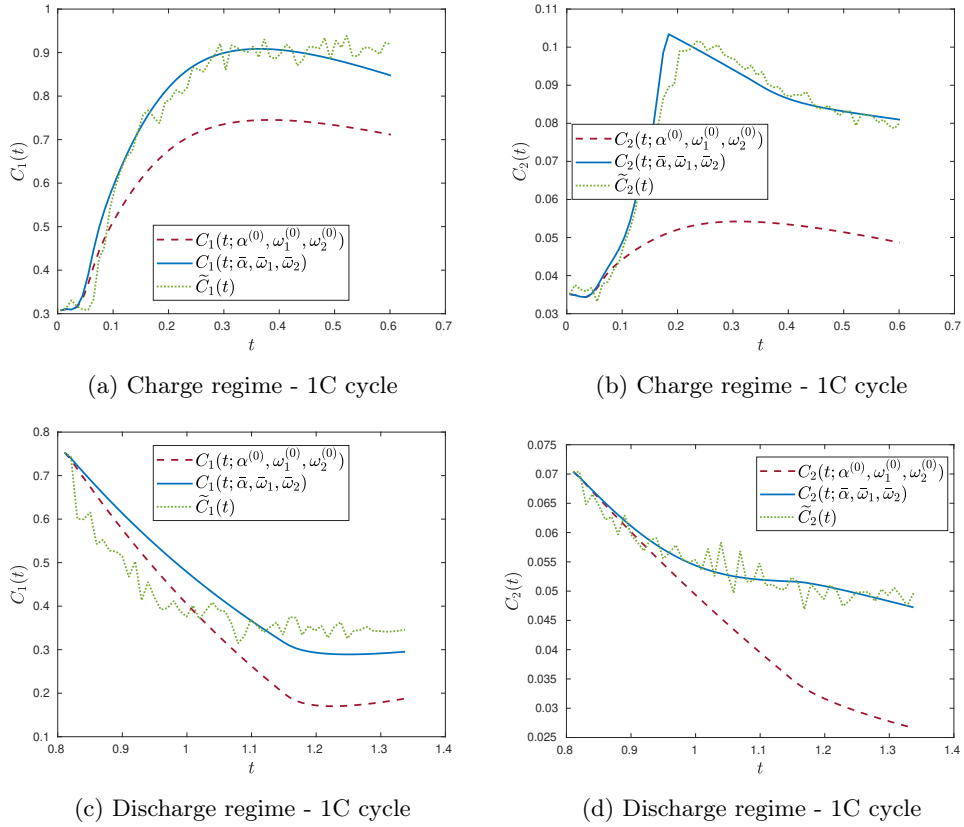


Figure 4.6: The dependence of concentrations  $C_1(t)$  and  $C_2(t)$  on time for the charge regime of the 1C cycle (a,b), and the discharge regime of the 1C cycle (c,d), using the initial guess for the parameter and constitutive relations  $(\alpha^{(0)}, \omega_1^{(0)}, \omega_2^{(0)})$  (dashed red line), and the optimal parameter and constitutive relations  $(\bar{\alpha}, \bar{\omega}_1, \bar{\omega}_2)$  (solid blue line) obtained by solving the inverse problem (4.44) using the data for the charge and discharge regimes of 1C cycle, namely,  $\mathcal{D}_{1C}^{ch}$  and  $\mathcal{D}_{1C}^{dch}$ , respectively. The experimental concentrations  $\tilde{C}_1$  and  $\tilde{C}_2(t)$  are shown using green dotted line.

$\tilde{C}_1(t)$  and  $\tilde{C}_2(t)$  are well captured by the model equipped with the optimally reconstructed constitutive relations and parameter. Note that the fine details of the measurements result from the noise in the NMR measurements, and hence, it is preferable for the model not to resolve such details. The optimal constitutive relations and parameter as the result of fitting (4.37) to individual cycles are not presented

here for brevity, as such results are similar with minor differences.

In principle, one uses the inverse problem (4.44) to train (4.37) on individual sequences of data corresponding to particular C-rates, and for charge and discharge regimes. It is known however that each of these models can only perform well in the vicinity of the original C-rate that it has been trained on. In order to systematically assess the prediction capability of the calibrated models, one is required to test the trained models on unseen data from other cycles. Individual models are therefore trained on each of the five cycles for charge and discharge regimes. These calibrated models will then be used to assess the performance of the model on the data from other cycles by generating performance metrics as cost functional error  $\mathcal{J}_2(\bar{\alpha}, \bar{\omega}_1, \bar{\omega}_2)$ . Additionally, in order to obtain a more robust model that can generalize well to a range of charge and discharge rates, the model is trained by using the optimization framework presented in Section 4.4.3. The charging regime comprising all cycles  $\mathcal{D}_t^{ch}$  will be used for training a robust model for the charging regime. A similar calibration procedure will be followed for the discharge regime by fitting the model to  $\mathcal{D}_t^{dch}$ . Also, in another attempt to find a robust model using a minimal amount of experimental measurements, model (4.37) is trained using the experimental measurements of the charging regime for the C3 and 3C cycles only, namely,  $\bigoplus_i \mathcal{D}_i^{ch}, i \in \{C3, 3C\}$ , using the optimization framework presented in Section 4.4.3. A similar calibration procedure will be followed for training model (4.37) using experimental measurements of the discharge regime, namely,  $\bigoplus_i \mathcal{D}_i^{dch}, i \in \{C3, 3C\}$ . The results of this analysis are depicted in Figure 4.7. Each solid line corresponds to model (4.37) trained on a particular individual cycle, with the dashed line corresponding to the robust model trained on all cycles, and the dotted line corresponding to the robust model trained on the C3 and 3C cycles only. As can be observed, each trained model performs best in the vicinity of the training cycle (C-rate), and the performance deteriorates as we deviate from the C-rate. Also, the robust model that is trained by fitting to data from all cycles shows an overall better and more robust performance in comparison to models that are trained on individual cycles. In most cycles shown in Figure 4.7, this robust model (which is trained on all cycles) outperforms most models on each cycle. Therefore, this robust model can be used for prediction and control. Also, the robust model that is trained by fitting to data from the C3 and 3C cycles (dotted lines in Figure 4.7) shows an overall good agreement with the model trained by fitting to data from all cycles (dashed lines in Figure 4.7), both for the charging and the discharge regimes. This agreement between the two robust models indicates that a minimal amount of experimental measurements is sufficient for calibrating a robust model without sacrificing accuracy, provided that the experimental cycles chosen cover the two extreme values of the C-rate. The results obtained by solving inverse model (4.44) using all cycles as training data, for charge ( $\mathcal{D}_t^{ch}$ ) and discharge regimes ( $\mathcal{D}_t^{dch}$ ) are demonstrated in Figures 4.8 and 4.9. The evolution of cost functional values and the parameter  $\alpha$  with iterations of the algorithm

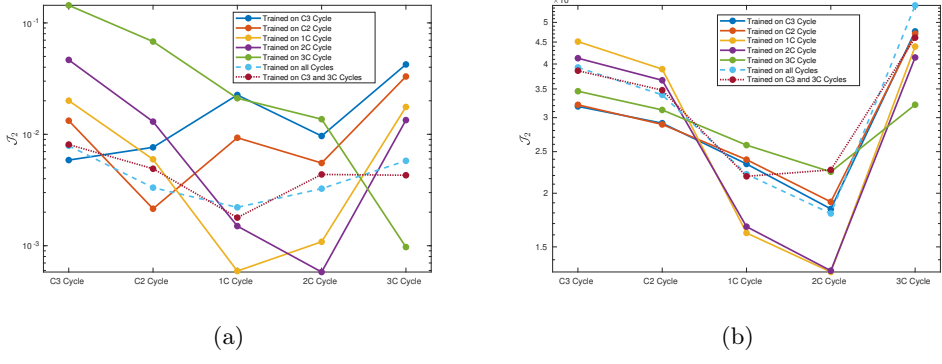


Figure 4.7: Dependence of the least-squares error  $J_2(\bar{\alpha}, \bar{\omega}_1, \bar{\omega}_2; \mathcal{D}_i^{ch})$  between the experimental data from different cycles  $i \in \mathcal{C}$ , and the predictions of model (4.37) using the optimally reconstructed parameter and constitutive relations  $(\bar{\alpha}, \bar{\omega}_1, \bar{\omega}_2)$  obtained by solving inverse problem (4.44) using the data corresponding to a given cycle, for the charge regime (a) and the discharge regime (b). For each line in the plots, model (4.37) is calibrated with Algorithm 3 using the data from the cycle indicated in the legend and then tested against data from all other cycles (indicated on the horizontal axis). Also, the performance of the model calibrated using aggregated data  $\mathcal{D}_t^{ch}$  for (a) and  $\mathcal{D}_t^{dch}$  for (b), is demonstrated by dashed line. Additionally, the performance of the model calibrated using data for C3 and 3C cycles ( $\bigoplus_i \mathcal{D}_i^{ch}, i \in \{C3, 3C\}$  for (a) and  $\bigoplus_i \mathcal{D}_i^{dch}, i \in \{C3, 3C\}$  for (b)), is as the dotted line.

are depicted in Figure 4.8, whereas the optimal reconstructed constitutive relations are shown in Figure 4.9. Although the optimal constitutive relations found by fitting forward model (4.37) to individual cycles for charge and discharge regimes are not presented here for brevity, they show a similar behaviour to the optimally reconstructed constitutive relations in Figure 4.9. Note the magnitude of the function  $\omega$  is in both cases of the order of 0.1, highlighting the dominating effect of the intercalation/deintercalation relative to plating/stripping. Also, it is clear from Figures 4.8 and 4.9 that the optimal reconstructions of constitutive relations and parameter  $\alpha$  are slightly different between the charge and discharge regimes. As can be observed, the reconstructed relations  $\omega_2$  for the charge and discharge regimes show similar behaviour, however, the relation  $\omega_1$  and the parameter  $\alpha$  demonstrate different behaviours in the charge and discharge regimes. This is contrary to what we expect to observe in the system, namely, that the constitutive relations deduced in the two regimes should be approximately the same. This could have a few potential reasons.

1. The dynamical behaviour of the system for charge and discharge regimes might show some irreversibility. Note that the function  $\omega$  is defined as the balance between Li plating and Li intercalation. This implies that the competition between side reaction and intercalation is different between the charge and discharge regimes. At a particular state of the cell, charging might result in an intercalation-plating competition that might be different from the deintercalation-stripping competition when discharging at the same state of the cell. This would indicate that Li metal does not get

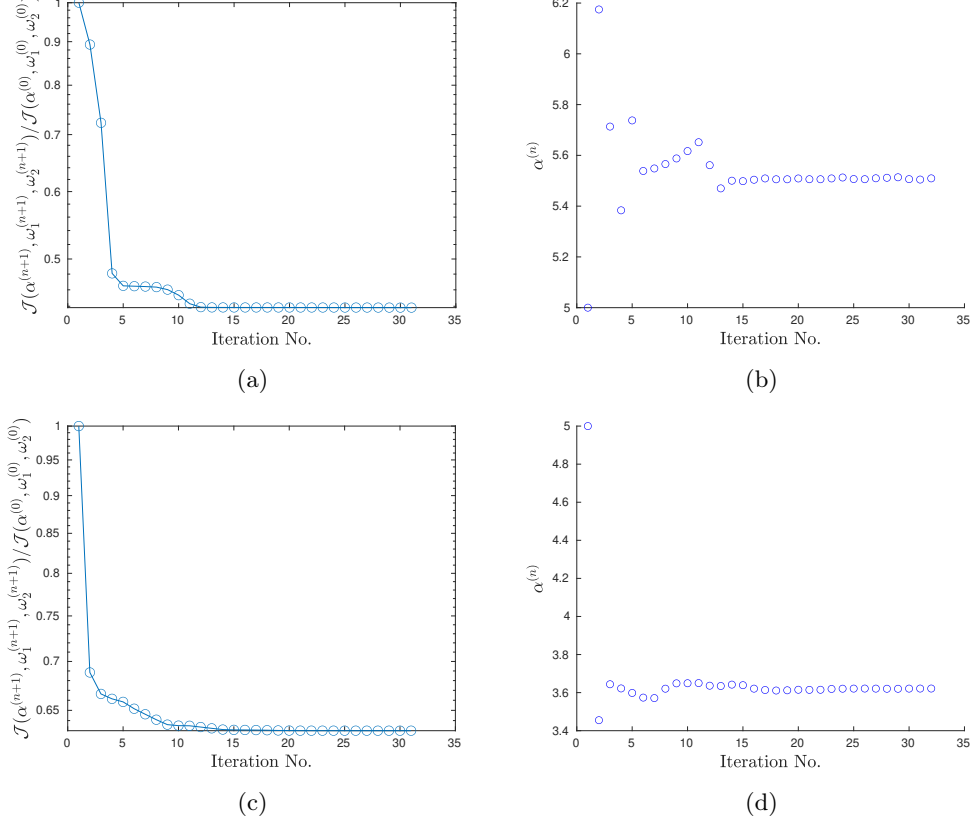


Figure 4.8: The decay of cost functional  $\mathcal{J}_2(\alpha, \omega_1, \omega_2)$  normalized with respect to its initial value with iterations (a,c), and the evolution of parameter  $\alpha$  with iterations (b,d) in the solution of the inverse problem (4.44) where model (4.37) is calibrated with stage II of Algorithm 3 using aggregated data for the charge regime  $\mathcal{D}_t^{ch}$  (a,b), and discharge regime  $\mathcal{D}_t^{dch}$  (c,d).

stripped in exactly the same manner as it gets plated. One possibility is that some plated Li loses electrical connectivity with the negative particles, and for this reason, it becomes electrochemically inactive. In other words, not all plated Li is recoverable, giving rise to slightly different behaviour of function  $\omega$  for stripping in comparison to plating.

2. The experimental conditions between the charge and discharge regimes might have slightly changed, hence, giving rise to different cell behaviour for each regime.
3. The noise in the experimental data could be a factor that affects the fitting process and results in slightly different behaviour between charge and discharge regimes. As the inverse problem tends to be ill-posed, the effect of noise could be significant.

The results of solving the forward problem (4.37) equipped with the optimally reconstructed constitutive relations and optimal parameters  $\alpha$  and  $\beta$  by fitting the model to all cycles are depicted in Figures 4.10 and 4.11. The optimal relations and parameters used correspond to the dashed line in Figure 4.7, i.e., model

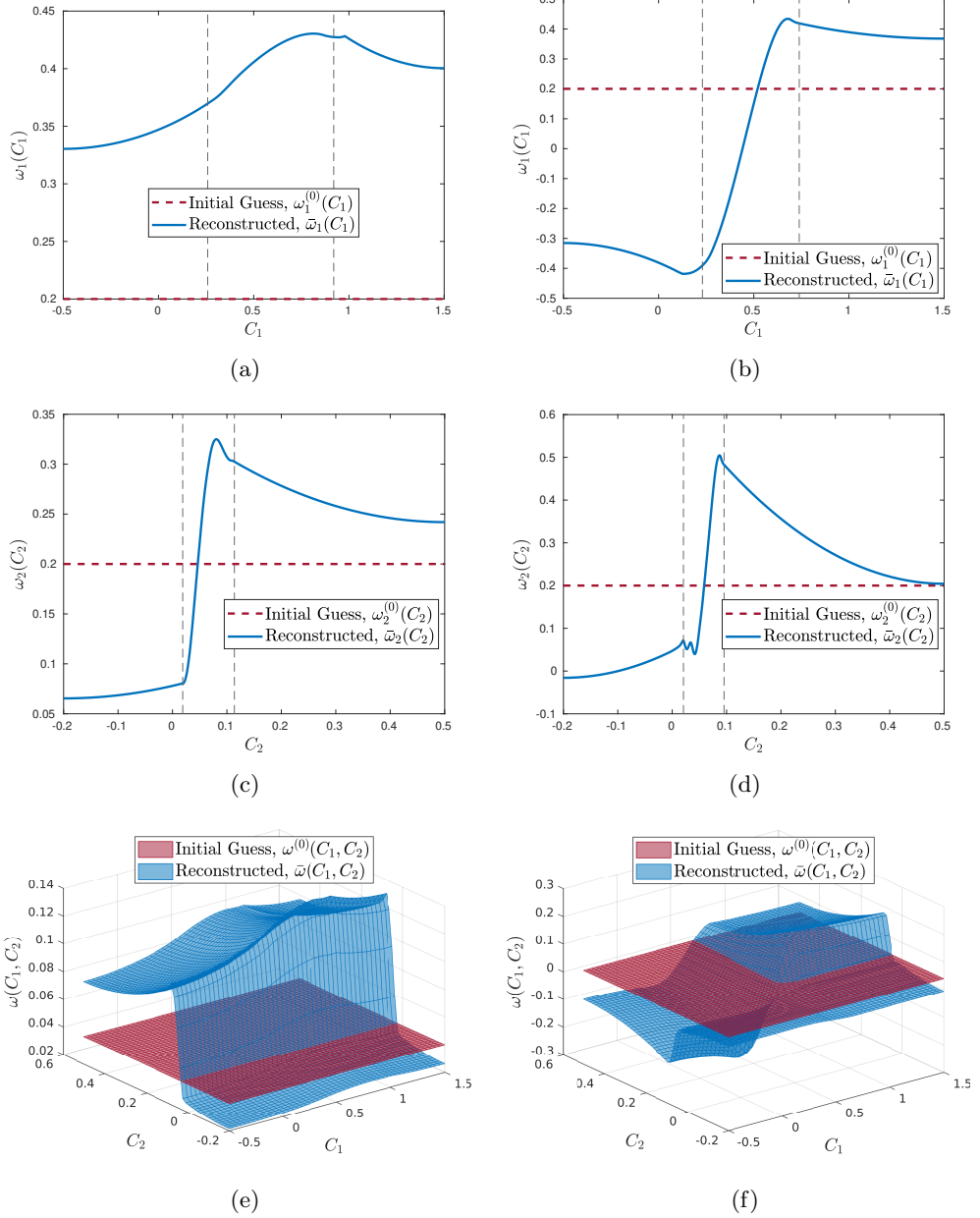


Figure 4.9: The initial guess for the constitutive relations  $\omega_1^{(0)}(C_1)$ ,  $\omega_2^{(0)}(C_2)$ , and  $\omega^{(0)}(C_1, C_2)$  (red), and the optimal form of the reconstructed constitutive relations  $\bar{\omega}_1(C_1)$ ,  $\bar{\omega}_2(C_2)$ , and  $\bar{\omega}(C_1, C_2)$  (blue) where model (4.37) is calibrated with stage II of Algorithm 3 using aggregated data for the charge regime  $\mathcal{D}_t^{ch}$  (a,c,e), and discharge regime  $\mathcal{D}_t^{dch}$  (b,d,f).

that is fitted to aggregated data according to Section 4.4.3. The results are shown for the time dependence of the reconstructed concentrations for all cycles, along with the true experimental concentrations. As can be observed, the concentrations from the model follow the overall behaviour of the dynamics of the system, with some minor deviations. There can be multiple reasons for this.

1. The noise in the NMR measurements is one source of inconsistency between the predictions of the

mathematical model and the measured concentrations.

2. The computational framework has one caveat which can potentially limit its performance. The separation of variables ( $\omega(C_1, C_2) = \omega_1(C_1) \cdot \omega_2(C_2)$ ) is assumed in the optimal reconstruction formulation. The "true" optimal form of constitutive relation might not be separable as assumed in the computational framework.
3. This model does not take into account other undesired processes in the cell that might consume some of the interfacial current density, such as secondary SEI growth. The current density applied to the cell is entirely consumed by intercalation/deintercalation and plating/stripping processes.
4. Model (4.37) is trained on a range of C-rates simultaneously. It is known that the dynamics of Li-ion cells highly depend on the C-rate, and different simplified models are developed for describing the dynamics of the cell at different ranges of C-rates, see [156] and [157]. Hence, one model could lose its accuracy when trained on a wide range of C-rates.
5. The optimization problems of this nature are typically non-convex and may therefore admit multiple local minima. We cannot guarantee that with the gradient-based approach we used the solutions we found are global minimizers.

Thus, due to these reasons, it is unlikely the optimal solutions presented in this section could be further improved.

As can be observed in Figure 4.11, the experimental concentrations of plated Li demonstrate a partial recovery (stripping) of plated Li. This implies that some of the plated Li is inactive, and hence the calibrated constitutive relation must take into account this phenomenon. As explained before, this could be one reason for different behaviour of the constitutive relations between charge and discharge regimes.

#### 4.6. Discussion

In this study, Li plating was investigated as one of the main degradation mechanisms in Li-ion cells using mathematical and computational tools. Physical modeling was employed in order to model the physical and chemical processes in the cell. Starting with the DFN model, we employed a variety of techniques, including asymptotic reduction and averaging, in order to simplify it to an SP model with side reactions, tailored to our experimental data. The resulting SP model with side reaction tracks the evolution of two lumped concentrations: intercalated Li and plated Li in the cell. Notably, the model has the following

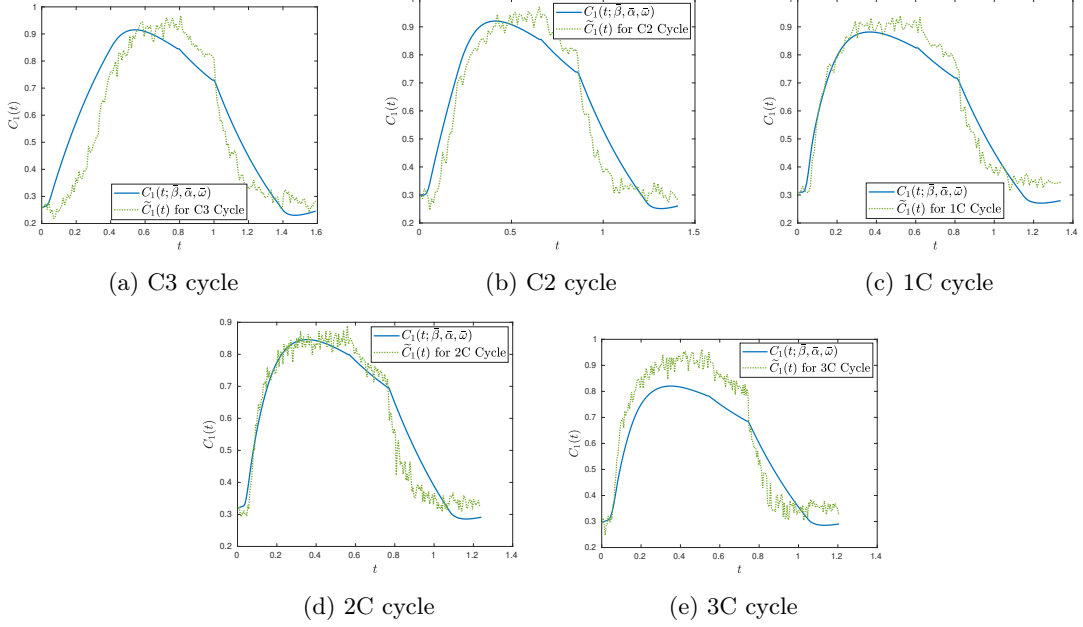


Figure 4.10: The dependence of the state variable  $C_1(t)$  on time in the solution of the forward problem (4.37) using the optimal parameters values and optimal forms of the constitutive relation  $(\bar{\beta}, \bar{\alpha}, \bar{\omega})$  reconstructed by calibrating system (4.37) using aggregated data  $\mathcal{D}_t$  for charge, discharge and OCV regimes, cf. Section 4.4.3. The dashed green and the solid blue lines represent the experimental concentrations and the solution of the forward problem (4.37) using optimal parameters and constitutive relations, respectively.

properties: (i) concentrations are averaged over their corresponding spatial domains to eliminate spatial dependence from the equations, (ii) the model takes the form of an ODE system describing the evolution of the averaged quantities, circumventing the need to solve for the potential distribution in the cell, as done in the DFN models, due to the simplifying assumptions of the proposed framework, such as uniformity of particles in negative and positive electrodes, (iii) the model accounts for both relaxation and excitation dynamics in the cell, with excitation being the primary cause of dynamics in the cell, and (iv) the model accounts for both plating and stripping processes in the cell, allowing for the recovery of some of the plated Li. These properties make the model a good candidate for online state estimations and monitoring of the cells. From the physical modeling perspective, the study by Brosa Planella et al. [155] bears the closest resemblance to this work, although it does not account for Li stripping. Sahu et al. [158] consider more interactions between different phases of Li in the cell and develop a more comprehensive mathematical model capable of predicting both plating and stripping. Our resulting physical model involved a multitude of physical parameters and constitutive relations that require calibration using experimental data. Inverse modeling and optimization techniques are employed for this purpose in order to determine the optimal value of parameters and the optimal form of constitutive relations, aiming to minimize discrepancies between model outputs and experimental data. To our knowledge, this study represents the

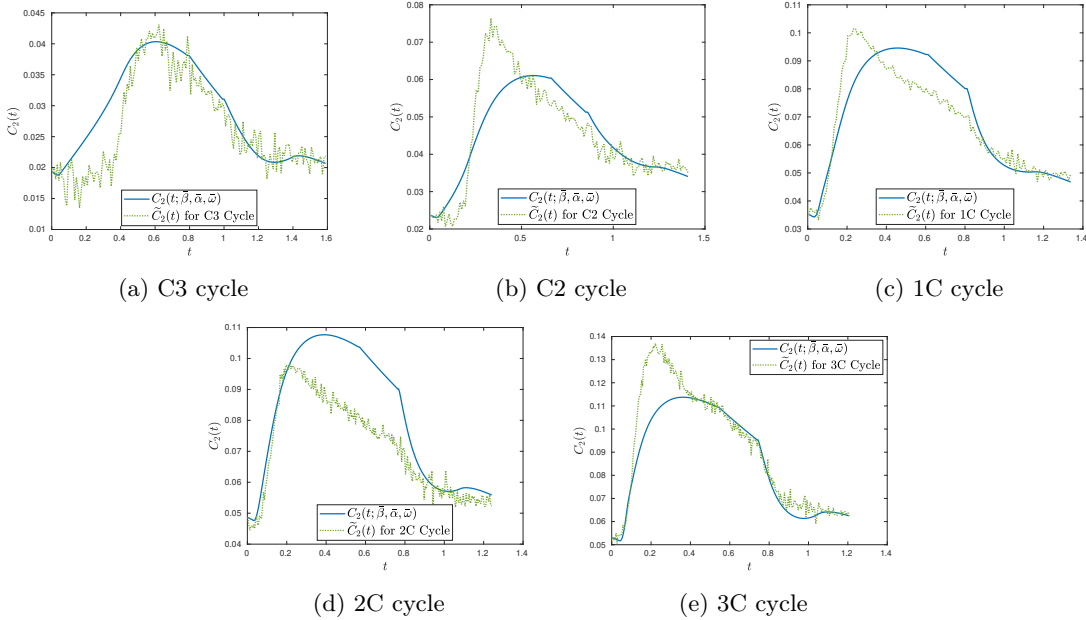


Figure 4.11: The dependence of the state variable  $C_2(t)$  on time in the solution of the forward problem (4.37) using the optimal parameters values and optimal forms of the constitutive relation  $(\bar{\beta}, \bar{\alpha}, \bar{\omega})$  reconstructed by calibrating system (4.37) using aggregated data  $\mathcal{D}_t$  for charge, discharge and OCV regimes, cf. Section 4.4.3. The dashed green and the solid blue lines represent the experimental concentrations and the solution of the forward problem (4.37) using optimal parameters and constitutive relations, respectively.

first instance of using inverse modeling to optimally predict Li plating and stripping in Li-ion cells.

We note that the negative electrode material utilized in this study is silicon. This material experiences significant volume variations during charge/discharge cycles of the cell, a phenomenon linked to its high charge density. These volume changes may influence the model's performance, as we have not explicitly accounted for this phenomenon. Nonetheless, the calibrated parameters and constitutive relations of the model can implicitly account for this effect.

An important consideration is the range of validity of Li-plating model. As highlighted by Marquis et al. [156], the SP model remains valid up to a C-rate of 1C, beyond which it begins to diverge from the DFN model. In this study, we have also developed a variant of the SP model that accounts for Li-plating as a side reaction. Consequently, it becomes imperative to investigate the range of validity of this model. As depicted in Figures 4.10 and 4.11, the model trained across a spectrum of cycles demonstrates the ability to predict intercalation/deintercalation and plating/stripping behaviours in an overall acceptable manner. Due to the fact that the mathematical model is calibrated using data, its fidelity may extend beyond 1C rate. Figure 4.7 suggests that a model calibrated on a specific C-rate performs well in its proximity, and its performance gradually deteriorates as the C-rate deviates from the C-rate used for training. Thus, the

range of validity of the model highly depends on the training process used to calibrate the model, which, in turn, is determined by the specific application assumed for the model.

The proposed physical modeling and computational framework can also be extended to differentiate between different phases of Li within the cell, particularly non-recoverable Li and recoverable Li. In the current study, these two phases are not distinguished as the experimental data for inactive Li is not available. Additionally, this framework does not account for other degradation mechanisms in the cell and solely focuses on the Li plating behaviour. However, it can be readily expanded to include other types of degradation mechanisms in the cell.

# *Chapter 5*

---

## *Summary, Conclusion and Outlook*

---

In this study, multiple problems revolving around Li-ion cells were investigated to model, identify, and predict degradation mechanisms, and improve reliability of such models. The models developed are used to (i) predict the lattice structure of the cathode phase, (ii) model the degradation mechanisms in the negative electrode of the cell, and (iii) predict the dynamic behaviour of the cell including its inefficiencies while in operation. These models were developed, calibrated, and tested against experimental data from lab-made or commercial Li-ion cells. Data-driven inverse modeling approaches were leveraged for calibrating models for each specific application. Two categories of models were used in this study, namely, data-driven techniques and physics-based techniques, to understand and model cell dynamics.

From the modeling point of view, this thesis focuses on modeling of cells based on ODEs and the calibration of such models using inverse modeling techniques as follows.

- In Chapter 2, an ODE model was used for the prediction of the cathode cell structure, calibrated via an inverse modeling technique, and the uncertainty of this model was quantified. A model was developed that tracks the evolution of the concentrations of different clusters in the lattice. Instead of tracking the state of the individual lattice sites using computationally expensive techniques, one can quantify the agglomerate information about different clusters in a lattice, which is computationally more efficient. The resulting model takes the form of an ODE for tracking the evolution of the concentrations of different clusters in the lattice. This model, calibrated with suitable experimental data, could be used to produce information about lattice structure. Learning the structure of the cathode can help in understanding the intercalation/deintercalation mechanisms in the cathode

phase and the local structures formed during this process. This modeling technique is an example of a system identification approach using prior knowledge about the physics of the system and about how interactions can take place in the lattice. The resulting ODE takes the form of a nonlinear hierarchical system with scalar parameters, to be determined. Data-driven techniques are leveraged to close the dynamical system in an optimal manner using regularization methods. This framework leads to an improvement of the closure models for hierarchical ODEs.

- In Chapter 3, data-driven modeling is used to enhance cell state estimates of LFP cells using the EIS operando technique. A hybrid data-driven approach is employed for system identification, where experimental data is used to find an optimal combination of candidate terms describing the evolution of the dynamics in the cell, drawn either from the physical knowledge of the system or from some empirical functions. This technique is a computationally inexpensive way of identifying system dynamics for predicting the state of the system while in operation. Accurate modeling of cell dynamics helps improve cell estimations and design more reliable feedback loops, used for monitoring and control.
- In Chapter 4, a data-driven modeling approach is used to identify degradation mechanisms in the cells. A physics-based modeling approach is employed to develop a system of ODEs for tracking the evolution of cell dynamics. In this case, the system of ODEs is derived from the physics of the system with the help of an asymptotic reduction; however, the model is not closed as some parameters are state-dependent. The behavior of this model's response depends on the form of the state-dependent constitutive relations that are unknown and need to be determined. Experimental data can help in learning the optimal form of these constitutive relations. In this model, only minimum a priori assumptions about the functional forms of the constitutive relations are used. Calibration of this model requires sophisticated computational tools to identify optimal parameters and constitutive relations. The resulting model can be used for monitoring and predicting cell inefficiencies while in operation.

From the computational point of view, three different model development techniques were used. (i) Physical modeling to get an ODE with scalar parameters: this approach is common in science and engineering. Standard techniques for solving inverse problems can be leveraged to calibrate such models. (ii) Data-driven modeling to get an ODE describing the dynamics of the system learned using measurement data: this technique is simple, inexpensive, and well-suited for predictive control to enhance state prediction. However, it is restricted by our choice of functionals and nonlinearities for the system's dynamics. (iii) Physical modeling to obtain an ODE for describing system's dynamics with minimal assumptions

about the functional forms of constitutive relations: this approach is superior to the two other previous modeling techniques as the resulting ODE model is interpretable and computationally inexpensive. In this case, the unknown parameters of the model are state-dependent and can better capture the system's dynamics compared to previous models. This technique allows for an accurate reconstruction of optimal forms of constitutive relations instead of imposing specific functional forms. This technique, combined with physics-based modeling, could result in accurate and interpretable estimations of the system.

# Appendix A

## Data-Driven Optimal Closures for Mean-Cluster Models

### A.1. Rotational Symmetry

**Theorem A.1.1.** *In a 2D triangular lattice (where each element is surrounded by 6 nearest-neighbours), if the energy function of the lattice is invariant with respect to the spatial orientation of the bonds, 2-clusters with different spatial orientations have the same concentrations in the ground state, i.e., the probability of finding a particular 2-cluster in the lattice is independent of its spatial orientation.*

*Proof.* The energy function used in the simulated annealing experiment in Section 2.2 is achieved by summing over energies of single oxygen sites i.e.  $E = \sum_i E_i$ . The energy over each oxygen site is calculated by considering its neighbor elements in 6 different positions. The energy over each oxygen site is independent of the orientation of the neighbouring sites and only depends on the type and charge of the neighbouring elements.  $\square$

### A.2. Bayesian Inference

In the Bayesian framework the distribution of the model parameters is given by the *posterior* probability distribution  $\mathbb{P}(\mathbf{K}|\tilde{\mathbf{C}})$  defined as the probability of obtaining parameters  $\mathbf{K}$  given the observed experimental data  $\tilde{\mathbf{C}}$ . According to Bayes' rule, we then have

$$\mathbb{P}(\mathbf{K}|\tilde{\mathbf{C}}) = \frac{\mathbb{P}(\tilde{\mathbf{C}}|\mathbf{K})\mathbb{P}(\mathbf{K})}{\mathbb{P}(\tilde{\mathbf{C}})}, \quad (\text{A.1})$$

where  $\mathbb{P}(\tilde{\mathbf{C}}|\mathbf{K})$  is the *likelihood* function describing the likelihood of obtaining observations  $\tilde{\mathbf{C}}$  given the model parameters  $\mathbf{K}$ ,  $\mathbb{P}(\mathbf{K})$  is the *prior* probability distribution reflecting some a priori assumptions on

the parameters  $\mathbf{K}$  (based, e.g., on direct measurements or literature data), whereas  $\mathbb{P}(\mathbf{C})$  can be viewed as a normalizing factor.

One approach to choosing the prior distribution  $\mathbb{P}(\mathbf{K})$  is to use an uniform distribution, leading to the so-called uninformative prior. Another common approach useful when no prior information is available is to employ a normal distribution with zero mean which allows one to explore parameter values with bounded magnitudes, and this is the approach we adopt here. In our problem the reaction rates in  $\mathbf{K}$  are non-negative, hence a half-Gaussian distribution truncated at zero is used as the prior.

As regards the likelihood function, it is usually defined as

$$\mathbb{P}(\tilde{\mathbf{C}}|\mathbf{K}) \propto e^{-\mathcal{J}(\mathbf{K})}. \quad (\text{A.2})$$

This definition of the likelihood function arises from the fact that parameter values are considered more likely if they produce model predictions  $\mathbf{C}$  closer to the data  $\tilde{\mathbf{C}}$ . Unlike the linear case where the inference problem can be often solved directly by exploiting connections with Tikhonov regularization [83], this is not possible here due to the nonlinearity of the inverse problem (2.23) and we can expect the posterior distribution  $\mathbb{P}(\mathbf{K}|\tilde{\mathbf{C}})$  to have a complicated form.

The main challenge is efficient sampling of the likelihood function  $\mathbb{P}(\tilde{\mathbf{C}}|\mathbf{K})$  and this can be performed using a Markov-Chain Monte-Carlo (MCMC) approach. It is a form of a random walk in the parameter space designed to preference the sampling of high-likelihood regions of the space while also exploring other regions. In the MCMC algorithm, a kernel  $\mathcal{Q}(\mathbf{K}^*|\mathbf{K})$  is used to generate a proposal for a move in the parameter space from the current point  $\mathbf{K}$  to a new point  $\mathbf{K}^*$ . This new point is accepted with a probability given by the Hastings ratio; otherwise, it is rejected (the “Metropolis rejection”). In order to preserve the reversibility of the Markov chain, the Hastings ratio for the acceptance probability is defined as

$$\alpha(\mathbf{K}^*, \mathbf{K}) = \min \left\{ 1, \frac{\mathbb{P}(\mathbf{K}^*|\tilde{\mathbf{C}}) \mathcal{Q}(\mathbf{K}|\mathbf{K}^*)}{\mathbb{P}(\mathbf{K}|\tilde{\mathbf{C}}) \mathcal{Q}(\mathbf{K}^*|\mathbf{K})} \right\}. \quad (\text{A.3})$$

Thus, the Markov chain is reversible with respect to the posterior distribution, meaning that a transition in space is equally probable during forward and backward evolution. This property makes the posterior distribution invariant on the Markov chain. In other words, if given enough iterations, the distribution converges to its equilibrium distribution. The most common choice of the random walk is in the form

$$\mathbf{K}^* = \mathbf{K} + \boldsymbol{\xi} \quad (\text{A.4})$$

such that  $\mathcal{Q}(\mathbf{K}^*|\mathbf{K}) = \mathcal{Q}(\mathbf{K}^* - \mathbf{K}) = \mathcal{Q}(\boldsymbol{\xi})$ , where  $\boldsymbol{\xi}$  is an 8-dimensional random variable drawn from a uniform distribution with scale  $\boldsymbol{\sigma} \in \mathbb{R}^8$ , i.e.,  $\boldsymbol{\xi} \sim \mathcal{U}[-\boldsymbol{\sigma}, \boldsymbol{\sigma}]$ . Note that the components of the scale  $\boldsymbol{\sigma}$  represent intervals defining the uniform distribution. It has been suggested that uniform kernels outperform Gaussian ones in terms of convergence of the MCMC algorithm [164], hence, we adopt the uniform kernel in our study. The choice of symmetric kernels simplifies relation (A.3) as the factors representing the density in the numerator and denominator cancel. However, the choice of scale for the proposal kernel is nontrivial. Small scales will result in slow convergence to the posterior distribution, whereas large scales will prevent sampling of desirable regions in the parameter space. Moreover, in our model there is no prior information about an appropriate scale for the proposal kernel. In order to tackle this issue, a two-step Delayed-Rejection Metropolis-Hastings (DR-MH) algorithm is used [77, 165, 166]. In this algorithm, the rejection of the first proposed point at a given iteration of the Markov chain is delayed by proposing a new step in the space based on a different scale. Normally, the scale of the first kernel is chosen to be large in order to explore a wider region of the high-dimensional parameter space and the scale of the second kernel is small to gather more samples from higher-likelihood regions. This approach combines exploration of large regions in a high dimensional space with focus on high-likelihood neighbourhoods. Here, we adopt the two scales to be equal to 1 and 0.1, respectively. The DR-MH algorithm also ensures the reversibility of the Markov chain, meaning that the direction of time in which the random walk is taking place does not affect the dynamics of the Markov chain. In other words, a random walk in the forward direction of the chain from state  $n$  to state  $n + 1$  is equally probable as the reverse walk from state  $n + 1$  to state  $n$ . This ensures that the chain remains in an equilibrium state as it evolves. This is an important property as the Markov chain is essentially a random walk in the posterior space and reversibility is required to ensure it remains in the same posterior space. The acceptance probability of the delayed proposed point is calculated using relation (A.6). To initialize the DR-MH algorithm, we require an initial set of model parameters which is drawn from a half-Gaussian prior distribution with zero mean and unit standard deviation. The total number of samples in the Markov chain is  $M = 10^4$ . Algorithm 4 outlines the entire procedure needed to approximate the posterior probability distribution  $\mathbb{P}(\mathbf{K}|\tilde{\mathbf{C}})$ . Additional details concerning MCMC approaches can be found in monographs [21, 167].

**Algorithm 4:** RANDOM WALK DELAYED REJECTION ALGORITHM**Input:**  $M$  — Number of samples to be drawn from the posterior distribution $\mathcal{Q}_1(\mathbf{K}^*|\mathbf{K})$  — Proposal density of the first trial $\mathbf{y}_1$  — initial point for the random walk in the space  $\mathbb{R}^8$  $\sigma_1, \sigma_2$  — scales defining the random walk**Output:**  $\mathbb{P}(\mathbf{K}|\tilde{\mathbf{C}})$  — Posterior probability distribution $n \leftarrow 1$ **repeat**    Propose a step:  $\xi \sim \mathcal{U}[-\sigma_1, \sigma_1]$     Propose a candidate:  $\mathbf{y}_1 = \mathbf{K}^{n-1} + \xi$     Accept the proposed step with probability  $\alpha_1$ :

$$\alpha_1(\mathbf{y}_1, \mathbf{K}^{n-1}) \propto \min \left\{ 1, \frac{\exp(-\mathcal{J}(\mathbf{y}_1))\mathbb{P}(\mathbf{y}_1)}{\exp(-\mathcal{J}(\mathbf{K}^{n-1}))\mathbb{P}(\mathbf{K}^{n-1})} \right\} \quad (\text{A.5})$$

    Draw a random number:  $r \sim \mathcal{U}[0, 1]$     **if**  $\alpha_1(\mathbf{y}_1, \mathbf{K}^{n-1}) < r$  **then**        Propose a new step with scale  $\sigma_2$ :  $\xi \sim \mathcal{U}[-\sigma_2, \sigma_2]$         Propose a new candidate:  $\mathbf{y}_2 = \mathbf{K}^{n-1} + \xi$         Accept the new proposed point with probability  $\alpha_2$ :

$$\alpha_2(\mathbf{K}^{n-1}, \mathbf{y}_1, \mathbf{y}_2) = \min \left\{ 1, \frac{\mathbb{P}(\mathbf{y}_2|\tilde{\mathbf{C}})\mathcal{Q}_1(\mathbf{y}_2|\mathbf{y}_1)\left[\max\left(0, 1 - \frac{\mathbb{P}(\mathbf{y}_1|\tilde{\mathbf{C}})}{\mathbb{P}(\mathbf{y}_2|\tilde{\mathbf{C}})}\right)\right]}{\mathbb{P}(\mathbf{K}^{n-1}|\tilde{\mathbf{C}})\mathcal{Q}_1(\mathbf{y}_1|\mathbf{K}^{n-1})\left[\max\left(0, 1 - \frac{\mathbb{P}(\mathbf{y}_1|\tilde{\mathbf{C}})}{\mathbb{P}(\mathbf{K}^{n-1}|\tilde{\mathbf{C}})}\right)\right]} \right\} \quad (\text{A.6})$$

    Draw a random number:  $r \sim \mathcal{U}[0, 1]$     **if**  $\alpha_2(\mathbf{K}^{n-1}, \mathbf{y}_1, \mathbf{y}_2) > r$  **then**         $\mathbf{K}^n \leftarrow \mathbf{y}_2$          $n \leftarrow n + 1$     **else**        discard  $\mathbf{y}_2$     **else**         $\mathbf{K}^n \leftarrow \mathbf{y}_1$          $n \leftarrow n + 1$ **until**  $M$  samples are drawn;

Construct the posterior probability distribution

# Appendix B

## *Small-Signal Excitation by Electrochemical Impedance Spectroscopy*

### B.1. Small-Signal Perturbation

The equivalent circuit model presented in Figure 3.3 is a large-signal model. The small-signal perturbation can be obtained by linearizing the large-signal model around an operating point. First, we derive the large-signal model. According to Kirchhoff's current law, the current is split between the two components of the parallel RC element as

$$I(t) = \frac{u_p(t)}{R_p} + C_p \frac{du_p(t)}{dt}. \quad (\text{B.1})$$

Hence, the large-signal model presented in (3.11) can be obtained by rearranging (B.1) as

$$\frac{du_p(t)}{dt} = \frac{I(t)}{C_p} - \frac{u_p(t)}{R_p C_p}. \quad (\text{B.2})$$

According to Kirchhoff's voltage law,

$$u_t(t) = u_{oc}(t) + I(t)R_0 + u_p(t). \quad (\text{B.3})$$

Now we linearize the equations around a reference point to obtain the small-signal model of the circuit. The current and the voltage are perturbed in time domain as  $I = \bar{I} + \epsilon\Delta I$ ,  $u_t = \bar{u}_t + \epsilon\Delta u_t$ , and  $u_p = \bar{u}_p + \epsilon\Delta u_p$ . Substituting these equations into (B.1) and (B.3), and arranging the equations with respect to  $\epsilon$ , we get

$$\begin{aligned} \Delta I &= \frac{\Delta u_p}{R_p} + C_p \frac{d\Delta u_p}{dt}, \\ \Delta u_t &= \Delta I R_0 + \Delta u_p. \end{aligned} \quad (\text{B.4})$$

Converting the equation (B.4) to frequency domain using the Laplace transform, we get

$$\begin{aligned}\Delta I(s) &= \frac{\Delta u_p(s)}{R_p} + C_p s \Delta u_p(s), \\ \Delta u_t(s) &= \Delta I(s) R_0 + \Delta u_p(s),\end{aligned}\tag{B.5}$$

where  $s = j\omega$ ,  $\mathcal{L}\{I(t)\} = I(s)$ ,  $\mathcal{L}\{\Delta u_t(t)\} = \Delta u_t(s)$ ,  $\mathcal{L}\{\Delta u_p(t)\} = \Delta u_p(s)$ , and  $\mathcal{L}$  denotes a Laplace transform. Using (B.5) the impedance of the circuit is then computed as

$$Z(s) = \frac{\Delta u_t(s)}{\Delta I(s)} = R_0 + \frac{R_p}{1 + (\omega R_p C_p)^2} - j \frac{\omega R_p^2 C_p}{1 + (\omega R_p C_p)^2}.\tag{B.6}$$

# Appendix C

## *Learning Optimal Forms of Constitutive Relations in Models Describing Lithium Plating*

### C.1. Relaxation Dynamics

In order to compute components of the gradient vector, adjoint sensitivity analysis is leveraged [37, 38, 162]. We begin by computing the directional derivatives

$$\begin{aligned} \mathcal{J}'_1(\boldsymbol{\beta}; \beta'_i) &= \lim_{\epsilon \rightarrow 0} \epsilon^{-1} [\mathcal{J}_1(\boldsymbol{\beta}; \beta_i + \epsilon \beta'_i) - \mathcal{J}_1(\boldsymbol{\beta})] = \int_0^T (\mathbf{w} \mathbf{r}(t; \boldsymbol{\beta}))^\top \mathbf{C}'(\beta'_i) dt, \\ \mathbf{C}'(\beta'_i) &= \begin{bmatrix} C'_1(\boldsymbol{\beta}; \beta'_i) \\ C'_2(\boldsymbol{\beta}; \beta'_i) \end{bmatrix}, \\ \mathbf{w} &= \begin{bmatrix} 1 & 0 \\ 0 & w \end{bmatrix}, \end{aligned} \tag{C.1}$$

where  $i \in \{1, 2, 3, 4\}$ , and  $\mathbf{C}'(\beta'_i)$  is the solution of a system of equations describing perturbations of the state variables resulting from the perturbations of each of the parameters. In order to derive this system, the parameters are perturbed, and the state variables are perturbed with respect to each of the parameters in  $\boldsymbol{\beta}$  as

$$\begin{aligned} \beta_i &= \hat{\beta}_i + \epsilon \beta'_i, \\ \mathbf{C}(\boldsymbol{\beta}) &= \widehat{\mathbf{C}}(\widehat{\boldsymbol{\beta}}) + \epsilon \mathbf{C}'(\boldsymbol{\beta}; \beta'_i) + \mathcal{O}(\epsilon^2), \end{aligned} \tag{C.2}$$

where  $i \in \{1, 2, 3, 4\}$ , the variables with a hat sign represent the unperturbed version of the variables, and the prime sign represents the perturbation. Substituting (C.2) into the system of equations (4.37), collecting terms with respect to different powers of  $\epsilon$ , at the leading-order we get one system of equations corresponding to the unperturbed version of equations,  $d\widehat{\mathbf{C}}/dt = \widehat{\mathbf{B}} + \widehat{\mathbf{A}}\widehat{\mathbf{C}}$ . At the order of  $\epsilon$ , four systems of equations are obtained corresponding to the perturbation of each of the parameters in the vector  $\boldsymbol{\beta}$ . The

four systems of equations are obtained as

$$\frac{d}{dt} \mathbf{C}'(\beta'_i) = \widehat{\mathbf{A}} \mathbf{C}'(\beta'_i) + \mathbf{I}_i \beta'_i \widehat{\mathbf{C}} + z_i \mathbf{I}_0,$$

$$\mathbf{I}_0 = \begin{bmatrix} 1 \\ 0 \end{bmatrix}, \mathbf{I}_1 = \begin{bmatrix} 0 & 0 \\ 0 & 0 \end{bmatrix}, \mathbf{I}_2 = \begin{bmatrix} 1 & 0 \\ 0 & 0 \end{bmatrix}, \mathbf{I}_3 = \begin{bmatrix} 0 & \lambda^{-1} \\ 0 & -1 \end{bmatrix}, \mathbf{I}_4 = \begin{bmatrix} 0 & 0 \\ 1 & 0 \end{bmatrix}, \quad (\text{C.3})$$

where  $i \in \{1, 2, 3, 4\}$ ,  $z_1 = \beta'_1$ , and  $z_i = 0$  for  $i \in \{2, 3, 4\}$ . Dotting this equation with the vectors of the adjoint variables  $\mathbf{C}_i^*(t) = [C_1^*(t), C_2^*(t)]^\top$ , and integrating in time we obtain

$$\int_0^T \mathbf{C}_i^{*\top} \frac{d}{dt} \mathbf{C}'(\beta'_i) dt - \int_0^T \mathbf{C}_i^{*\top} \widehat{\mathbf{A}} \mathbf{C}'(\beta'_i) dt - \int_0^T \mathbf{C}_i^{*\top} \mathbf{I}_i \beta'_i \widehat{\mathbf{C}} dt - \int_0^T \mathbf{C}_i^{*\top} z_i \mathbf{I}_0 dt = 0. \quad (\text{C.4})$$

Note that four different adjoint vectors are required, each of which correspond to one system of equations resulting from perturbation of one parameter. Performing integration by parts on the first term, and applying initial conditions, we get

$$-\mathbf{C}_i^{*\top}(T) \mathbf{C}'(\beta'_i)(T) + \int_0^T \frac{d}{dt} \mathbf{C}_i^{*\top} \mathbf{C}'(\beta'_i) dt + \int_0^T \mathbf{C}_i^{*\top} \widehat{\mathbf{A}} \mathbf{C}'(\beta'_i) dt + \int_0^T \mathbf{C}_i^{*\top} \mathbf{I}_i \beta'_i \widehat{\mathbf{C}} dt + \int_0^T \mathbf{C}_i^{*\top} z_i \mathbf{I}_0 dt = 0. \quad (\text{C.5})$$

Factoring out  $\mathbf{C}'$  results in

$$-\mathbf{C}_i^{*\top}(T) \mathbf{C}'(\beta'_i)(T) + \int_0^T \left[ \frac{d}{dt} \mathbf{C}_i^{*\top} + \mathbf{C}_i^{*\top} \widehat{\mathbf{A}} \right] \mathbf{C}'(\beta'_i) dt = - \int_0^T \mathbf{C}_i^{*\top} \mathbf{I}_i \beta'_i \widehat{\mathbf{C}} dt - \int_0^T \mathbf{C}_i^{*\top} z_i \mathbf{I}_0 dt. \quad (\text{C.6})$$

Thus, we define the adjoint system in a judicious manner to provide a convenient expression for the directional derivative as

$$\frac{d}{dt} \mathbf{C}^{*\top} = (\mathbf{w} \mathbf{r}(t; \boldsymbol{\beta}))^\top - \mathbf{C}^{*\top} \widehat{\mathbf{A}},$$

$$\mathbf{C}^*(T) = \mathbf{0}. \quad (\text{C.7})$$

Note that different adjoint systems defined for each adjoint vector  $\mathbf{C}_i^*$ ,  $i \in \{1, 2, 3, 4\}$  are identical, and hence, the subscript  $i$  is removed. Consequently, with this definition of the adjoint system equation (C.6) reduces to

$$\mathcal{J}'_1(\boldsymbol{\beta}; \beta'_i) = - \int_0^T \mathbf{C}^{*\top} \mathbf{I}_i \beta'_i \widehat{\mathbf{C}} dt - \int_0^T \mathbf{C}^{*\top} z_i \mathbf{I}_0 dt. \quad (\text{C.8})$$

Note that we can also compute the directional derivative as  $\mathcal{J}'_1(\boldsymbol{\beta}; \beta'_i) = \partial \mathcal{J}_1 / \partial \beta_i \cdot \beta'_i$ . Thus, the gradient of cost functional is obtained as

$$\nabla_{\boldsymbol{\beta}} \mathcal{J}_1 = \left[ -\int_0^T \mathbf{C}^{*\top} \mathbf{I}_0 dt \quad -\int_0^T \mathbf{C}^{*\top} \mathbf{I}_2 \widehat{\mathbf{C}} dt \quad -\int_0^T \mathbf{C}^{*\top} \mathbf{I}_3 \widehat{\mathbf{C}} dt \quad -\int_0^T \mathbf{C}^{*\top} \mathbf{I}_4 \widehat{\mathbf{C}} dt \right]. \quad (\text{C.9})$$

## C.2. Model Validation

### C.2.1 Validation of Gradients

To validate the derivation and computation of the gradients computed using adjoint analysis we will compare the adjoint-based expression for the Gateaux differential, cf. (4.53) and (4.63), with a finite-difference approximation of the differential. In order to determine the consistency of the gradients, we define the ratio of the directional derivative evaluated as described above for each of the gradients as

$$\begin{aligned} \kappa_1(\epsilon) &= \frac{\epsilon^{-1} [\mathcal{J}_2(\alpha, \omega_1 + \epsilon \omega'_1, \omega_2) - \mathcal{J}_2(\alpha, \omega_1, \omega_2)]}{\int_{C_1^\alpha}^{C_1^\beta} \nabla_{\omega_1}^{L^2} \mathcal{J}_2 \cdot \omega'_1 ds}, \\ \kappa_2(\epsilon) &= \frac{\epsilon^{-1} [\mathcal{J}_2(\alpha, \omega_1, \omega_2 + \epsilon \omega'_2) - \mathcal{J}_2(\alpha, \omega_1, \omega_2)]}{\int_{C_2^\alpha}^{C_2^\beta} \nabla_{\omega_2}^{L^2} \mathcal{J}_2 \cdot \omega'_2 ds}, \\ \kappa_3(\epsilon) &= \frac{\epsilon^{-1} [\mathcal{J}_2(\alpha + \epsilon \alpha', \omega_1, \omega_2) - \mathcal{J}_2(\alpha, \omega_1, \omega_2)]}{\frac{\partial \mathcal{J}_2}{\partial \alpha} \cdot \alpha'}, \end{aligned} \quad (\text{C.10})$$

which we will refer to as the  $\kappa$ -test. We note that either functional spaces,  $L^2$  or  $H^1$ , could be used to evaluate the expressions in the denominator and for simplicity we choose the  $L^2$  gradients here. When the gradients are approximated correctly, the quantities  $\kappa_1$ ,  $\kappa_2$  and  $\kappa_3$  should be close to unity for a broad range of  $\epsilon$  values. However, these quantities deviate from the unity for very small or very large values of  $\epsilon$  due to round-off and truncation errors, respectively, which are well-understood effects. The results of the  $\kappa$ -test are demonstrated in Figure C.1. In this test, two different discretizations of the interval  $\mathcal{L}$  are used. In Figures C.1a,b we see that, as expected, when the discretization  $N$  of the state interval  $\mathcal{L}$  is refined, the quantities  $\kappa_1(\epsilon)$  and  $\kappa_2(\epsilon)$  approach unity for a broad range of values of epsilon  $\epsilon$ . This trend is absent from Figure C.1c, since approximation of the derivative (4.63) does not depend on the discretization of the interval  $\mathcal{L}$ . The results of constructing the  $L^2$  and  $H^1$  gradients of the constitutive relations in the first iteration of the Algorithm 3 are demonstrated in Figure C.2, with  $\omega_1^{(0)} = \omega_2^{(0)} = 0.7$  and  $\alpha^{(0)} = 3$  as the initial guess and 5000 grid points in the  $\mathcal{L}$  interval. Note that  $\boldsymbol{\beta} = [-0.1, -0.1, -0.1, -0.1]$  in this experiment. As it can be observed in Figure C.2, the  $L^2$  gradients are discontinuous and vanish outside the identifiability region (the discontinuity occurs on the boundary of the identifiability region). However,

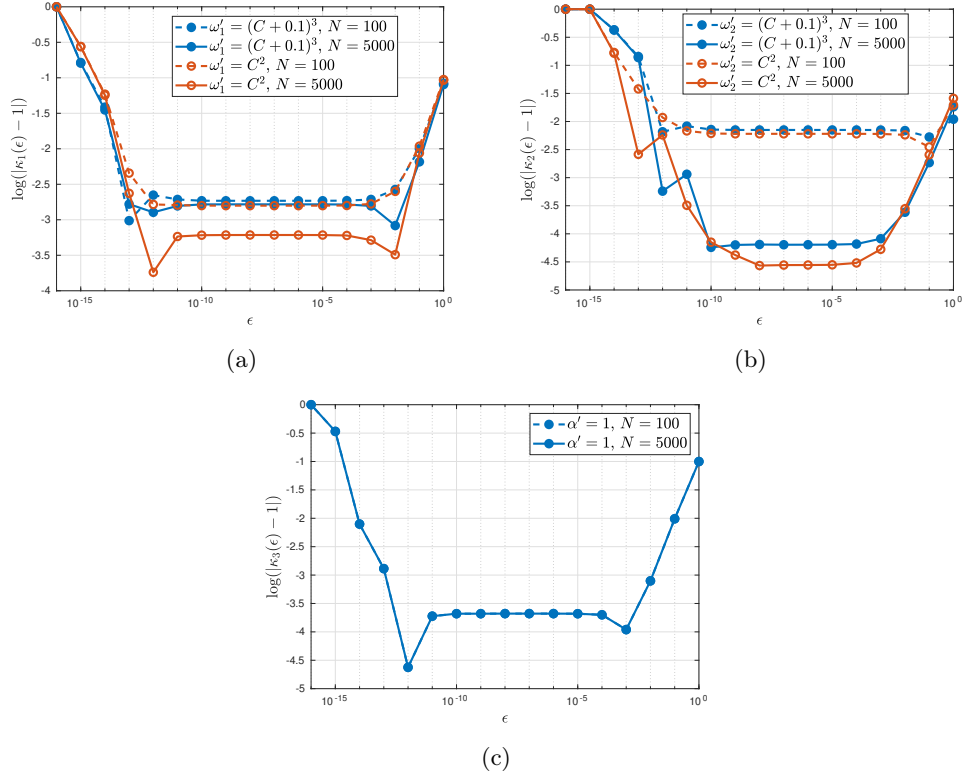


Figure C.1: The behaviour of  $\kappa_1(\epsilon)$  (a),  $\kappa_2(\epsilon)$  (b), and  $\kappa_3(\epsilon)$  (c), over a wide range of  $\epsilon$  values, by using  $\omega_1^{(0)} = \omega_2^{(0)} = 0.7$ ,  $\alpha^{(0)} = 3$  as the starting point, and using different perturbations of constitutive relations and parameters. Two different discretizations of the interval  $\mathcal{L}$  are used, namely,  $N = 100$  (dashed lines) and  $N = 5000$  (solid lines). Note that discretization of the state interval  $\mathcal{L}$  does not affect the quantity  $\kappa_3(\epsilon)$ , as its partial derivative (4.63) is computed without discretizing the state space  $\mathcal{L}$ . Note that  $\beta = [-0.1, -0.1, -0.1, -0.1]$  in this experiment.

the  $H^1$  gradients behave well outside the identifiability region where their behavior is determined by the choice of the boundary conditions in (4.67) and (4.68) whereas their smoothness is controlled by the parameter  $l$  in the definition of the  $H^1$  inner product (4.64). A Neumann boundary condition, and a smoothing parameter of  $l = 1$  is used for this experiment.

### C.2.2 Validation of Computational Framework

In order to validate the computational framework, one can manufacture synthetic "experimental" data using some assumed forms of the constitutive relations and parameter values, and then seek to reconstruct them based on the manufactured data using Algorithm 3, starting from arbitrary initial guesses. One can assume an arbitrary functional form of the factors  $\omega_1$  and  $\omega_2$  defining the constitutive relation, along with an arbitrary parameter  $\alpha$ . Subsequently, synthetic experimental concentrations can be manufactured based on these assumed functional forms and parameters. Finally, the manufactured experimental concentrations can be employed to reconstruct the "unknown" parameters and relations optimally. By

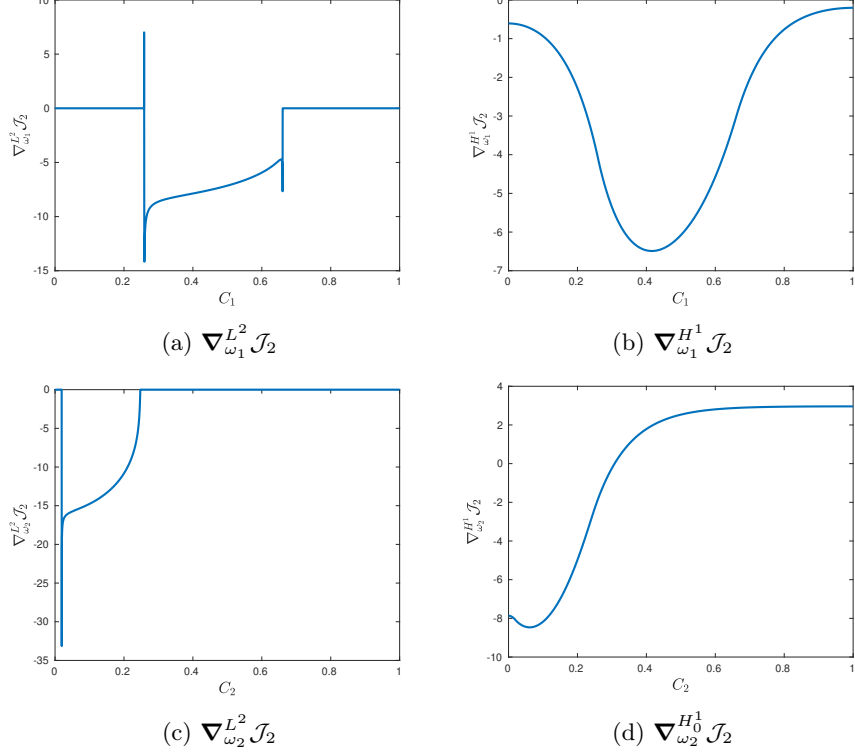


Figure C.2:  $\nabla_{\omega_1}^{L^2} \mathcal{J}_2$  (a),  $\nabla_{\omega_2}^{L^2} \mathcal{J}_2$  (c),  $\nabla_{\omega_1}^{H^1} \mathcal{J}_2$  (b), and  $\nabla_{\omega_2}^{H^1} \mathcal{J}_2$  (d) at the first iteration of Algorithm 3. Note the mean of the gradient in (d), as it is reconstructed in  $H_0^1$  space.

comparing the reconstructed relations to their assumed forms, this process allows for the validation of the proposed methodology and ensures its effectiveness under controlled conditions. Note that for the purpose of computational validation, we only perform the validation on the adjoint analysis of the excitation dynamics (stage II of Algorithm 3) as it is computationally more complex. The analogous tests have also been performed for the relaxation dynamics, but are omitted here due to the simpler nature of the problem. Figure C.5 demonstrates the assumed functional forms of the factors determining the constitutive relation and the resulting relation. Also, the optimal parameter value is chosen as  $\alpha = 5$  for this experiment. Based on the forms of the constitutive relations presented in Figure C.5, the corresponding manufactured concentrations with some arbitrary initial conditions will be generated, as shown in Figure C.4. This data will be used as the "true" data for computation of cost functionals in the current section.

The results of the optimal reconstruction of the constitutive relations are presented in Figure C.5, along with their "true" forms. In this experiment the initial guesses of the algorithm are chosen as  $\omega_1^{(0)} = 0.4$ ,  $\omega_2^{(0)} = 0.85$  and  $\alpha^{(0)} = 0.1$ . Algorithm 3 is terminated when the relative decrease of the objective functional between two consecutive iterations becomes smaller than a prescribed tolerance ( $TOL = 10^{-6}$ ) or the maximum number of iterations ( $N = 300$ ) has been exceeded. Note that the mean squared

error for the omega relation between the true and the reconstructed one is defined as

$$\mathcal{E}(\omega) = \frac{1}{(C_1^b - C_1^a)(C_2^b - C_2^a)} \int_{C_1^a}^{C_1^b} \int_{C_2^a}^{C_2^b} [\omega(C_1, C_2) - \tilde{\omega}]^2 dC_2 dC_1. \quad (\text{C.11})$$

The performance of the algorithm is illustrated in Figure C.3, in which the mean squared error of the reconstruction of  $\omega$  with iterations, the relative decay of cost functional with respect to its initial value, and the evolution of the parameter  $\alpha$  with iterations are plotted. As can be observed, the parameter  $\alpha$  is approaching to its true value,  $\alpha = 5$ .

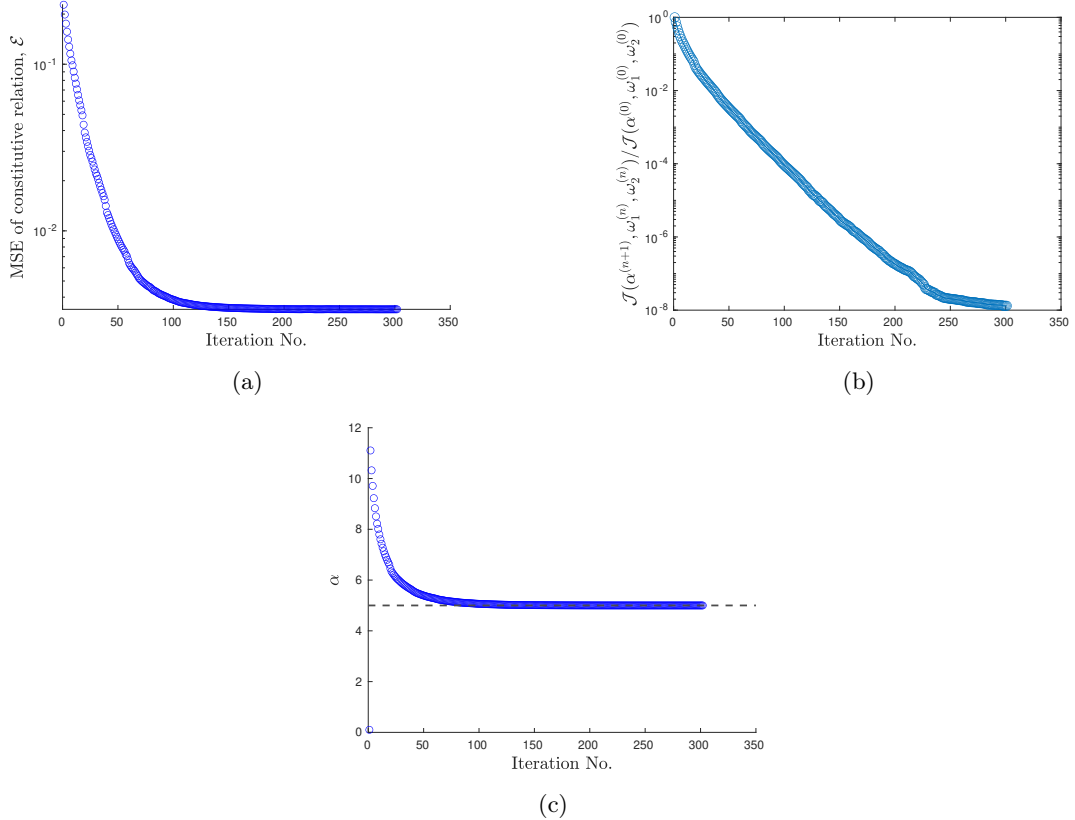


Figure C.3: Performance evaluation of the iterative algorithm according to Algorithm 3. The mean squared error between the true and the reconstructed constitutive relations (a), the relative decay of cost functional normalized with respect to its initial value (b), and the evolution of parameter  $\alpha$  (c) are shown as functions of iterations  $n$ .

The time histories of concentrations corresponding to the true constitutive relations  $\tilde{C}_1(t; \tilde{\alpha}, \tilde{\omega}_1, \tilde{\omega}_2)$  and  $\tilde{C}_2(t; \tilde{\alpha}, \tilde{\omega}_1, \tilde{\omega}_2)$ , the time evolution of concentrations corresponding to the initial guess of parameter and relations  $C_1(t; \alpha^{(0)}, \omega_1^{(0)}, \omega_2^{(0)})$  and  $C_2(t; \alpha^{(0)}, \omega_1^{(0)}, \omega_2^{(0)})$ , and the time evolution of concentrations corresponding to the optimal reconstructed relations  $C_1(t; \bar{\alpha}, \bar{\omega}_1, \bar{\omega}_2)$  and  $C_2(t; \bar{\alpha}, \bar{\omega}_1, \bar{\omega}_2)$  are shown in Figure C.4. As can be observed, the model (4.37) equipped with the optimally reconstructed constitu-

tive relations and parameters can very well predict the time evolution of concentrations. The optimal

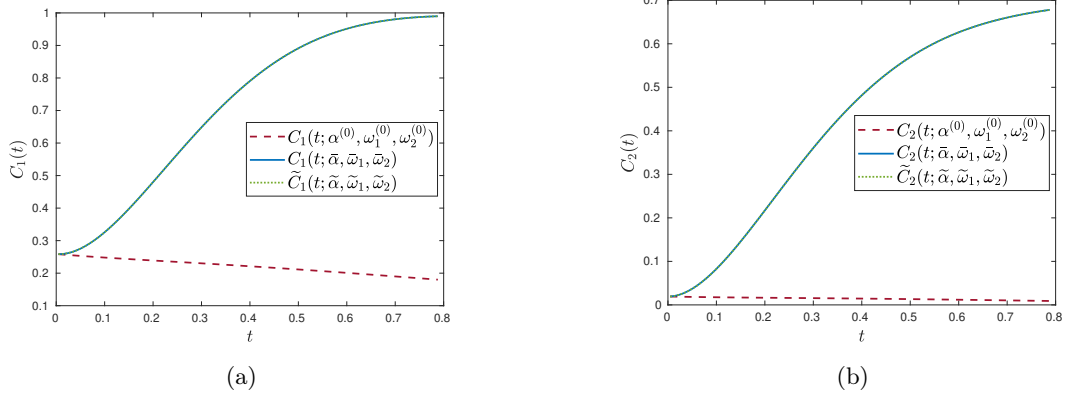


Figure C.4: Time history of concentrations  $C_1(t)$  (a) and  $C_2(t)$  (b) obtained using the true parameter and constitutive relations (dotted green line), the initial guess of parameter and relations (dashed red line), and the optimal reconstructed parameter and relations (solid blue line).

reconstruction of constitutive relation is demonstrated in Figure C.5. As can be observed, there are slight differences between the true and the reconstructed relations, however, the time evolution of concentrations matches the true data very accurately, cf. Figure C.4. This provides information about the degree of sensitivity of the concentrations to the form of constitutive relations. Comparing the initial guess for constitutive relation  $\omega^{(0)}$  to its optimal reconstruction  $\bar{\omega}$ , it is clear that there is a significant improvement. The small differences between the true and the reconstructed relations have two main reasons. First, the sensitivity of the concentrations to the constitutive relations is small, meaning that small perturbations in constitutive relation will not have significant impact on the results. This is a measure of the ill-posedness of the inverse problem (4.44). Second, the constitutive relations are extended beyond the identifiability region based on some boundary conditions that might not be completely correct. For this reason, the deviation between the reconstructed function and the true one beyond the identifiability region becomes larger. This concludes the validation of the computational framework. It is shown that the computational framework is capable of reconstructing constitutive relations to minimize the mismatch between experimental and predicted concentrations.

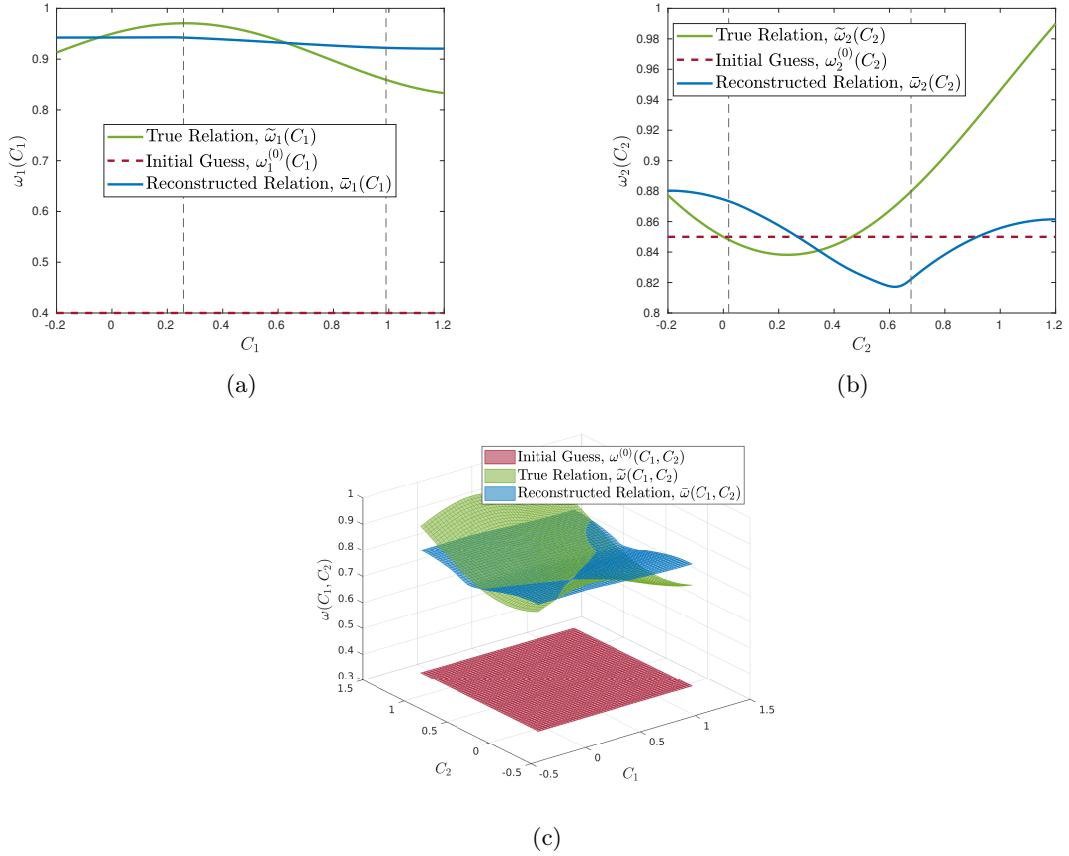


Figure C.5: Constitutive relations (a)  $\omega_1(C_1)$ , (b)  $\omega_2(C_2)$ , and (c)  $\omega(C_1, C_2)$ . Optimally reconstructed constitutive relations  $\bar{\omega}$  (blue), along with the initial guess of relations  $\omega^{(0)}$  (red) and the true relations  $\tilde{\omega}$  (green) are shown. Note that grey vertical lines in panels (a) and (b) denote the identifiability region for the last iteration of the Algorithm 3.

## **Bibliography**

- [1] K. J. Harris, J. M. Foster, M. Z. Tessaro, M. Jiang, X. Yang, Y. Wu, B. Protas, and G. R. Goward, “Structure Solution of Metal-Oxide Li Battery Cathodes from Simulated Annealing and Lithium NMR Spectroscopy,” *Chemistry of Materials*, vol. 29, no. 13, pp. 5550–5557, 2017.
- [2] Y. Liang, C.-Z. Zhao, H. Yuan, Y. Chen, W. Zhang, J.-Q. Huang, D. Yu, Y. Liu, M.-M. Titirici, Y.-L. Chueh *et al.*, “A review of rechargeable batteries for portable electronic devices,” *InfoMat*, vol. 1, no. 1, pp. 6–32, 2019.
- [3] M. Rouholamini, C. Wang, H. Nehrir, X. Hu, Z. Hu, H. Aki, B. Zhao, Z. Miao, and K. Strunz, “A review of modeling, management, and applications of grid-connected Li-ion battery storage systems,” *IEEE Transactions on Smart Grid*, vol. 13, no. 6, pp. 4505–4524, 2022.
- [4] M. A. Hannan, M. M. Hoque, A. Hussain, Y. Yusof, and P. J. Ker, “State-of-the-art and energy management system of Lithium-ion batteries in electric vehicle applications: Issues and recommendations,” *Ieee Access*, vol. 6, pp. 19 362–19 378, 2018.
- [5] N. Mohamed and N. K. Allam, “Recent advances in the design of cathode materials for Li-ion batteries,” *Rsc Advances*, vol. 10, no. 37, pp. 21 662–21 685, 2020.
- [6] S. Goriparti, E. Miele, F. De Angelis, E. Di Fabrizio, R. P. Zaccaria, and C. Capiglia, “Review on recent progress of nanostructured anode materials for Li-ion batteries,” *Journal of power sources*, vol. 257, pp. 421–443, 2014.
- [7] M. Kabir and D. E. Demirocak, “Degradation mechanisms in Li-ion batteries: a state-of-the-art review,” *International Journal of Energy Research*, vol. 41, no. 14, pp. 1963–1986, 2017.
- [8] J. S. Edge, S. O’Kane, R. Prosser, N. D. Kirkaldy, A. N. Patel, A. Hales, A. Ghosh, W. Ai, J. Chen, J. Yang *et al.*, “Lithium ion battery degradation: what you need to know,” *Physical Chemistry Chemical Physics*, vol. 23, no. 14, pp. 8200–8221, 2021.

- [9] C. Pastor-Fernández, T. F. Yu, W. D. Widanage, and J. Marco, “Critical review of non-invasive diagnosis techniques for quantification of degradation modes in Lithium-ion batteries,” *Renewable and Sustainable Energy Reviews*, vol. 109, pp. 138–159, 2019.
- [10] Z. Deng, X. Lin, Z. Huang, J. Meng, Y. Zhong, G. Ma, Y. Zhou, Y. Shen, H. Ding, and Y. Huang, “Recent progress on advanced imaging techniques for Lithium-ion batteries,” *Advanced Energy Materials*, vol. 11, no. 2, p. 2000806, 2021.
- [11] R. Mehta and A. Gupta, “Mathematical modelling of electrochemical, thermal and degradation processes in Lithium-ion cells—A comprehensive review,” *Renewable and Sustainable Energy Reviews*, vol. 192, p. 114264, 2024.
- [12] Z. Chen, D. L. Danilov, R.-A. Eichel, and P. H. Notten, “Porous electrode modeling and its applications to Li-ion batteries,” *Advanced Energy Materials*, vol. 12, no. 32, p. 2201506, 2022.
- [13] U. Janakiraman, T. R. Garrick, and M. E. Fortier, “Lithium plating detection methods in Li-ion batteries,” *Journal of The Electrochemical Society*, vol. 167, no. 16, p. 160552, 2020.
- [14] U. Westerhoff, K. Kurbach, F. Lienesch, and M. Kurrat, “Analysis of Lithium-ion battery models based on electrochemical impedance spectroscopy,” *Energy Technology*, vol. 4, no. 12, pp. 1620–1630, 2016.
- [15] S. J. Navas, G. C. González, F. Pino, and J. Guerra, “Modelling Li-ion batteries using equivalent circuits for renewable energy applications,” *Energy Reports*, vol. 9, pp. 4456–4465, 2023.
- [16] J. Newman and N. P. Balsara, *Electrochemical systems*. John Wiley & Sons, 2021.
- [17] C. Lv, X. Zhou, L. Zhong, C. Yan, M. Srinivasan, Z. W. Seh, C. Liu, H. Pan, S. Li, Y. Wen *et al.*, “Machine learning: an advanced platform for materials development and state prediction in Lithium-ion batteries,” *Advanced Materials*, vol. 34, no. 25, p. 2101474, 2022.
- [18] Y. Zhang and Y.-F. Li, “Prognostics and health management of Lithium-ion battery using deep learning methods: A review,” *Renewable and sustainable energy reviews*, vol. 161, p. 112282, 2022.
- [19] H. Tu, S. Moura, Y. Wang, and H. Fang, “Integrating physics-based modeling with machine learning for Lithium-ion batteries,” *Applied energy*, vol. 329, p. 120289, 2023.

- [20] S. Singh, Y. E. Ebongue, S. Rezaei, and K. P. Birke, “Hybrid modeling of Lithium-ion battery: Physics-informed neural network for battery state estimation,” *Batteries*, vol. 9, no. 6, p. 301, 2023.
- [21] J. Kaipio and E. Somersalo, *Statistical and computational inverse problems*. Springer Science & Business Media, 2006, vol. 160.
- [22] S. Zhang, Z. Liu, X. Zhang, X. Wu, G. Han, Y. Zhao, X. Yu, C. Liu, Y. Liu, S. Wu *et al.*, “Coupled data assimilation and parameter estimation in coupled ocean–atmosphere models: a review,” *Climate Dynamics*, vol. 54, pp. 5127–5144, 2020.
- [23] D. S. Oliver, A. C. Reynolds, and N. Liu, *Inverse theory for petroleum reservoir characterization and history matching*, 2008.
- [24] M. Raissi, P. Perdikaris, and G. E. Karniadakis, “Physics-informed neural networks: A deep learning framework for solving forward and inverse problems involving nonlinear partial differential equations,” *Journal of Computational physics*, vol. 378, pp. 686–707, 2019.
- [25] P. Matharu and B. Protas, “Optimal closures in a simple model for turbulent flows,” *SIAM Journal on Scientific Computing*, vol. 42, no. 1, pp. B250–B272, 2020.
- [26] S. R. Arridge, “Optical tomography in medical imaging,” *Inverse problems*, vol. 15, no. 2, p. R41, 1999.
- [27] A. K. Sethurajan, S. A. Krachkovskiy, I. C. Halalay, G. R. Goward, and B. Protas, “Accurate characterization of ion transport properties in binary symmetric electrolytes using in situ NMR imaging and inverse modeling,” *The Journal of Physical Chemistry B*, vol. 119, no. 37, pp. 12 238–12 248, 2015.
- [28] A. Jokar, B. Rajabloo, M. Désilets, and M. Lacroix, “An inverse method for estimating the electrochemical parameters of Lithium-ion batteries,” *Journal of The Electrochemical Society*, vol. 163, no. 14, p. A2876, 2016.
- [29] A. K. Sethurajan, J. M. Foster, G. Richardson, S. A. Krachkovskiy, J. D. Bazak, G. R. Goward, and B. Protas, “Incorporating Dendrite Growth into Continuum Models of Electrolytes: Insights from NMR Measurements and Inverse Modeling,” *Journal of The Electrochemical Society*, vol. 166, no. 8, pp. A1591–A1602, 2019.

- [30] J. M. Escalante, W. Ko, J. M. Foster, S. Krachkovskiy, G. Goward, and B. Protas, “Discerning models of phase transformations in porous graphite electrodes: Insights from inverse modelling based on MRI measurements,” *Electrochimica Acta*, vol. 349, p. 136290, 2020.
- [31] L. Daniels, S. Sahu, K. J. Sanders, G. R. Goward, J. M. Foster, and B. Protas, “Learning Optimal Forms of Constitutive Relations Characterizing Ion Intercalation from Data in Mathematical Models of Lithium-Ion Batteries,” *The Journal of Physical Chemistry C*, vol. 127, no. 35, pp. 17 508–17 523, 2023.
- [32] A. Ahmadi, J. M. Foster, and B. Protas, “Data-driven optimal closures for mean-cluster models: Beyond the classical pair approximation,” *Physical Review E*, vol. 106, no. 2, p. 025313, 2022.
- [33] A. Sethurajan, S. Krachkovskiy, G. Goward, and B. Protas, “Bayesian uncertainty quantification in inverse modeling of electrochemical systems,” *Journal of Computational Chemistry*, vol. 40, no. 5, pp. 740–752, 2019.
- [34] J. M. Escalante, S. Sahu, J. M. Foster, and B. Protas, “On uncertainty quantification in the parametrization of Newman-type models of Lithium-ion batteries,” *Journal of The Electrochemical Society*, vol. 168, no. 11, p. 110519, 2021.
- [35] A. Maheshwari, M. A. Dumitrescu, M. Destro, and M. Santarelli, “Inverse parameter determination in the development of an optimized Lithium iron phosphate–Graphite battery discharge model,” *Journal of Power Sources*, vol. 307, pp. 160–172, 2016.
- [36] M. Kespe, M. Gleiß, S. Hammerich, and H. Nirschl, “Numerical optimization of the spatial conductivity distribution within cathode microstructures of Lithium-ion batteries considering the cell performance,” *International Journal of Energy Research*, vol. 41, no. 14, pp. 2282–2296, 2017.
- [37] V. Bukshtynov, O. Volkov, and B. Protas, “On optimal reconstruction of constitutive relations,” *Physica D: Nonlinear Phenomena*, vol. 240, no. 16, pp. 1228 – 1244, 2011.
- [38] V. Bukshtynov and B. Protas, “Optimal reconstruction of material properties in complex multi-physics phenomena,” *Journal of Computational Physics*, vol. 242, pp. 889 – 914, 2013.
- [39] A. M. Stuart, “Inverse problems: a Bayesian perspective,” *Acta numerica*, vol. 19, pp. 451–559, 2010.
- [40] A. M. Ellison, “Bayesian inference in ecology,” *Ecology letters*, vol. 7, no. 6, pp. 509–520, 2004.

- [41] U. Von Toussaint, “Bayesian inference in physics,” *Reviews of Modern Physics*, vol. 83, no. 3, pp. 943–999, 2011.
- [42] M. Hasenbusch, “Monte Carlo studies of the three-dimensional Ising model in equilibrium,” *International Journal of Modern Physics C*, vol. 12, no. 07, pp. 911–1009, 2001.
- [43] J. Strecka and M. Jascur, “A brief account of the Ising and Ising-like models: Mean-field, effective-field and exact results,” *arXiv: Statistical Mechanics*, 2015.
- [44] H. Matsuda, N. Ogita, A. Sasaki, and K. Sato, “Statistical Mechanics of Population: The Lattice Lotka-Volterra Model,” *Progress of Theoretical Physics*, vol. 88, no. 6, pp. 1035–1049, 1992.
- [45] Y. Harada and Y. Iwasa, “Lattice population dynamics for plants with dispersing seeds and Vegetative propagation,” *Researches on Population Ecology*, vol. 36, no. 2, pp. 237–249, 1994.
- [46] D. H. Silva, F. A. Rodrigues, and S. C. Ferreira, “High prevalence regimes in the pair-quenched mean-field theory for the susceptible-infected-susceptible model on networks,” *Physical Review E*, vol. 102, no. 1, pp. 1–9, 2020.
- [47] M. J. Keeling, “The effects of local spatial structure on epidemiological invasions,” *The Structure and Dynamics of Networks*, vol. 9781400841, no. 1421, pp. 480–488, 2011.
- [48] K. T. Eames and M. J. Keeling, “Modeling dynamic and network heterogeneities in the spread of sexually transmitted diseases,” *Proceedings of the National Academy of Sciences of the United States of America*, vol. 99, no. 20, pp. 13 330–13 335, 2002.
- [49] T. B. Pedro, W. Figueiredo, and A. L. Ferreira, “Mean-field theory for the long-range contact process with diffusion,” *Physical Review E - Statistical, Nonlinear, and Soft Matter Physics*, vol. 92, no. 3, pp. 1–7, 2015.
- [50] K. Satō, H. Matsuda, and A. Sasaki, “Pathogen invasion and host extinction in lattice structured populations,” *Journal of Mathematical Biology*, vol. 32, no. 3, pp. 251–268, 1994.
- [51] M. J. Keeling, D. A. Rand, and A. J. Morris, “Correlation models for childhood epidemics,” *Proceedings of the Royal Society B: Biological Sciences*, vol. 264, no. 1385, pp. 1149–1156, 1997.
- [52] C. T. Bauch, “The spread of infectious diseases in spatially structured populations: An invasory pair approximation,” *Mathematical Biosciences*, vol. 198, no. 2, pp. 217–237, 2005.

- [53] M. M. De Oliveira, S. G. Alves, and S. C. Ferreira, “Dynamical correlations and pairwise theory for the symbiotic contact process on networks,” *Physical Review E*, vol. 100, no. 5, p. 52302, 2019.
- [54] A. S. Mata and S. C. Ferreira, “Pair quenched mean-field theory for the susceptible-infected-susceptible model on complex networks,” *Europhysics Letters*, vol. 103, no. 4, p. 48003, 2013.
- [55] Z. H. Lin, M. Feng, M. Tang, Z. Liu, C. Xu, P. M. Hui, and Y. Lai, “Non-Markovian recovery makes complex networks more resilient against large-scale failures,” *Nature Communications*, vol. 11, no. 1, pp. 1–10, 2020.
- [56] X. Pei, X. X. Zhan, and Z. Jin, “Application of pair approximation method to modeling and analysis of a marriage network,” *Applied Mathematics and Computation*, vol. 294, pp. 280–293, 2017.
- [57] D. Ben-Avraham and J. Köhler, “Mean-field (n,m)-cluster approximation for lattice models,” *Physical Review A*, vol. 45, no. 12, pp. 8358–8370, 1992.
- [58] T. Morita, “Pair (Bethe) approximation applied to a frustrated Ising model,” *Physics Letters A*, vol. 132, no. 1, pp. 1–3, 1988.
- [59] M. Tamashiro and S. Salinas, “Bethe-Peierls approximation for the triangular Ising antiferromagnet in a field,” *Physical Review B*, vol. 56, no. 13, p. 8241, 1997.
- [60] A. Pelizzola, “Cluster variation method in statistical physics and probabilistic graphical models,” *Journal of Physics A: Mathematical and General*, vol. 38, no. 33, p. R309, 2005.
- [61] K. E. Sugden and M. R. Evans, “A dynamically extending exclusion process,” *Journal of Statistical Mechanics: Theory and Experiment*, vol. 2007, no. 11, 2007.
- [62] J. Joo and J. L. Lebowitz, “Pair approximation of the stochastic susceptible-infected-recovered-susceptible epidemic model on the hypercubic lattice,” *Physical Review E - Statistical Physics, Plasmas, Fluids, and Related Interdisciplinary Topics*, vol. 70, no. 3, p. 9, 2004.
- [63] A. S. Mata, R. S. Ferreira, and S. C. Ferreira, “Heterogeneous pair-approximation for the contact process on complex networks,” *New Journal of Physics*, vol. 16, 2014.
- [64] J. A. Filipe and M. M. Maule, “Analytical methods for predicting the behaviour of population models with general spatial interactions,” *Mathematical Biosciences*, vol. 183, no. 1, pp. 15–35, 2003.

- [65] D. H. Seo, J. Lee, A. Urban, R. Malik, S. Kang, and G. Ceder, “The structural and chemical origin of the oxygen redox activity in layered and cation-disordered Li-excess cathode materials,” *Nature Chemistry*, vol. 8, no. 7, pp. 692–697, 2016.
- [66] A. K. Shukla, Q. M. Ramasse, C. Ophus, H. Duncan, F. Hage, and G. Chen, “Unravelling structural ambiguities in Lithium- and Manganese-rich transition metal oxides,” *Nature Communications*, vol. 6, no. May, pp. 1–9, 2015.
- [67] J. Lisiecki and P. Szabelski, “Designing 2D covalent networks with lattice Monte Carlo simulations: precursor self-assembly,” *Physical Chemistry Chemical Physics*, vol. 23, no. 10, pp. 5780–5796, 2021.
- [68] F. O. Sanchez-Varretti, F. M. Bulnes, and A. J. Ramirez-Pastor, “Order and disorder in the adsorption model of repulsively interacting binary mixtures on triangular lattices: theory and Monte Carlo simulations,” *European Physical Journal E*, vol. 44, no. 3, 2021.
- [69] H.-A. Chen, P.-H. Tang, G.-J. Chen, C.-C. Chang, and C.-W. Pao, “Microstructure Maps of Complex Perovskite Materials from Extensive Monte Carlo Sampling Using Machine Learning Enabled Energy Model,” *The Journal of Physical Chemistry Letters*, vol. 12, no. 14, pp. 3591–3599, 2021.
- [70] R. Dickman, “Kinetic phase transitions in a surface-reaction model: Mean-field theory,” *Physical review. A, General physics*, vol. 34, 1986.
- [71] K. Satō and Y. Iwasa, “Pair Approximations for Lattice-based Ecological Models,” in *The Geometry of Ecological Interactions*. Cambridge University Press, may 2000, pp. 341–358.
- [72] M. van Baalen, “Pair Approximations for Different Spatial Geometries,” in *The Geometry of Ecological Interactions*. Cambridge University Press, may 2000, pp. 359–387.
- [73] J. Morris, Andrew, “Representing spatial interactions in simple ecological models,” PhD, University of Warwick, 1997.
- [74] J. Nocedal and S. Wright, *Numerical Optimization*. Springer, 2002.
- [75] Q. Zhou, T. Yu, X. Zhang, and J. Li, “Bayesian inference and uncertainty quantification for medical image reconstruction with poisson data,” *SIAM Journal on Imaging Sciences*, vol. 13, no. 1, pp. 29–52, 2019.

- [76] S. Huo, “Bayesian Modeling of Complex High-Dimensional Data Bayesian Modeling of Complex High-Dimensional Data,” Ph.D. dissertation, Virginia Polytechnic Institute and State University, 2020.
- [77] M. Laine, “Adaptive MCMC methods with applications in environmental and geophysical models,” Ph.D. dissertation, Lappeenranta University of technology, 2008.
- [78] D. D. Lucas, M. Simpson, P. Cameron-Smith, and R. L. Baskett, “Bayesian inverse modeling of the atmospheric transport and emissions of a controlled tracer release from a nuclear power plant,” *Atmospheric Chemistry and Physics*, vol. 17, no. 22, pp. 13 521–13 543, 2017.
- [79] O. Camli and Z. Kalaylioglu, “Bayesian predictive model selection in circular random effects models with applications in ecological and environmental studies,” *Environmental and Ecological Statistics*, 2020.
- [80] S. Mignani and R. Rosa, “Markov Chain Monte Carlo in Stastical Mechanics: The Problem of Accuracy,” *Technometrics*, vol. 43, no. 3, pp. 347–355, 2001.
- [81] A. Tarantola, *Inverse Problem Theory and Methods for Model Parameter Estimation*. SIAM, 2005.
- [82] R. Smith, *Uncertainty Quantification: Theory, Implementation, and Applications*. SIAM, 2013.
- [83] R. C. Aster, B. Borchers, and C. H. Thurber, *Parameter estimation and inverse problems*. Elsevier, 2018.
- [84] Q. Liu, C. Du, B. Shen, P. Zuo, X. Cheng, Y. Ma, G. Yin, and Y. Gao, “Understanding undesirable anode Lithium plating issues in Lithium-ion batteries,” *RSC advances*, vol. 6, no. 91, pp. 88 683–88 700, 2016.
- [85] J. Zhao, Y. Zhu, B. Zhang, M. Liu, J. Wang, C. Liu, and X. Hao, “Review of State Estimation and Remaining Useful Life Prediction Methods for Lithium–Ion Batteries,” *Sustainability*, vol. 15, no. 6, p. 5014, 2023.
- [86] I. B. Espedal, A. Jinasena, O. S. Burheim, and J. J. Lamb, “Current trends for state-of-charge (SoC) estimation in Lithium-ion battery electric vehicles,” *Energies*, vol. 14, no. 11, p. 3284, 2021.

- [87] D. N. How, M. Hannan, M. H. Lipu, and P. J. Ker, “State of charge estimation for Lithium-ion batteries using model-based and data-driven methods: A review,” *Ieee Access*, vol. 7, pp. 136 116–136 136, 2019.
- [88] W. Zhou, Y. Zheng, Z. Pan, and Q. Lu, “Review on the battery model and SoC estimation method,” *Processes*, vol. 9, no. 9, p. 1685, 2021.
- [89] R. Zhang, B. Xia, B. Li, L. Cao, Y. Lai, W. Zheng, H. Wang, and W. Wang, “State of the art of lithium-ion battery SOC estimation for electrical vehicles,” *Energies*, vol. 11, no. 7, p. 1820, 2018.
- [90] M. Doyle, T. F. Fuller, and J. Newman, “Modeling of galvanostatic charge and discharge of the lithium/polymer/insertion cell,” *Journal of the Electrochemical society*, vol. 140, no. 6, p. 1526, 1993.
- [91] Z. Cui, L. Wang, Q. Li, and K. Wang, “A comprehensive review on the state of charge estimation for Lithium-ion battery based on Neural Network,” *International Journal of Energy Research*, vol. 46, no. 5, pp. 5423–5440, 2022.
- [92] P. Shrivastava, T. K. Soon, M. Y. I. B. Idris, and S. Mekhilef, “Overview of model-based online state-of-charge estimation using Kalman filter family for Lithium-ion batteries,” *Renewable and Sustainable Energy Reviews*, vol. 113, p. 109233, 2019.
- [93] M. Hossain, M. Haque, and M. Arif, “Kalman filtering techniques for the online model parameters and state of charge estimation of the Li-ion batteries: A comparative analysis,” *Journal of Energy Storage*, vol. 51, p. 104174, 2022.
- [94] H. R. Eichi and M.-Y. Chow, “Modeling and analysis of battery hysteresis effects,” in *2012 IEEE Energy Conversion Congress and Exposition (ECCE)*. IEEE, 2012, pp. 4479–4486.
- [95] F. B. Planella, W. Ai, A. Boyce, A. Ghosh, I. Korotkin, S. Sahu, V. Sulzer, R. Timms, T. Tranter, M. Zyskin *et al.*, “A continuum of physics-based Lithium-ion battery models reviewed,” *Progress in Energy*, 2022.
- [96] E. J. Dickinson and A. J. Wain, “The Butler-Volmer equation in electrochemical theory: Origins, value, and practical application,” *Journal of Electroanalytical Chemistry*, vol. 872, p. 114145, 2020.

- [97] W. Choi, H.-C. Shin, J. M. Kim, J.-Y. Choi, and W.-S. Yoon, “Modeling and applications of electrochemical impedance spectroscopy (EIS) for lithium-ion batteries,” *Journal of Electrochemical Science and Technology*, vol. 11, no. 1, pp. 1–13, 2020.
- [98] J. Kim and J. Kowal, “A Method for Monitoring State-of-Charge of Lithium-Ion Cells Using Multi-Sine Signal Excitation,” *Batteries*, vol. 7, no. 4, p. 76, 2021.
- [99] G. L. Plett, “Extended Kalman filtering for battery management systems of LiPB-based HEV battery packs: Part 3. State and parameter estimation,” *Journal of Power sources*, vol. 134, no. 2, pp. 277–292, 2004.
- [100] D. Di Domenico, A. Stefanopoulou, and G. Fiengo, “Lithium-ion battery state of charge and critical surface charge estimation using an electrochemical model-based extended Kalman filter,” *Journal of dynamic systems, measurement, and control*, vol. 132, no. 6, 2010.
- [101] H. He, R. Xiong, and H. Guo, “Online estimation of model parameters and state-of-charge of LiFePO<sub>4</sub> batteries in electric vehicles,” *Applied Energy*, vol. 89, no. 1, pp. 413–420, 2012.
- [102] X. Li, Z. Wang, and L. Zhang, “Co-estimation of capacity and state-of-charge for lithium-ion batteries in electric vehicles,” *Energy*, vol. 174, pp. 33–44, 2019.
- [103] Y. Shen, “Adaptive extended Kalman filter based state of charge determination for Lithium-ion batteries,” *Electrochimica Acta*, vol. 283, pp. 1432–1440, 2018.
- [104] Z. Chen, L. Yang, X. Zhao, Y. Wang, and Z. He, “Online state of charge estimation of Li-ion battery based on an improved unscented Kalman filter approach,” *Applied Mathematical Modelling*, vol. 70, pp. 532–544, 2019.
- [105] S. Zhang, C. Zhang, S. Jiang, and X. Zhang, “A comparative study of different adaptive extended/unscented Kalman filters for Lithium-ion battery state-of-charge estimation,” *Energy*, vol. 246, p. 123423, 2022.
- [106] Y. Wang, C. Zhang, and Z. Chen, “A method for state-of-charge estimation of LiFePO<sub>4</sub> batteries at dynamic currents and temperatures using particle filter,” *Journal of power sources*, vol. 279, pp. 306–311, 2015.
- [107] C. Chen, R. Xiong, and W. Shen, “A Lithium-ion battery-in-the-loop approach to test and validate multiscale dual H infinity filters for state-of-charge and capacity estimation,” *IEEE Transactions*

- on power Electronics*, vol. 33, no. 1, pp. 332–342, 2017.
- [108] Y. Liu, Y. He, H. Bian, W. Guo, and X. Zhang, “A review of Lithium-ion battery state of charge estimation based on deep learning: Directions for improvement and future trends,” *Journal of Energy Storage*, vol. 52, p. 104664, 2022.
  - [109] D. Jiménez-Bermejo, J. Fraile-Ardanuy, S. Castaño-Solis, J. Merino, and R. Alvaro-Hermana, “Using dynamic neural networks for battery state of charge estimation in electric vehicles,” *Procedia computer science*, vol. 130, pp. 533–540, 2018.
  - [110] M. Messing, T. Shoa, R. Ahmed, and S. Habibi, “Battery SoC estimation from EIS using neural nets,” in *2020 IEEE Transportation Electrification Conference & Expo (ITEC)*. IEEE, 2020, pp. 588–593.
  - [111] Z. Huang, F. Yang, F. Xu, X. Song, and K.-L. Tsui, “Convolutional gated recurrent unit–recurrent neural network for state-of-charge estimation of lithium-ion batteries,” *Ieee Access*, vol. 7, pp. 93 139–93 149, 2019.
  - [112] X. Song, F. Yang, D. Wang, and K.-L. Tsui, “Combined CNN-LSTM network for state-of-charge estimation of lithium-ion batteries,” *Ieee Access*, vol. 7, pp. 88 894–88 902, 2019.
  - [113] C. Qian, B. Xu, L. Chang, B. Sun, Q. Feng, D. Yang, Y. Ren, and Z. Wang, “Convolutional neural network based capacity estimation using random segments of the charging curves for lithium-ion batteries,” *Energy*, vol. 227, p. 120333, 2021.
  - [114] S. L. Brunton, J. L. Proctor, and J. N. Kutz, “Discovering governing equations from data by sparse identification of nonlinear dynamical systems,” *Proceedings of the national academy of sciences*, vol. 113, no. 15, pp. 3932–3937, 2016.
  - [115] S. L. Brunton, “Applying machine learning to study fluid mechanics,” *Acta Mechanica Sinica*, pp. 1–9, 2022.
  - [116] M. Dam, M. Brøns, J. Juul Rasmussen, V. Naulin, and J. S. Hesthaven, “Sparse identification of a predator-prey system from simulation data of a convection model,” *Physics of Plasmas*, vol. 24, no. 2, p. 022310, 2017.
  - [117] K. Fukami, T. Murata, K. Zhang, and K. Fukagata, “Sparse identification of nonlinear dynamics with low-dimensionalized flow representations,” *Journal of Fluid Mechanics*, vol. 926, 2021.

- [118] M. Hoffmann, C. Fröhner, and F. Noé, “Reactive SINDy: Discovering governing reactions from concentration data,” *The Journal of chemical physics*, vol. 150, no. 2, p. 025101, 2019.
- [119] N. M. Mangan, S. L. Brunton, J. L. Proctor, and J. N. Kutz, “Inferring biological networks by sparse identification of nonlinear dynamics,” *IEEE Transactions on Molecular, Biological and Multi-Scale Communications*, vol. 2, no. 1, pp. 52–63, 2016.
- [120] J. H. Horrocks, “Sparse identification of epidemiological models from empirical data,” Master’s thesis, University of Waterloo, 2018.
- [121] Y.-X. Jiang, X. Xiong, S. Zhang, J.-X. Wang, J.-C. Li, and L. Du, “Modeling and prediction of the transmission dynamics of COVID-19 based on the SINDy-LM method,” *Nonlinear Dynamics*, vol. 105, no. 3, pp. 2775–2794, 2021.
- [122] “pulsenics.com,” <https://www.pulsenics.com/hardware>.
- [123] D. Salazar and M. Garcia, “Estimation and comparison of SoC in batteries used in electromobility using the Thevenin model and Coulomb Ampere counting,” *Energies*, vol. 15, no. 19, p. 7204, 2022.
- [124] O. O. Solomon, W. Zheng, J. Chen, and Z. Qiao, “State of charge estimation of Lithium-ion battery using an improved fractional-order extended Kalman filter,” *Journal of Energy Storage*, vol. 49, p. 104007, 2022.
- [125] A. C. Lazanas and M. I. Prodromidis, “Electrochemical Impedance Spectroscopy - A Tutorial,” *ACS Measurement Science Au*, 2023.
- [126] C. Huang, Z. Wang, Z. Zhao, L. Wang, C. S. Lai, and D. Wang, “Robustness evaluation of extended and unscented Kalman filter for battery state of charge estimation,” *Ieee Access*, vol. 6, pp. 27 617–27 628, 2018.
- [127] U. Fasel, E. Kaiser, J. N. Kutz, B. W. Brunton, and S. L. Brunton, “Sindy with control: A tutorial,” in *2021 60th IEEE Conference on Decision and Control (CDC)*. IEEE, 2021, pp. 16–21.
- [128] J. N. Kutz, S. L. Brunton, B. W. Brunton, and J. L. Proctor, *Dynamic mode decomposition: data-driven modeling of complex systems*. SIAM, 2016.
- [129] S. L. Brunton, M. Budišić, E. Kaiser, and J. N. Kutz, “Modern koopman theory for dynamical systems,” *SIAM Review*, vol. 64, no. 2, pp. 229–340, 2022.

- [130] K. Champion, P. Zheng, A. Y. Aravkin, S. L. Brunton, and J. N. Kutz, “A unified sparse optimization framework to learn parsimonious physics-informed models from data,” *IEEE Access*, vol. 8, pp. 169 259–169 271, 2020.
- [131] J. Friedman, T. Hastie, R. Tibshirani *et al.*, *The elements of statistical learning*. Springer series in statistics New York, 2001, vol. 1, no. 10.
- [132] L. Boninsegna, F. Nüske, and C. Clementi, “Sparse learning of stochastic dynamical equations,” *The Journal of chemical physics*, vol. 148, no. 24, p. 241723, 2018.
- [133] A. A. Kaptanoglu, B. M. de Silva, U. Fasel, K. Kaheman, J. L. Callaham, C. B. Delahunt, K. Champion, J.-C. Loiseau, J. N. Kutz, and S. L. Brunton, “PySINDy: A comprehensive Python package for robust sparse system identification,” *arXiv preprint arXiv:2111.08481*, 2021.
- [134] S. Tamilselvi, S. Gunasundari, N. Karuppiah, A. Razak RK, S. Madhusudan, V. M. Nagarajan, T. Sathish, M. Z. M. Shamim, C. A. Saleel, and A. Afzal, “A review on battery modelling techniques,” *Sustainability*, vol. 13, no. 18, p. 10042, 2021.
- [135] N. Ding, K. Prasad, T. T. Lie, and J. Cui, “State of charge estimation of a composite lithium-based battery model based on an improved extended kalman filter algorithm,” *Inventions*, vol. 4, no. 4, p. 66, 2019.
- [136] G. L. Plett, “Extended Kalman filtering for battery management systems of LiPB-based HEV battery packs: Part 2. Modeling and identification,” *Journal of Power Sources*, vol. 134, no. 2, pp. 262–276, 2004.
- [137] H. He, R. Xiong, H. Guo, and S. Li, “Comparison study on the battery models used for the energy management of batteries in electric vehicles,” *Energy Conversion and Management*, vol. 64, pp. 113–121, 2012.
- [138] A. Swiderska-Mocek and A. Lewandowski, “Kinetics of Li-ion transfer reaction at LiMn<sub>2</sub>O<sub>4</sub>, LiCoO<sub>2</sub>, and LiFePO<sub>4</sub> cathodes,” *Journal of Solid State Electrochemistry*, vol. 21, pp. 1365–1372, 2017.
- [139] E. A. Wan and R. Van Der Merwe, “The unscented Kalman filter for nonlinear estimation,” in *Proceedings of the IEEE 2000 adaptive systems for signal processing, communications, and control symposium (Cat. No. 00EX373)*. Ieee, 2000, pp. 153–158.

- [140] X. Su, Q. Wu, J. Li, X. Xiao, A. Lott, W. Lu, B. W. Sheldon, and J. Wu, “Silicon-based nanomaterials for Lithium-ion batteries: a review,” *Advanced Energy Materials*, vol. 4, no. 1, p. 1300882, 2014.
- [141] C. R. Birkl, M. R. Roberts, E. McTurk, P. G. Bruce, and D. A. Howey, “Degradation diagnostics for Lithium ion cells,” *Journal of Power Sources*, vol. 341, pp. 373–386, 2017.
- [142] X. Lin, K. Khosravinia, X. Hu, J. Li, and W. Lu, “Lithium plating mechanism, detection, and mitigation in Lithium-ion batteries,” *Progress in Energy and Combustion Science*, vol. 87, p. 100953, 2021.
- [143] G. Zhang, X. Wei, S. Chen, G. Han, J. Zhu, and H. Dai, “Investigation the Degradation Mechanisms of Lithium-Ion Batteries under Low-Temperature High-Rate Cycling,” *ACS Applied Energy Materials*, vol. 5, no. 5, pp. 6462–6471, 2022.
- [144] S. Santhanagopalan, P. Ramadass, and J. Z. Zhang, “Analysis of internal short-circuit in a Lithium ion cell,” *Journal of Power Sources*, vol. 194, no. 1, pp. 550–557, 2009.
- [145] Y. Fang, A. J. Smith, R. W. Lindström, G. Lindbergh, and I. Furó, “Quantifying Lithium lost to plating and formation of the solid-electrolyte interphase in graphite and commercial battery components,” *Applied Materials Today*, vol. 28, p. 101527, 2022.
- [146] R. V. Bugga and M. C. Smart, “Lithium plating behavior in Lithium-ion cells,” *ECS transactions*, vol. 25, no. 36, p. 241, 2010.
- [147] P. P. Paul, E. J. McShane, A. M. Colclasure, N. Balsara, D. E. Brown, C. Cao, B.-R. Chen, P. R. Chinnam, Y. Cui, E. J. Dufek *et al.*, “A Review of Existing and Emerging Methods for Lithium Detection and Characterization in Li-Ion and Li-Metal Batteries,” *Advanced Energy Materials*, vol. 11, no. 17, p. 2100372, 2021.
- [148] Y. Tian, C. Lin, H. Li, J. Du, and R. Xiong, “Detecting undesired Lithium plating on anodes for Lithium-ion batteries—A review on the in-situ methods,” *Applied Energy*, vol. 300, p. 117386, 2021.
- [149] K. J. Sanders, A. A. Ciezki, A. Berno, I. C. Halalay, and G. R. Goward, “Quantitative Operando  $^{7}\text{Li}$  NMR Investigations of Silicon Anode Evolution during Fast Charging and Extended Cycling,” *Journal of the American Chemical Society*, vol. 145, no. 39, pp. 21 502–21 513, 2023.

- [150] S. E. O’Kane, W. Ai, G. Madabattula, D. Alonso-Alvarez, R. Timms, V. Sulzer, J. S. Edge, B. Wu, G. J. Offer, and M. Marinescu, “Lithium-ion battery degradation: how to model it,” *Physical Chemistry Chemical Physics*, vol. 24, no. 13, pp. 7909–7922, 2022.
- [151] Y. Guo, R. B. Smith, Z. Yu, D. K. Efetov, J. Wang, P. Kim, M. Z. Bazant, and L. E. Brus, “Li intercalation into graphite: direct optical imaging and Cahn–Hilliard reaction dynamics,” *The journal of physical chemistry letters*, vol. 7, no. 11, pp. 2151–2156, 2016.
- [152] T. F. Fuller, M. Doyle, and J. Newman, “Simulation and Optimization of the Dual Lithium Ion Insertion Cell,” *Journal of The Electrochemical Society*, vol. 141, no. 1, pp. 1–10, 1994.
- [153] S. Atlung, K. West, and T. Jacobsen, “Dynamic aspects of solid solution cathodes for electrochemical power sources,” *Journal of The Electrochemical Society*, vol. 126, no. 8, p. 1311, 1979.
- [154] E. Prada, D. Di Domenico, Y. Creff, J. Bernard, V. Sauvant-Moynot, and F. Huet, “Simplified electrochemical and thermal model of LiFePO<sub>4</sub>-graphite Li-ion batteries for fast charge applications,” *Journal of The Electrochemical Society*, vol. 159, no. 9, p. A1508, 2012.
- [155] F. B. Planella and W. D. Widanage, “A Single Particle model with electrolyte and side reactions for degradation of Lithium-ion batteries,” *Applied Mathematical Modelling*, vol. 121, pp. 586–610, 2023.
- [156] S. G. Marquis, V. Sulzer, R. Timms, C. P. Please, and S. J. Chapman, “An asymptotic derivation of a single particle model with electrolyte,” *Journal of The Electrochemical Society*, vol. 166, no. 15, p. A3693, 2019.
- [157] G. Richardson, I. Korotkin, R. Ranom, M. Castle, and J. Foster, “Generalised single particle models for high-rate operation of graded Lithium-ion electrodes: Systematic derivation and validation,” *Electrochimica Acta*, vol. 339, p. 135862, 2020.
- [158] S. Sahu and J. M. Foster, “A continuum model for Lithium plating and dendrite formation in Lithium-ion batteries: Formulation and validation against experiment,” *Journal of Energy Storage*, vol. 60, p. 106516, 2023.
- [159] P. Arora, M. Doyle, and R. E. White, “Mathematical modeling of the Lithium deposition overcharge reaction in Lithium-ion batteries using carbon-based negative electrodes,” *Journal of The Electrochemical Society*, vol. 146, no. 10, p. 3543, 1999.

- [160] X.-G. Yang, S. Ge, T. Liu, Y. Leng, and C.-Y. Wang, “A look into the voltage plateau signal for detection and quantification of Lithium plating in Lithium-ion cells,” *Journal of Power Sources*, vol. 395, pp. 251–261, 2018.
- [161] V. Ovejas and A. Cuadras, “Effects of cycling on Lithium-ion battery hysteresis and overvoltage,” *Scientific reports*, vol. 9, no. 1, p. 14875, 2019.
- [162] B. Protas, B. R. Noack, and M. Morzynski, “An Optimal Model Identification For Oscillatory Dynamics With a Stable Limit Cycle,” *Journal of Nonlinear Science*, vol. 24, pp. 245–275, 2014.
- [163] W. H. Press, B. P. Flanner, S. A. Teukolsky, and W. T. Vetterling, *Numerical Recipes: the Art of Scientific Computations*. Cambridge University Press, 1986.
- [164] Thawornwattana, Yuttapong and Dalquen, Daniel and Yang, Ziheng, “Designing simple and efficient Markov chain Monte Carlo proposal kernels,” *Bayesian Analysis*, vol. 13, no. 4, pp. 1033–1059, 2018.
- [165] M. Bédard, R. Douc, and E. Moulines, “Scaling Analysis of Delayed Rejection MCMC Methods,” *Methodology and Computing in Applied Probability*, vol. 16, no. 4, pp. 811–838, 2014.
- [166] P. J. Green and A. Mira, “Delayed rejection in reversible jump Metropolis–Hastings,” *Biometrika*, vol. 88, no. 4, pp. 1035–1053, 2001.
- [167] P. C. Robert and C. George, *Monte Carlo Statistical Methods*, 2nd ed. New York: Springer, 2004.